

Dissertation zur Erlangung des Doktorgrades
der Fakultät für Chemie und Pharmazie
der Ludwig-Maximilians-Universität München

COVALENT TRIAZINE FRAMEWORKS: STRUCTURE, PROPERTIES AND APPLICATIONS IN GAS STORAGE AND ENERGY CONVERSION

Stephan Hug

aus

Frankfurt am Main, Deutschland

2014

ERKLÄRUNG

Diese Dissertation wurde im Sinne von § 7 der Promotionsordnung vom 28. November 2011 von Frau Prof. Dr. Bettina Lotsch betreut.

EIDESSTATTLICHE VERSICHERUNG

Diese Dissertation wurde eigenständig und ohne unerlaubte Hilfe erarbeitet.

München, 02.06.2014

.....
(Stephan Hug)

Dissertation eingereicht am

1. Gutachterin: Prof. Dr. Bettina Lotsch

2. Gutachter: Prof. Dr. Jürgen Senker

Mündliche Prüfung am 18.07.2014

Für meine Familie

ACKNOWLEDGMENTS

An erster Stelle danke ich Prof. Dr. Bettina Lotsch für die Betreuung meiner Arbeit und das spannende Thema, das ich bearbeiten durfte. Die vielen Diskussionen und Anregungen haben in großem Maße zum Erfolg dieser Arbeit beigetragen.

Prof. Dr. Jürgen Senker danke ich für die Übernahme des Zweitgutachtens und die hervorragende Kooperation mit den halbjährlichen Treffen, die immer spannende Diskussionen und Forschungsansätze hervor brachten.

Prof. Dr. Dina Fattakhova-Rohlfing, Prof. Dr. Hans-Christian Böttcher, Prof. Dr. Konstantin Karaghiosoff und Prof. Dr. Thomas Bein danke ich für ihren Beisitz in meiner Promotionskommission. Ein wichtiger Teil dieser Doktorarbeit waren die Kooperationen, die einen wesentlichen Beitrag zu dieser Arbeit lieferten. Ganz besonderen Dank gelten hier Maria Mesch, Nadine Popp und Prof. Dr. Jürgen Senker (Universität Bayreuth), Hyunchul Oh und Dr. Michael Hirscher (Max Planck Institut für Intelligente Systeme) und Kimberly See und Prof. Dr. Ram Seshadri (University of California).

Prof. Dr. Tina Scheu danke ich, dass sie mir als Zweitbetreuerin im Exzellenzcluster „Nanosystems Initiative Munich“ (NIM) zur Verfügung stand.

Katharina Schwinghammer, Kimberly See, Linus Stegbauer, Christian Ziegler und Olaf Alberto von Mankowski danke ich für das Korrekturlesen weiter Teile meiner Arbeit.

Ein besonderer Dank gilt meinen Forschungspraktikanten und Bacheloranten, die mich beim Ausführen der umfangreichen experimentellen Arbeit unterstützt haben: Katharina Schwinghammer, Ursula Pachmayr, Kristina Ritter, Laura Hermanns, Nina Vrielink, Stefan Datz, Marius Reymann und Niklas Cordes.

Christian Minke danke ich für das Durchführen zahlreicher Festkörper-NMR und REM/EDX Messungen. Viola Duppel danke ich für TEM und ebenfalls REM/EDX Messungen. Weitere TEM Untersuchungen wurden dankenswerterweise von Andreas Wisnet und Dr. Teresa Dennenwaldt durchgeführt. Helmut Hartl und Marie-Luise Schreiber danke ich für die Durchführung von ICP Messungen. Dr. Sophia Makowski, Katrin Rudolf und Christine Pösl danke ich für zahlreiche DTA/TG Messungen.

Ein großer Dank gilt den Kollegen vom Arbeitskreis Lotsch, die alltäglich für eine gute Atmosphäre gesorgt haben und trotz der Aufspaltung auf zwei Standorte immer eine Gemeinschaft gebildet haben. Besonders danke ich hier meinen Labornachbarn Dr. Michael Tauchert, Dr. Shen Li und Linus Stegbauer, die dem „OC-Labor“ alle Ehre gemacht haben.

Den Mitarbeitern der Arbeitskreise Schnick, Johrendt und Oeckler danke ich für die zahlreichen lustigen Veranstaltung in Form von Wandertagen, Ausflügen und Weihnachtsfeiern.

Ganz besonders danke ich meinen Kollegen Chris, Dr. Sepp und Werner für all die lustigen, süffigen und abwechslungsreichen Abendveranstaltungen, die immer wieder erfolgreich vom Uni-Alltag abgelenkt haben. Mit Euch habe ich wahre Freunde gefunden!

Meinen Freunden vom Semester(essen), Ines, Doro, Sandra, Meli, Alex, Michi, Klaus, Christian und Jürgen danke ich für die einzigartigen Berg- und Fahrradtouren und natürlich die allwöchentlichen Mensasessions!

Meinen Mitspielern vom TSV Grünwald danke ich für die hervorragende Ablenkung vom Alltag, die mir das wöchentliche Training, die Spiele und die Turniere gegeben haben.

Meinen engsten Freunden Teresa, Fabienne, Max, Eric, Oli, Simon, Niklas, Luci, Jan und Alex bin ich unendlich dankbar für die einzigartigen Freundschaften, die zahlreichen unvergesslichen Erlebnisse und die Leichtigkeit mit der sie mich immer wieder meinen Uni-Stress vergessen lassen haben.

Meiner WG, die mir ein echtes Zuhause gegeben hat, danke ich vom ganzen Herzen. Katharina, Albi und Martin wir werden immer die Vier aus der Landwehrstraße bleiben!

Albi, Dir möchte ich ganz besonders danken. Dich werde ich am Meisten an München vermissen und ich bin sehr froh mit Dir einen Freund fürs Leben gefunden zu haben.

Zu guter Letzt danke ich meiner gesamten Familie, die mich all die Jahre immer unterstützt hat, mir immer ein Zuhause und viel Kraft gegeben hat. Ohne Euch wäre diese Arbeit nie möglich gewesen!

Ich kann mich glücklich schätzen Euch zu haben und Teil dieser Familie zu sein.

*Der Beginn aller Wissenschaften ist das Erstaunen,
dass die Dinge so sind, wie sie sind.
(Aristoteles)*

TABLE OF CONTENTS

1	INTRODUCTION.....	1
1.1	POROUS MATERIALS	2
1.1.1	POROUS ORGANIC POLYMERS.....	2
1.2	CARBON CAPTURE AND STORAGE	10
1.2.1	POSTCOMBUSTION CAPTURE.....	13
1.3	OBJECTIVES	16
1.4	REFERENCES	16
2	METHODS	23
2.1	PHYSISORPTION.....	23
2.1.2	PHYSISORPTION ISOTHERMS.....	23
2.1.3	LANGMUIR THEORY	25
2.1.4	BET THEORY	26
2.1.5	PORE SIZE DISTRIBUTION ANALYSIS.....	26
2.1.6	HEAT OF ADSORPTION.....	27
2.1.7	GAS SELECTIVITY	27
2.1.8	EXPERIMENTAL DETAILS.....	29
2.2	POWDER X-RAY DIFFRACTION	30
2.3	INFRARED SPECTROSCOPY	30
2.4	ULTRAVIOLET-VISIBLE SPECTROSCOPY	31
2.5	ELEMENTAL ANALYSIS	31
2.5.1	CHNS-ANALYSIS	31
2.5.2	INDUCTIVELY COUPLED PLASMA ATOMIC EMISSION SPECTROSCOPY.....	31
2.6	ELECTRON MICROSCOPY	32
2.6.1	TRANSMISSION ELECTRON MICROSCOPY.....	32
2.6.2	SCANNING ELECTRON MICROSCOPY	32
2.7	NUCLEAR MAGNETIC RESONANCE SPECTROSCOPY	33
2.7.3	SOLUTION-STATE NMR SPECTROSCOPY	33
2.7.4	SOLID-STATE NMR SPECTROSCOPY	33
2.8	DIFFERENTIAL THERMAL ANALYSIS AND THERMOGRAVIMETRY.....	34
2.9	MASS SPECTROMETRY.....	34
2.10	REFERENCES	35
3	COVALENT TRIAZINE FRAMEWORKS AS METAL COORDINATION SCAFFOLDS	36

3.1	A FUNCTIONAL TRIAZINE FRAMEWORK BASED ON <i>N</i>-HETEROCYCLIC BUILDING BLOCKS.....	37
3.1.1	INTRODUCTION.....	38
3.1.2	EXPERIMENTAL.....	39
3.1.3	RESULTS AND DISCUSSION.....	41
3.1.4	CONCLUSIONS.....	50
3.1.5	BIBLIOGRAPHY.....	50
4	COVALENT TRIAZINE FRAMEWORKS FOR GAS CAPTURE AND STORAGE.....	53
4.1	A FLUORENE BASED COVALENT TRIAZINE FRAMEWORK WITH HIGH CO₂ AND H₂ CAPTURE AND STORAGE CAPACITIES.....	54
4.1.1	INTRODUCTION.....	55
4.1.2	EXPERIMENTAL SECTION.....	56
4.1.3	RESULTS AND DISCUSSION.....	59
4.1.4	CONCLUSIONS.....	66
4.1.5	BIBLIOGRAPHY.....	67
4.2	NITROGEN-RICH COVALENT TRIAZINE FRAMEWORKS AS EFFICIENT PLATFORMS FOR SELECTIVE GAS CAPTURE AND STORAGE.....	70
4.2.1	INTRODUCTION.....	70
4.2.2	EXPERIMENTAL SECTION.....	71
4.2.3	RESULTS AND DISCUSSION.....	73
4.2.4	CONCLUSION.....	82
4.2.5	BIBLIOGRAPHY.....	83
5	COVALENT TRIAZINE FRAMEWORKS IN ENERGY CONVERSION AND STORAGE.....	86
5.1	COVALENT TRIAZINE FRAMEWORKS FOR PHOTOCATALYTIC HYDROGEN EVOLUTION.....	87
5.1.1	INTRODUCTION.....	87
5.1.2	EXPERIMENTAL.....	88
5.1.3	RESULTS AND DISCUSSION.....	89
5.1.4	CONCLUSION AND OUTLOOK.....	99
5.1.5	REFERENCES.....	99
5.2	COVALENT TRIAZINE FRAMEWORKS AS BIPOLAR ELECTRODE MATERIALS IN ENERGY STORAGE DEVICES..	101
5.2.1	INTRODUCTION.....	101
5.2.2	EXPERIMENTAL.....	101
5.2.3	RESULTS AND DISCUSSION.....	102
5.2.4	CONCLUSION AND OUTLOOK.....	106
5.2.5	REFERENCES.....	106

6	SUMMARY	108
6.1	SYNTHESIS OF NEW COVALENT TRIAZINE FRAMEWORKS	108
6.2	METAL DOPING OF <i>bipy</i> -CTFs	109
6.3	CARBON DIOXIDE UPTAKES AND GAS SELECTIVITIES OF COVALENT TRIAZINE FRAMEWORKS	109
6.4	HYDROGEN STORAGE OF COVALENT TRIAZINE FRAMEWORKS	110
6.5	COVALENT TRIAZINE FRAMEWORKS IN PHOTOCATALYSIS	111
6.6	COVALENT TRIAZINE FRAMEWORKS IN ENERGY STORAGE DEVICES	111
7	CONCLUSION AND OUTLOOK	113
7.1	REFERENCES	115
8	APPENDIX	118
8.1	SUPPORTING INFORMATION	119
8.1.1	SUPPORTING INFORMATION FOR CHAPTER 3.1	119
8.1.2	SUPPORTING INFORMATION FOR CHAPTER 4.1	125
8.1.3	SUPPORTING INFORMATION FOR CHAPTER 4.2	146
8.2	LIST OF PUBLICATIONS.....	170
8.3	CONTRIBUTIONS TO CONFERENCES	171

1 INTRODUCTION

The “Fifth Assessment Report” of the Intergovernmental Panel on Climate Change (IPCC)^[1-3] has recently attracted a great deal of attention. The main statements conclude that the climate change is unequivocal, ascribed to an observed warming of the atmosphere and ocean, diminishing amounts of snow and ice and a rising sea level.^[1] The future perspectives based on different scenarios forecast continuing global warming resulting in further changes in all components of the climate system with mostly unpredictable consequences. Since the largest contributor to the climate change, the rising emissions of CO₂, is man-made, the main objective in slowing down the global warming is to control and reduce these anthropogenic emissions. The main strategies for this process include increasing the energy efficiency of established processes, the growth of the renewable energy share and the capture and storage of carbon dioxide. All these objectives are part of wide-spread research and especially in material science the search for new materials and their applications is an important task. The field of synthetically manufactured porous materials is comparably young and produced numerous new classes of materials which are promising for the use in catalysis, optoelectronics, photovoltaics, biotechnology, gas capture and storage, as well as energy storage.^[4] Especially porous organic polymers (POPs) are of rising interest because of their easy and cheap synthesis and large variety.^[5-7]

The introduction to this thesis will focus on the classification of porous materials. Special attention will be paid to two POP classes, covalent organic frameworks (COFs) and covalent triazine frameworks (CTFs), and their applications. Furthermore, the concept of carbon capture and storage (CCS) will be discussed with a focus on the applications of POPs in that field. Finally, this introduction will close with the objectives of this thesis.

1.1 POROUS MATERIALS

The surface area of materials can be divided in internal and external surface area. The external surface area is defined as the cover surrounding the discrete particles or agglomerates including all cracks, which are wider than they are deep.^[8] Therefore the internal surface area is described by all cavities which are deeper than they are wide and accessible to gas molecules. Such cavities are called pores and are described by their diameters as micropores (<2 nm), mesopores (2-50 nm) and macropores (>50 nm), as classified by the International Union of Pure and Applied Chemistry (IUPAC).^[8] The porosity of a material is defined as the ratio of the volume of pore space to the volume of the material. If the porosity exceeds 0.2, the material is described as a porous material.^[4] A further specification of porous materials is the term “nanoporous materials” which describes all porous materials in a pore size range up to 100 nm. Nanoporous materials can be classified into five groups: Zeolites, mesoporous silicas, porous carbons, metal-organic frameworks (MOFs) and POPs. The key properties combining all these materials are their high specific surface areas and porosities. The applications of nanoporous materials depend on their pore structure, surface composition, thermal and chemical stability, toxicity and availability. Commercially important applications are molecular sieving, ion exchange and catalysis, in which zeolites have been used for decades. Because of their unique structures, porous materials are promising materials for various other applications such as gas capture and storage, biotechnology, microelectronics, membranes, sensing, photocatalysis and photovoltaics.^[4]

1.1.1 POROUS ORGANIC POLYMERS

Classic polymers are primarily built up by one-dimensional chains, whereas POPs, a special class of polymers, exhibit two- or three-dimensional structures which create and stabilize the pores in the materials. The field of POPs has emerged in the last decades (Figure 1.1.1), but unfortunately the accompanied classification and nomenclature of new POPs in the literature has developed into a rather confusing state. Some POPs are simply described by their general characteristics as being a POP, such as microporous organic polymers (MOPs),^[9] polymeric organic frameworks (POFs)^[10] or porous polymer frameworks (PPFs)^[11] without giving an idea of the linking nature or the functional groups. Others are more specifically defined using their chemical binding characteristics such as conjugated microporous polymers (CMPs)^[12] or hypercrosslinked organic polymers (HCPs).^[13] A rather preferred way of naming POPs is to include the functional groups or the type of linker involved. Examples are azo-linked polymers (ALPs),^[14] benzimidazole-linked polymers (BILPs),^[15] imine-linked polymers (ILPs)^[16] or covalent triazine frameworks (CTFs),^[17] but these examples do not

refer to the type of porosity observed. There are numerous other nomenclatures which will not be listed here.

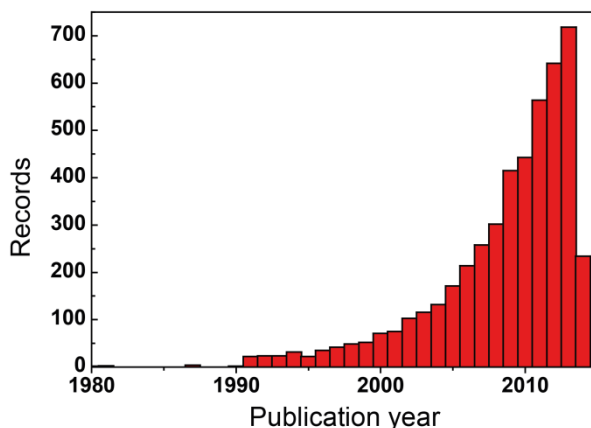
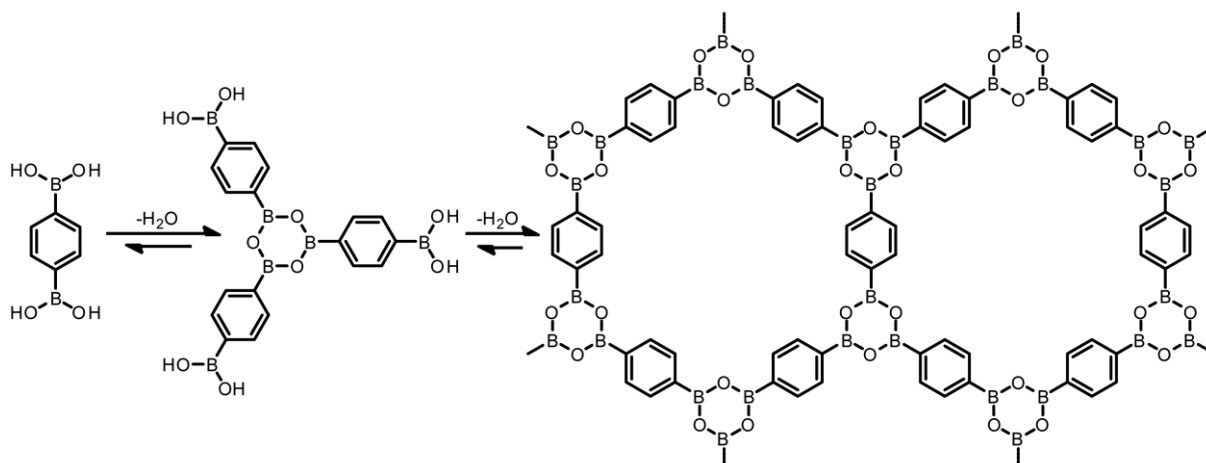


Figure 1.1.1. Publications per year based on the search of the topic “porous organic polymer” in the Web of Science™ database. Accessed 2014-05-05.

As POPs summarize a wide area of porous materials with different linking types and functional groups, they differ a lot in their properties and applications. Overall, they show a wide range of surface areas up to $6461 \text{ m}^2 \text{ g}^{-1}$ ^[18] and are often cheap and easy to synthesize. With some exceptions they are amorphous in nature and therefore show mostly broad and hardly controllable pore size distributions. The synthetic diversity and porous nature of POPs makes them interesting for various applications, such as gas storage and separation and catalysis^[5] or more special applications, which are dependent on targeted design like electronic capacitors,^[19-20] biotechnology,^[21] membranes^[22] and optoelectronics.^[6]

Covalent organic frameworks

The only crystalline class of POPs are COFs, which were first synthesized by Yaghi and co-workers in 2005.^[23] Until then, it was believed that the synthesis of crystalline extended organic structures linked by covalent bonds is very difficult if not impossible, because it would require microscopic



Scheme 1.1.1. Self-condensation reaction of 1,4-benzenediboric acid leads to the formation of COF-1.

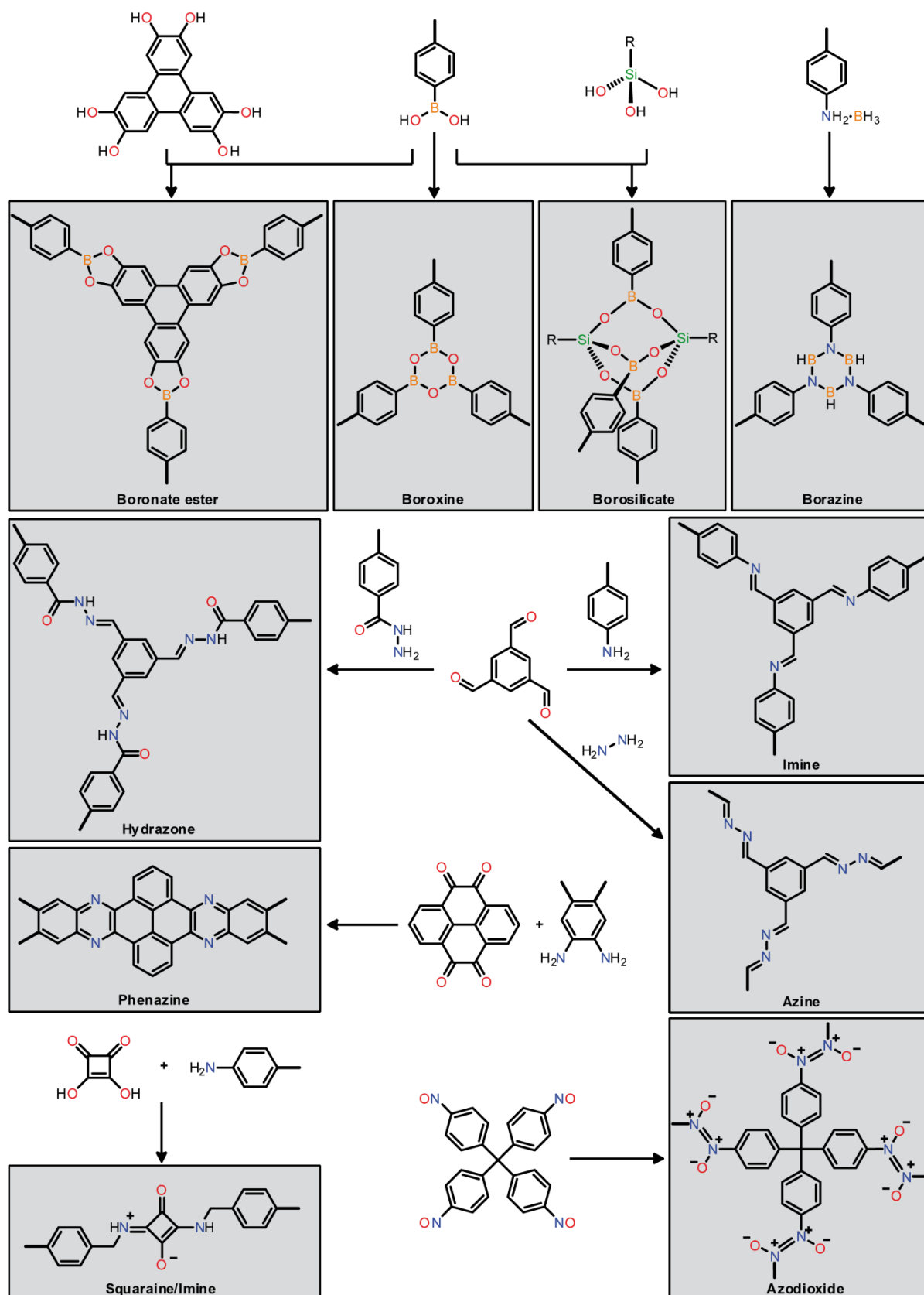


Figure 1.1.2. Schematic illustrations of different COF linking types.

reversibility of the covalent bond formation. Yaghi *et al.* solved this problem by using reversible dehydration reactions of boronic acids to form boroxines or boronate esters (see Scheme 1.1.1 and

Figure 1.1.2, top left). The use of closed reaction vessels under vacuum, long reaction times (72 h), moderate heating (120 °C) and a solvent mixture (mesitylene/dioxane) which sparingly dissolves boronic acids were found suitable for the production of crystalline materials. The produced materials called COF-1 and COF-5 showed permanent porosity, high surface areas (711 and 1590 m² g⁻¹) and high thermal stabilities (500-600 °C).

In the following years the synthesis of new COFs increased rapidly, resulting in more than 100 different COFs. Almost two thirds of the synthesized COFs are based on the boronate ester linkage^[23-51] and only six on boroxines.^[23-24,52-54] As can be seen in Figure 1.1.2 other linkages such as imines,^[20,34,55-65] hydrazones,^[66-67] borosilicates,^[68] borazines,^[69] squaraines,^[70] phenazines,^[71] azines^[72] and azodioxides^[73] were used to produce COFs. Especially imines became very popular in the past years, because of their high thermal and chemical stabilities. The covalent triazine frameworks CTF-0,^[74] CTF-1^[17] and CTF-2^[75] are assigned to the COF family as well, but will be discussed in more details in the next chapter.

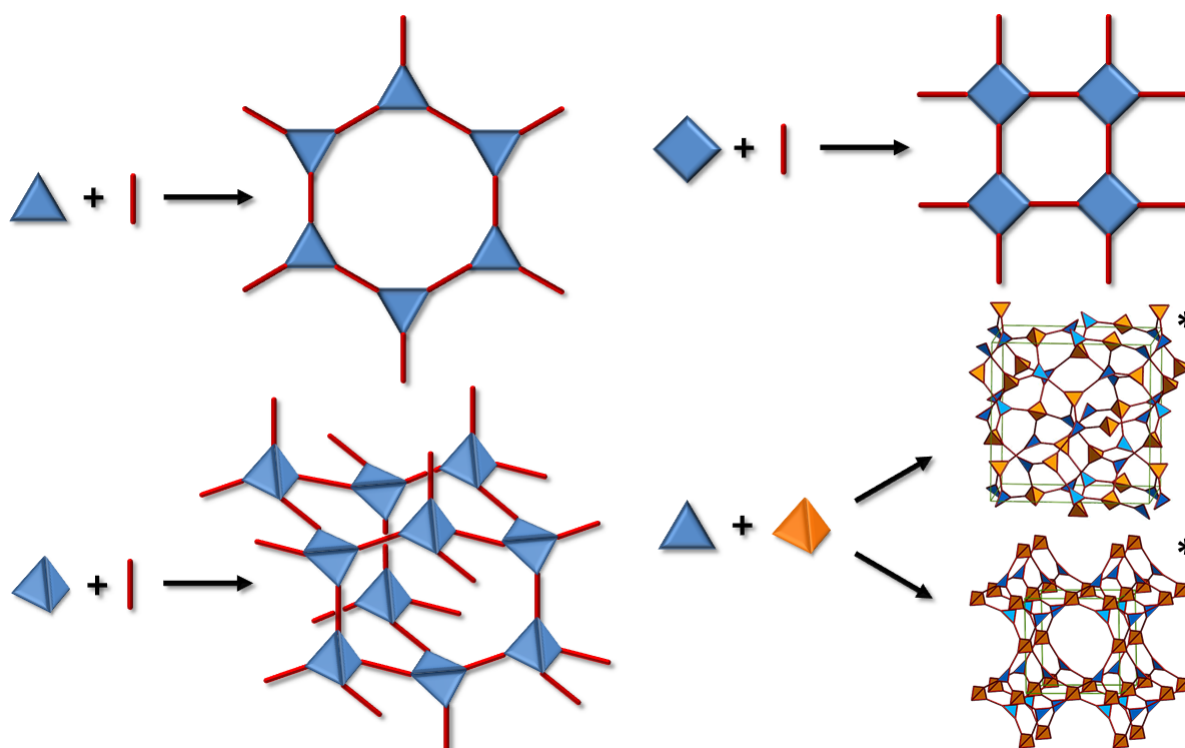


Figure 1.1.3. Combination of different SBUs with the resulting framework units. The combination of a triangle and a tetrahedron can form either a cubic framework with $P43m$ (top) or with $I43d$ (bottom) symmetry. The two graphics marked with an asterisk were used with permission from Omar M. Yaghi from Reference [76].

By analogy to the principle of reticular chemistry introduced for MOFs by Yaghi and O'Keefe *et al.* implying the potential of targeted structure and pore design,^[77-78] COFs can be designed and built from secondary building units (SBUs) to form specific topologies (Figure 1.1.3). The choice of linkers and linking types can lead to two- or three-dimensional frameworks with a broad range of pore sizes and surface areas. The smallest pore size was found for the 3D COF MCOF-1^[48] with 0.64 nm and the

largest for the 2D stacked COFs $D_{TP-A_{NDI}}\text{-COF}$ and $D_{TP-A_{PyrDI}}\text{-COF}$ ^[49] with 5.3 nm. The lowest density and the highest surface areas were found for the 3D COFs COF-108 ($0.17\text{ cm}^3\text{ g}^{-1}$) and COF-102 ($4210\text{ m}^2\text{ g}^{-1}$).^[24]

The synthetic versatility of COFs was also shown when Jiang and co-workers synthesized functionalized COFs by co-condensation with linkers carrying functional groups.^[33,56,59] Remarkably, the crystallinity was not affected by using different types of linkers. Once linkers were used which carry azide or ethynyl groups, post-modification of the COFs was possible by click reactions with various molecules.^[33,56] Similar results were found by Dichtel and co-workers when they functionalized COF-102 using tetrahedral co-condensates carrying only three boronic acids and one functional terminal group.^[53-54,79] After employing a co-condensation strategy using allyl groups, post-modification *via* thiol-ene reactions was possible.^[54]

The synthetic variety combined with the high thermal and in many cases chemical stability makes COFs promising for various applications. First research was done on gas adsorption and separation. Especially the adsorption of H_2 ,^[36,45,47,58,62,65,69,80-81] CO_2 ^[9,45,58,62,65,80] and CH_4 ^[45,47-48,58,64,80] has been studied, where the 3D COF-102 showed remarkably high uptakes for various gases (H_2 : 6.75 wt% at 77 K and 35 bar, CO_2 : 30.0 mmol g^{-1} at 298 K and 55 bar, CH_4 : 11.7 mmol g^{-1} at 298 K and 35 bar).^[80] Additionally it was found that the incorporation of palladium nanoparticles in COF-102 led to a significant enhancement of H_2 uptake at 298 K.^[81] Worth mentioning are the gas adsorption of ammonia in COF-10 with the highest amount found for all porous materials so far (15 mmol g^{-1} , 298 K, 1 bar)^[82] and the exceptionally high selectivity of MCOF-1 for C_2H_4 and C_2H_6 towards CH_4 .^[48]

Since most 2D COFs show an eclipsed AA-type layer stacking caused by strong interlayer π - π -interactions, studies on the electronic properties of COFs were done soon after their discovery. The first semiconducting and luminescent COF was synthesized by Jiang and co-workers and was based on pyrene units, showing *p*-type electronic behavior.^[28] The same group presented the first photoconductive COF^[52] and the first *n*-channel semiconducting COF, which showed relatively high charge carrier mobility ($0.6\text{ cm}^2\text{ V}^{-1}\text{ s}^{-1}$) and photoconductivity up to 1000 nm.^[31] The highest charge carrier mobility ($3.0\text{-}8.1\text{ cm}^2\text{ V}^{-1}\text{ s}^{-1}$) was found for porphyrine based COFs.^[34] Jiang and co-workers also presented different COFs, which are based on donor and acceptor units and were shown to be photoconductive.^[43-44,49] Phthalocyanine based COFs were found to absorb visible light as well and to show photoconductivity in the visible light region.^[29-30,42] Very recently the groups of Bein and Jiang presented ordered heterojunction-type solar cells based on COFs.^[40,71] Bein and co-workers used a thiophene-based boronate COF as electron donor and infiltrated the pores with the electron acceptor [6,6]-phenyl- C_{61} -butyric acid methyl ester (PCBM). The resulting solar cell had a conversion efficiency of 0.053%.^[40] Jiang and co-workers were able to produce a solar cell with a conversion efficiency of 0.9% by using a phenazine based COF infiltrated with fullerene.^[71] But not only the

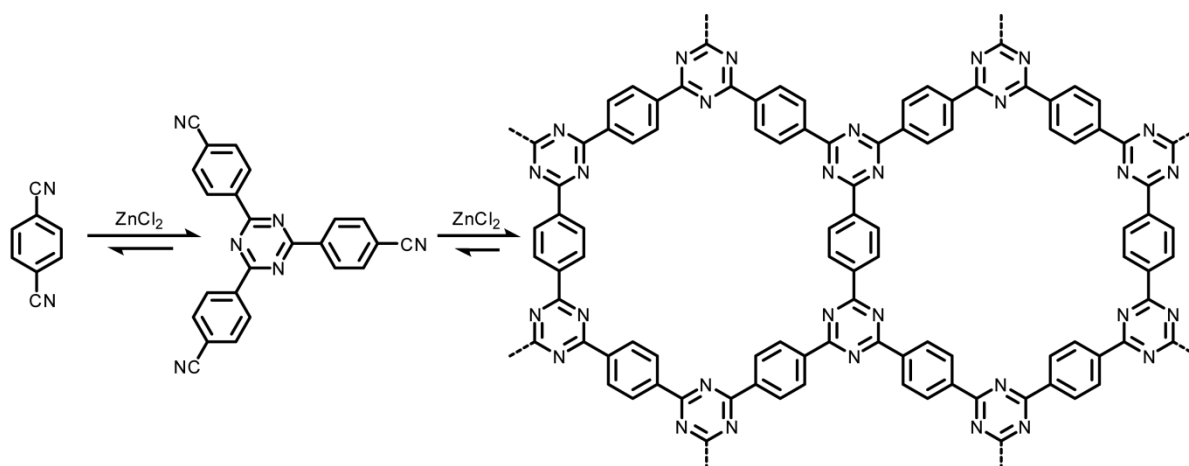
possible application of COFs for solar cells was studied, but COFs were also investigated as capacitors by using redox-active 2,6-diaminoanthraquinone as building block.^[20] Another recent application was demonstrated by using a hydrazone-linked COF as photocatalyst for the production of H₂, which exhibited continuous H₂ production for many hours under visible light irradiation.^[66]

Although catalysis plays an important role in the application of zeolites and MOFs, only a few examples of COFs used in catalysis were reported so far, while all were based on imine-linkages, due to their higher chemical stability compared to boronate-linked COFs.^[56,60,83-84] COF-LZU1 was post-modified by incorporation of Pd(OAc)₂ and used as catalyst for Suzuki-Miyaura couplings.^[60] It showed high yields (96-98%) with eight different aryl halides and required less catalyst loading and shorter reaction times compared to a Pd(II)-containing MOF. A second example of a COF used for catalysis was published recently. A series of porphyrin-COFs with different amounts of ethynyl units linked to the pore walls were synthesized and post-modified by click chemistry with pyrrolidine functions.^[56] Pyrrolidines are well-known organocatalysts for Michael addition reactions and therefore this reaction was tested on the COFs, showing comparable yields and stereoselectivity, but faster reaction times than the monomeric catalyst. The group of Banerjee incorporated gold and palladium nanoparticles in an imine-based COF.^[83-84] The former one was used as catalyst in the reduction of 4-nitrophenol,^[83] and the latter one in Heck and Sonogashira cross-coupling reactions,^[84] both showing high yields and good recyclability.

A very recent and rather special application of COFs was that as a chemosensor, where Py-Azine COF showed high selectivity towards the explosive 2,4,6-trinitrophenol compared to other nitro compounds.^[72]

Covalent triazine frameworks

CTFs are very often referred as a subclass of COFs since the three CTFs CTF-0,^[74] CTF-1^[17] and CTF-2^[75] are crystalline porous frameworks. However, most of the synthesized CTFs exhibit poor crystallinity and therefore should be described as a subclass of POPs. Here we will refer to CTFs as any porous



Scheme 1.1.2. Synthesis of CTF-1 by trimerization of 1,4-dicyanobenzene under ionothermal conditions.

material which has been synthesized by the polymerization of nitriles.

CTFs are synthesized by the trimerization of nitriles under Lewis acidic conditions, which was probably done for the first time in 1973 by Miller, who polymerized numerous nitriles under ionothermal conditions without analyzing the potentially porous nature of the materials.^[85] This concept was adapted by Antonietti and co-workers in 2008 when they introduced five different CTFs which they synthesized in a ZnCl_2 melt at 400 °C.^[17] In this work they also presented CTF-1 as the first crystalline CTF (Scheme 1.1.2). The materials exhibited high thermal and chemical stabilities in combination with surface areas up to 2475 $\text{m}^2 \text{g}^{-1}$. Further works by the same group showed that synthesis at temperatures up to 700 °C can lead to higher surface areas (up to 3270 $\text{m}^2 \text{g}^{-1}$) but is

Table 1.1.1. BET surface areas of CTFs along with the used reaction types. The table only includes the lowest synthesis temperature for each monomer and the synthesis conditions which leads to the highest surface area.

Monomer ^a	Synthesis temperature [°C]	Reaction type ^b	BET surface area [$\text{m}^2 \text{g}^{-1}$]	Reference
1	400	A	791	[17]
1	400/600	A	3270	[86]
1	25	B	2	[87]
1	110	C	4	[87]
2	400	A	810	[88]
2	400/600	A	2810	[88]
3	400	A	650	[88]
4	400	A	730	[88]
4	400/600	A	2011	[74]
5	300	A	162	[88]
6	400	A	90	[75]
6	450	A	2255	[75]
7	400	A	730	[17]
7	400/600	A	2130	[88]
8	400	A	584	[17]
9	400	A	2475	[17]
9	25	B	776	[87]
9	110	C	464	[87]
10	400	A	0	[88]
11	400	A	1345	[88]
11	25	B	867	[87]
11	110	C	542	[87]
12	400	A	862	[88]
12	25	B	960	[87]
12	110	C	542	[87]
13	25	B	1152	[87]
13	110	C	947	[87]
14	400	A	1130	[89]
14	600	A	1166	[89]
15	400	A	1618	[88]
16	300	A	640	[90]
16	500	A	1510	[90]
17	400	A	1900	[88]
18	25	B	571	[87]
18	110	C	523	[87]
19	400	A	662	[91]
19	600	A	1535	[91]
20	400	A	2235	[92]

^aSee Figure 1.1.4; ^bA = ionothermal in ZnCl_2 , B = in CHCl_3 ($\text{CF}_3\text{SO}_3\text{H}$ catalyzed), C = in $\text{CF}_3\text{SO}_3\text{H}$ (microwave assisted).

accompanied by loss of nitrogen and in particular the triazine units.^[86,88,93] In 2012 the group of Cooper introduced an alternative method to produce CTFs at lower temperatures.^[87] They used the Lewis acid trifluoromethanesulfonic acid ($\text{CF}_3\text{SO}_3\text{H}$) as catalyst in a room temperature synthesis and in a microwave assisted synthesis which led to CTFs with surface areas up to $1152 \text{ m}^2 \text{ g}^{-1}$ and nitrogen contents close to the theoretical values. Notably, the materials were of pale yellow to brown color in contrast to the black materials synthesized by the Antonietti group through syntheses in salt melts. UV-Vis measurements showed broad absorption bands and the materials exhibited bright fluorescence under UV light. A summary of all monomers which have been used for the synthesis of CTFs so far is shown in Figure 1.1.4 and the resulting BET surface areas under different synthesis conditions are summarized in Table 1.1.1.

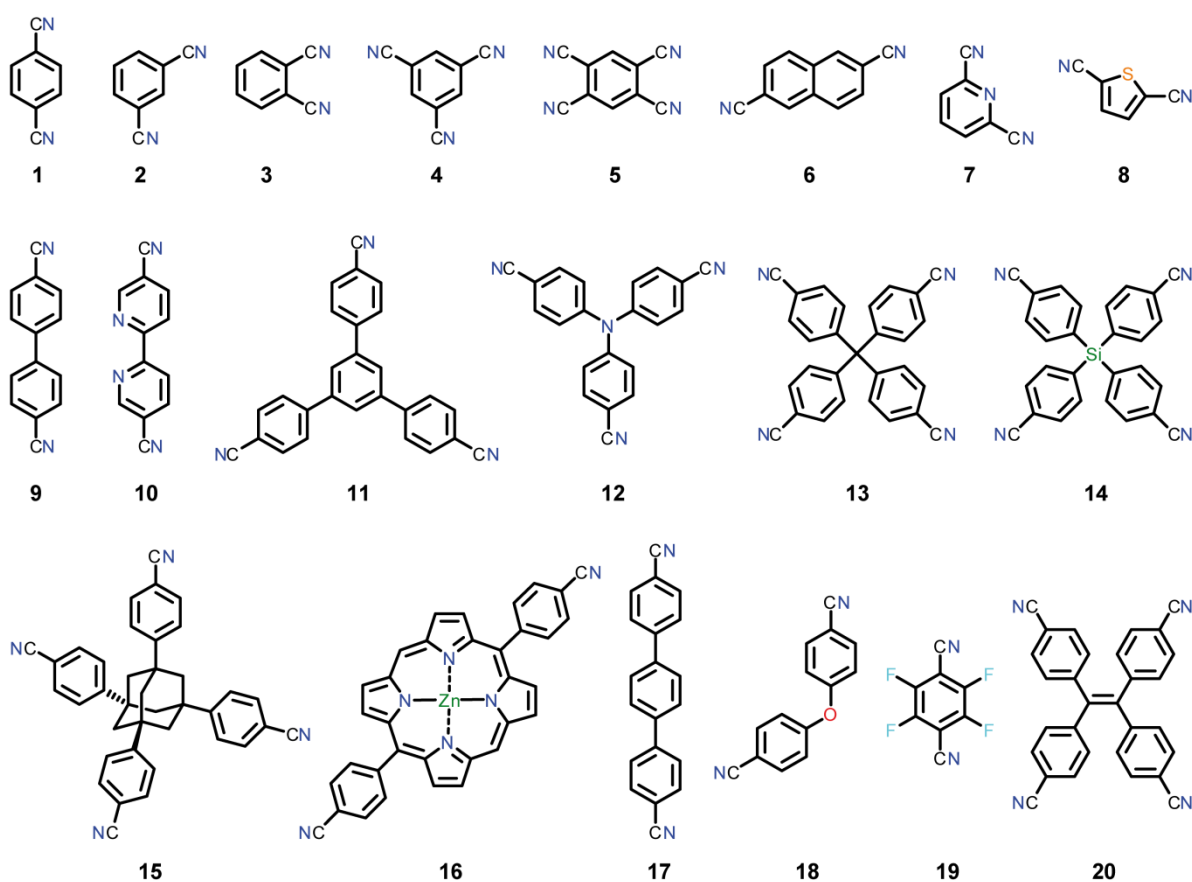


Figure 1.1.4. Building blocks used for CTF synthesis.

Because of the high thermal and chemical stabilities combined with high surface areas and large nitrogen contents, CTFs are promising materials for numerous applications. Most of the CTFs were tested towards their hydrogen,^[17,92,94-95] carbon dioxide^[74,87,89-92,94] and methane^[92,94] sorption capacities as gas storage or capture materials. The highest uptakes for hydrogen and methane were found for PCTF-1 based on monomer **20** ($1.86 \text{ wt}\% \text{ H}_2$ at 77 K, 1 bar and $0.97 \text{ mmol g}^{-1} \text{ CH}_4$ at 293 K, 1 bar)^[92] and the highest sorption capacity for carbon dioxide was reported for FCTF-600 based on **19** (5.53 mmol g^{-1} at 273 K, 1 bar),^[91] which was the second highest uptake found for all POPs at that

time. Additionally, membranes based on CTFs were synthesized in super-acidic conditions and successfully tested for gas separation.^[96] Besides gas capture, the adsorption of organic dyes in very good quantities^[97-98] and of the pollutant 4,4'-(propane-2,2-diyl)diphenol has been demonstrated.^[99] Another focus in terms of possible applications of CTFs is on using the materials as matrices for catalysts giving the advantages of easy recyclability and high stability.^[100-102] An interesting approach was put forward by Schüth and co-workers who used a CTF based on monomer **7** to uniformly coordinate Pt^{2+} across the material and test it as “single-site” heterogeneous catalyst in the low temperature oxidation of methane to methanol.^[100] Their catalyst was inspired by the molecular Periana catalyst (Figure 1.1.5) which showed exceptionally high turnover numbers and yields, but was very difficult to recycle.^[103] The catalyst based on the CTF showed comparable turnover numbers even after many cycles, making the material a promising candidate for industrial application.

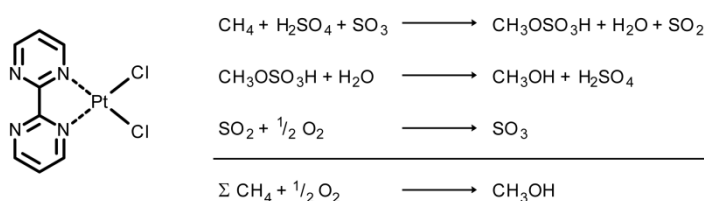


Figure 1.1.5. Periana catalyst (left) and reaction equations of the low temperature methane oxidation.

CTFs were also used to stabilize palladium nanoparticles and therefore enhance the catalytic activities in oxidations of glycerol or benzyl alcohol.^[101-102] The palladium-loaded CTFs proved to be significantly more active than the standard catalyst systems based on palladium on activated carbon. The basic nitrogen sites of the CTFs can function as catalytic sites as well, which was demonstrated in the conversion of carbon dioxide to cyclic carbonates by cycloaddition to epoxides.^[74,104] Recently, CTF1 was found to be an effective bipolar cathode material in lithium and sodium batteries^[19,105] and as an electrode material for supercapacitors.^[106] Especially the use in sodium batteries showed to be promising since it exhibited exceptionally high specific power, long cycle life and good energy efficiency.^[105]

1.2 CARBON CAPTURE AND STORAGE

As mentioned in the beginning of this introduction, the global warming is mainly caused by the anthropogenic emission of greenhouse gases. As can be seen in Figure 1.1.6, the main part of these greenhouse gases is carbon dioxide, which also has the highest growth rate in emissions. In fact, the carbon dioxide concentrations increased by 40% since pre-industrial times and the ocean has absorbed about 30% of the anthropogenically emitted carbon dioxide, which has resulted in an acidification of the ocean.^[1] Other consequences of the climate change are the warming of the atmosphere and ocean, diminishing amounts of snow and ice, as well as a rising sea level. This will

continue in the future by further emissions of greenhouse gases and limiting the climate change will require substantial and sustained reduction of greenhouse gas emissions.

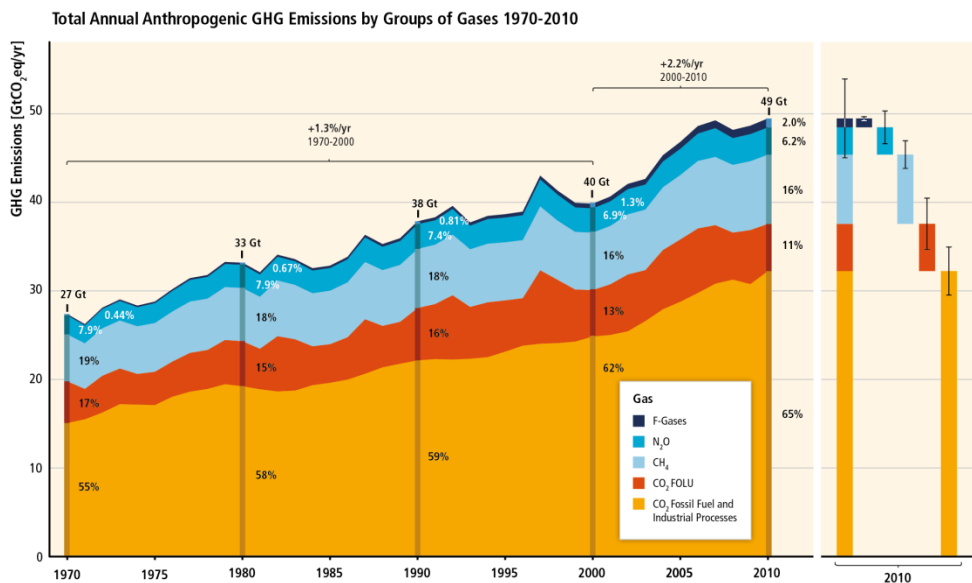


Figure 1.1.6. Total annual anthropogenic GHG (greenhouse gas) emissions (GtCO₂eq yr⁻¹) by groups of gases 1970-2010. FOLU = forestry and other land use. From Reference [3]. © 2014 IPCC.

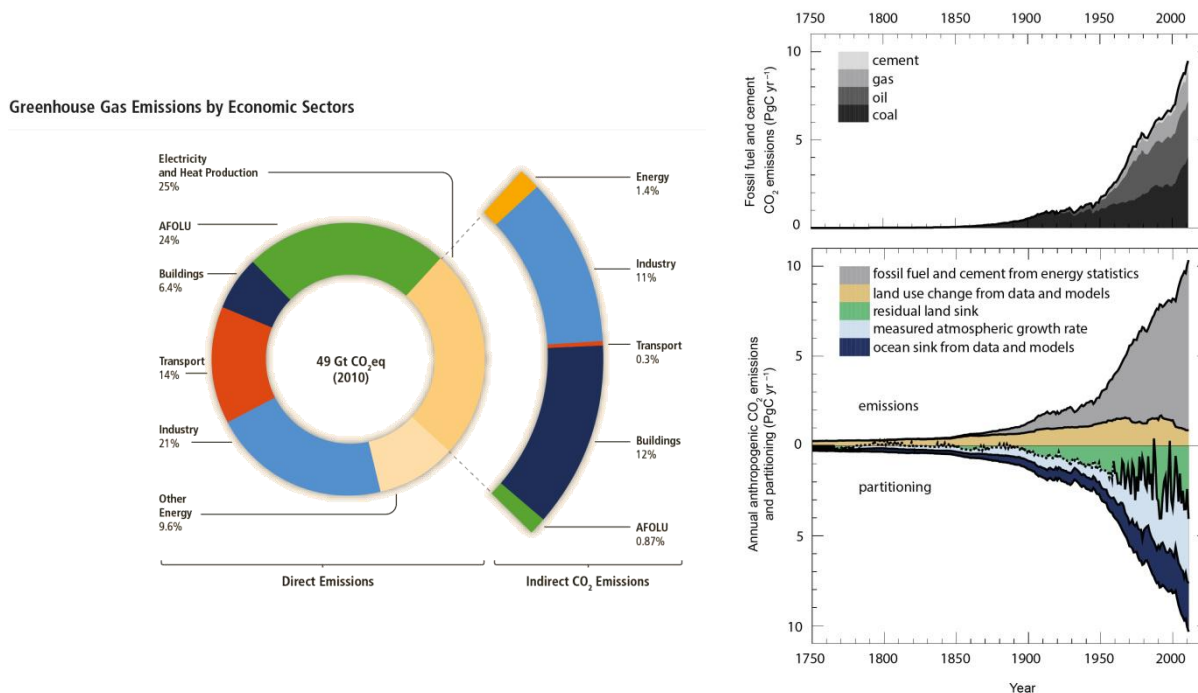


Figure 1.1.7. (Left) Total anthropogenic GHG emissions (GtCO₂eq yr⁻¹) by economic sectors. Inner circle shows direct GHG emission shares (in % of total anthropogenic GHG emissions) of economic sectors in 2010. The pull-out shows how indirect carbon dioxide emission shares (in % of total anthropogenic GHG emissions) from electricity and heat production are attributed to sectors of final energy use. AFOLU = agriculture, forestry and other land use. From Reference [3]. © 2014 IPCC. (Right) Annual anthropogenic carbon dioxide emissions and their partitioning among the atmosphere, land and ocean (PgC yr⁻¹) from 1750 to 2011. From Reference [1]. © 2013 IPCC.

Figure 1.1.7 shows the greenhouse gas emissions of different economic sectors and the partitioning of the carbon dioxide emissions among the consequences of the global warming. As can be seen, the main share of the anthropogenic emissions comes from the energy and industry sector. Therefore, the main strategies for the reduction of greenhouse gas emissions are to increase the energy efficiency of current industrial processes and energy production, increasing the share of renewable energy sources in energy production and the capture and storage of carbon dioxide (referred to as carbon capture and storage, CCS). CCS is the most undeveloped field in the reduction of carbon dioxide emissions. Although all needed components for CCS do exist, complete end-to-end systems only exist in pilot state.^[3] But there are good reasons why CCS is still discussed as one of the main strategies for the carbon dioxide reduction: CCS has the potential to decrease the emissions of carbon dioxide up to 20%,^[107] and if coupled with bio-energy it could even result in negative emissions, being one of the few technologies capable to reduce carbon dioxide concentrations in the atmosphere.^[3] A theoretical life-cycle chain of fossil fuels is shown in Figure 1.1.8.^[108] The key challenges for CCS are the capture and the storage of the carbon dioxide. The former can be accomplished by precombustion, postcombustion or oxyfuel combustion capture, while the latter one would require geologic storage sites at least 800 m below the ground, in order to store the carbon dioxide safely for hundreds of years.^[3] The most promising storage sites are saline aquifers, deep coal seams and depleted oil and gas fields. The former one offers the largest storage capacities, while the latter ones offer the advantage of additional fuel recovery, when carbon dioxide is injected.

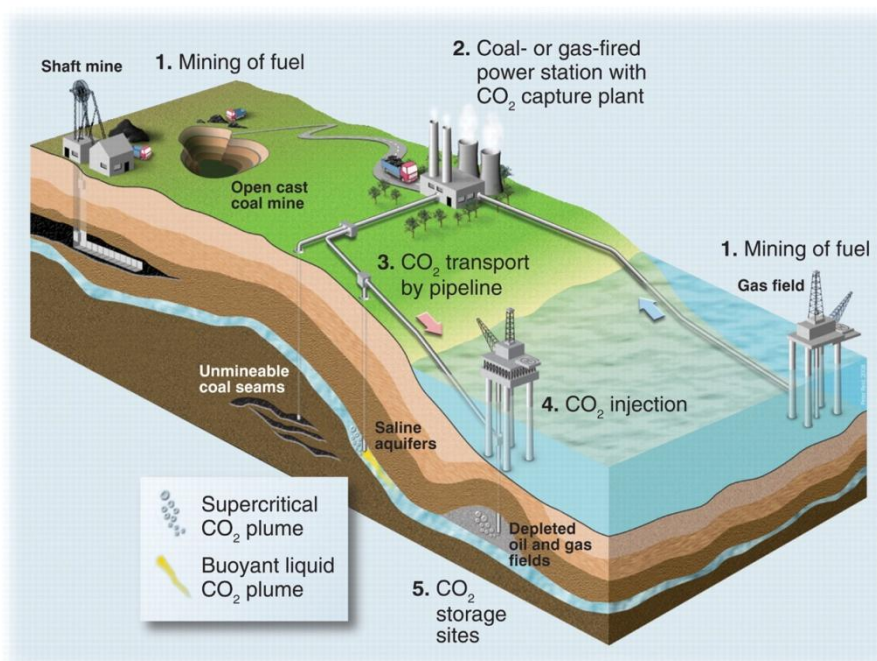
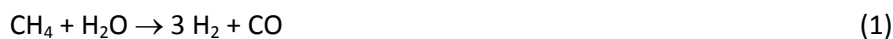


Figure 1.1.8. Diagrammatic representation of the theoretical life-cycle chain of fossil fuel use when implemented in CCS. From Reference [108]. © 2009 AAAS. Reprinted with permission from AAAS.

The precombustion capture of carbon dioxide can be applied to natural gas or syngas plants in a so-called steam methane reforming process where methane and water steam is converted to carbon monoxide and hydrogen (Equation 1). In a second stage, the carbon monoxide reacts with water to carbon dioxide and hydrogen (Equation 2).



In a water-gas shift reactor the final products are separated to produce very pure carbon dioxide and hydrogen, of which the latter one can be used in fuel cells. The energy penalty for this process is 10-16%, which is way better compared to current postcombustion methods (see Chapter 1.2.1).^[109]

Fossil fuel consumption is usually done under air, causing the emission of gas mixtures, consisting mainly of nitrogen. In oxyfuel combustion the fuel is burned in a stream of pure oxygen and carbon dioxide – carbon dioxide is needed to moderate the flame temperature – to produce only carbon dioxide and water without high concentrations of nitrogen (Equation 3).



The accumulated water can easily be separated by condensation and the resulting gas stream consists of highly pure carbon dioxide concentrations ready for sequestration. The energy penalty is comparable to precombustion capture (8-12%) and primarily comes from the oxygen production by air separation and the pressurizing of the carbon dioxide.^[110]

Both precombustion and oxyfuel combustion capture are promising technologies for CCS, but come at the cost of requiring significant and expensive changes to existing plants, making them most likely to be incorporated only in new power plants.

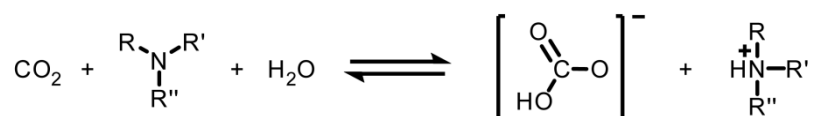
1.2.1 POSTCOMBUSTION CAPTURE

In postcombustion capture the carbon dioxide emissions of a combustion source are captured by chemical or physical sorption, then evaporated as purified gas and pressurized. The key steps are the sorption process and the recycling of the adsorbent. One primary challenge for postcombustion capture is the composition of the emitted gas which besides the targeted carbon dioxide (15-16%) consists of nitrogen (70-75%), water (5-7%), oxygen (3-4%) and small concentrations of carbon monoxide, sulfur oxides and nitrogen oxides.^[111] Therefore, the adsorbent has to be highly selective for the capture of carbon dioxide in the presence of the other emitted gases and stable towards these. Additionally, the adsorbent must be regenerative at moderate conditions to limit the energy penalty of this step. Postcombustion capture is supposed to be easily installable in existing power

plants and therefore the most interesting tool for CCS at those plants. The most established process is amine scrubbing, which will be discussed in the next section, followed by the rather new capture technique based on physical adsorbents.

Amine scrubbing

Amine scrubbing is an established method for separating carbon dioxide from flue gases and hydrogen and in use since the 1930s.^[112] The stream of the emitted gas is pumped through an aqueous amine solution where the carbon dioxide reacts to hydrogen carbonate (Scheme 1.1.3), building an ion pair with the protonated amine.



Scheme 1.1.3. Reaction of carbon dioxide with tertiary amines in the presence of water.

The chemically adsorbed carbon dioxide is then released by heating the solvent to 100-150 °C under pressures up to 8 bar. The maximum capacities of amine solutions are 1.23 mmol g⁻¹.^[113] The main disadvantage of amine scrubbing is an energy penalty of 20-30%.^[113] Additionally, issues are the oxidation of amines by oxygen impurities, the production of toxic nitrosamines and vapor losses. For all these issues there are acceptable solutions in the development state, but at the same time they show the sensitivity and drawbacks of this process.

Physical adsorbents

Besides chemical sorption there is also the possibility of physical adsorption for capturing carbon dioxide. Because of the high energy penalty of amine scrubbing there have been many investigations regarding this topic. Research covers essentially all classes of nanoporous materials, including zeolites, MOFs, porous carbons, mesoporous silica and POPs. In principle, the requirements for the materials are the same as for amine scrubbing: high capture capacities, high selectivity, stability towards impurities and easy recovery. A strategy for improving the first two requirements was presented by Dawson *et al.*: First, increasing the surface area of a material, thus providing more interaction sites between sorbent and sorbate; second, increasing the average interaction energy between sorbent and sorbate and third, engineering of pore sizes ideal for carbon dioxide, providing preferred adsorption of carbon dioxide over competing species.^[114] For all approaches the molecular properties of the carbon dioxide molecule play a significant role. For the 1st and 2nd strategies the quadrupole moment is of particular importance, whereas for the 3rd the smaller kinetic diameter (3.30 Å) compared to nitrogen (3.64 Å) is decisive. The quadrupole moment leads to quadrupole-dipole and quadrupole-induced dipole interactions, imparting both Lewis acid and base properties to carbon dioxide.^[115] These properties have been utilized by applying a number of nitrogen rich

compounds, where the free electron pair of the nitrogen atom leads to the formation of electron-donor-complexes with the carbon dioxide molecule.^[115-116]

Zeolites have very uniform pore size distributions and their polar surfaces make them good adsorbents for carbon dioxide. One of the most promising material is 13X which shows uptakes of 2-3 mmol g⁻¹ at 0.1 bar (at 288-308 K) and is therefore used as benchmark material.^[113] The main problem of zeolites is that they are usually very hydrophilic and the presence of water reduces the quadrupolar interaction between carbon dioxide and the cations.^[117]

Non-functionalized mesoporous silica materials have poor carbon dioxide capture capacities because of their large pore sizes. Nevertheless, when functionalizing the popular MCM-41 with amine groups, an uptake increase by a factor of 24 was found.^[118]

MOFs are versatile supramolecular platforms which allow modifying their pore sizes and functionalities by changing their building blocks. In principle, this opens up the opportunity to produce a tailor-made material having an ideal pore size and shape combined with the desired attractive forces for carbon dioxide capture. The best performing MOFs are of the MOF-74 family, where Mg-MOF-74 shows exceptionally high uptakes of 8.61 mmol g⁻¹ (298 K, 1 bar) and high selectivities towards nitrogen (195).^[119-120] But also here the high affinities towards carbon dioxide are coupled with hydrophilic character, which leads to a significantly lower carbon dioxide uptake in the presence of small amounts of water.^[121-122]

Porous carbons are easily synthesized at low cost by thermal treatment or chemical activation of carbonaceous materials. They exhibit rather undefined pore structures and therefore their performance in carbon dioxide capture is mostly unpredictable. Uyama and co-workers produced a series of nitrogen enriched porous carbons by thermal treatment of polyacrylonitriles, which showed unprecedented carbon dioxide uptakes of 11.51 mmol g⁻¹ (273 K, 1 bar).^[123]

The use of POPs as carbon capture material was mentioned in Section 1.1.2. POPs furnish advantages analogous to MOFs, and mostly possess even higher chemical stabilities. Additionally, POPs are mostly hydrophobic which lowers the risk of reducing carbon dioxide uptakes in the presence of water. A summary of the carbon dioxide uptakes and selectivities of POPs is shown in Table 8.1.2.7 (Appendix). Recent studies revealed that the incorporation of nitrogen scaffolds increases significantly the CO₂ adsorption capacities of POPs.^[14-15,124-128] The highest uptake of all POPs was found for PPF-1 (6.12 mmol g⁻¹, 273 K, 1 bar) followed by FCTF-1-600 (5.53 mmol g⁻¹, 273 K, 1 bar). Interestingly, upon post-modification of the highly porous PAF-1 (5460 m² g⁻¹)^[129] with polyamines the carbon dioxide uptake is increased up to a factor four and the carbon dioxide over nitrogen selectivity is high as 442.^[125]

1.3 OBJECTIVES

The modular and versatile synthesis of POPs has opened many doors for the applicability of these materials in catalysis, gas capture and separation, optoelectronics, biotechnology or energy storage devices. In particular, the easy and cheap synthesis as well as the robustness of POPs is promoting this evolution. CTFs, a subclass of POPs, stand out with their high thermal and chemical stabilities combined with the incorporation of nitrogen-rich triazine units. The latter can enhance the carbon dioxide uptakes^[74,89-92,94] and are beneficial for the utilization of CTFs as catalyst supports.^[100-102] Therefore, the incorporation of further nitrogen scaffolds could improve these properties even more, which was found to be successful for a CTF based on a pyridine unit,^[100] but additional examples are missing. The integration of 2,2'-bipyridine (*bipy*), which is a well-known bidentate chelating ligand that forms numerous complexes with various metals due to its strong ligand field,^[130] would be a very promising CTF building unit. The incorporation of chelate ligands in stable frameworks is rare, but recently Yaghi and co-workers presented the first MOF with open *bipy* coordination sites.^[131] However, the use of MOFs in heterogeneous catalysis is problematic due to their low chemical stabilities. First trials to build a CTF based on 5,5'-dicyano-2,2'-bipyridine was done by Antonietti and co-workers, but their fully condensed network showed almost no porosity.^[88] Therefore, the first objective and starting point of this thesis is to synthesize a porous CTF based on 5,5'-dicyano-2,2'-bipyridine and its utilization as a metal scaffold, along with the investigation of the stabilities of the formed hybrid materials. Secondly, the carbon capture and hydrogen storage capacities of *bipy*-CTF and other new functional CTFs based on fluorine-, lutidine- and pyrimidine-linkers shall be explored in detail and compared to the model system CTF1. A third objective will be the investigation of CTF syntheses at lower temperatures and the in-depth study of the properties of the resulting materials. Finally, the electronic, optical, electrochemical and photocatalytic properties of the as-obtained CTFs shall be explored for prospective applications in photocatalysis and electrochemical energy storage, and the relationships between structure, porosity and property in these materials will be discussed.^[19,105]

1.4 REFERENCES

- [1] *Climate Change 2013: The Physical Science Basis. Contribution of Working Group I to the Fifth Assessment Report of the Intergovernmental Panel on Climate Change* Cambridge University Press, Cambridge, United Kingdom and New York, USA, **2013**.
- [2] *Climate Change 2014: Impacts, Adaptation, and Vulnerability. Contribution of Working Group II to the Fifth Assessment Report of the Intergovernmental Panel on Climate Change*, Cambridge University Press, Cambridge, United Kingdom and New York, USA, **2014**.

- [3] *Climate Change 2014: Mitigation of Climate Change. Contribution of Working Group III to the Fifth Assessment Report of the Intergovernmental Panel on Climate Change*, Cambridge University Press, Cambridge, United Kingdom and New York, USA, **2014**.
- [4] G. Q. Lu, X. S. Zhao, *Nanoporous Materials: Science and Engineering, Vol. 4*, Imperial College Press, London, UK, **2006**.
- [5] R. Dawson, A. I. Cooper, D. J. Adams, *Prog. Polym. Sci.* **2012**, *37*, 530-563.
- [6] S.-Y. Ding, W. Wang, *Chem. Soc. Rev.* **2013**, *42*, 548-568.
- [7] J.-X. Jiang, A. Cooper, in *Functional Metal-Organic Frameworks: Gas Storage, Separation and Catalysis, Vol. 293* (Ed.: M. Schröder), Springer Berlin Heidelberg, **2010**.
- [8] K. S. W. Sing, D. H. Everett, R. A. W. Haul, L. Moscou, R. A. Pierotti, J. Rouquérol, T. Siemieniowska, *Pure Appl. Chem.* **1985**, *57*, 603-619.
- [9] R. Dawson, E. Stockel, J. R. Holst, D. J. Adams, A. I. Cooper, *Energy Environ. Sci.* **2011**, *4*, 4239-4245.
- [10] A. P. Katsoulidis, M. G. Kanatzidis, *Chem. Mater.* **2011**, *23*, 1818-1824.
- [11] Y. Zhu, H. Long, W. Zhang, *Chem. Mater.* **2013**, *25*, 1630-1635.
- [12] R. Dawson, D. J. Adams, A. I. Cooper, *Chem. Sci.* **2011**, *2*, 1173-1177.
- [13] C. F. Martin, E. Stockel, R. Clowes, D. J. Adams, A. I. Cooper, J. J. Pis, F. Rubiera, C. Pevida, *J. Mater. Chem.* **2011**, *21*, 5475-5483.
- [14] P. Arab, M. G. Rabbani, A. K. Sekizkardes, T. İslamoğlu, H. M. El-Kaderi, *Chem. Mater.* **2014**, *26*, 1385-1392.
- [15] M. G. Rabbani, H. M. El-Kaderi, *Chem. Mater.* **2011**, *23*, 1650-1653.
- [16] J. Wang, I. Senkovska, M. Oschatz, M. R. Lohe, L. Borchardt, A. Heerwig, Q. Liu, S. Kaskel, *ACS Appl. Mater. Interfaces* **2013**, *5*, 3160-3167.
- [17] P. Kuhn, M. Antonietti, A. Thomas, *Angew. Chem. Int. Ed.* **2008**, *47*, 3450-3453.
- [18] D. Yuan, W. Lu, D. Zhao, H.-C. Zhou, *Adv. Mater.* **2011**, *23*, 3723-3725.
- [19] K. Sakaushi, G. Nickerl, F. M. Wisser, D. Nishio-Hamane, E. Hosono, H. Zhou, S. Kaskel, J. Eckert, *Angew. Chem. Int. Ed.* **2012**, *51*, 7850-7854.
- [20] C. R. DeBlase, K. E. Silberstein, T.-T. Truong, H. D. Abruña, W. R. Dichtel, *J. Am. Chem. Soc.* **2013**, *135*, 16821-16824.
- [21] H. P. Hentze, M. Antonietti, *Rev. Mol. Biotechnol.* **2002**, *90*, 27-53.
- [22] P. M. Budd, N. B. McKeown, *Polym. Chem.* **2010**, *1*, 63-68.
- [23] A. P. Côté, A. I. Benin, N. W. Ockwig, M. O'Keeffe, A. J. Matzger, O. M. Yaghi, *Science* **2005**, *310*, 1166-1170.
- [24] H. M. El-Kaderi, J. R. Hunt, J. L. Mendoza-Cortés, A. P. Côté, R. E. Taylor, M. O'Keeffe, O. M. Yaghi, *Science* **2007**, *316*, 268-272.

- [25] A. P. Côté, H. M. El-Kaderi, H. Furukawa, J. R. Hunt, O. M. Yaghi, *J. Am. Chem. Soc.* **2007**, *129*, 12914-12915.
- [26] R. W. Tilford, W. R. Gemmill, H.-C. zur Loye, J. J. Lavigne, *Chem. Mater.* **2006**, *18*, 5296-5301.
- [27] R. W. Tilford, S. J. Mugavero, P. J. Pellechia, J. J. Lavigne, *Adv. Mater.* **2008**, *20*, 2741-2746.
- [28] S. Wan, J. Guo, J. Kim, H. Ihee, D. Jiang, *Angew. Chem. Int. Ed.* **2008**, *47*, 8826-8830.
- [29] E. L. Spitler, W. R. Dichtel, *Nat. Chem.* **2010**, *2*, 672-677.
- [30] X. Ding, J. Guo, X. Feng, Y. Honsho, J. Guo, S. Seki, P. Maitarad, A. Saeki, S. Nagase, D. Jiang, *Angew. Chem. Int. Ed.* **2011**, *50*, 1289-1293.
- [31] X. Ding, L. Chen, Y. Honsho, X. Feng, O. Saengsawang, J. Guo, A. Saeki, S. Seki, S. Irle, S. Nagase, V. Parasuk, D. Jiang, *J. Am. Chem. Soc.* **2011**, *133*, 14510-14513.
- [32] E. L. Spitler, B. T. Koo, J. L. Novotney, J. W. Colson, F. J. Uribe-Romo, G. D. Gutierrez, P. Clancy, W. R. Dichtel, *J. Am. Chem. Soc.* **2011**, *133*, 19416-19421.
- [33] A. Nagai, Z. Guo, X. Feng, S. Jin, X. Chen, X. Ding, D. Jiang, *Nat. Commun.* **2011**, *2*, 536.
- [34] S. Wan, F. Gándara, A. Asano, H. Furukawa, A. Saeki, S. K. Dey, L. Liao, M. W. Ambrogio, Y. Y. Botros, X. Duan, S. Seki, J. F. Stoddart, O. M. Yaghi, *Chem. Mater.* **2011**, *23*, 4094-4097.
- [35] E. L. Spitler, J. W. Colson, F. J. Uribe-Romo, A. R. Woll, M. R. Giovino, A. Saldivar, W. R. Dichtel, *Angew. Chem. Int. Ed.* **2012**, *51*, 2623-2627.
- [36] J.-T. Yu, Z. Chen, J. Sun, Z.-T. Huang, Q.-Y. Zheng, *J. Mater. Chem.* **2012**, *22*, 5369-5373.
- [37] X. Feng, L. Liu, Y. Honsho, A. Saeki, S. Seki, S. Irle, Y. Dong, A. Nagai, D. Jiang, *Angew. Chem. Int. Ed.* **2012**, *51*, 2618-2622.
- [38] X. Feng, L. Chen, Y. Dong, D. Jiang, *Chem. Commun.* **2011**, *47*, 1979-1981.
- [39] G. H. V. Bertrand, V. K. Michaelis, T.-C. Ong, R. G. Griffin, M. Dincă, *Proc. Natl. Acad. Sci. U. S. A.* **2013**, *110*, 4923-4928.
- [40] M. Dogru, M. Handloser, F. Auras, T. Kunz, D. Medina, A. Hartschuh, P. Knochel, T. Bein, *Angew. Chem. Int. Ed.* **2013**, *52*, 2920-2924.
- [41] X. Feng, Y. Dong, D. Jiang, *CrystEngComm* **2013**, *15*, 1508-1511.
- [42] X. Ding, X. Feng, A. Saeki, S. Seki, A. Nagai, D. Jiang, *Chem. Commun.* **2012**, *48*, 8952-8954.
- [43] X. Feng, L. Chen, Y. Honsho, O. Saengsawang, L. Liu, L. Wang, A. Saeki, S. Irle, S. Seki, Y. Dong, D. Jiang, *Adv. Mater.* **2012**, *24*, 3026-3031.
- [44] S. Jin, X. Ding, X. Feng, M. Supur, K. Furukawa, S. Takahashi, M. Addicoat, M. E. El-Khouly, T. Nakamura, S. Irle, S. Fukuzumi, A. Nagai, D. Jiang, *Angew. Chem. Int. Ed.* **2013**, *52*, 2017-2021.
- [45] Z. Kahveci, T. Islamoglu, G. A. Shar, R. Ding, H. M. El-Kaderi, *CrystEngComm* **2013**, *15*, 1524-1527.
- [46] M. Dogru, A. Sonnauer, S. Zimdars, M. Doblinger, P. Knochel, T. Bein, *CrystEngComm* **2013**, *15*, 1500-1502.

- [47] V. S. P. K. Neti, X. Wu, M. Hosseini, R. A. Bernal, S. Deng, L. Echegoyen, *CrystEngComm* **2013**, *15*, 7157-7160.
- [48] H. Ma, H. Ren, S. Meng, Z. Yan, H. Zhao, F. Sun, G. Zhu, *Chem. Commun.* **2013**, *49*, 9773-9775.
- [49] S. Jin, K. Furukawa, M. Addicoat, L. Chen, S. Takahashi, S. Irle, T. Nakamura, D. Jiang, *Chem. Sci.* **2013**, *4*, 4505-4511.
- [50] D. D. Medina, V. Werner, F. Auras, R. Tautz, M. Dogru, J. Schuster, S. Linke, M. Döblinger, J. Feldmann, P. Knochel, T. Bein, *ACS Nano* **2014**.
- [51] M. Dogru, A. Sonnauer, A. Gavryushin, P. Knochel, T. Bein, *Chem. Commun.* **2011**, *47*, 1707-1709.
- [52] S. Wan, J. Guo, J. Kim, H. Ihee, D. Jiang, *Angew. Chem. Int. Ed.* **2009**, *48*, 5439-5442.
- [53] D. N. Bunck, W. R. Dichtel, *Angew. Chem. Int. Ed.* **2012**, *51*, 1885-1889.
- [54] D. N. Bunck, W. R. Dichtel, *Chem. Commun.* **2013**, *49*, 2457-2459.
- [55] S. Kandambeth, A. Mallick, B. Lukose, M. V. Mane, T. Heine, R. Banerjee, *J. Am. Chem. Soc.* **2012**, *134*, 19524-19527.
- [56] H. Xu, X. Chen, J. Gao, J. Lin, M. Addicoat, S. Irle, D. Jiang, *Chem. Commun.* **2014**, *50*, 1292-1294.
- [57] F. J. Uribe-Romo, J. R. Hunt, H. Furukawa, C. Klöck, M. O'Keeffe, O. M. Yaghi, *J. Am. Chem. Soc.* **2009**, *131*, 4570-4571.
- [58] M. G. Rabbani, A. K. Sekizkardes, Z. Kahveci, T. E. Reich, R. Ding, H. M. El-Kaderi, *Chem. Eur. J.* **2013**, *19*, 3324-3328.
- [59] X. Chen, M. Addicoat, S. Irle, A. Nagai, D. Jiang, *J. Am. Chem. Soc.* **2013**, *135*, 546-549.
- [60] S.-Y. Ding, J. Gao, Q. Wang, Y. Zhang, W.-G. Song, C.-Y. Su, W. Wang, *J. Am. Chem. Soc.* **2011**, *133*, 19816-19822.
- [61] B. P. Biswal, S. Chandra, S. Kandambeth, B. Lukose, T. Heine, R. Banerjee, *J. Am. Chem. Soc.* **2013**, *135*, 5328-5331.
- [62] S. Chandra, S. Kandambeth, B. P. Biswal, B. Lukose, S. M. Kunjir, M. Chaudhary, R. Babarao, T. Heine, R. Banerjee, *J. Am. Chem. Soc.* **2013**, *135*, 17853-17861.
- [63] W. Huang, Y. Jiang, X. Li, X. Li, J. Wang, Q. Wu, X. Liu, *ACS Appl. Mater. Interfaces* **2013**, *5*, 8845-8849.
- [64] Y.-B. Zhang, J. Su, H. Furukawa, Y. Yun, F. Gándara, A. Duong, X. Zou, O. M. Yaghi, *J. Am. Chem. Soc.* **2013**, *135*, 16336-16339.
- [65] J.-R. Song, J. Sun, J. Liu, Z.-T. Huang, Q.-Y. Zheng, *Chem. Commun.* **2014**, *50*, 788-791.
- [66] L. Stegbauer, K. Schwinghammer, B. V. Lotsch, *Chem. Sci.* **2014**, DOI: 10.1039/C4SC00016A.
- [67] F. J. Uribe-Romo, C. J. Doonan, H. Furukawa, K. Oisaki, O. M. Yaghi, *J. Am. Chem. Soc.* **2011**, *133*, 11478-11481.

- [68] J. R. Hunt, C. J. Doonan, J. D. LeVangie, A. P. Côté, O. M. Yaghi, *J. Am. Chem. Soc.* **2008**, *130*, 11872-11873.
- [69] K. T. Jackson, T. E. Reich, H. M. El-Kaderi, *Chem. Commun.* **2012**, *48*, 8823-8825.
- [70] A. Nagai, X. Chen, X. Feng, X. Ding, Z. Guo, D. Jiang, *Angew. Chem. Int. Ed.* **2013**, *52*, 3770-3774.
- [71] J. Guo, Y. Xu, S. Jin, L. Chen, T. Kaji, Y. Honsho, M. A. Addicoat, J. Kim, A. Saeki, H. Ihee, S. Seki, S. Irle, M. Hiramoto, J. Gao, D. Jiang, *Nat. Commun.* **2013**, *4*.
- [72] S. Dalapati, S. Jin, J. Gao, Y. Xu, A. Nagai, D. Jiang, *J. Am. Chem. Soc.* **2013**, *135*, 17310-17313.
- [73] D. Beaudoin, T. Maris, J. D. Wuest, *Nat. Chem.* **2013**, *5*, 830-834.
- [74] P. Katekomol, J. Roeser, M. Bojdys, J. Weber, A. Thomas, *Chem. Mater.* **2013**, *25*, 1542-1548.
- [75] M. J. Bojdys, J. Jeromenok, A. Thomas, M. Antonietti, *Adv. Mater.* **2010**, *22*, 2202-2205.
- [76] <http://yaghi.berkeley.edu/gallery/070.jpg> and <http://yaghi.berkeley.edu/gallery/074.jpg>, accessed 2014-05-08.
- [77] O. M. Yaghi, H. Li, C. Davis, D. Richardson, T. L. Groy, *Acc. Chem. Res.* **1998**, *31*, 474-484.
- [78] M. Eddaoudi, D. B. Moler, H. Li, B. Chen, T. M. Reineke, M. O'Keeffe, O. M. Yaghi, *Acc. Chem. Res.* **2001**, *34*, 319-330.
- [79] S. D. Brucks, D. N. Bunck, W. R. Dichtel, *Polymer* **2014**, *55*, 330-334.
- [80] H. Furukawa, O. M. Yaghi, *J. Am. Chem. Soc.* **2009**, *131*, 8875-8883.
- [81] S. B. Kalidindi, H. Oh, M. Hirscher, D. Esken, C. Wiktor, S. Turner, G. Van Tendeloo, R. A. Fischer, *Chem. Eur. J.* **2012**, *18*, 10848-10856.
- [82] C. J. Doonan, D. J. Tranchemontagne, T. G. Glover, J. R. Hunt, O. M. Yaghi, *Nat. Chem.* **2010**, *2*, 235-238.
- [83] P. Pachfule, S. Kandambeth, D. Diaz Diaz, R. Banerjee, *Chem. Commun.* **2014**, *50*, 3169-3172.
- [84] P. Pachfule, M. K. Panda, S. Kandambeth, S. M. Shivaprasad, D. D. Diaz, R. Banerjee, *J. Mater. Chem. A* **2014**, *2*, 7944-7952.
- [85] G. H. Miller (Texaco Inc.), US 3775380, **1973**.
- [86] P. Kuhn, A. I. Forget, D. Su, A. Thomas, M. Antonietti, *J. Am. Chem. Soc.* **2008**, *130*, 13333-13337.
- [87] S. Ren, M. J. Bojdys, R. Dawson, A. Laybourn, Y. Z. Khimyak, D. J. Adams, A. I. Cooper, *Adv. Mater.* **2012**, *24*, 2357-2361.
- [88] P. Kuhn, A. Thomas, M. Antonietti, *Macromolecules* **2009**, *42*, 319-326.
- [89] W. Wang, H. Ren, F. Sun, K. Cai, H. Ma, J. Du, H. Zhao, G. Zhu, *Dalton Trans.* **2012**, *41*, 3933-3936.
- [90] X. Liu, H. Li, Y. Zhang, B. Xu, S. A. H. Xia, Y. Mu, *Polym. Chem.* **2013**, *4*, 2445-2448.
- [91] Y. Zhao, K. X. Yao, B. Teng, T. Zhang, Y. Han, *Energy Environ. Sci.* **2013**, *6*, 3684-3692.
- [92] A. Bhunia, V. Vasylyeva, C. Janiak, *Chem. Commun.* **2013**, *49*, 3961-3963.

- [93] P. Kuhn, A. Forget, J. Hartmann, A. Thomas, M. Antonietti, *Adv. Mater.* **2009**, *21*, 897-901.
- [94] A. Bhunia, I. Boldog, A. Moller, C. Janiak, *J. Mater. Chem. A* **2013**, *1*, 14990-14999.
- [95] W. Zhang, C. Li, Y.-P. Yuan, L.-G. Qiu, A.-J. Xie, Y.-H. Shen, J.-F. Zhu, *J. Mater. Chem.* **2010**, *20*, 6413-6415.
- [96] X. Zhu, C. Tian, S. M. Mahurin, S.-H. Chai, C. Wang, S. Brown, G. M. Veith, H. Luo, H. Liu, S. Dai, *J. Am. Chem. Soc.* **2012**, *134*, 10478-10484.
- [97] P. Kuhn, K. Kruger, A. Thomas, M. Antonietti, *Chem. Commun.* **2008**, 5815-5817.
- [98] T. Wang, K. Kailasam, P. Xiao, G. Chen, L. Chen, L. Wang, J. Li, J. Zhu, *Microporous Mesoporous Mater.* **2014**, *187*, 63-70.
- [99] J. Liu, H. Chen, S. Zheng, Z. Xu, *J. Chem. Eng. Data* **2013**, *58*, 3557-3562.
- [100] R. Palkovits, M. Antonietti, P. Kuhn, A. Thomas, F. Schüth, *Angew. Chem. Int. Ed.* **2009**, *48*, 6909-6912.
- [101] C. E. Chan-Thaw, A. Villa, P. Katekomol, D. Su, A. Thomas, L. Prati, *Nano Lett.* **2010**, *10*, 537-541.
- [102] C. E. Chan-Thaw, A. Villa, L. Prati, A. Thomas, *Chem. Eur. J.* **2011**, *17*, 1052-1057.
- [103] R. A. Periana, D. J. Taube, S. Gamble, H. Taube, T. Satoh, H. Fujii, *Science* **1998**, *280*, 560-564.
- [104] J. Roeser, K. Kailasam, A. Thomas, *ChemSusChem* **2012**, *5*, 1793-1799.
- [105] K. Sakaushi, E. Hosono, G. Nickerl, T. Gemming, H. Zhou, S. Kaskel, J. Eckert, *Nat. Commun.* **2013**, *4*, 1485.
- [106] L. Hao, B. Luo, X. Li, M. Jin, Y. Fang, Z. Tang, Y. Jia, M. Liang, A. Thomas, J. Yang, L. Zhi, *Energy Environ. Sci.* **2012**, *5*, 9747-9751.
- [107] *Energy technology perspectives 2008*, International Energy Agency, Paris, **2008**.
- [108] R. S. Haszeldine, *Science* **2009**, *325*, 1647-1652.
- [109] L. Eide, I., D. Bailey, W., *Oil Gas Sci. Technol.* **2005**, *60*, 475-484.
- [110] B. J. P. Buhre, L. K. Elliott, C. D. Sheng, R. P. Gupta, T. F. Wall, *Progr. Energy Combust. Sci.* **2005**, *31*, 283-307.
- [111] D. M. D'Alessandro, B. Smit, J. R. Long, *Angew. Chem. Int. Ed.* **2010**, *49*, 6058-6082.
- [112] G. T. Rochelle, *Science* **2009**, *325*, 1652-1654.
- [113] M. E. Boot-Handford, J. C. Abanades, E. J. Anthony, M. J. Blunt, S. Brandani, N. Mac Dowell, J. R. Fernandez, M.-C. Ferrari, R. Gross, J. P. Hallett, R. S. Haszeldine, P. Heptonstall, A. Lyngfelt, Z. Makuch, E. Mangano, R. T. J. Porter, M. Pourkashanian, G. T. Rochelle, N. Shah, J. G. Yao, P. S. Fennell, *Energy Environ. Sci.* **2014**, *7*, 130-189.
- [114] R. Dawson, A. I. Cooper, D. J. Adams, *Polym. Int.* **2013**, *62*, 345-352.
- [115] K. D. Vogiatzis, A. Mavrandonakis, W. Klopper, G. E. Froudakis, *Chem. Phys. Chem.* **2009**, *10*, 374-383.

- [116] P.-Z. Li, Y. Zhao, *Chem. Asian J.* **2013**, *8*, 1680-1691.
- [117] F. Brandani, D. M. Ruthven, *Ind. Eng. Chem. Res.* **2004**, *43*, 8339-8344.
- [118] X. Xu, C. Song, J. M. Andresen, B. G. Miller, A. W. Scaroni, *Energy Fuels* **2002**, *16*, 1463-1469.
- [119] S. R. Caskey, A. G. Wong-Foy, A. J. Matzger, *J. Am. Chem. Soc.* **2008**, *130*, 10870-10871.
- [120] Z. Bao, L. Yu, Q. Ren, X. Lu, S. Deng, *J. Colloid Interface Sci.* **2011**, *353*, 549-556.
- [121] J. Liu, Y. Wang, A. I. Benin, P. Jakubczak, R. R. Willis, M. D. LeVan, *Langmuir* **2010**, *26*, 14301-14307.
- [122] J. Liu, J. Tian, P. K. Thallapally, B. P. McGrail, *J. Phys. Chem. C* **2012**, *116*, 9575-9581.
- [123] M. Nandi, K. Okada, A. Dutta, A. Bhaumik, J. Maruyama, D. Derks, H. Uyama, *Chem. Commun.* **2012**, *48*, 10283-10285.
- [124] T. Islamoglu, M. Gulam Rabbani, H. M. El-Kaderi, *J. Mater. Chem. A* **2013**, *1*, 10259-10266.
- [125] W. Lu, J. P. Sculley, D. Yuan, R. Krishna, Z. Wei, H.-C. Zhou, *Angew. Chem. Int. Ed.* **2012**, *51*, 7480-7484.
- [126] L.-H. Xie, M. P. Suh, *Chem. Eur. J.* **2013**, *19*, 11590-11597.
- [127] M. G. Rabbani, H. M. El-Kaderi, *Chem. Mater.* **2012**, *24*, 1511-1517.
- [128] S. Altarawneh, S. Behera, P. Jena, H. M. El-Kaderi, *Chem. Commun.* **2014**, *50*, 3571-3574.
- [129] T. Ben, C. Pei, D. Zhang, J. Xu, F. Deng, X. Jing, S. Qiu, *Energy Environ. Sci.* **2011**, *4*, 3991-3999.
- [130] A. F. Holleman, E. Wiberg, N. Wiberg, *Lehrbuch der Anorganischen Chemie, Vol. 102*, Walter de Gruyter & Co., Berlin, Germany, **2007**.
- [131] E. D. Bloch, D. Britt, C. Lee, C. J. Doonan, F. J. Uribe-Romo, H. Furukawa, J. R. Long, O. M. Yaghi, *J. Am. Chem. Soc.* **2010**, *132*, 14382-14384.

2 METHODS

2.1 PHYSISORPTION

There are many experimental methods for the characterization of pore sizes and the surface of porous materials. These include gas adsorption, small angle X-ray and neutron scattering, mercury porosimetry, electron microscopy, thermoporometry and nuclear magnetic resonance methods.^[1] All methods have limitations of applicability in porosity characterization, concerning accuracy, pore size resolution and sample interaction and handling. Gas adsorption is one of the most popular methods, because it can describe a wide range of pore sizes (0.35-100 nm) in combination with easy handling and comparably low costs.^[2] By definition, adsorption is the enrichment of one or more components in an interfacial layer.^[3] In gas adsorption the interface between a gas and a solid is considered. The adsorbable gas is called the *adsorptive*, while the solid is called the *adsorbent* and the gas in the adsorbed state the *adsorbate*.^[3] Additionally, one can distinguish between chemical and physical adsorption. The former is called chemisorption and consists of true chemical bonding between the adsorbate and adsorbent.^[2] The process of chemisorption is often associated with an activation energy and restricted to a single layer. In contrast, physical adsorption, called physisorption, is a fully reversible process with no activation energy. The interfacial interactions are of lower energies but not restricted to specific sites or monolayer formation. Therefore physisorption allows full surface coverage and complete pore filling, without violent or disruptive structural changes during measurements. This gives physisorption analysis the advantages of analyzing pore structure and sizes and surface areas of porous materials.

2.1.2 PHYSISORPTION ISOTHERMS

The shape of physisorption isotherms depends on the interaction of the adsorptive and the adsorbent as well as on the adsorptive-adsorptive interactions. In macroporous materials the pore walls are so far apart that the adsorption process is comparable to that of flat surfaces, whereas in micropores the adsorption potentials of the opposite pore walls are overlapping, resulting in strong adsorptive-adsorbent interactions. In mesopores the adsorption process depends on both, the

adsorptive-adsorbent and the adsorptive-adsorptive interactions. This can lead to capillary condensation, where the gas molecules occur in a liquid-like state in the pores. Therefore the shape of physisorption isotherms can reveal interesting features of the analyzed material. The different types of physisorption isotherms were defined by the IUPAC and are shown in Figure 2.1.1 (left).^[3]

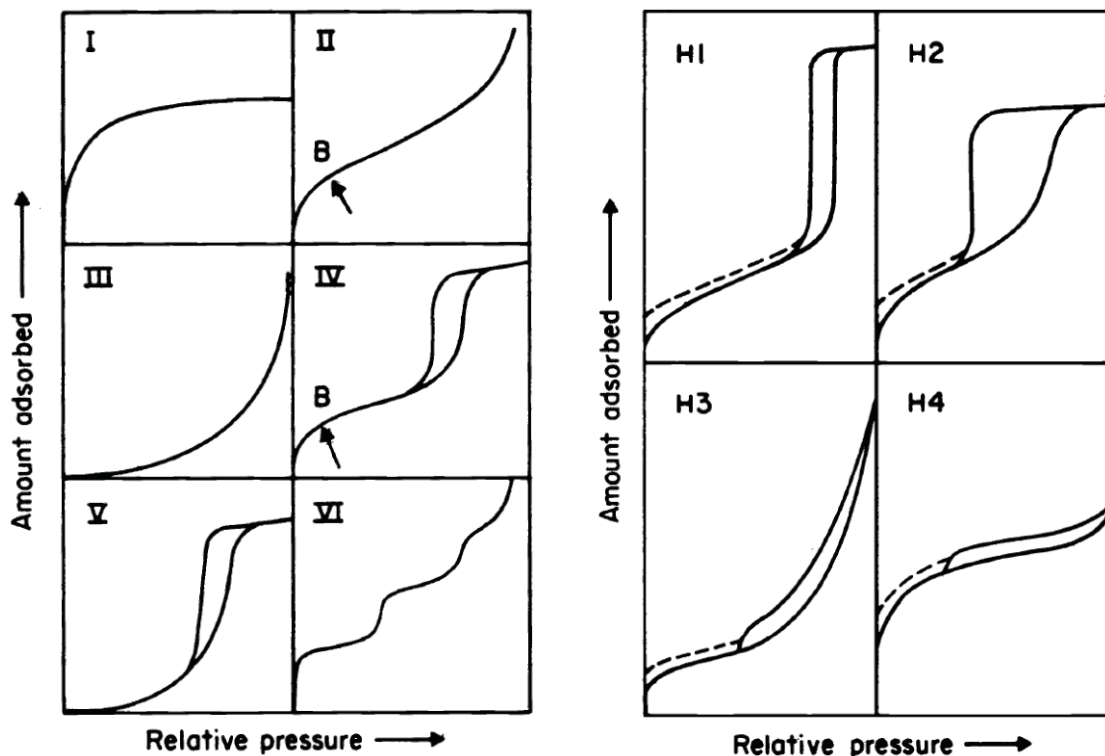


Figure 2.1.1. (Left) Types of physisorption isotherms and (right) types of hysteresis loops classified by the IUPAC. From Reference [3]. © 1985 IUPAC.

The type I isotherm describes microporous materials with high adsorption potentials. The adsorption occurs at relatively low pressures and reaches a limiting value at $p/p_0 < 1$.

The type II isotherm is typically found for non-porous or macroporous materials. Point B describes complete monolayer coverage and the beginning of multilayer adsorption.

The uncommon type III isotherm indicates weak adsorptive-adsorbent interactions and pronounced adsorptive-adsorptive interactions, *e. g.* nitrogen adsorption on polyethylene.^[3]

Type IV isotherm describes most of the mesoporous materials. The initial part of the isotherm is comparable to the type II isotherm with monolayer adsorption, followed by multilayer adsorption (at point B). At a second point capillary condensation commences with a rapid uptake of gas molecules before reaching a limiting value at $p/p_0 < 1$. A characteristic feature of type IV isotherm is the hysteresis loop, which is due to capillary condensation. The latter one describes the phenomenon in which an adsorptive undergoes a first-order phase transition from a gas-like state to a liquid-like state in a pore at pressures below the saturation pressure of the bulk liquid. This process is

controlled by intermolecular forces in the core fluid and can be described in a first approximation for cylindrical pores by the Kelvin equation

$$\ln\left(\frac{p}{p_0}\right) = \frac{-2\gamma V_m}{rRT} \quad (1)$$

where γ is the surface tension, V_m the molar volume of the fluid, r the pore radius, R the gas constant and T the temperature. This provides a correlation between pore radius and pore condensation pressure, where pore condensation commences first in pores with smaller diameters, while in the desorption process the evaporation from the pores will occur primarily in larger pores.^[2]

Type V isotherm can be understood as a combination of type III and the second part of type IV isotherm, which is rather uncommon, but found for example for the adsorption of water on porous carbons.^[4]

The type VI isotherm describes uniform non-porous surfaces where each step reflects the formation of a new layer in multilayer adsorption.

Like the isotherms, the hysteresis loops (Figure 2.1.1, right) can give insights into the pore structure. Type H1 and H4 are the extreme shapes of the loops, whereas H2 and H3 describe intermediates between these two extremes. Type H1 hysteresis consists of narrow pore size distributions and is typical for uniform cylindrical pores or agglomerates of uniform spheres in regular arrays. Type H2 hysteresis is found for materials with disordered pore sizes and ill-defined pore shapes, while type H3 hysteresis does not exhibit any limiting adsorption at high p/p_0 , which describes aggregates of plate-like particles forming slit-shaped pores. Finally, type H4 hysteresis is found for narrow slit-pores and covers also pores in the micropore region.

2.1.3 LANGMUIR THEORY

The Langmuir theory was the first model to calculate the numbers of molecules adsorbed on a surface and from that the surface area of the analyzed material was deduced.^[5] The basic, simplifying assumptions of the model are:

1. The surface of the adsorbent is a perfectly flat plane.
2. The adsorptive is adsorbed into an immobile state.
3. All adsorbing sites are equivalent.
4. Each adsorbing site can adsorb up to one molecule giving coverage of a monolayer at most.
5. The adsorbed molecules do not interact with each other.

The resulting equation, the so-called *Langmuir equation*, is

$$\frac{W}{W_m} = \frac{K_L P}{1 + K_L P} \quad (2)$$

where W and W_m are the adsorbed weight and monolayer weights of the adsorbate, respectively, K_L is the Langmuir adsorption constant and P is the adsorbate pressure.

The surface area is given by

$$S_t = \frac{W_m N_A A_x}{M} \quad (3)$$

where N_A is Avogadro's number, A_x the cross-sectional area and M the molecular weight of the adsorbate. The specific Langmuir surface area can easily be calculated by dividing S_t by the sample weight.

The Langmuir theory describes type I isotherms very well, although surface areas obtained are subject to uncertainties. Additionally, it fails to be suitable for analysis of the other isotherm types, where multilayer adsorption is an essential factor.

2.1.4 BET THEORY

The most common method for determining the surface area of a material is the Brunauer-Emmett-Teller (BET) theory which allows multilayer adsorption and assumes that the adsorptive is adsorbed on the surface in infinite layers, that no interaction occurs between each layer and the Langmuir theory can be applied to each layer.^[6] The resulting equation is

$$\frac{1}{W \left[\frac{p_0}{p} - 1 \right]} = \frac{1}{W_m C} + \frac{C-1}{W_m C} \left(\frac{p}{p_0} \right) \quad (4)$$

where p and p_0 are the equilibrium and the saturation pressure, respectively, and C is the BET constant. A plot of $1/W[(p_0/p)-1]$ versus p/p_0 usually gives a linear correlation in the range $0.05 \leq p_0/p \leq 0.35$ and is called a BET plot. The slope s and the intercept i of the plot are used to calculate W_m and C as follows

$$W_m = \frac{1}{s+i} \quad (5)$$

$$C = 1 + \frac{s}{i} \quad (6)$$

According to the Langmuir theory the total surface area S_t is described by Equation (3). The specific BET surface area is simply calculated by dividing S_t by the sample weight.

2.1.5 PORE SIZE DISTRIBUTION ANALYSIS

Pore size distributions (PSD) are preferably determined by density functional theory (DFT) methods which allow the calculation of equilibrium density profiles of a fluid adsorbed on surfaces.^[2] The most popular is the non-local DFT (NLDFT) method which provides PSD analysis over the whole micro- and mesopore range featuring an accurate description of a fluid in narrow pores and the strong oscillation characteristics of a fluid density profile at an adsorptive-adsorbent interface.^[7] In this method a set of isotherms is calculated for a set of pore sizes for a given adsorptive, building a model database, the so-called *kernel*. The calculation of the PSD is done by correlating the kernel with the experimental isotherm based on the Generalized Adsorption Isotherm equation

$$N\left(\frac{p}{p_0}\right) = \int_{W_{min}}^{W_{max}} N\left(\frac{p}{p_0}, W\right) f(W) dW \quad (7)$$

where $N(p/p_0)$ is the experimental adsorption isotherm data, W the pore width, $N(p/p_0, W)$ the kernel of theoretical isotherms with pores of different widths and $f(W)$ the PSD function.^[2]

There are various commercially available kernels which take different pore shapes into account and can be used with the adsorptives argon, nitrogen and carbon dioxide. The main drawback of the NLDFT method is that it does not pay any attention to geometrical heterogeneity of the pore walls, assuming structureless, smooth surfaces.^[8] The consequence is a calculated isotherm exhibiting multiple steps which are related to the formation of a monolayer, a second layer and so on. Since these kinds of isotherms are only observed for smooth surfaces, the theoretical isotherms cause artificial gaps on the calculated PSD.^[9] A novel approach is the quenched solid DFT (QSDFD) model in which the adsorbate atoms are considered as quenched components of the adsorptive-adsorbate system.^[10] This allows taking surface roughness and heterogeneity into account.

2.1.6 HEAT OF ADSORPTION

The process of adsorption is exothermic, therefore heat is generally released, when a gas molecule adsorbs on a surface. The heat of adsorption can provide knowledge of the chemical affinity of the surface towards the adsorptive. The differential heat of adsorption Q_{st} is defined as the heat released by adding a small increment of adsorbate to the surface.^[2] Since the value of Q_{st} depends on the bond strength formed upon adsorption and the degree of surface already covered by the adsorbate, Q_{st} is often expressed as a variation of the surface coverage θ . This so-called *isosteric heat of adsorption* can be calculated from at least two isotherms measured at different temperatures according to the Clausius-Clapeyron equation

$$Q_{st} = R \cdot \left(\frac{\partial \ln(p)}{\partial \frac{1}{T}} \right)_{\theta} \quad (8)$$

where R is the gas constant, p the pressure and T the temperature. When $\ln(p)$ is plotted versus the reciprocal temperature $1/T$ for different surface coverages θ , the slope of the linear fit to this data for each surface coverage θ is proportional to the isosteric heat of adsorption.

2.1.7 GAS SELECTIVITY

To determine the gas selectivity of a material towards one gas over another, independent isotherms of the two adsorptives are recorded at the same temperatures and fitted by theoretical methods.

Henry calculation

Henry selectivity calculations are a quick and easy method to determine gas selectivities. The model is based on the assumption that the amount of adsorbate is directly proportional to the partial pressure of the adsorptive, expressed by following equation

$$\theta = K_H \frac{p}{p_0} \quad (9)$$

where θ is the surface coverage and K_H the Henry constant giving a linear isotherm. Generally, this isotherm can be used to describe the initial slope of the experimental isotherms. Therefore, in Henry selectivity calculations the selectivity is calculated by the ratio of the initial slopes in the Henry region of the adsorption isotherms of two different gases.

Ideal adsorbed solution theory

The ideal adsorbed solution theory (IAST) allows calculations of the adsorption equilibria for different gases in a gas mixture by using the experimental data of pure-component adsorption.^[11] The heart of the model is expressed by the equation

$$P_t y_i = P_i^0(\pi) x_i \quad (\text{constant } T) \quad (10)$$

where P_t is the total pressure of the gas mixture, y_i the mole fraction of component i in the gas phase, $P_i^0(\pi)$ the pure adsorbate vapor pressure for a component i at the temperature T and spreading pressure π of the mixture, and x_i the mole fraction of component i in the adsorbed phase.

The advantages of the IAST are that the molar ratio of gases in a gas mixture can be taken into account and the model fits the whole pressure range of the isotherms. For IAST calculations the experimental isotherms are fitted by single or dual-site Langmuir models.

The single-site Langmuir model is defined as

$$q(p) = \frac{q_{sat} b p}{1 + b p} \quad (11)$$

where q is the molar loading of adsorbate, q_{sat} the saturation loading, b the Langmuir constant and p the bulk phase pressure.

The dual-site Langmuir model is defined as

$$q(p) = q_A + q_B = \frac{q_{sat,A} b_A p}{1 + b_A p} + \frac{q_{sat,B} b_B p}{1 + b_B p} \quad (12)$$

where A and B are distinct adsorption sites.

The IAST gives the analytic relationship of two functions $q_1(p)$ and $q_2(p)$ for two different gases by

$$\int_0^{x_1} \frac{P_t y_1}{x_1} q_1(p) d \ln p = \int_0^{x_2} \frac{P_t y_2}{x_2} q_2(p) d \ln p \quad (13)$$

and integration of (13) with two single-site Langmuir functions leads to

$$q_{sat1} \ln \left(1 + b_1 \frac{P_t y_1}{x_1} \right) = q_{sat2} \ln \left(1 + b_2 \frac{P_t y_2}{x_2} \right) \quad (14)$$

The values of y_1 and y_2 are known and the ones of $q_{\text{sat}1}$, $q_{\text{sat}2}$, b_1 and b_2 are given from the Langmuir fits. Additionally, it holds that

$$x_1 + x_2 = 1 \quad (15)$$

Therefore x_1 and x_2 can be calculated for specified quantities of P_t .

Finally, the selectivities are calculated using the following equation

$$S = \frac{x_1/y_1}{x_2/y_2} \quad (16)$$

2.1.8 EXPERIMENTAL DETAILS

In this thesis argon, carbon dioxide and nitrogen adsorption/desorption measurements were performed at 77, 87, 273, 298 or 313 K with an Autosorb-iQ surface analyzer (Quantachrome Instruments, USA). Samples were outgassed in vacuum (10^{-7} mbar) at 150-300 °C for 6-12 h to remove all guests. Pore-size distributions were determined using the calculation model for Ar at 87 K on carbon (slit pore, QSDFT equilibrium model), for N₂ at 77 K on carbon (slit-/cylinder pores, NLDFT equilibrium model) or for CO₂ at 273 K on carbon (NLDFT model) of the ASiQwin software (v3.01) from Quantachrome. For multipoint BET calculations pressure ranges of the Ar isotherms were chosen with the help of the BET Assistant in the ASiQwin software, which chooses BET tags equal or below the maximum in $V \cdot (1 - P/P_0)$ in accordance with the ISO recommendations.^[12] The isosteric heats of adsorption were calculated from the CO₂ adsorption isotherms using the ASiQwin software based on Equation 8.

Cryogenic hydrogen adsorption/desorption measurements at 19.5 K were measured with laboratory-designed volumetric adsorption equipment with a temperature-controlled cryostat. The experimental set-up has been described in detail elsewhere.^[13-14] Samples were activated under vacuum (10^{-4} mbar) at 150 °C for 12 h, prior to each measurement. For the laboratory-designed cryostat, the temperature control was calibrated by measuring the liquefaction pressure for hydrogen and nitrogen in the empty sample chamber at various temperatures. Measurements were performed by Dr. Hyunchul Oh from the group of Dr. Michael Hirscher (Max Planck Institute for Intelligent Systems, Stuttgart).

High-pressure hydrogen adsorption/desorption measurements were performed on an automated Sievert's type apparatus (PCTPro-2000) with a so-called micro-doser (MD) from HyEnergy. The original setup was upgraded by a heating and cooling device to regulate the sample temperature. The adsorption and desorption isotherms (0-25 bar) were measured at various temperatures (77 to 298 K) in a sample cell volume of ≈ 1.3 mL using ultra high purity hydrogen gas (99.999%). Samples were outgassed in vacuum ($4.5 \cdot 10^{-6}$ mbar) at 200 °C for 6 h to remove all guests. The isosteric heat of adsorption is calculated from the absolute adsorbed hydrogen according to Equation 8.

Measurements were performed by Dr. Hyunchul Oh from the group of Dr. Michael Hirscher (Max Planck Institute for Intelligent Systems, Stuttgart).

2.2 POWDER X-RAY DIFFRACTION

The symmetry, phase purity, particle size and crystallinity, including the stacking order of layered materials, can be analyzed with the help of powder X-ray diffraction (XRD). In XRD the sample is irradiated with X-rays which are scattered by sets of different crystal lattice planes following Bragg's law^[15]

$$\sin\theta = \frac{n\cdot\lambda}{2d} \quad (17)$$

where θ is the scattering angle, d the lattice plane, λ the wavelength and n the reflection order (see Figure 2.1.2).

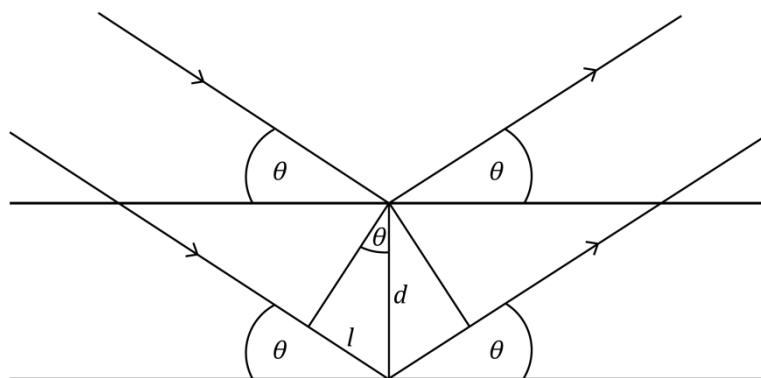


Figure 2.1.2. Geometrical derivation of the Bragg equation.

The angle θ is the so-called *Bragg angle* and describes the angle at which constructive interference occurs. This constructive interference is only observed for periodic structures such as crystal lattices, highly ordered pore systems and equally spaced, stacked layers.

Powder diffraction patterns were measured on a BRUKER D8 Avance (Bruker AXS, USA) in Bragg-Brentano geometry or on a HUBER G670 (HUBER Difraktionstechnik, Germany) in Guinier geometry equipped with an imaging plate detector.

2.3 INFRARED SPECTROSCOPY

Infrared spectroscopy uses the infrared region of the electromagnetic spectrum for excitation of the vibrational and rotational modes of molecules and extended solids. The amount of absorbed radiation as a function of energy is detected, yielding information about the rotational and vibrational excitations of the compounds under study. Interaction between the molecule and the electromagnetic radiation can only occur if a change of the permanent electrical dipole moment

occurs. Infrared measurements were performed on a Perkin Elmer Spektrum BX II (Perkin Elmer, USA) with an attenuated total reflectance unit on freeze-dried samples.

2.4 ULTRAVIOLET-VISIBLE SPECTROSCOPY

In ultraviolet-visible (UV-Vis) spectroscopy the absorption of UV and visible light by materials is recorded. The absorption is caused by excitation of electrons in the material. Optical diffuse reflectance spectra of the solids were collected at room temperature with a UV-Vis-NIR diffuse reflectance spectrometer Cary 5000 (Agilent Technologies, USA) at a photometric range of 250-800 nm. Powders were prepared in a sample carrier with a quartz glass window at the edge of the integrating sphere with BaSO₄ as the optical standard. Kubelka-Munk spectra were calculated from the reflectance data.

2.5 ELEMENTAL ANALYSIS

Elemental analysis is used for the determination of the composition of the materials. The CTFs were measured by CHNS-analysis, giving the weight percent of the elements C, H, N and indirectly O. The metal loaded CTFs were measured by inductively coupled plasma emission spectrometry (ICP-AES), to determine the amount of adsorbed metals.

2.5.1 CHNS-ANALYSIS

Elemental analysis of the elements C, H, N and S is accomplished by high temperature digestion coupled with dynamic gas components separation. The samples are burned explosively at 1150 °C in a highly oxygenated helium atmosphere. The combustion products are CO₂, H₂O, N₂, NO, NO₂, SO₂, and SO₃. The detection of the gases is done by a thermal conductivity measurement cell. The accuracy is ≈ 0.30%. Measurements were carried out on an Elementar vario EL (Elementar Analysensysteme, Germany).

2.5.2 INDUCTIVELY COUPLED PLASMA ATOMIC EMISSION SPECTROSCOPY

In inductively coupled plasma emission spectrometry (ICP-AES) the atoms and molecules are heated in a high temperature plasma up to 7000 K, where the molecules dissociate into atoms and ions. In the plasma the elements form electron-hole-pairs which recombine repeatedly and the emitted characteristic wavelength of this process is detected. ICP-AES was measured on a VARIAN VISTA RL simultaneous spectrometer (Agilent Technologies, USA) with a CCD-detector.

2.6 ELECTRON MICROSCOPY

Electron microscopy relies on similar basic principles as light microscopy but uses an electron beam instead of light. Since the resolution of a microscope is mainly limited by the wavelength of the irradiation source, the utilization of electrons as source enhance the resolution from approximately 200 nm for a light microscope to 0.1 nm for an electron microscope. Besides the better resolution, which can give important information about the surface structure and topologies of the samples, advanced techniques, such as electron scattering can be applied on elected sections of the analysed material to get insights into the crystal structure and the material composition. The electron beam is generated by a tungsten filament or a field emission gun and accelerated by a potential difference between 40 and 3000 kV. Focusing is done by electrostatic and electromagnetic lenses.

2.6.1 TRANSMISSION ELECTRON MICROSCOPY

In a transmission electron microscope (TEM) the electron beam is focused on a very thin sample film (at most 100 nm thickness) and the transmitted beam is magnified by a series of electromagnetic lenses. The electrons interact with the sample and therefore carry information about the inner structure. The signal is recorded by a phosphor screen or a charge-coupled device (CCD) camera. TEM furnishes information on both the morphology and structure of the sample, by imaging and electron diffraction, respectively. TEM was operated on a Philips CM30 ST, 300 kV S/TEM (FEI, USA) with a Si/Li EDX-detector (Thermo Fischer, USA) by Viola Duppel (Max Planck Institute for Solid State Research, Stuttgart) and on a FEI Titan 80-300 kV S/TEM (FEI, USA) with Gatan Tridien and an EDX-detector at 300 keV by Andreas Wisnet and Dr. Teresa Dennenwaldt from the group of Prof. Christina Scheu (Ludwig-Maximilians-Universität, Munich).

2.6.2 SCANNING ELECTRON MICROSCOPY

Scanning electron microscopy (SEM) detects secondary and backscattered electrons, which carry information about the topography and element contrast of the sample. Secondary electrons are inelastically scattered electrons with low energies and hence, only electrons from the surface are emitted. Therefore, secondary electrons can be used for imaging the topography of the sample. Backscattered electrons are electrons which are scattered elastically on the surface. The energy of these electrons depends on the mean atomic number of the material, giving rise to elemental contrast between areas with different chemical compositions. Additionally, the electron beam can excite electrons in the inner shell of the atoms, causing an electron hole which is immediately filled by an electron from an outer shell. The emitted X-rays are characteristic for each element and can be detected by energy-dispersive X-ray (EDX) spectroscopy. SEM and EDX were performed using either a

JEOL JSM-6500F electron microscope (JEOL, Japan) with a field emission source equipped with an EDX detector (model 7418, Oxford Instruments, UK) by Christian Minke (Ludwig-Maximilians-Universität, Munich) or a Tescan Vega TS 5130MM electron microscope equipped with a Si/Li EDX detector (Oxford Instruments, UK) by Viola Duppel (Max Planck Institute for Solid State Research, Stuttgart).

2.7 NUCLEAR MAGNETIC RESONANCE SPECTROSCOPY

Nuclear magnetic resonance (NMR) spectroscopy allows to investigate the local structure of materials. All isotopes that contain a nonzero spin have an intrinsic magnetic moment which can interact with an external magnetic field. The resonance frequency of this interaction depends on the external magnetic field and the magnetic properties of the nuclear isotope. The latter ones are influenced by the structure, dynamics, reaction state and chemical environments in which the isotope is contained. Especially the chemical environment and bonds of two isotopes have substantial influence on the resonance frequency and are usually orientation dependent.

2.7.3 SOLUTION-STATE NMR SPECTROSCOPY

In solution-state NMR spectroscopy the molecules are rotating due to Brownian motion, which averages out the orientation dependent interactions. Solution-state NMR spectroscopy was performed on a JEOL DELTA NMR (JEOL, Japan) by single pulse experiments. The spectra were referenced against CDCl_3 ($\delta(^1\text{H})$ 7.26 ppm, $\delta(^{13}\text{C}\{^1\text{H}\})$ 77.16 ppm).

2.7.4 SOLID-STATE NMR SPECTROSCOPY

In solid-state NMR (ssNMR) spectroscopy several orientation dependent interactions such as the chemical shift anisotropy, dipolar coupling, quadrupole coupling and spin-spin coupling leads to substantial line broadening, which are not averaged out by rapid molecular tumbling like in solution. The dipolar coupling is an important source of line broadening especially for abundant NMR active nuclei such as ^1H , where the orientation of the isotope with respect to the external field is described by

$$\Delta B = \frac{\mu_0}{4\pi} (3 \cos^2 \theta - 1) \mu r^{-3} \quad (18)$$

where ΔB is the variation in the local magnetic field, μ_0 is the permeability of free space, μ the magnetic moment of the isotope, r the distance vector and θ the angle between r and the direction of the external magnetic field. When the sample is rotated in an angle θ of 54.74° , the term $3 \cos^2 \theta - 1$ equals zero and the dipolar coupling can be averaged out to a large extent. This technique is called magic-angle spinning (MAS). Additionally, cross-polarization (CP) can be used to

increase the signal strength of isotopes with low natural abundance and low gyromagnetic ratio such as ^{15}N , by transferring the magnetization of a more abundant isotope, usually ^1H , to the rare isotope. Cross polarization with polarization inversion (CPPI) measurements^[16-17] can give information about the number and type of covalently bonded protons. Starting from maximum magnetization the signal decays and becomes negative with increasing inversion time. This decay has a characteristic form according to the number of bonded protons, yielding information on the hybridization state of the probed nucleus. MAS ssNMR spectra were recorded at ambient temperature on a BRUKER DSX500 Avance NMR spectrometer (Bruker Biospin, Germany) by Christian Minke or a BRUKER Avance III HD 400 NMR spectrometer (Bruker Biospin, Germany) by Maria Mesch from the Prof. Jürgen Senker group (University of Bayreuth) with an external magnetic field of 11.75 T and 9.4 T, respectively. The operating frequencies are 500.1 MHz, 125.7 MHz and 400.1 MHz, 100.6 MHz for ^1H and ^{13}C , respectively, and the spectra were referenced relative to TMS (^1H , ^{13}C). The samples were contained either in 2.4, 3.2 or 4 mm ZrO_2 rotors. The 1D $^1\text{H}^{13}\text{C}$ CP MAS spectra were acquired with a ramped-amplitude (RAMP) CP sequence and contact times between 2 and 10 ms. CPPI experiments were carried out to get information about the number of hydrogen atoms directly attached to the carbon. An initial contact time of 2 ms was used and spectra with inversion times up to 400 μs were measured. The measurements were carried out using spinning frequencies of 10 kHz and 15 kHz for CP, and 5.1 kHz for CPPI measurements, respectively. During acquisition broadband proton decoupling using a SPINAL64 or TPPM sequence was carried out.

2.8 DIFFERENTIAL THERMAL ANALYSIS AND THERMOGRAVIMETRY

Differential thermal analysis (DTA) and thermogravimetry (TG) are used to determine the thermal behavior of materials. Both techniques are employed at the same time by heating a sample in an atmosphere. In DTA the temperature difference of the samples compared to an inert reference are recorded to obtain information about exothermic or endothermic changes in the material, for example as a result of phase transition. In TG the sample weight is measured constantly yielding information about decomposition temperature and contents of volatile compounds. DTA and TG were measured on a SETARAM TG-DTA92-2400 combined DTA-TG-thermobalance (SETARAM Instrumentation, France) in aluminum oxide crucibles. Heating was performed from room temperature to 1000 $^\circ\text{C}$ with a heating rate of 5 $^\circ\text{C min}^{-1}$ under helium atmosphere.

2.9 MASS SPECTROMETRY

In mass spectrometry (MS) a sample is ionized, causing the molecules of the sample to break into charged fragments. These fragments can be separated due to their mass-to-charge ratio, which is done by an applied magnetic or electric field. The ionization can be done by several techniques,

which can handle different type of samples. The most common methods are electron impact ionization (EI), chemical ionization (CI), electrospray ionization (ESI), fast atom bombardment (FAB) and matrix assisted laser desorption ionization (MALDI). High resolution MS (HRMS) was measured on a JEOL MS700 (JEOL, Japan), by direct electron ionization (DEI).

2.10 REFERENCES

- [1] J. Rouquerol, D. Avnir, C. W. Fairbridge, D. H. Everett, J. M. Haynes, N. Pernicone, J. D. F. Ramsay, K. S. W. Sing, K. K. Unger, *Pure Appl. Chem.* **1994**, *66*, 1739-1758.
- [2] S. Lowell, J. E. Shields, M. A. Thomas, M. Thommes, *Characterization of Porous Solids and Powders: Surface Area, Pore Size and Density*, Springer, Dordrecht, Netherlands, **2006**.
- [3] K. S. W. Sing, D. H. Everett, R. A. W. Haul, L. Moscou, R. A. Pierotti, J. Rouquérol, T. Siemieniewska, *Pure Appl. Chem.* **1985**, *57*, 603-619.
- [4] J. K. Brennan, T. J. Bandoz, K. T. Thomson, K. E. Gubbins, *Colloids and Surfaces A: Physicochemical and Engineering Aspects* **2001**, *187–188*, 539-568.
- [5] I. Langmuir, *J. Am. Chem. Soc.* **1918**, *40*, 1361-1403.
- [6] S. Brunauer, P. H. Emmett, E. Teller, *J. Am. Chem. Soc.* **1938**, *60*, 309-319.
- [7] C. Lastoskie, K. E. Gubbins, N. Quirke, *J. Phys. Chem.* **1993**, *97*, 4786-4796.
- [8] G. Y. Gor, M. Thommes, K. A. Cychosz, A. V. Neimark, *Carbon* **2012**, *50*, 1583-1590.
- [9] A. V. Neimark, Y. Lin, P. I. Ravikovitch, M. Thommes, *Carbon* **2009**, *47*, 1617-1628.
- [10] P. I. Ravikovitch, A. V. Neimark, *Langmuir* **2006**, *22*, 11171-11179.
- [11] A. L. Myers, J. M. Prausnitz, *AIChE J.* **1965**, *11*, 121-127.
- [12] *Determination of the specific surface area of solids by gas adsorption - BET method*, ISO 9277:2010, Geneva, Switzerland, **2010**.
- [13] B. Streppel, M. Hirscher, *Phys. Chem. Chem. Phys.* **2011**, *13*, 3220-3222.
- [14] B. Streppel, Ph.D. Thesis, Universität Stuttgart **2011**.
- [15] W. H. Bragg, W. L. Bragg, *Proc. R. Soc. Lond. A* **1913**, *88*, 428-438.
- [16] X. L. Wu, K. W. Zilm, *J. Magn. Reson. A* **1993**, *102*, 205-213.
- [17] B. Jürgens, E. Irran, J. Senker, P. Kroll, H. Müller, W. Schnick, *J. Am. Chem. Soc.* **2003**, *125*, 10288-10300.

3 COVALENT TRIAZINE FRAMEWORKS AS METAL COORDINATION SCAFFOLDS

The synthesis of a covalent triazine framework based on pyridine building units and their application in heterogeneous catalysis already suggests the vast potential of CTFs as stable and highly porous metal coordination scaffolds. The incorporation of 2,2'-bipyridine units promises even stronger interactions with metal cations due to the chelating effect of the bipyridine units. Although the synthesis of a 2,2'-bipyridine based porous CTF had previously been reported to be unsuccessful (see below), this chapter presents the first successful synthesis and comprehensive characterization of porous *bipy*-CTFs with compositions, degree of order and porosities depending on the reaction medium and synthesis temperature. The CTF materials were found to have high adsorption capacities for various metal cations and showed high thermal and chemical stabilities.

3.1 A FUNCTIONAL TRIAZINE FRAMEWORK BASED ON *N*-HETEROCYCLIC BUILDING BLOCKS

Stephan Hug, Michael E. Tauchert, Shen Li, Ursula E. Pachmayr and Bettina V. Lotsch

published in *J. Mater. Chem.* **2012**, 22, 13956-13964
DOI: 10.1039/C2JM31248D
<http://pubs.rsc.org/en/content/articlelanding/2012/jm/c2jm31248d>
Reproduced with permission from The Royal Society of Chemistry

Abstract

Covalent organic frameworks constitute a subclass of polymeric materials offering enhanced porosity, functionality and stability. In this work a covalent triazine framework based on bipyridine building blocks is presented, along with a comprehensive elucidation of its local structure, porosity, and capacity for metal uptake. A typical synthesis was carried out under ionothermal conditions at 400 - 700 °C using ZnCl₂ as a Lewis acidic trimerization catalyst. A high degree of local order and the presence of triazine and bipyridine moieties are ascertained at a synthesis temperature of 400 °C, along with micropores and specific surface areas of up to 1100 m² g⁻¹. Mesopores are increasingly formed at synthesis temperatures above 450 °C, yielding highly porous frameworks with hierarchical porosity and exceptionally large surface areas in excess of 3200 m² g⁻¹ at 700 °C. We demonstrate the capability of the bipyridine unit to provide specific and strong binding sites for a large variety of transition metal ions, including Co, Ni, Pt and Pd. The degree of metal loading (up to 38 wt%) can be tuned by the metal concentration in solution and is dependent on both the type of metal as well as the temperature at which the CTF was synthesized. Evidence for site-specific metal coordination bodes well for the use of metal-loaded CTFs as heterogeneous catalysts carrying homogeneous-type active sites.

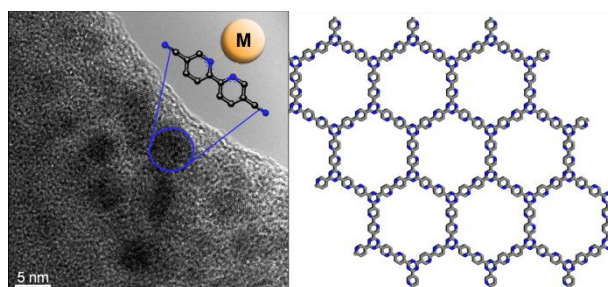


Table of content. A functional triazine framework based on 2,2'-bipyridine building blocks is obtained via ionothermal synthesis, featuring hierarchical porosity upon thermal treatment with surface areas in excess of 3000 m² g⁻¹. The bipyridine units act as specific binding sites for various transition metals.

3.1.1 INTRODUCTION

The rational design of porous solids from molecular building blocks as seen in the rise of metal-organic framework (MOF) chemistry has pushed the borders of porous materials from inorganic oxidic materials into the realm of supramolecular and polymer chemistry.^[1-3] Assembling well-defined organic building blocks into regular, porous arrays enables a unique combination of local, molecular properties embedded within a supramolecular matrix whose properties are governed by the interaction and mutual arrangement of the molecular building blocks, as well as the overall periodic structure and morphology of the bulk material.

The development of new representatives of MOFs has lately been driven by the quest for rationally designed framework topologies with inherent and well-dispersed functional groups. Whereas a range of textbook examples of MOFs with exceptionally high porosities and specific surface areas has been prepared to date, the design of MOFs featuring functional organic linkers tailor-made for specific applications has been hampered by the requirement of unconventional synthetic approaches combined with low framework stability and loss of porosity upon framework modification.

In general, framework stability may be greatly enhanced by replacing the metal clusters or ions connecting the organic ligands in MOFs by another set of organic linkers, thereby substituting potentially reactive electrostatic bonds between the building blocks by strong, covalent bonds, which are less prone to hydrolysis and thermal degradation. The resulting, all-organic class of porous solids, dubbed porous cross-linked polymers (PCPs)^[4-7] or porous organic polymers (POPs),^[8-10] is devoid of structurally active metal ions and entirely constructed of light-weight, rigid and covalently linked organic building blocks. Covalent organic frameworks (COFs) constitute a subclass of POPs, often featuring long-range order similar to their metal-organic counterparts. The prototypical COF topologies created initially by Yaghi, Lavigne and others,^[1,11-13] are composed of boronic acid building blocks forming ester linkages with polyalcohols or boroxine rings by self-condensation under relatively mild conditions. Recently, Antonietti, Thomas and co-workers pioneered COF chemistry by introducing a new generation of COFs based on triazine linkages, termed covalent triazine frameworks (CTFs).^[2,14] CTFs are prepared by trimerization of the cyano groups of aromatic nitriles via ionothermal synthesis in a Lewis acidic medium, typically in ZnCl₂ salt melts. Except for a few examples,^[2,15] CTFs oftentimes lack long-range order, yet excel by their high porosities paired with exceptional chemical inertness and high thermal stability owing to their graphite-like composition and robust carbon-carbon and carbon-nitrogen linkages. The presence of stoichiometric and well-defined nitrogen sites in the triazine frameworks has recently been shown to render CTFs promising catalysts and catalyst supports,^[16-18] as catalytically active metal ions may be site-selectively anchored to the CTF matrix by strong nitrogen-metal interactions in large amount owing to the large

accessible surface area. Moreover, the metal ions can be reduced *in situ* or the CTF may be impregnated with already formed metal nanoparticles, yielding hybrid materials with well-dispersed nanoparticles immobilized on the CTF support. Apparently, N-doping has a beneficial influence on the dispersion efficiency and binding of the surface-anchored nanoparticles to the porous support, as seen for instance in N-doped carbon nanotubes or N-doped activated carbons as compared to their unmodified counterparts.^[19-22] Likewise, metal-modified CTF catalysts exhibit superior activity, stability and hence, recyclability in oxidation reactions as compared to other carbon supports modified with smaller amounts of nitrogen.^[16-17]

In order to provide a larger amount of possibly more Lewis basic binding sites compared to triazine rings, a heteroaromatic CTF building block featuring well-defined N-sites capable of strong binding to various metal ions would be desirable. Along these lines, Kuhn *et al.* recently introduced *o*-dicyanopyridine as a CTF building block featuring a higher amount of nitrogen than the prototypic dicyanobenzene linker.^[2,14] As expected by the higher nitrogen content, the resulting Pt-modified framework showed high activity and superior stability compared to the homogeneously catalyzed Periana-type selective oxidation of methane to methanol featuring a 2,2'-dipyrimidine as a ligand.^[18,23] In this system, however, no detailed information on the local structure of the catalyst and type of metal binding was accessible owing to the poor long-range order of the CTF scaffold.

With these design principles in mind, we targeted a CTF based on the 5,5'-dicyano-2,2'-bipyridine (DCBPY) building block, where the bipyridine (*bipy*) unit acts as a scaffold to site-specifically coordinate the metal cations. Owing to the abundance of metal-*bipy* complexes known and the versatility of the *bipy* ligand in homogeneous catalysis, a CTF framework based on this ubiquitous type of ligand may ultimately provide a link between a homogeneous catalyst and its heterogeneous counterpart, both featuring a metal-*bipy* unit as the catalytically active site. First attempts to synthesize a *bipy*-CTF have been made by Kuhn *et al.* recently,^[14] yet the resulting amorphous powders were reported to possess no apparent porosity and a surface area of essentially zero. In the present paper we demonstrate the synthesis of a highly porous *bipy*-CTF and give a detailed account of the complex interplay between local and long-range order, porosity, and nitrogen content to enable a deeper understanding of the structure and a more rational approach to the design of covalent triazine frameworks.

3.1.2 EXPERIMENTAL

Materials

All reactions were carried out under an argon atmosphere in flame-dried glassware. Anhydrous solvents and liquid reagents were transferred by syringe or cannula. Unless otherwise noted, all

materials were obtained from commercial suppliers (see supporting information, Table 8.1.1.1) and used without further purification. Column chromatography was performed using silica gel (0.035-0.070 mm, 60 Å, Acros Organics). Tetrakis-(triphenylphosphine)palladium^[24] and tri(2-furyl)phosphine (tfp)^[25] were synthesized according to published procedures. THF was continuously refluxed and freshly distilled from sodium benzophenone ketyl under nitrogen. Detailed information about the methods used is available in Chapter 8.1.1.

(5-Bromopyridin-2-yl)zinc(II) chloride

In a Schlenk tube LiCl (2.79 g, 66.0 mmol) and Mg turnings (1.82 g, 75.0 mmol) were suspended in THF (6.75 mL). 1,2-Dibromoethane (0.14 mL, 1.50 mmol) and chlorotrimethylsilane (200 µL, 1.50 mmol) were added and the suspension heated shortly to reflux. The reaction was cooled to 25 °C and a solution of ZnCl₂ in THF (0.65 M, 51.0 mL, 33.0 mmol) and, subsequently, 5-bromo-2-iodopyridine (8.52 g, 30.0 mmol) in THF (20.3 mL) were added. The mixture was stirred for 6 h at 25 °C and left over night to precipitate metal residues. The resulting solution was used without any further purification. The concentration of (5-bromopyridin-2-yl)zinc(II) chloride was determined by iodolysis^[26] (0.37 M, 97%).

5,5'-Dibromo-2,2'-bipyridine^[27]

(5-Bromopyridin-2-yl)zinc(II) chloride (0.37 M in THF, 54.0 mL, 20.0 mmol), Pd(dba)₂ (287 mg, 0.50 mmol), and tri(2-furyl)phosphine (232 mg, 1.00 mmol) were mixed in a Schlenk flask. 5-Bromo-2-iodopyridine (4.73 g, 16.7 mmol) in THF (11.5 mL) was slowly added and the mixture was stirred for 1 h at 50 °C. The reaction was quenched by the addition of a saturated aqueous solution of NH₄Cl (150 mL) and the resulting mixture was extracted with CHCl₃ (5 × 150 mL). The combined organic layers were washed with brine (200 mL), dried over MgSO₄ and concentrated *in vacuo*. The crude product (4.73 g) was purified by flash column chromatography (CH₂Cl₂/n-hexane 1:1) yielding 5,5'-dibromo-2,2'-bipyridine as colorless crystals (1.30 g, 4.14 mmol, 25%). ¹H NMR (270 MHz; CDCl₃): δ 8.70 (2 H, d, ⁴J_{HH} = 2 Hz, C^{5/5'}H), 8.29 (2 H, d, ³J_{HH} = 9 Hz, C^{2/2'}H), 7.93 (2 H, dd, ³J_{HH} = 9 Hz, ⁴J_{HH} = 2 Hz, C^{3/3'}H); ¹³C{¹H} NMR (68 MHz; CDCl₃): δ 153.6 (C^{1/1'}), 150.3 (C^{5/5'}), 139.8 (C^{3/3'}), 122.4 (C^{2/2'}), 121.6 (C^{4/4'}).

5,5'-Dicyano-2,2'-bipyridine^[28]

A microwave vial was charged with degassed DMF (20.0 mL), 5,5'-dibromo-2,2'-bipyridine (1.25 g, 4.00 mmol), Zn(CN)₂ (0.94 g, 8.00 mmol), Pd(PPh₃)₄ (0.28 g, 0.24 mmol), and bis(diphenylphosphino)pentane (0.11 g, 0.24 mmol). A stream of argon was then bubbled through the mixture for 2 min and the vial was sealed. The yellow mixture was heated in the microwave for 5 min at 150 °C. The now turquoise suspension was poured into H₂O (300 mL) and CHCl₃ (300 mL)

and was stirred for 1 h. The solvent layers were separated and the water layer extracted with CHCl_3 (3×300 mL). The combined organic layers were dried over MgSO_4 and concentrated *in vacuo*. The crude product was purified by flash column chromatography (CH_2Cl_2 /ethyl acetate 9:1) to give 5,5'-dicyano-2,2'-bipyridine as colorless crystals (0.76 g, 3.69 mmol, 92%). ^1H NMR (400 MHz; CDCl_3): δ 8.96 (2 H, d, $^4J_{\text{HH}} = 2$ Hz, $\text{C}^{5/5'}$ H), 8.63 (2 H, dd, $^3J_{\text{HH}} = 8$ Hz, $^5J_{\text{HH}} = 1$ Hz, $\text{C}^{2/2'}$ H), 8.13 (2 H, dd, $^3J_{\text{HH}} = 8$ Hz, $^4J_{\text{HH}} = 2$ Hz, $\text{C}^{3/3'}$ H); $^{13}\text{C}\{^1\text{H}\}$ NMR (100 MHz; CDCl_3) δ 157.0 ($\text{C}^{1/1'}$), 152.2 ($\text{C}^{5/5'}$), 140.6 ($\text{C}^{3/3'}$), 121.8 ($\text{C}^{2/2'}$), 116.6 ($\text{C}^{4/4'}$), 110.8 ($\text{C}^{6/6'}$).

Synthesis of covalent triazine frameworks

In a typical synthesis a *Duran* or quartz ampoule (1 x 14 cm) was charged with 5,5'-dicyano-2,2'-bipyridine (100 mg, 480 μmol) and ZnCl_2 (332 mg, 2.40 mmol) within a glove box. The ampoule was flame sealed under vacuum and was subjected in a tube oven to the temperature programs outlined in Table 8.1.1.2. After cooling to ambient temperature, the ampoule was opened and its content was grinded thoroughly. The crude product was stirred in H_2O (150 mL) for 3 h, filtered, and washed with H_2O (150 mL) and acetone (75 mL). The mixture was then refluxed in 1 M HCl (150 mL) over night, filtered, and subsequently washed with 1 M HCl (3×75 mL), H_2O (15×75 mL), THF (3×75 mL) and acetone (3×75 mL). Finally, the product was dried under vacuum for 6 h at 300 °C.

Metal doping experiments

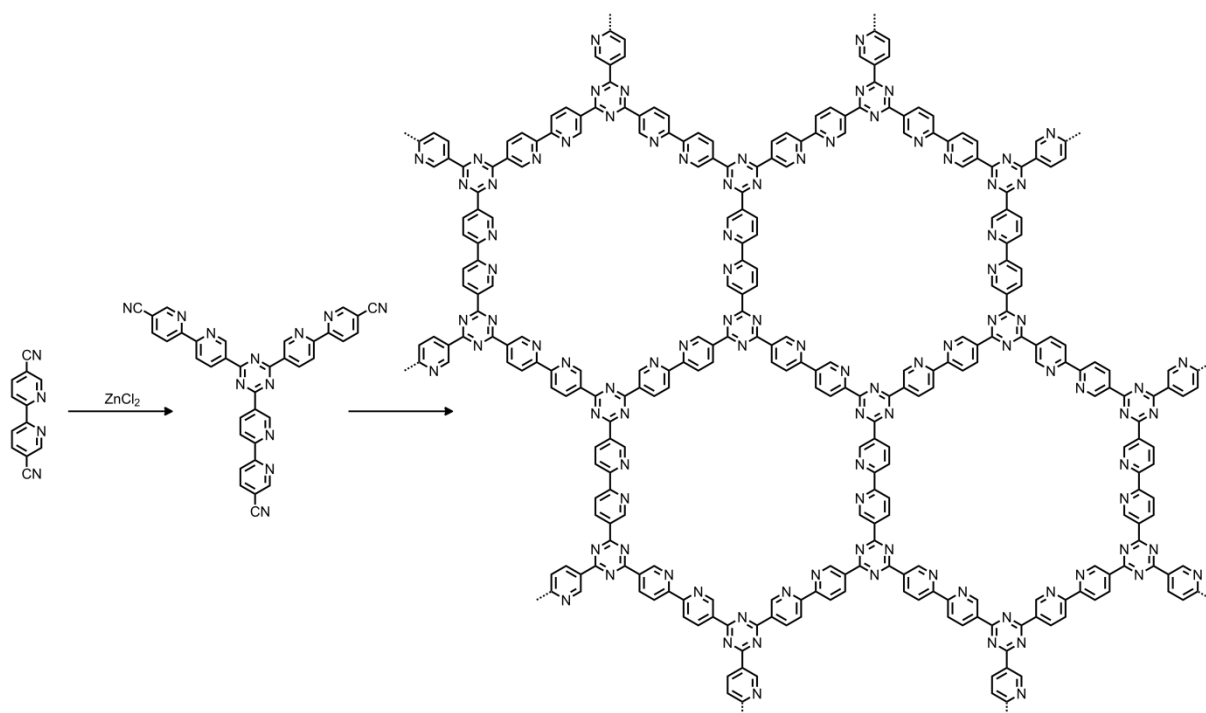
In a typical experiment the CTF (10 mg, 0.05 mmol) was suspended in a solution of the desired metal salt (500 mol% with respect to the 2,2'-bipyridine building block) in 10 mL water and stirred overnight at 60 °C. The doped CTF was filtered, washed with H_2O (50 mL) and acetone (15 mL) and dried over night at 90 °C.

3.1.3 RESULTS AND DISCUSSION

Synthesis and Porosity

The synthesis of the DCBPY was carried out starting from 5-bromo-2-iodopyridine in a three-step microwave-assisted process as outlined in the Experimental Section.

A standard CTF synthesis was performed under ionothermal conditions in sealed glass ampoules at 400 °C for 48 h using a ZnCl_2 salt melt both as solvent and Lewis acidic trimerization catalyst (Scheme 3.1.1). As opposed to typical COF syntheses, which are usually carried out in high-boiling solvents, the salt melt approach has turned out beneficial in CTF systems with respect to ensuring chemical equilibrium and hence, reversibility by keeping the as-formed oligomers and polymers solvated throughout the polymerization process and preventing them from phase-separating and precipitating irreversibly.^[2,14] In accordance with previous studies, the monomer to salt ratio, as well



Scheme 3.1.1. Schematic illustration of the synthesis of *bipy*-CTF. The bifunctional DCBPY trimerizes to an extended network under ionothermal conditions.

as the reaction temperature both have a strong impact on the degree of framework order (local and long range) and porosity of the resulting material.^[14,29] As outlined in Table 3.1.1 (entries 1-8), a DCBPY:ZnCl₂ ratio of 1:5 yielded samples with the highest porosities, whereas higher salt contents lead to slightly lower porosities, and one equivalent ZnCl₂ to none. The order of the material did not show any significant dependency on the salt concentration, in contrast to observations made by Kuhn *et al.*^[14] In order to probe the influence of temperature on the chemical composition and

Table 3.1.1. Overview of the reaction conditions and porosity properties of different *bipy*-CTF materials.

Sample	Temp [°C]	Time [h]	ZnCl ₂ [mol equiv]	S _{BET} [m ² g ⁻¹]	total pore vol ^a [cm ³ g ⁻¹]
1	375	48	1	-	-
2	375	48	5	928	0.46
3	375	48	7.5	876	0.43
4	375	48	10	800	0.40
5	400	48	5	671	0.37
6	400	48	5	1108	0.58
7	400	48	7.5	1108	0.58
8	400	48	10	964	0.49
9	450	48	5	945	0.46
10	500	48	5	1432	0.68
11	600	48	5	2393	1.19
12	700	48	5	3219	1.66
13	400/600	40/0.2	5	1663	0.81
14	400/600	40/20	5	2187	1.10
15	400/600	40/40	5	2761	1.44
16	400/600	40/80	5	2509	1.22

^aAt P/P₀ = 0.99.

structure of the obtained materials, the reaction temperatures were varied between 375 and 700 °C. Although materials with drastically different surface areas (SA) between ~ 670 and $3220 \text{ m}^2 \text{ g}^{-1}$ were obtained, the standard synthesis temperature was adjusted to 400 °C to maximize porosity and at the same time prevent partial framework decomposition. The impact of temperature on porosity will be discussed in more detail in the Section *Thermal behavior: Porosity tuning*.

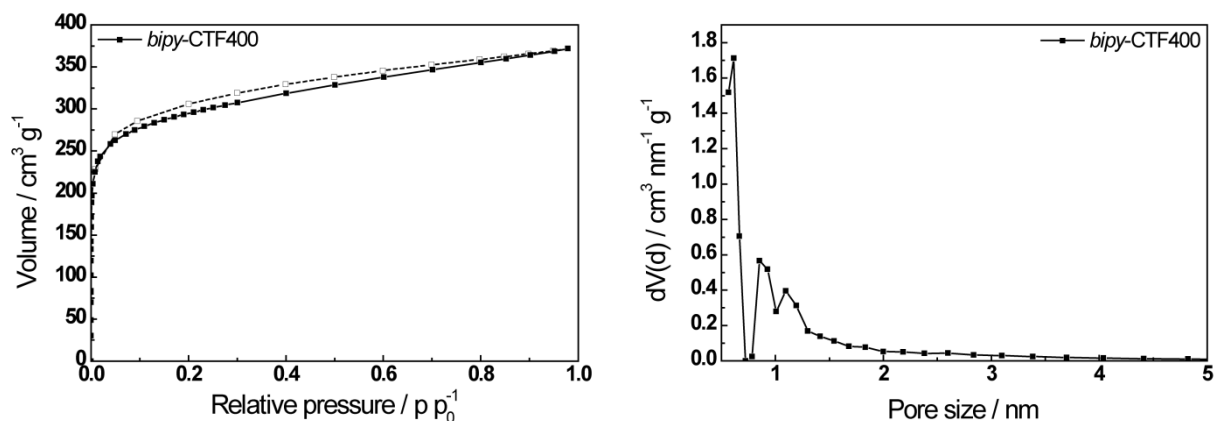


Figure 3.1.1. (Left) N_2 adsorption (filled symbols) and desorption (open symbols) isotherm of *bipy*-CTF400. (Right) Pore size distribution of *bipy*-CTF400.

The adsorption isotherm and pore size distribution of a sample obtained at 400 °C (*bipy*-CTF400) is shown in Figure 3.1.1. The sorption behavior is indicative of a highly microporous material with a large fraction of ultramicropores with sizes just below 6 Å and a smaller fraction of micropores with diameters around 1 nm. Interestingly, we found significant variations in the porosity for different samples (SA $671\text{--}1108 \text{ m}^2 \text{ g}^{-1}$; tot. pore vol. $0.36\text{--}0.58 \text{ cm}^3 \text{ g}^{-1}$) despite using the same reaction conditions (Table 3.1.1, entries 5-6) and chemical composition. This observation can be rationalized by the fact that even slight variations in the synthesis conditions (heating rate, temperature inhomogeneities, etc.) shift the pore size distribution towards slightly smaller ultramicropores with sizes just below 5 Å, which are not accessible any more to nitrogen used as a probe molecule in the physisorption measurements (see Figure 8.1.1.1). Consequently, the apparent total surface area is noticeably reduced if the fraction of ultramicropores with pore sizes below the N_2 -accessibility threshold is increased.

Local Structure

With applications ranging from sensing to heterogeneous catalysis with homogeneous (*i.e.* molecular) reaction sites, the versatility and functionality of a CTF is largely governed – besides its porosity – by its local structure. This is especially true for CTFs carrying functional groups such as the *bipy* unit, which needs to withstand the harsh ionothermal synthesis conditions described above. To the best of our knowledge, little is known yet about the local structure of CTF materials, irrespective of the building blocks used, as most porous CTFs prepared so far show little or no crystallinity, even

at the local scale. In order to probe the structural properties of the *bipy*-CTF400 and ascertain the influence of the synthesis conditions on the *bipy* group, the *bipy*-CTF400 was studied by X-ray powder diffraction (XRD), FTIR and solid-state NMR (ssNMR) spectroscopy.

As familiar from other CTFs except CTF-1 and a non-porous naphthalene-CTF,^[2,15] *bipy*-CTF400 was found to be largely amorphous, except for broad peaks around ~ 13 and $25^\circ 2\theta$, the latter of which we attribute to the 001 reflection indicating a “graphitic” layer stacking with an interlayer distance of $\sim 3.6 \text{ \AA}$ (Figure 8.1.1.2). Contrary to its X-ray amorphous character which indicates a lack of long-range order of the polymeric network, the IR spectrum exhibits a number of well-resolved, sharp bands suggesting a high degree of order on the local scale (Figure 3.1.2).

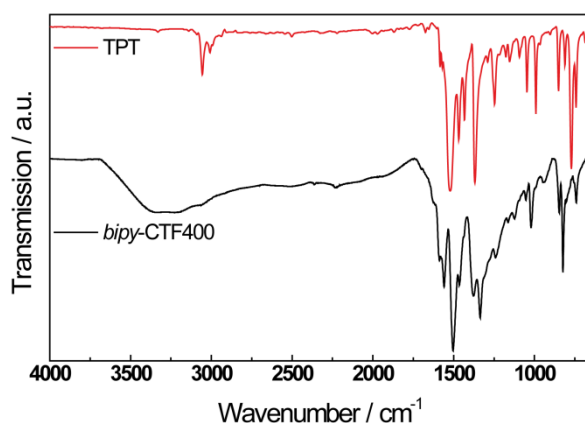


Figure 3.1.2. IR spectra of *bipy*-CTF400 and TPT.

Notably, the strong bands at 1506 (in-plane deformation vibration of the triazine ring) and 822 cm^{-1} (out-of-plane deformation vibration), as well as the absence of nitrile bands at 2364 and 2336 cm^{-1} compared to the starting material indicate the formation of triazine rings.^[30-31] The doublet band around $1550\text{-}1600 \text{ cm}^{-1}$, as well as the less well resolved bands between 1000 and 1450 cm^{-1} and the sharp band at 740 cm^{-1} may be largely attributed to the C=N and ring stretching vibrations of the *bipy* moiety.^[32] For comparison, the IR spectrum of the model compound 2,4,6-tri(pyridin-2-yl)-1,3,5-triazine (TPT) is shown in Figure 3.1.2. This molecular compound features building blocks (triazine, pyridine) similar to those expected to be present in the *bipy*-CTF400. The bands of the TPT spectra mostly correspond well to those of the *bipy*-CTF400, showing triazine bands at 1522 and 815 cm^{-1} and a doublet around $1580\text{-}1600 \text{ cm}^{-1}$, as well as a two strong bands at 775 and 745 cm^{-1} which we ascribe to pyridine ring vibrations.^[32]

For further information on the local structure we performed ^{13}C and ^{15}N MAS ssNMR measurements and compared the former to the ^{13}C spectrum of TPT. As depicted in Figure 3.1.3, the ^{13}C spectrum of *bipy*-CTF400 shows six well-resolved signals at 170 (1), 157 (2), 149 (3), 134 (4), 130 (5), and 119 ppm (6). The peak positions nicely correspond to those of TPT, which shows an essentially identical pattern, except for a single, broadened signal around 151 ppm (2-3) instead of two well-resolved

signals in the *bipy*-CTF400 at 149 (3) and 157 ppm (2) owing to the different substitution patterns. The peak at 170 ppm (1) can unambiguously be assigned to the triazine ring carbon atoms.^[33] Likewise, the assignment of the peak pattern of the *bipy* part is well established and consistent with an increasing downfield shift of the carbon atoms located in meta, para and ortho-position to the nitrogen atoms in the two rings, respectively. Our proposed overall assignment scheme is given in Figure 3.1.3. Although the pyridine moiety adjacent to the triazine ring in the model compound has a different substitution pattern compared to that in the *bipy*-CTF400, the NMR spectra are essentially insensitive to this difference in the local connection scheme.

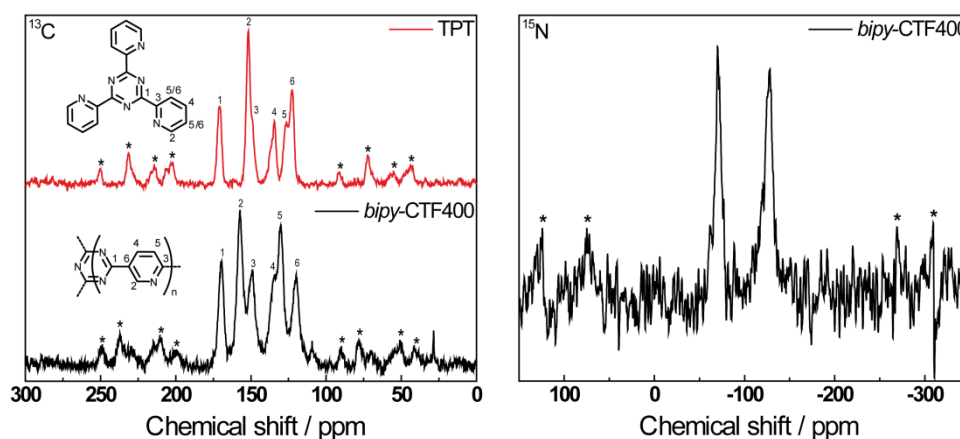


Figure 3.1.3. (Left) ^{13}C MAS ssNMR spectrum of *bipy*-CTF400 (bottom) compared to the model compound TPT (top). (Right) ^{15}N MAS ssNMR spectrum of *bipy*-CTF400.

The intact local structure is additionally confirmed by the ^{15}N ssNMR spectrum of the *bipy*-CTF400 (Figure 3.1.3, right). The signal at -128 ppm can be assigned to the triazine moiety (compare CTF-1 in Figure 8.1.1.3) and likewise, the signal at -70 ppm is characteristic of the bipyridine unit.^[34] Note that in addition to the well defined building blocks present in the material after synthesis, the *bipy*-CTF400 is highly stable in concentrated acids and bases such as H_2SO_4 and KOH for several hours without showing any sign of degradation.

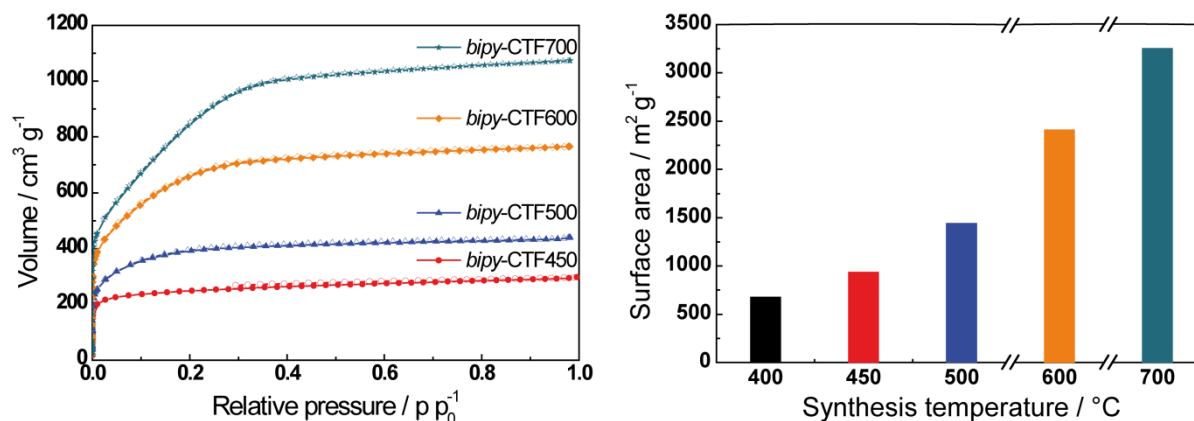


Figure 3.1.4. (Left) N_2 adsorption (filled symbols) and desorption (open symbols) isotherms of samples synthesized at 450–700 °C. (Right) Surface areas of samples synthesized at 400–700 °C.

Thermal behavior: Porosity tuning

As noted by Kuhn *et al.* the synthesis conditions such as temperature, heating rate, salt–precursor ratio etc. greatly impact the structural properties of the obtained materials.^[14,29] Notably, we detected a strong correlation between the SA and porosity of our materials and the temperature at which they were synthesized, thus furnishing a dynamic system that is highly tunable in terms of porosity. Whereas samples obtained at 400 °C show SA between 600 and 1100 m² g⁻¹ (see above), samples synthesized at temperatures between 450 and 700 °C (Table 3.1.1, entries 9-12) exhibit drastically increased SA with up to 3219 m² g⁻¹ for *bipy*-CTF700 (Figure 3.1.4). On a microscopic level, this significant increase in SA is the consequence of a gradual widening of the pores, accompanied by a shift of the pore size distribution toward the mesopore range without affecting the micropores (Figure 3.1.5). While for *bipy*-CTF400 a bimodal pore size distribution at 5 and 10 Å is observed and essentially no mesopores are present, the sizes of both the ultramicropores and micropores slightly widen and small mesopores are increasingly formed above 500 °C. Although micropores are present at all temperatures, the volume fraction of mesopores with pore diameters between 2 and 4 nm is dominant for *bipy*-CTF700.

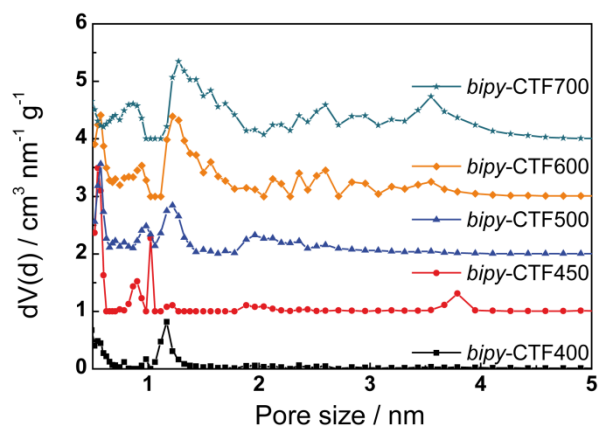


Figure 3.1.5. Comparison of the pore size distributions of samples synthesized at 400-700 °C. The curves are shifted vertically in steps of 1 cm³ nm⁻¹ g⁻¹.

In order to correlate the porosity changes with the composition and structure of the materials, the compounds obtained at different temperatures were studied by DTA/TG, elemental analysis (EA), FTIR and MAS ssNMR spectroscopy. As can be seen from the DTA/TG of *bipy*-CTF400, thermal degradation commences around 450 °C and becomes quite rapid above 500 °C (Figure 8.1.1.4). Whereas about 10% of weight are lost below 150 °C due to adsorbed water or solvents occluded in the pores, the weight loss due to framework degradation amounts to ~ 20-23% at 700 °C and ~ 46% at 1000 °C. EA conclusively indicates a gradual nitrogen loss at temperatures higher than 400 °C, accompanied by an equally pronounced loss of hydrogen and a slight increase in the relative carbon content, thereby indicating progressive carbonization of the materials (Table 8.1.1.3, entries 5, 9-12 and Figure 3.1.6, left). If the weight loss associated with framework degradation observed in the TG is

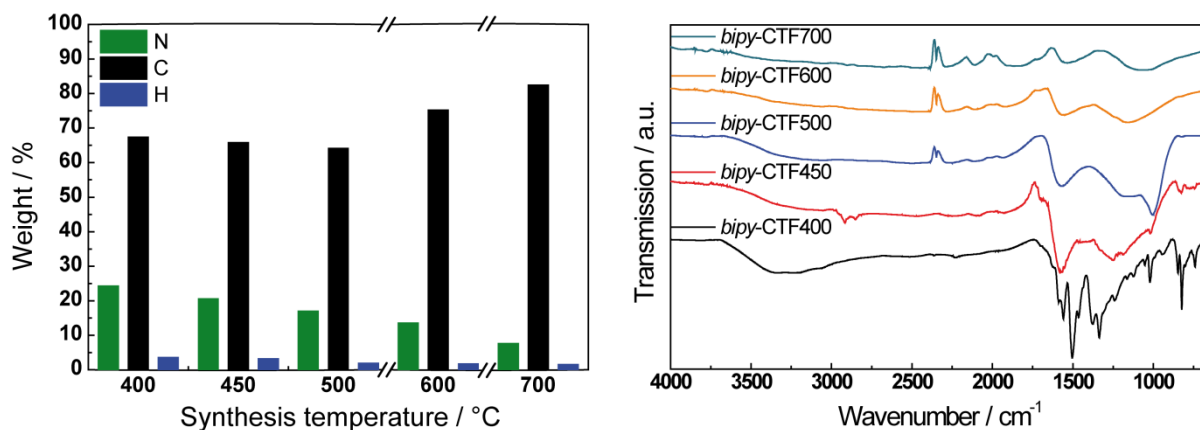


Figure 3.1.6. (Left) Variation of carbon (black), hydrogen (blue) and nitrogen (green) contents as a function of synthesis temperature of *bipy*-CTF. (Right) IR spectra of *bipy*-CTFs subjected to different temperature programs.

assumed to be exclusively due to nitrogen, at 700 °C approximately 80% of nitrogen is gone, whereas at 600 °C a loss of only about 26% nitrogen is observed. Similarly, by extrapolation we expect a loss of ~50% nitrogen at about 650 °C, which corresponds to either all bipyridine or all triazine nitrogens. Chemically, the compositional changes were monitored most conclusively by IR and ssNMR spectroscopy (Figure 3.1.6, right and Figure 3.1.7). Notably, the triazine signature is lost already at a temperature as low as 500 °C, indicated by the absence of the triazine ring breathing mode around 820 cm⁻¹ and the increasingly featureless fingerprint region in the IR, as well as by the complete loss of the triazine signal at 170 ppm in the ¹³C NMR in a sample treated at 400 and 600 °C for 40 h each. Also, the low field ¹³C signals of the bipyridine unit lose intensity relative to those at higher field, indicating the delayed, yet gradual loss of nitrogen from the bipyridine ring starting at temperatures around 600 °C. Note, however, that the degradation temperatures cannot directly be compared to those obtained from DTA/TG, as the temperature program and especially the holding times significantly varied compared to the *ex situ* studies. We conclude that the initial and rapid loss of nitrogen can be attributed almost exclusively to the degradation of triazine rings, which is then

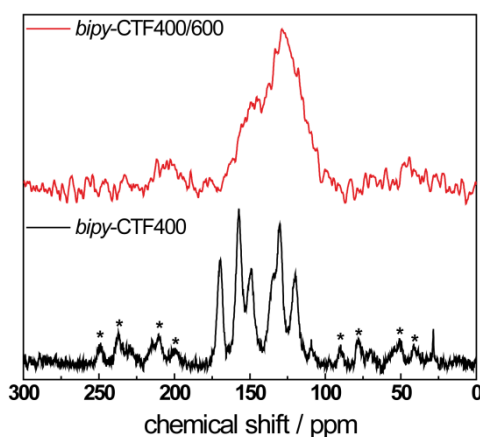


Figure 3.1.7. ¹³C MAS ssNMR spectrum of *bipy*-CTF400 (bottom) compared with sample 15 obtained at 600 °C (top).

followed by decomposition of the bipyridine rings and carbonization at higher temperatures. A likely degradation mechanism is the thermally induced retro-trimerization of the triazine rings and subsequent rearrangements, giving rise to loss of N_2 and possibly irreversible formation of new C-C bonds. The former may lead to “foaming” of the network and the latter to cross-linking between the layers, both resulting in the observed local expansion of the network and the drastic enhancement of porosity and SA.

Insights into the kinetics of the thermal degradation were obtained by heating a sample synthesized at 400 °C to 600 °C for increasing periods of time. Even at only 12 min at 600 °C, noticeable framework amorphization and significantly reduced triazine ring vibrations are visible in the IR, whereas at 20 h only broad, featureless IR bands are observed and at 80 h at 600 °C no bands pertaining to specific functional groups are visible (Figure 8.1.1.6). Therefore, thermal degradation at 600 °C is a very rapid process yielding highly porous, yet disordered nitrogen-containing carbon materials.

Metal doping

The functionality of the *bipy*-CTFs is largely determined by their high nitrogen content and – in the samples synthesized at 400 °C – by the molecularly well-defined metal adsorption sites of the *bipy* linker. The interplay between the high surface area and micropore volume, and the resulting high density of metal coordination sites was probed by impregnating the framework with a solution containing an excess (fivefold with respect to the monomer providing one coordination site) of metal salt and monitoring the amount of metal taken up by the framework as well as its distribution in the material.

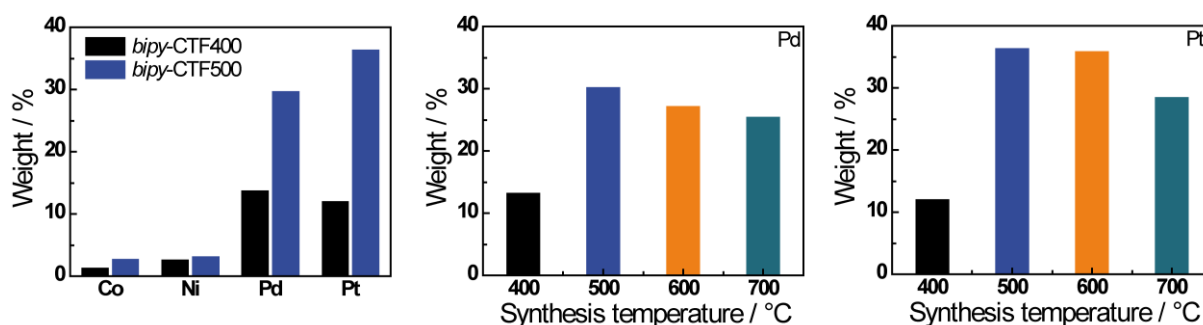


Figure 3.1.8. (Left) Metal uptakes by *bipy*-CTF400 (black) and *bipy*-CTF500 (blue) in wt%. (Middle) palladium and (right) platinum uptakes by *bipy*-CTFs synthesized at different temperatures.

To this end, two *bipy*-CTFs (*bipy*-CTF400 and *bipy*-CTF500) dispersed in water were exposed to different metal chlorides (K_2PtCl_4 , $Na_2PdCl_4 \cdot 3H_2O$, $CoCl_2 \cdot 6H_2O$, $NiCl_2 \cdot 6H_2O$) and the suspension was stirred at 60 °C over night. After filtration and washing, the metal content adsorbed by the framework was determined by ICP analysis, and the uniformity of metal distribution in the framework was ascertained by EDX analysis as shown in Figure 8.1.1.7. The two CTF materials were

selected in order to probe how the metal uptake varies as a function of synthesis temperature and, hence, porosity as well as nitrogen content and the resulting amount of specific bipyridine coordination sites.

As outlined in Figure 3.1.8 (left) and Table 8.1.1.4, the highest metal uptake (in wt%) was observed for Pt, followed by Pd, Ni and Co. In general, the uptake by *bipy*-CTF500 increases by a factor of 1.5 to 3 compared to the uptake by *bipy*-CTF400, as *bipy*-CTF500 exhibits larger porosity and hence, accessibility of the coordination sites. The uptake of the heavier transition metal salts is generally larger than that of the lighter ones. The Pt and Pd uptake as a function of *bipy*-CTF synthesis temperature shows a maximum for *bipy*-CTF500 and decreases towards higher synthesis temperatures (Figure 3.1.8, middle and right). The NMR and IR results suggest that while in *bipy*-CTF500 the triazine nitrogen content is already essentially zero, there are still most of the *bipy* coordination sites available. TEM and EDX data of the Pt and Pd samples show a uniform dispersion of the metals throughout the CTF (Figure 3.1.9a-b). The atomic ratio of Pt and Cl is close to the theoretical one (1:2), indicating a coordination of PtCl_2 to the available *bipy* units (Figure 8.1.1.7). Remarkably, a small amount of Pt^0 and Pd^0 nanoparticles are also visible in the TEM (Figure 3.1.9c), which is in agreement with the findings of Palkovits *et al.*^[18] Note that the total amount of Pd^0 found in the samples is significantly higher than that of Pt^0 . In both cases, however, the amount of metal formed is too small to be seen by XRD. In accordance with these results, the Pt and Pd uptake is governed by two counteracting trends – the increase in surface area towards higher temperatures leads to increasing Pt and Pd uptake, while the concomitant decrease of available metal coordination sites by depletion of nitrogen leads to reduced Pt and Pd uptakes. As a consequence, the maximum of Pt and Pd uptake for *bipy*-CTF500 can be taken as an indirect evidence of the *bipy*-specific binding of Pt^{2+} and Pd^{2+} .

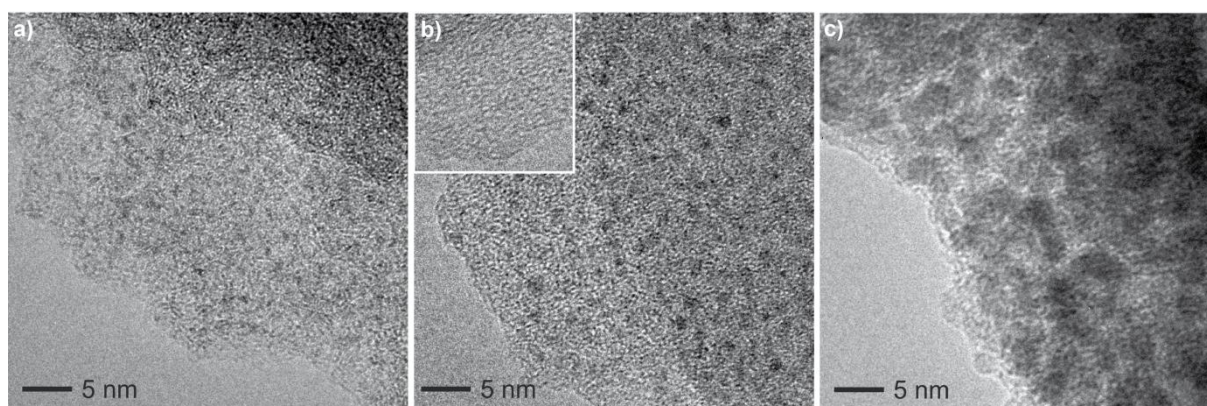


Figure 3.1.9. TEM pictures of a) Pt-loaded and b) Pd-loaded samples (the inset shows an unloaded spot). c) Pd nanoparticles in a Pd-loaded sample.

3.1.4 CONCLUSIONS

The presented *bipy*-functionalized CTF lends itself as a model system to study the effects of different synthesis parameters on the structural and chemical properties of the obtained frameworks. We have demonstrated a significant degree of tunability of the surface area and porosity as a function of temperature, resulting in hierarchically micro- and mesoporous frameworks with high sorption capacity for various metal ions. The frameworks show variable metal uptake, depending on the type of metal as well as the temperature at which the adsorbent was synthesized. Notably, enhanced Pt and Pd uptake at 500-600 °C suggests a rather specific Pt and Pd binding rather than mere dispersion of the metal on the CTF substrate. This type of binding ensures a “homogeneous” environment of the metal ions in the framework, which is highly robust and insoluble in essentially all organic solvents and strong acids. This finding bodes well for the use of metal-modified *bipy*-CTFs with high specific surface areas and high nitrogen content as heterogeneous catalysts with well-defined metal coordination sites. Studies exploring the metal-CTF interaction as well as the catalytic activity of metal-doped *bipy*-CTFs are currently underway.

3.1.5 BIBLIOGRAPHY

Acknowledgment

We acknowledge support by the German Excellence Initiative of the Deutsche Forschungsgemeinschaft (DFG) *via* the Nanosystems Initiative Munich (NIM), the Center for Nanoscience (CeNS) and the Fonds der Chemischen Industrie (FCI). M.E.T. thanks the Dr. Alexander und Dr. Rosemarie Bauer-Stiftung for kind financial support. We thank Viola Duppel for TEM and SEM measurements, Christian Minke for SEM and ssNMR measurements, Andreas Wisnet, Teresa Dennenwaldt and Prof. Christina Scheu for TEM measurements, and Marie-Luise Schreiber and Helmut Hartl for ICP-AES measurements. We thank Mario Liebl and Prof. Jürgen Senker for providing us with the ¹⁵N ssNMR spectrum of CTF-1, and Prof. Thomas Bein, Prof. Wolfgang Schnick, and Prof. Wintterlin for access to the respective measurement facilities.

References

- [1] A. P. Côté, A. I. Benin, N. W. Ockwig, M. O’Keeffe, A. J. Matzger, O. M. Yaghi, *Science* **2005**, *310*, 1166-1170.
- [2] P. Kuhn, M. Antonietti, A. Thomas, *Angew. Chem. Int. Ed.* **2008**, *47*, 3450-3453.
- [3] J. L. C. Rowsell, O. M. Yaghi, *Microporous Mesoporous Mater.* **2004**, *73*, 3-14.
- [4] J.-X. Jiang, F. Su, A. Trewin, C. D. Wood, N. L. Campbell, H. Niu, C. Dickinson, A. Y. Ganin, M. J. Rosseinsky, Y. Z. Khimyak, A. I. Cooper, *Angew. Chem. Int. Ed.* **2008**, *47*, 1167-1167.

- [5] J.-Y. Lee, C. D. Wood, D. Bradshaw, M. J. Rosseinsky, A. I. Cooper, *Chem. Commun.* **2006**, 2670-2672.
- [6] M. P. Tsyurupa, V. A. Davankov, *React. Funct. Polym.* **2006**, *66*, 768-779.
- [7] C. D. Wood, B. Tan, A. Trewin, H. Niu, D. Bradshaw, M. J. Rosseinsky, Y. Z. Khimyak, N. L. Campbell, R. Kirk, E. Stöckel, A. I. Cooper, *Chem. Mater.* **2007**, *19*, 2034-2048.
- [8] P. M. Budd, B. S. Ghanem, S. Makhseed, N. B. McKeown, K. J. Msayib, C. E. Tattershall, *Chem. Commun.* **2004**, 230-231.
- [9] N. B. McKeown, P. M. Budd, K. J. Msayib, B. S. Ghanem, H. J. Kingston, C. E. Tattershall, S. Makhseed, K. J. Reynolds, D. Fritsch, *Chem. Eur. J.* **2005**, *11*, 2610-2620.
- [10] N. B. McKeown, B. Gahnem, K. J. Msayib, P. M. Budd, C. E. Tattershall, K. Mahmood, S. Tan, D. Book, H. W. Langmi, A. Walton, *Angew. Chem. Int. Ed.* **2006**, *45*, 1804-1807.
- [11] A. P. Côté, H. M. El-Kaderi, H. Furukawa, J. R. Hunt, O. M. Yaghi, *J. Am. Chem. Soc.* **2007**, *129*, 12914-12915.
- [12] R. W. Tilford, W. R. Gemmill, H.-C. zur Loye, J. J. Lavigne, *Chem. Mater.* **2006**, *18*, 5296-5301.
- [13] S. Wan, J. Guo, J. Kim, H. Ihee, D. Jiang, *Angew. Chem. Int. Ed.* **2008**, *47*, 8826-8830.
- [14] P. Kuhn, A. Thomas, M. Antonietti, *Macromolecules* **2009**, *42*, 319-326.
- [15] M. J. Bojdys, J. Jeromenok, A. Thomas, M. Antonietti, *Adv. Mater.* **2010**, *22*, 2202-2205.
- [16] C. E. Chan-Thaw, A. Villa, P. Katekomol, D. Su, A. Thomas, L. Prati, *Nano Lett.* **2010**, *10*, 537-541.
- [17] C. E. Chan-Thaw, A. Villa, L. Prati, A. Thomas, *Chem. Eur. J.* **2011**, *17*, 1052-1057.
- [18] R. Palkovits, M. Antonietti, P. Kuhn, A. Thomas, F. Schüth, *Angew. Chem. Int. Ed.* **2009**, *48*, 6909-6912.
- [19] A. Villa, D. Wang, P. Spontoni, R. Arrigo, D. Su, L. Prati, *Catal. Today* **2010**, *157*, 89-93.
- [20] K. Jiang, A. Eitan, L. S. Schadler, P. M. Ajayan, R. W. Siegel, N. Grobert, M. Mayne, M. Reyes-Reyes, H. Terrones, M. Terrones, *Nano Lett.* **2003**, *3*, 275-277.
- [21] X. Hou, L. Wang, F. Zhou, F. Wang, *Carbon* **2009**, *47*, 1209-1213.
- [22] H. Yoon, S. Ko, J. Jang, *Chem. Commun.* **2007**, 1468-1470.
- [23] R. A. Periana, D. J. Taube, S. Gamble, H. Taube, T. Satoh, H. Fujii, *Science* **1998**, *280*, 560-564.
- [24] F. Tellier, R. Sauvêtre, J.-F. Normant, *J. Organomet. Chem.* **1985**, *292*, 19-28.
- [25] D. W. Allen, B. G. Hutley, M. T. J. Mellor, *J. Chem. Soc., Perkin Trans. 2* **1972**, 63-67.
- [26] A. Krasovskiy, P. Knochel, *Synthesis* **2006**, *2006*, 0890-0891.
- [27] F. M. Romero, R. Ziessel, *Tetrahedron Lett.* **1995**, *36*, 6471-6474.
- [28] P. N. W. Baxter, J. A. Connor, *J. Organomet. Chem.* **1988**, *355*, 193-196.
- [29] P. Kuhn, A. I. Forget, D. Su, A. Thomas, M. Antonietti, *J. Am. Chem. Soc.* **2008**, *130*, 13333-13337.

- [30] V. G. Manecke, D. Wöhrle, *Makromol. Chem.* **1968**, *120*, 176-191.
- [31] W. M. Padgett, W. F. Hamner, *J. Am. Chem. Soc.* **1958**, *80*, 803-808.
- [32] N. Neto, M. Muniz-Miranda, L. Angeloni, E. Castellucci, *Spectrochim. Acta, Part A* **1983**, *39*, 97-106.
- [33] B. Jürgens, E. Irran, J. Senker, P. Kroll, H. Müller, W. Schnick, *J. Am. Chem. Soc.* **2003**, *125*, 10288-10300.
- [34] L. Pazderski, J. Toušek, J. Sitkowski, L. Kozerski, E. Szłyk, *Magn. Reson. Chem.* **2007**, *45*, 1045-1058.

4 COVALENT TRIAZINE FRAMEWORKS FOR GAS CAPTURE AND STORAGE

Various works have shown the high potential of CTFs as CCS materials due to their high degree of microporosity and large nitrogen contents. Additionally, the chemical and thermal stability is beneficial for postcombustion capture, where impurities of nitrogen, oxygen, sulfur oxides and nitrogen oxides are present in the gas stream. In the following chapters 4.1 and 4.2 we report on the synthesis of three new CTFs based on fluorine, lutidine and pyrimidine building units, and their structural characterization. Furthermore, we discuss the carbon dioxide and hydrogen storage capacities of these materials as well as *bipy*-CTFs and CTF1, which are competitive with or even superior to the best carbon capture and storage performances reported for polymeric materials to date. The trends revealed in this work are interesting for future researches into the rational development of new powerful gas capture and storage materials.

4.1 A FLUORENE BASED COVALENT TRIAZINE FRAMEWORK WITH HIGH CO₂ AND H₂ CAPTURE AND STORAGE CAPACITIES

Stephan Hug, Maria B. Mesch, Hyunchul Oh, Nadine Popp, Michael Hirscher, Jürgen Senker and Bettina V. Lotsch

published in *J. Mater. Chem. A* **2014**, 2, 5928-5936
DOI: 10.1039/C3TA15417C
<http://pubs.rsc.org/en/content/articlelanding/2014/ta/c3ta15417c>
Reproduced with permission from The Royal Society of Chemistry

Abstract

Porous organic polymers have come into focus recently for the capture and storage of post combusted CO₂. Covalent triazine frameworks (CTFs) constitute a nitrogen-rich subclass of porous polymers, which offer enhanced tunability and functionality combined with high chemical and thermal stability. In this work a new covalent triazine framework based on fluorene building blocks is presented, along with a comprehensive elucidation of its local structure, porosity, and capacity for CO₂ capture and H₂ storage. The framework is synthesized under ionothermal conditions at 300-600 °C using ZnCl₂ as a Lewis acidic trimerization catalyst and reaction medium. Whereas the materials synthesized at lower temperatures mostly feature ultramicropores and moderate surface areas as probed by CO₂ sorption (297 m² g⁻¹ at 300 °C), the porosity is significantly increased at higher synthesis temperatures, giving rise to surface areas in excess of 2800 m² g⁻¹. With a high fraction of micropores and a surface area of 1235 m² g⁻¹, the CTF obtained at 350 °C shows an excellent CO₂ sorption capacity at 273 K (4.28 mmol g⁻¹), which is one of the highest observed among all porous organic polymers. Additionally, the materials have CO₂/N₂selectivities of up to 37. Hydrogen adsorption capacity of 4.36 wt% at 77 K and 20 bar is comparable to that of other POPs, yet the highest among all CTFs studied to date.

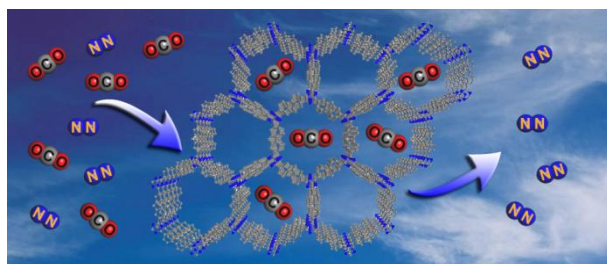


Table of content. We present a fluorene based covalent triazine framework with high CO₂ capture and storage capacities, as well as good selectivities towards CO₂ over nitrogen.

4.1.1 INTRODUCTION

Lately, the development of covalent triazine frameworks (CTFs), a subclass of porous organic polymers (POPs), garnered significant attention owing to their high surface areas combined with a highly robust nature, that is, high thermal (>300 °C) and chemical stabilities towards concentrated acids and bases.^[1-5] Therefore, CTFs are considered ideal scaffolds for applications such as heterogeneous catalysis,^[6-9] gas storage and separation.^[9-16] Recently, low temperature synthesis of CTFs set the stage for further applications such as for chemo- and size-selective membranes^[17] and in optoelectronics.^[10]

The development of potent gas storage systems has been fueled by the need for highly selective gas capture materials apt to selectively filter out or enrich relevant gases such as methane or carbon dioxide. The anthropogenic emission of CO₂ is known to be a major source of global warming. The global emission of CO₂ by power plants and public transportation has risen remarkably in the last decades.^[18] According to the International Energy Agency (IEA), appropriate capture and storage of post combusted CO₂ (CCS) has the potential of decreasing the emissions up to 20%.^[19] Typically, flue gas of a coal-fired power plant consists of approximately 15% CO₂, 5% H₂O, 5% O₂ and 75% N₂ and is emitted at 40-80 °C and 1 bar.^[20-21] Therefore, materials suitable for CCS require a high preference for adsorption of CO₂ under these conditions. Amine scrubbing and cryogenic cooling are the only established technologies for CO₂ capture up to date, which however come with the disadvantage of increasing the energy requirements of a power plant by 25-40%.^[20,22] Especially amine scrubbing needs large volumes of solvents, high temperatures for regeneration and costly disposal when expired.^[22-23] The disposal and the formation of toxic byproducts during the regeneration step additionally raise environmental concerns about this technology. Lately, the use of solid physical adsorbents for CO₂ capture, such as metal organic frameworks (MOFs) and POPs, was part of several reviews.^[20-21,24-27] Main advantages of solid adsorbents are their long lifetimes and recovery at moderate temperatures. Especially POPs are promising because of their high chemical and thermal stabilities as well as synthetic versatility, giving rise to a large variety of functional and structural designs.

In this work we present the synthesis and characterization of a new fluorene-based covalent triazine framework (*fl*-CTF) at different temperatures. We tested the materials properties regarding CO₂ adsorption at 273 K, 298 K and 313 K, along with the CO₂ over N₂ selectivity, showing high capture capacities and good selectivities. Additionally, we measured high-pressure adsorption of H₂ at 77 K and 298 K, yielding uptakes at the forefront of polymeric hydrogen storage systems.

4.1.2 EXPERIMENTAL SECTION

Materials and Methods

All starting materials and solvents were obtained from commercial sources and were used without further purification. 2,7-dibromo-9H-fluorene (99%) was purchased from Acros Organics. Zinc cyanide (98%) and trifluoromethanesulphonic acid (99%) were obtained from ABCR. Anhydrous zinc chloride (99.995%), 2-bromo-9H-fluorene (95%) and tetrakis(triphenyl-phosphine)palladium(0) (99%) were purchased from Sigma Aldrich. Dimethylformamide (99%) and 1,5-bis(diphenylphosphino)pentane (97%) were obtained from Alfa Aesar.

Argon, Carbon dioxide and nitrogen adsorption/desorption measurements were performed at 87, 273, 298 and 313 K with an Autosorb-iQ surface analyzer (Quantachrome Instruments, USA). Samples were outgassed in vacuum (10^{-7} mbar) at 200-300 °C for 6 h to remove all guests. Pore-size distributions were determined using the calculation model for Ar at 87 K on carbon (slit pore, QSDFT equilibrium model) or for CO₂ at 273 K on carbon (NLDFT model) of the ASiQwin software (v2.0) from Quantachrome. For BET calculations pressure ranges of the Ar isotherms were chosen with the help of the BET Assistant in the ASiQwin software. In accordance with the ISO recommendations multipoint BET tags equal or below the maximum in $V \cdot (1 - P/P_0)$ were chosen. The isosteric heats of adsorption were calculated from the CO₂ adsorption isotherms using the Quantachrome software ASiQwin (v2.0) based on the Clausius-Clapeyron equation (see chapter 8.1.2).

High-pressure hydrogen adsorption/desorption measurements were performed on an automated Sievert's type apparatus (PCTPro-2000) with a so-called micro-doser (MD) from HyEnergy. The original setup was upgraded by a heating and cooling device to regulate the sample temperature. The adsorption and desorption isotherms (0-20 bar) were measured at various temperatures (77 to 298 K) in a sample cell volume of ≈ 1.3 mL using ultra high purity hydrogen gas (99.999%). Samples were outgassed in vacuum ($4.5 \cdot 10^{-6}$ mbar) at 200 °C for 6 h to remove all guests. The isosteric heat of adsorption is calculated from the absolute adsorbed hydrogen according to a variant of the Clausius-Clapeyron equation (see chapter 8.1.2).

Cryogenic hydrogen adsorption/desorption measurements at 19.5 K were measured with laboratory-designed volumetric adsorption equipment with a temperature controlled cryostat. The experimental set-up has been described in detail elsewhere.^[28-29] Samples were activated under vacuum (10^{-4} mbar) at 150 °C for 12 h, prior to each measurement. For the laboratory-designed cryostat, the temperature control was calibrated by measuring the liquefaction pressure for hydrogen and nitrogen in the empty sample chamber at various temperatures.

Infrared (IR) spectroscopy measurements were carried out on a Perkin Elmer Spektrum BX II (Perkin Elmer, USA) with an attenuated total reflectance unit.

Powder X-ray diffraction (XRD) was measured on a BRUKER D8 Avance (Bruker AXS, USA) in Bragg-Brentano geometry or on a HUBER G670 (HUBER Difraktionstechnik, Germany) in Guinier geometry equipped with an imaging plate detector.

Elemental analysis (EA) was carried out with an Elementar vario EL (Elementar Analysensysteme, Germany).

Magic angle spinning (MAS) solid-state nuclear magnetic resonance (ssNMR) spectra were recorded at ambient temperature on a BRUKER DSX500 Avance NMR spectrometer or a BRUKER AvanceIII HD 400 NMR spectrometer (Bruker Biospin, Rheinstetten, Germany) with an external magnetic field of 11.75 T and 9.4 T, respectively. The operating frequencies are 500.1 MHz, 125.7 MHz and 400.1 MHz, 100.6 MHz for ^1H and ^{13}C , respectively and the spectra were referenced relative to TMS (^1H , ^{13}C). The samples were contained either in 2.4, 3.2 mm or 4 mm ZrO_2 rotors. The 1D $^1\text{H}^{13}\text{C}$ cross-polarization (CP) MAS spectra were acquired with a ramped-amplitude (RAMP) CP sequence and contact times between 2 and 10 ms. CPPI (cross-polarization combined with polarization inversion) experiments were carried out to get information about the number of hydrogen atoms directly attached to the carbon. An initial contact time of 2 ms was used and spectra with inversion times up to 400 μs were measured. The measurements were carried out using spinning frequencies of 10 kHz and 15 kHz for CP, and 5.1 kHz for CPPI measurements, respectively. During acquisition broadband proton decoupling using SPINAL64 or TPPM was carried out.

Solution-state NMR spectroscopy was performed on a JEOL DELTA NMR (JEOL, Japan) by single pulse experiments. The spectra were referenced against CDCl_3 ($\delta(^1\text{H})$ 7.26 ppm, $\delta(^{13}\text{C}\{^1\text{H}\})$ 77.16 ppm).

High resolution mass spectroscopy (HRMS) was carried out on a JEOL MS700 (JEOL, Japan), by direct electron ionization (DEI).

Differential thermal analysis and thermogravimetry (DTA/TG) were measured on a SETARAM TG-DTA92-2400 combined DTA-TG-thermobalance (SETARAM Instrumentation, France) in aluminum oxide crucibles. Heating was performed from room temperature to 800 $^\circ\text{C}$ with a heating rate of 5 $^\circ\text{C min}^{-1}$ under helium atmosphere.

Microwave reactions were carried out in a Biotage Initiator (Biotage AB, Sweden) in 10-20 mL microwave vials from Biotage.

9H-fluorene-2-carbonitrile^[30]

A microwave vial was charged with DMF (20.0 mL) and a stream of argon was bubbled through the solvent for 30 min. 2-bromo-9H-fluorene (1.03 g, 4.00 mmol), $\text{Zn}(\text{CN})_2$ (939 mg, 8.00 mmol), $\text{Pd}(\text{PPh}_3)_4$ (185 mg, 0.16 mmol), and 1,5-bis(diphenyl-phosphino)pentane (72.7 mg, 0.16 mmol) were added and the stream of argon was continued for 2 min. The vial was sealed and the yellow mixture

was heated in the microwave for 5 min at 150 °C. The now orange suspension was poured into sat. NaHCO₃-sol. (200 mL) and extracted with CHCl₃ (3 × 200 mL). The combined organic layers were dried over MgSO₄ and concentrated *in vacuo*. The crude product was purified by column chromatography (hexane/ethyl acetate 95:5) to yield 9*H*-fluorene-2-carbonitrile as light tanned solid (0.59 g, 3.09 mmol, 77%). δ_H (300 MHz; CDCl₃) 7.86-7.79 (3 H, m, Ph), 7.68-7.64 (1 H, m, Ph), 7.67-7.57 (1 H, m, Ph), 7.47-7.37 (2 H, m, Ph), 3.93 (2 H, s, CH₂); δ_C (68 MHz; CDCl₃) 146.3, 144.0, 143.7, 140.0, 131.3, 128.72, 128.68, 127.4, 125.4, 121.1, 120.5, 119.8, 109.8, 36.9.

9*H*-fluorene-2,7-dicarbonitrile^[31]

A microwave vial was charged with DMF (20.0 mL) and a stream of argon was bubbled through the solvent for 30 min. 2,7-dibromo-9*H*-fluorene (1.31 g, 4.00 mmol), Zn(CN)₂ (939 mg, 8.00 mmol), Pd(PPh₃)₄ (277 mg, 0.24 mmol), and 1,5-bis(diphenylphosphino)pentane (109 mg, 0.24 mmol) were added and the stream of argon was continued for 2 min. The vial was sealed and the yellow mixture was heated in the microwave for 5 min at 150 °C. The now orange suspension was poured into H₂O (300 mL) and extracted with CHCl₃ (4 × 300 mL). The combined organic layers were dried over MgSO₄ and concentrated *in vacuo*. The crude product was recrystallized from CH₂Cl₂ to give 9*H*-fluorene-2,7-dicarbonitrile as light green crystals (0.66 g, 3.05 mmol, 76%). δ_H (270 MHz; CDCl₃) 7.93 (2 H, d, ³J_{HH} = 8.1 Hz, Ph), 7.89 (2 H, d, ⁴J_{HH} = 0.7 Hz, Ph), 7.74 (2 H, dd, ³J_{HH} = 8.0 Hz, ⁴J_{HH} = 0.7 Hz, Ph), 4.04 (2 H, s, CH₂); δ_C (68 MHz; CDCl₃) 144.4, 144.3, 131.7, 129.1, 121.7, 119.1, 111.8, 36.9.

Tris(9*H*-fluoren-2-yl)-1,3,5-triazine

In an outgassed 25 mL *Schlenk* tube trifluoromethanesulphonic acid (0.80 mL, 9.00 mmol) was cooled to -18 °C and under stirring 9*H*-fluorene-2-carbonitrile (574 mg, 3 mmol) was added in portions. The mixture was left in the ice bath for 40 h giving a dark green solid. The solid was slowly added to ice, turning into an orange suspension. After neutralizing with ammonia (25% in H₂O) the suspension turned light purple and the precipitate was filtered off. Washing with water and little amounts of acetone yielded tris(9*H*-fluoren-2-yl)-1,3,5-triazine as light tanned solid (477 mg, 83%). MS (DEI+) *m/z* (relative intensity) 574 (MH⁺, 18%), 573 (M⁺, 40), 192 (C₁₄H₁₀N⁺, 100), 191 (C₁₄H₉N⁺, 92), 190 (C₁₄H₈N⁺, 79), 165 (C₁₃H₉⁺, 24), 164 (C₁₃H₈⁺, 21). HRMS (DEI) *m/z*: [M]⁺ Calc. for C₄₂H₂₇N₃ 573.2205; Found 573.2219. Anal. Calc. for C₄₂H₂₇N₃: C, 87.93; H, 4.74; N, 7.32. Found: C, 86.69; H, 4.86; N 7.18%. Mp 350-356 °C (decomp.).

Synthesis of Covalent Triazine Frameworks

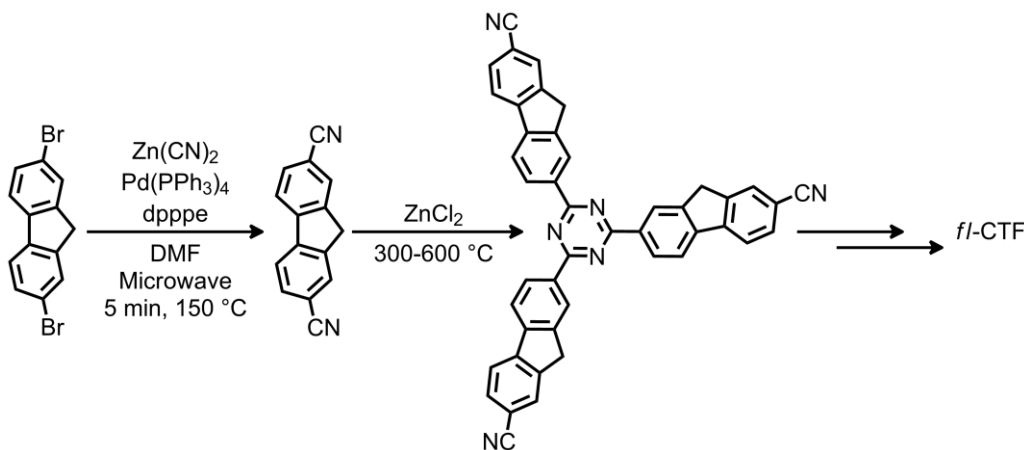
In a typical synthesis a *Duran* ampoule (1.5x12 cm) was charged with 9*H*-fluorene-2,7-dicarbonitrile (500 mg, 2.31 mmol) and ZnCl₂ (1.57 g, 11.6 mmol) within a glove box. The ampoule was flame sealed under vacuum and was subjected in a tube oven to temperatures between 300-600 °C (for

temperature programs, see Table 8.1.2.1). After cooling to ambient temperature, the ampoule was opened and its content ground thoroughly. The crude product was stirred in H₂O (150 mL) for 1 h, filtered, and washed with 1 M HCl (75 mL) and ethanol (75 mL). The mixture was then stirred at 90 °C in 1 M HCl (80 mL) over night, filtered, and subsequently washed with 1 M HCl (3 × 75 mL), H₂O (12 × 75 mL), THF (2 × 75 mL), and acetone (1 × 75 mL). Finally, the black powder was dried over night at 60 °C.

4.1.3 RESULTS AND DISCUSSION

Synthesis and Characterization

The standard procedure for preparing CTFs is by ionothermal synthesis using ZnCl₂ both as “solvent” and as Lewis acidic catalyst at temperatures above 300 °C.^[1-4] CTFs synthesized at low temperatures (300-400 °C) may show little crystallinity, yet at the same time may have well-defined local structures.^[1,5,9,32] Synthesis at higher temperatures typically leads to dramatic increases in the surface areas accompanied by the loss of structural elements, especially the triazine moieties.^[4-5] In this work we followed this procedure using 9*H*-fluorene-2,7-dicarbonitrile as precursor. The precursor was synthesized by a Negishi cross coupling reaction from 2,7-dibromo-9*H*-fluorene in the microwave with just 5 min reaction time (Scheme 4.1.1). This straightforward method to produce aromatic dinitriles is analogous to the synthesis described by us previously.^[5] Work-up was done by recrystallization and gave good yields of 76%. The syntheses of the CTFs were performed at temperatures between 300-600 °C, yielding fluorene-CTFs at 300 °C (*fl*-CTF300), 350 °C (*fl*-CTF350), 400 °C (*fl*-CTF400), 500 °C (*fl*-CTF500) and 600 °C (*fl*-CTF600). The reaction times were 48 h for all samples, except for *fl*-CTF300 and *fl*-CTF350, where the reaction times were raised to 96 h after very low yields had been obtained due to unreacted monomers or oligomers. Reaction times of 168 h did not give higher yields or changes in the material properties.



Scheme 4.1.1. Synthesis route for *fl*-CTFs.

CTF-0, CTF-1 and CTF-2 are the only three examples of CTFs which show moderate crystallinity.^[1,12,32] Therefore, it was little surprising that our materials were found to be largely amorphous in the XRD measurements, except for broad peaks at 14.8, 22.7 and 33.6° 2 θ . The peak at 22.7° 2 θ we attribute to a 00 l reflection indicating a “graphitic” layer stacking with an interlayer distance of ~3.9 Å, which is rather large and consistent with only weak interlayer coupling (Figure 8.1.2.1).

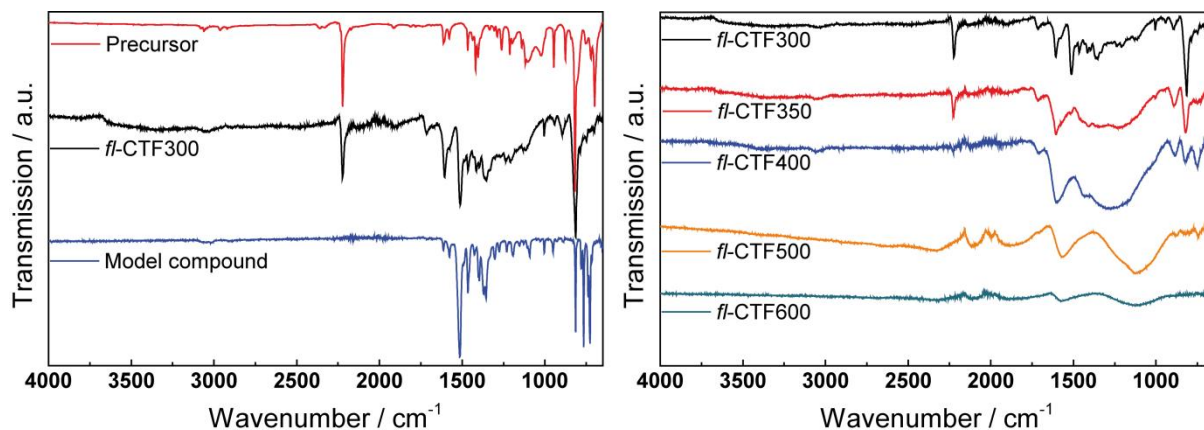


Figure 4.1.1. (Left) IR spectra of 9H-fluorene-2,7-dicarbonitrile, *fl*-CTF300 and tris(9H-fluorene-2-yl)-1,3,5-triazine. (Right) IR spectra of the samples *fl*-CTF300, *fl*-CTF350, *fl*-CTF400, *fl*-CTF500 and *fl*-CTF600.

To probe whether trimerization in these samples was completed with the fluorene units still being intact, we used IR spectroscopy and ssNMR measurements and compared the results with the model compound tris(9H-fluorene-2-yl)-1,3,5-triazine. Figure 4.1.1 depicts the IR and Figures 4.1.2 and 8.1.2.2 the ¹³C ssNMR spectra of the as-synthesized materials. *fl*-CTF300 shows well resolved signals in the IR spectrum, whereas the signals weaken at higher synthesis temperatures and are flattened out to a large extent for *fl*-CTF600, indicating graphitization of the networks. This is confirmed by the ¹³C ssNMR measurements, which show a broadening and weakening of the signals with rising temperature. Remarkably, the NMR spectrum of *fl*-CTF600 could not be measured owing to the high degree of graphitization. The IR and ssNMR spectra of *fl*-CTF300 and *fl*-CTF350 show the presence of a nitrile band (2223 cm⁻¹, 109.5 ppm), indicating that there are still unreacted nitrile groups in the polymer. Those signals are not visible at higher synthesis temperatures. The strong IR band in the *fl*-CTF300 spectrum at 1511 cm⁻¹ can be assigned to the C-N stretching mode of the triazine ring,^[32-33] whereas the band at 1352 cm⁻¹ is due to in-plane triazine ring stretching vibrations.^[3,34] This and the corresponding NMR shift at 168.6 ppm evidences successful formation of the triazine moieties (Figure 4.1.2, bottom left). The signals between 144 and 118 ppm and the peak at 36.9 ppm belong to the fluorene unit, which accordingly stays intact at 300 °C. The signal at 50 ppm is assigned to a sp³ CH group, which was corroborated by a CPPI measurement (Figure 8.1.2.4). This resonance suggests the formation of 9,9'-bifluorenyl units via cross linking. A broadening of the bands between 1500-1100 cm⁻¹ and the decrease of the triazine bands in the IR spectrum of *fl*-CTF350 indicates commencing degradation of the system. Again, ssNMR measurements confirm these results. The

bands at 1607 and 814 cm^{-1} appear both in the precursor and in *fl*-CTF300 and can hence likely be assigned to the fluorene species. These bands are still retained in the spectra of *fl*-CTF350 and *fl*-CTF400, indicating intact fluorene units in those samples. The spectra of *fl*-CTF500 and *fl*-CTF600 do not show the fluorene signature anymore, which confirms the ongoing degradation of the system at elevated temperatures.

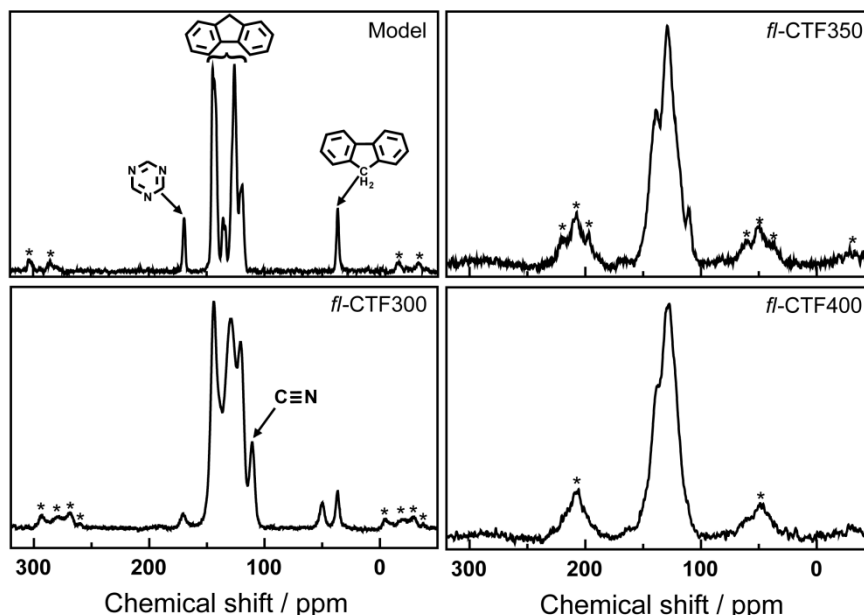


Figure 4.1.2. ^{13}C MAS ssNMR spectra of tris(9*H*-fluoren-2-yl)-1,3,5-triazine (top left), *fl*-CTF300 (bottom left), *fl*-CTF350 (top right) and *fl*-CTF400 (bottom left). Asterisks mark rotational side bands.

In summary, both IR spectroscopy and ssNMR measurements indicate degradation of the networks at temperatures higher than 300 $^{\circ}\text{C}$, which is in line with observations made for all synthesized CTFs so far. Temperatures in excess of 400 $^{\circ}\text{C}$ are not tolerated by the triazine rings and likely induce retro-trimerization reactions with subsequent rearrangements, giving rise to irreversible formation of C–C bonds accompanied by loss of N_2 .

To gain more information about the degree and course of degradation, we utilized EA measurements. EA data shown in Table 8.1.2.2 reveal a trend which is very similar to many synthesized CTFs: By raising the synthesis temperature, the nitrogen and hydrogen content decreases and the carbon content increases. The loss of nitrogen is very significant with a nitrogen loss of more than 40% for *fl*-CTF600 compared to *fl*-CTF300. Notably, the nitrogen content of *fl*-CTF300 is already lower than the calculated value, thus confirming the IR results, which reveal smaller amounts of triazine compared to the model compound.

To confirm the thermal stability of the materials we carried out DTA/TG measurements on the samples *fl*-CTF300 and *fl*-CTF600. The results (Figures 8.1.2.25–26) show degradation temperatures close to the synthesis temperatures and a rather low weight loss, especially for the *fl*-CTF600 sample.

Porosity Measurements

Although an increase in the synthesis temperature leads to materials with less local order and nitrogen content, it typically entails materials with higher surface areas (SAs).^[2-3,5] The porosities of the *fl*-CTFs were determined by argon and carbon dioxide physisorption measurements. Figure 4.1.3 (left) shows the argon isotherms of the samples *fl*-CTF350, *fl*-CTF400, *fl*-CTF500 and *fl*-CTF600. It should be mentioned that *fl*-CTF300 (Figure 8.1.2.6) adsorbed only small amounts of argon and therefore shows overall poor porosity. The isotherm of *fl*-CTF350 is typical for microporous materials in that it shows rapid argon uptake at low relative pressures ($p/p_0^{-1} < 0.05$). Nevertheless, it cannot be described as a type I isotherm because of continuous adsorption of argon at higher pressures, indicating additional mesoporosity with a broad mesopore size distribution and a hysteresis almost spanning the entire range of $p/p_0^{-1} = 0-0.9$. The hysteresis resembles type H4, typical for materials with slit-shaped pores. The low pressure character of the hysteresis indicates pores within the size range of the adsorbate, causing delayed desorption.^[35] The isotherm of *fl*-CTF400 shows rapid argon adsorption at low relative pressures as well. The continuous adsorption at higher relative pressures is higher than in *fl*-CTF350, which should be ascribed to an increased fraction of mesopores. The isotherms of *fl*-CTF500 and *fl*-CTF600 show similar shape and can be described as a combination of isotherms of type I and IV. The micropore filling is followed by mesopore filling showing a type H2 hysteresis around $p/p_0^{-1} = 0.4$. H2 hysteresis describe systems with rather ill-defined pore sizes and shapes and are often observed for amorphous materials.

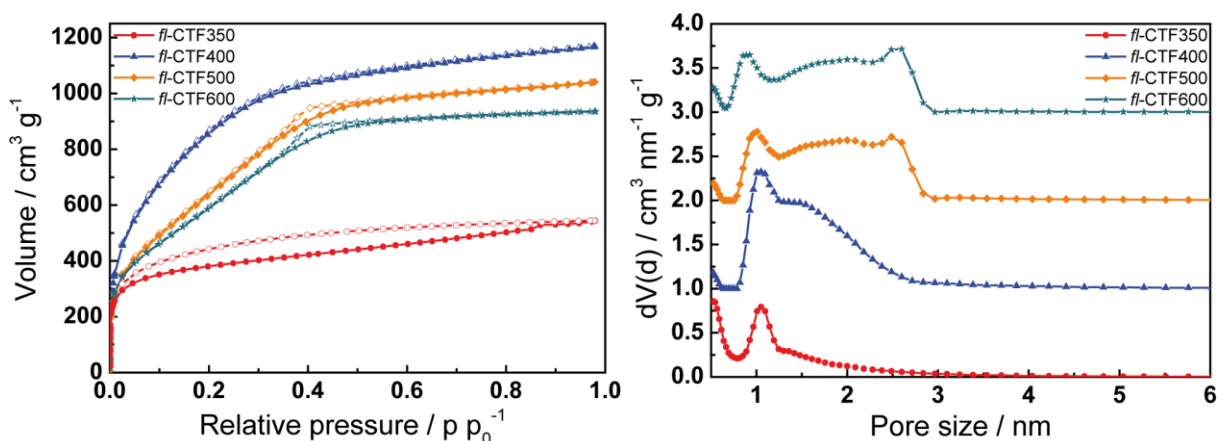


Figure 4.1.3. (Left) Argon adsorption (filled symbols) and desorption (open symbols) isotherms at 87 K of *fl*-CTF350, *fl*-CTF400, *fl*-CTF500 and *fl*-CTF600. (Right) Pore size distributions of *fl*-CTF350, *fl*-CTF400, *fl*-CTF500 and *fl*-CTF600 from DFT calculations. The curves are shifted vertically in steps of $1 \text{ cm}^3 \text{ nm}^{-1} \text{ g}^{-1}$.

The SAs of the materials were calculated from the isotherms based on the BET model and are listed in Table 4.1.1.^[36] The highest SA of $2862 \text{ m}^2 \text{ g}^{-1}$ is found for *fl*-CTF400, which is the third highest for all CTFs after CTF-1 ($400/600 \text{ }^\circ\text{C}$, $3270 \text{ m}^2 \text{ g}^{-1}$)^[2] and *bipy*-CTF ($700 \text{ }^\circ\text{C}$, $3219 \text{ m}^2 \text{ g}^{-1}$).^[5] For *fl*-CTF500 and *fl*-CTF600 the values are decreasing, which is unexpected, since for all published CTFs a rise in

synthesis temperature showed an increase in the SA, accompanied by a continuous decomposition of the materials (“foaming”). This phenomenon can be explained by the pore size distribution of the materials which was calculated by QSDFT methods (Figure 4.1.3, right). For *fl*-CTF350 mainly micropores are observed with two main peaks at 1.05 and 0.5 nm. The latter indicates pores smaller than 0.5 nm (ultramicropores), which are not observable by argon measurements. For *fl*-CTF400 the peak at 1.05 nm increases and additionally a wide distribution of pores from 1.2 to 3 nm is observed, with mainly pores in the micropore region. *fl*-CTF500 and *fl*-CTF600 show comparable distributions, with an additional peak around 2.5 nm, which can be assigned to small mesopores. Overall, an increasingly mesoporous character with rising synthesis temperature is typical for CTFs, yet normally the increasing amount of mesopores is not accompanied by a significant decrease of the micropores.^[2,5]

Table 4.1.1. BET surface areas, CO₂ and N₂ uptakes, heats of adsorption and CO₂/N₂selectivities of *fl*-CTFs.

Sample	BET SA [m ² g ⁻¹]	Pore Volume [cm ³ g ⁻¹]			CO ₂ uptake [mmol g ⁻¹] ^a			N ₂ uptake ^b [mmol g ⁻¹]	Q _{st} ^c [kJ mol ⁻¹]	Selectivity ^d	
		V _{Ar,mic,DFT} ^e	V _{Ar,tot,DFT} ^f	V _{Ar,mic,DFT} / V _{Ar,tot,DFT}	273 K	298 K	313 K			Henry	IAST
<i>fl</i> -CTF300	15	-	-	-	1.27	0.71	0.42	0.04	43.1	35	37
<i>fl</i> -CTF350	1235	0.57	0.67	0.85	4.28	2.29	1.59	0.18	32.7	27	23
<i>fl</i> -CTF400	2862	1.13	1.45	0.78	4.13	1.97	1.31	0.17	30.7	15	16
<i>fl</i> -CTF500	2322	0.77	1.29	0.60	3.26	1.65	1.11	0.21	31.7	13	12
<i>fl</i> -CTF600	2113	0.70	1.16	0.60	3.48	1.80	1.22	0.22	32.4	14	12

^aAt 1 bar. ^bAt 1 bar and 298 K. ^cAt zero coverage. ^dAt 298 K. ^ePore volume for pores smaller than 2 nm calculated from the Ar QSDFT model. ^fTotal pore volume from the Ar QSDFT model.

The amount of micropores compared to mesopores can be calculated by the ratio of the microporous volume V_{mic} to the total pore volume V_{tot} . These pore volumes can be calculated from the amount of vapor adsorbed at chosen relative pressures assuming the pores are filled with liquid adsorbate, and from DFT calculations. The results for the *fl*-CTFs are listed in Tables 4.1.1 and 8.1.2.4 and confirm the previous observations. *fl*-CTF400 features the largest absolute amount of micropores followed by *fl*-CTF500 and *fl*-CTF600. Remarkably, *fl*-CTF350 has the highest fraction of micropores with respect to the total pore volume (85%), which is clearly higher than for *fl*-CTF500 and *fl*-CTF600 (both 60%). The widening of the pores can favorably be explained by the degradation of the networks at elevated synthesis temperatures, leading to a “swelling” (“foaming”) of the materials.

The pore size distributions of the *fl*-CTFs indicate ultramicropores, which cannot be detected by argon measurements, but by carbon dioxide physisorption measurements, which allow us to probe pore sizes down to ≈ 0.35 nm. The isotherms shown in Figure 4.1.4 have comparable shapes, which is consistent with the literature. Contrary to its non-porous character established by Ar physisorption, *fl*-CTF300 adsorbs moderate amounts of CO₂, which can be rationalized by the presence of pores that are accessible to CO₂ but not to Ar. A comparable phenomenon is observed for *fl*-CTF350, which adsorbs more CO₂ than all other *fl*-CTFs, although having around half as much accessible SA as

determined by argon physisorption. The accessible CO₂ SAs were calculated with DFT simulations and are shown in Table 8.1.2.6. The values are much lower than those for argon measurements, since the calculations only take pores smaller than 1.45 nm into account. Nevertheless, *fl*-CTF300 shows a SA of 297 m² g⁻¹ which is nearly half as much as that of *fl*-CTF500 and *fl*-CTF600. The highest SA is observed for *fl*-CTF400, followed by *fl*-CTF350. All samples show a broad pore size distribution ranging from 0.35-1.00 nm (Figure 8.1.2.16). A hydrogen physisorption measurement at 20 K validated the SA of *fl*-CTF400 giving a BET SA of 2829 m² g⁻¹ (Figures 8.1.2.12-13).

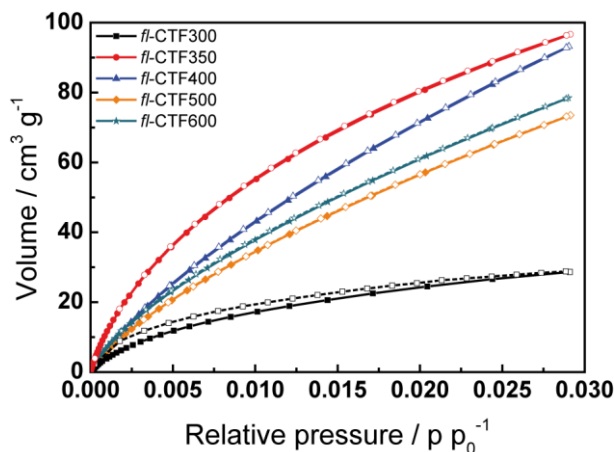


Figure 4.1.4. Carbon dioxide adsorption (filled symbols) and desorption (open symbols) isotherms at 273 K of *fl*-CTF300, *fl*-CTF350, *fl*-CTF400, *fl*-CTF500 and *fl*-CTF600.

Gas Storage and Selectivity Studies

The high capacities of the *fl*-CTFs for CO₂ sorption at 273 K are promising for the usage as CCS material. Therefore, temperature-dependent sorption studies at 298 and 313 K were carried out and the heats of adsorption were calculated (Figure 4.1.5).

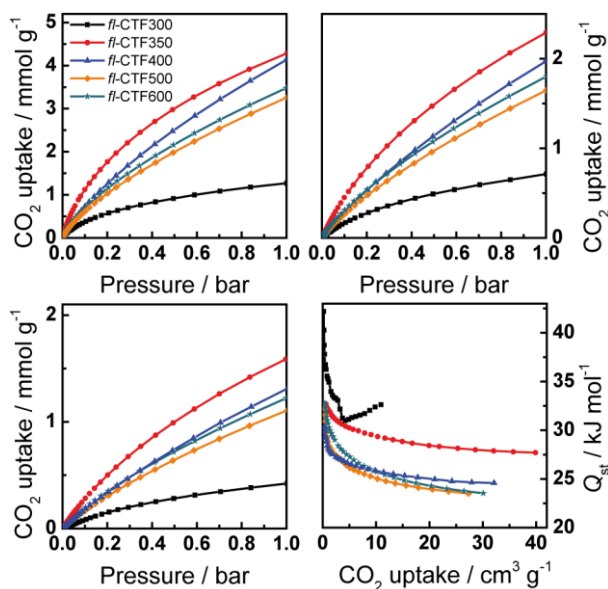


Figure 4.1.5. Carbon dioxide adsorption isotherms of *fl*-CTF300, *fl*-CTF350, *fl*-CTF400, *fl*-CTF500 and *fl*-CTF600 at 273 K (top left), 298 K (top right), 313 K (bottom left) and corresponding heats of adsorption (bottom right).

The uptakes at 1 bar and the heats of adsorption at zero coverage are summarized in Table 4.1.1. With 4.28 mmol g^{-1} at 273 K *fl*-CTF350 shows the highest uptake of all materials. This value is lower than that of recently reported FCTF-1 ($4.67\text{--}5.53 \text{ mmol g}^{-1}$),^[16] but higher than the reported values for all other CTFs such as CTF-0 (4.22 mmol g^{-1}),^[9] CTF-1 ($2.47\text{--}3.82 \text{ mmol g}^{-1}$),^[16] CTF-P2-P6 ($1.88\text{--}3.39 \text{ mmol g}^{-1}$),^[10] CTF-P1M-P6M ($0.94\text{--}4.20 \text{ mmol g}^{-1}$),^[10] MCTF300-500 ($2.25\text{--}3.16 \text{ mmol g}^{-1}$),^[12] PCTF-1-7 ($1.84\text{--}3.23 \text{ mmol g}^{-1}$)^[11,15] and TPI-1-7 ($0.68\text{--}2.45 \text{ mmol g}^{-1}$).^[34] In addition, they are higher than the uptake capacities of numerous POPs such as covalent organic frameworks (COFs; $1.21\text{--}3.86 \text{ mmol g}^{-1}$),^[37-38] microporous polyimides (MPis; $2.25\text{--}3.81 \text{ mmol g}^{-1}$),^[39] and hyper-crosslinked organic polymers (HCPs; $1.91\text{--}3.92 \text{ mmol g}^{-1}$)^[40-41] (for an expanded list see Table 8.1.2.7). Higher values were reported so far for benzimidazole-linked polymers (BILPs; $2.91\text{--}5.34 \text{ mmol g}^{-1}$),^[42-44] and porous polymer frameworks (PPFs; $2.09\text{--}6.12 \text{ mmol g}^{-1}$).^[45] For the amounts adsorbed at 298 K similar results were found.

As mentioned above, CO_2 uptakes depend on the surface area, the pore sizes and the interaction energy between sorbent and sorbate. The latter can be expressed by the heats of adsorption Q_{st} which we calculated for our materials (Figure 4.1.5, bottom right). The values at the limit of zero coverage are shown in Table 4.1.1 and are highest for *fl*-CTF300 and almost the same for the other *fl*-CTFs, ranging in the upper field compared to other POPs (see Table 8.1.2.7).

For the use of *fl*-CTFs as potential flue gas sorbents the selectivities of CO_2 over N_2 need to be examined. Therefore, the *Henry* equation and the ideal adsorbed solution theory (IAST) were used (Chapter 8.1.2.8). The calculated values are listed in Table 4.1.1. As expected, *fl*-CTF300 and *fl*-CTF350 show the highest selectivities, due to the low adsorption potential towards argon compared to CO_2 . The selectivities range in the upper level of POPs and, remarkably, *fl*-CTF300 shows a higher selectivity than FCTF-1.^[16]

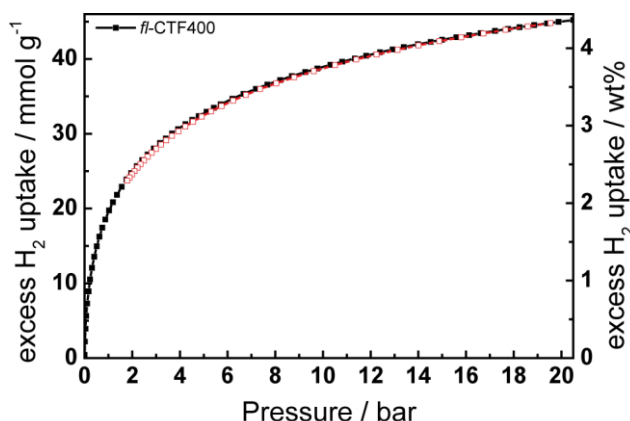


Figure 4.1.6. Excess hydrogen adsorption (filled symbols) and desorption (open symbols) isotherm of *fl*-CTF400 at 77 K.

Motivated by the high values of adsorbed CO_2 at 273 K and the large number of micropores, we tested *fl*-CTF400 as hydrogen storage material by carrying out hydrogen physisorption measurements

at 77 K and 298 K up to 20 bar. The isotherm at 77 K is displayed in Figure 4.1.6 and shows adsorption of 4.36 wt% (45.2 mmol g^{-1}), which is higher than that observed for 2D COFs (1.46-3.88 wt%, sat. pressure)^[38] and polymers of intrinsic microporosity (PIMs, 1.45-2.71 wt%, 10 bar),^[46-50] but lower than that of the highly porous 3D COFs (6.98-7.16 wt%, sat. pressure),^[38] PAFs (4.2-7.0 wt%)^[51-52] and PPNs (8.34 wt%, 55 bar),^[53] which however were measured at higher pressures. Up to date, only three CTFs were examined for their H₂ capacities and the measurements were done only up to 1 bar. CTF-1 adsorbs 1.55 wt%,^[1] PCTF-1 1.86 wt%^[11] and PCTF-2 0.9 wt%,^[11] which is substantially lower than the uptake capacity of our material (1.95 wt%).

For hydrogen storage applications, knowledge of the heat of adsorption, along with the storage capacity, is of importance to better understand the microscopic host-guest interactions. Figure 8.1.2.10 shows the temperature variations of the absolute hydrogen adsorption curves (77-117 K), which provides the strength of the binding potential for hydrogen in *fl*-CTF400. In Figure 8.1.2.11, the isosteric heat of adsorption is shown as a function of the surface coverage normalized to saturation coverage (20 bar, 77 K). Analysis of the hydrogen adsorption enthalpy gives a maximum value of 6.25 kJ mol^{-1} at near zero surface coverage, decreasing to 3.65 kJ mol^{-1} with increasing H₂ loading. The overall average heat of adsorption equals 4.9 kJ mol^{-1} . It is worth noting that the average heat of adsorption of 4.9 kJ mol^{-1} is relatively high after considering the rather large pore diameter (1.05-3 nm) and by comparison with most MOFs of similar pore sizes.^[54] This relatively high average heat of adsorption can be either due to stronger adsorption sites (possibly N sites of *fl*-CTF400) or due to the ultramicropores inside *fl*-CTF400 as detected by CO₂ NLDFT simulations (0.35-1.45 nm). Table 8.1.2.5 summarizes the textural characteristics and hydrogen storage capacity of *fl*-CTF400.

4.1.4 CONCLUSIONS

The presented *fl*-CTFs were analyzed with respect to their local structure, porosity, and capacity for CO₂ capture. An intact fluorene network connected by triazines could be established for *fl*-CTF300. The materials showed high SAs up to $2862 \text{ m}^2 \text{ g}^{-1}$ and high capacities for the adsorption of CO₂, which can be rationalized by their high fraction of ultramicropores. We find that *fl*-CTF350 with the highest fraction of micropores and moderate surface area shows the best CO₂ uptake (4.28 mmol g^{-1} at 273 K) and thus ranks in the upper level among all POPs. Additionally, hydrogen adsorption of *fl*-CTF400 shows comparable values to other POPs. Finally, the gas selectivities of CO₂ over N₂ of the *fl*-CTFs were tested and reveal high values for *fl*-CTF300 and *fl*-CTF350, thus rendering these materials promising candidates for gas capture and storage.

4.1.5 BIBLIOGRAPHY

Acknowledgment

The authors acknowledge financial support by the Deutsche Forschungsgemeinschaft, DFG (SPP 1362, SE 1417/5-1 and LO 1801/2-1), the Nanosystems Initiative Munich (NIM), the Center for Nanoscience (CeNS) and the Fonds der Chemischen Industrie (FCI). H. Oh was supported for this research through a stipend from the International Max Planck Research School for Advanced Materials (IMPRS-AM). We thank Marius Reymann and Niklas Cordes for synthetic assistance, Stephan Werner for XRD measurements, Christian Minke for ssNMR measurements and Katrin Rudolf and Christine Pösl for DTA/TG measurements. We acknowledge Prof. Thomas Bein and Prof. Wolfgang Schnick for access to the respective measurement facilities.

References

- [1] P. Kuhn, M. Antonietti, A. Thomas, *Angew. Chem. Int. Ed.* **2008**, *47*, 3450-3453.
- [2] P. Kuhn, A. I. Forget, D. Su, A. Thomas, M. Antonietti, *J. Am. Chem. Soc.* **2008**, *130*, 13333-13337.
- [3] P. Kuhn, A. Thomas, M. Antonietti, *Macromolecules* **2009**, *42*, 319-326.
- [4] P. Kuhn, A. Forget, J. Hartmann, A. Thomas, M. Antonietti, *Adv. Mater.* **2009**, *21*, 897-901.
- [5] S. Hug, M. E. Tauchert, S. Li, U. E. Pachmayr, B. V. Lotsch, *J. Mater. Chem.* **2012**, *22*, 13956-13964.
- [6] C. E. Chan-Thaw, A. Villa, P. Katekomol, D. Su, A. Thomas, L. Prati, *Nano Lett.* **2010**, *10*, 537-541.
- [7] R. Palkovits, M. Antonietti, P. Kuhn, A. Thomas, F. Schüth, *Angew. Chem. Int. Ed.* **2009**, *48*, 6909-6912.
- [8] C. E. Chan-Thaw, A. Villa, L. Prati, A. Thomas, *Chem. Eur. J.* **2011**, *17*, 1052-1057.
- [9] P. Katekomol, J. Roeser, M. Bojdys, J. Weber, A. Thomas, *Chem. Mater.* **2013**, *25*, 1542-1548.
- [10] S. Ren, M. J. Bojdys, R. Dawson, A. Laybourn, Y. Z. Khimyak, D. J. Adams, A. I. Cooper, *Adv. Mater.* **2012**, *24*, 2357-2361.
- [11] A. Bhunia, V. Vasylyeva, C. Janiak, *Chem. Commun.* **2013**, *49*, 3961-3963.
- [12] X. Liu, H. Li, Y. Zhang, B. Xu, S. A. H. Xia, Y. Mu, *Polym. Chem.* **2013**, *4*, 2445-2448.
- [13] W. Wang, H. Ren, F. Sun, K. Cai, H. Ma, J. Du, H. Zhao, G. Zhu, *Dalton Trans.* **2012**, *41*, 3933-3936.
- [14] H. Ren, T. Ben, E. Wang, X. Jing, M. Xue, B. Liu, Y. Cui, S. Qiu, G. Zhu, *Chem. Commun.* **2010**, *46*, 291-293.
- [15] A. Bhunia, I. Boldog, A. Moller, C. Janiak, *J. Mater. Chem. A* **2013**, *1*, 14990-14999.

- [16] J. Liu, H. Chen, S. Zheng, Z. Xu, *J. Chem. Eng. Data* **2013**, *58*, 3557-3562.
- [17] X. Zhu, C. Tian, S. M. Mahurin, S.-H. Chai, C. Wang, S. Brown, G. M. Veith, H. Luo, H. Liu, S. Dai, *J. Am. Chem. Soc.* **2012**, *134*, 10478-10484.
- [18] M. R. Raupach, G. Marland, P. Ciais, C. Le Quéré, J. G. Canadell, G. Klepper, C. B. Field, *Proc. Natl. Acad. Sci. U. S. A.* **2007**, *104*, 10288-10293.
- [19] *Energy technology perspectives 2008*, International Energy Agency, Paris, **2008**.
- [20] D. M. D'Alessandro, B. Smit, J. R. Long, *Angew. Chem. Int. Ed.* **2010**, *49*, 6058-6082.
- [21] R. Dawson, A. I. Cooper, D. J. Adams, *Polym. Int.* **2013**, *62*, 345-352.
- [22] R. S. Haszeldine, *Science* **2009**, *325*, 1647-1652.
- [23] G. T. Rochelle, *Science* **2009**, *325*, 1652-1654.
- [24] Z. Xiang, D. Cao, *J. Mater. Chem. A* **2013**, *1*, 2691-2718.
- [25] S.-Y. Ding, W. Wang, *Chem. Soc. Rev.* **2013**, *42*, 548-568.
- [26] R. Dawson, A. I. Cooper, D. J. Adams, *Prog. Polym. Sci.* **2012**, *37*, 530-563.
- [27] K. Sumida, D. L. Rogow, J. A. Mason, T. M. McDonald, E. D. Bloch, Z. R. Herm, T.-H. Bae, J. R. Long, *Chem. Rev.* **2011**, *112*, 724-781.
- [28] B. Streppel, M. Hirscher, *Phys. Chem. Chem. Phys.* **2011**, *13*, 3220-3222.
- [29] B. Streppel, Ph.D. Thesis, Universität Stuttgart **2011**.
- [30] M. Y. Wong, L. M. Leung, *Tetrahedron* **2010**, *66*, 3973-3977.
- [31] D. Vonlanthen, A. Rudnev, A. Mishchenko, A. Käslin, J. Rotzler, M. Neuburger, T. Wandlowski, M. Mayor, *Chem. Eur. J.* **2011**, *17*, 7236-7250.
- [32] M. J. Bojdys, J. Jeromenok, A. Thomas, M. Antonietti, *Adv. Mater.* **2010**, *22*, 2202-2205.
- [33] V. G. Manecke, D. Wöhrle, *Makromol. Chem.* **1968**, *120*, 176-191.
- [34] M. R. Liebl, J. Senker, *Chem. Mater.* **2013**, *25*, 970-980.
- [35] K. S. W. Sing, D. H. Everett, R. A. W. Haul, L. Moscou, R. A. Pierotti, J. Rouquérol, T. Siemieniowska, *Pure Appl. Chem.* **1985**, *57*, 603-619.
- [36] S. Brunauer, P. H. Emmett, E. Teller, *J. Am. Chem. Soc.* **1938**, *60*, 309-319.
- [37] R. Dawson, E. Stockel, J. R. Holst, D. J. Adams, A. I. Cooper, *Energy Environ. Sci.* **2011**, *4*, 4239-4245.
- [38] H. Furukawa, O. M. Yaghi, *J. Am. Chem. Soc.* **2009**, *131*, 8875-8883.
- [39] X. Zhu, C.-L. Do-Thanh, C. R. Murdock, K. M. Nelson, C. Tian, S. Brown, S. M. Mahurin, D. M. Jenkins, J. Hu, B. Zhao, H. Liu, S. Dai, *ACS Macro Lett.* **2013**, *2*, 660-663.
- [40] Y. Luo, S. Zhang, Y. Ma, W. Wang, B. Tan, *Polym. Chem.* **2013**, *4*, 1126-1131.
- [41] C. F. Martin, E. Stockel, R. Clowes, D. J. Adams, A. I. Cooper, J. J. Pis, F. Rubiera, C. Pevida, *J. Mater. Chem.* **2011**, *21*, 5475-5483.
- [42] M. G. Rabbani, H. M. El-Kaderi, *Chem. Mater.* **2011**, *23*, 1650-1653.

- [43] M. G. Rabbani, H. M. El-Kaderi, *Chem. Mater.* **2012**, *24*, 1511-1517.
- [44] M. G. Rabbani, A. K. Sekizkardes, O. M. El-Kadri, B. R. Kaafarani, H. M. El-Kaderi, *J. Mater. Chem.* **2012**, *22*, 25409-25417.
- [45] Y. Zhu, H. Long, W. Zhang, *Chem. Mater.* **2013**, *25*, 1630-1635.
- [46] N. B. McKeown, P. M. Budd, D. Book, *Macromol. Rapid Commun.* **2007**, *28*, 995-1002.
- [47] N. B. McKeown, B. Ghanem, K. J. Msayib, P. M. Budd, C. E. Tattershall, K. Mahmood, S. Tan, D. Book, H. W. Langmi, A. Walton, *Angew. Chem. Int. Ed.* **2006**, *45*, 1804-1807.
- [48] B. S. Ghanem, K. J. Msayib, N. B. McKeown, K. D. M. Harris, Z. Pan, P. M. Budd, A. Butler, J. Selbie, D. Book, A. Walton, *Chem. Commun.* **2007**, 67-69.
- [49] J.-Y. Lee, C. D. Wood, D. Bradshaw, M. J. Rosseinsky, A. I. Cooper, *Chem. Commun.* **2006**, 2670-2672.
- [50] P. M. Budd, A. Butler, J. Selbie, K. Mahmood, N. B. McKeown, B. Ghanem, K. Msayib, D. Book, A. Walton, *Phys. Chem. Chem. Phys.* **2007**, *9*, 1802-1808.
- [51] T. Ben, C. Pei, D. Zhang, J. Xu, F. Deng, X. Jing, S. Qiu, *Energy Environ. Sci.* **2011**, *4*, 3991-3999.
- [52] T. Ben, H. Ren, S. Ma, D. Cao, J. Lan, X. Jing, W. Wang, J. Xu, F. Deng, J. M. Simmons, S. Qiu, G. Zhu, *Angew. Chem. Int. Ed.* **2009**, *48*, 9457-9460.
- [53] W. Lu, J. P. Sculley, D. Yuan, R. Krishna, Z. Wei, H.-C. Zhou, *Angew. Chem. Int. Ed.* **2012**, *51*, 7480-7484.
- [54] M. Schlichtenmayer, M. Hirscher, *J. Mater. Chem.* **2012**, *22*, 10134-10143.

4.2 NITROGEN-RICH COVALENT TRIAZINE FRAMEWORKS AS EFFICIENT PLATFORMS FOR SELECTIVE GAS CAPTURE AND STORAGE

Stephan Hug, Hyunchul Oh, Michael Hirscher, Bettina V. Lotsch

This chapter is a pre-peer reviewed version of a manuscript to be submitted to Energy Environ. Sci.

Abstract

The search for new efficient physisorbents for gas capture and storage is the objective of active research in the realm of functional framework materials. Here we present two new nitrogen rich covalent triazine frameworks (CTFs) based on lutidine and pyrimidine units and comprehensively analyze their CO₂ and H₂ uptake capacities. Furthermore, the gas uptakes of bipyridine CTF (*bipy*-CTF) as well as the prototype CTF1 are studied for the first time and trends in the gas sorption behavior within the CTF family of compounds and nitrogen-containing porous polymers in general are carved out, revealing the dominant role of the micropore surface area for maximum CO₂ uptake. The nitrogen-rich and predominantly microporous materials show very high gas uptakes (up to 5.58 mmol g⁻¹ CO₂ and 4.34 wt% H₂) and very good CO₂ selectivities towards N₂. The CO₂ uptake of a *bipy*-CTF synthesized at 600 °C (5.58 mmol g⁻¹, 273 K) is the highest reported for all CTFs so far and the second highest for all porous organic polymers (POPs). Moreover, the CO₂ selectivities towards N₂ of a nitrogen-rich pyrimidine-based CTF synthesized at 500 °C (Henry: 189, IAST: 502) are the highest reported so far for all POPs, and the H₂ uptake of CTF1 synthesized at 600 °C at 1 bar (2.12 wt%, 77 K) is the highest found for all CTFs to date as well. Finally, H₂ uptakes at high pressures (4.34 wt%, 25 bar, 77 K) are found to be competitive with those of other POPs with high H₂ storage capacities.

4.2.1 INTRODUCTION

Anthropogenic emission of CO₂ is the main contributor to global warming, as stated recently by the Intergovernmental Panel on Climate Change (IPCC).^[1] The power sector's share of the globally emitted CO₂ amounts to around 40%,^[2] thus attesting carbon capture and storage (CCS) a high potential for reducing the emissions and, ultimately, slowing down climate change. The most established techniques for CCS are amine scrubbing and oxyfuel combustion,^[3] which however come at the cost of increasing the energy requirements of a power plant by as much as 25-40%.^[4-5] Additionally, amine scrubbing uses toxic solvents which are difficult to dispose and are subject to decomposition and evaporation.^[5-6] Therefore physical adsorbents such as zeolites, metal organic

frameworks (MOFs) and porous organic polymers (POPs) came into focus owing to their high CO₂ capture capacities and low energy requirements for regeneration.^[3-4,7] Especially POPs combine the advantages of high selectivities, good chemical and thermal stabilities and high tolerance towards water vapors, which has been shown in several recent reviews.^[8-11] Newer research revealed that the incorporation of nitrogen scaffolds significantly increases the CO₂ adsorption capacities of POPs,^[7,12-18] mainly caused by Lewis acid - Lewis base electrostatic interactions of the nitrogen atoms with the carbon atoms of the CO₂ molecules, which in turn result from dipole-induced dipole and dipole-quadrupole interactions.^[19] Therefore, inherently nitrogen rich materials such as covalent triazine frameworks (CTFs),^[20-22] a subclass of POPs, are promising candidates for CCS. Several works already discussed the potential of CTFs for CO₂ capture,^[23-30] while a systematic relationship between nitrogen content and CO₂ capture capacities has not been explicitly treated, since comparison among various sorbents with different synthesis histories is challenging.

In this work we present the CO₂ and H₂ capture capacities of the known CTFs *bipy*-CTF^[31] and CTF1^[20,22] synthesized at different temperatures and two new CTFs based on lutidine (*lut*-CTF) and pyrimidine (*pym*-CTF) building units, and we find CO₂ uptakes higher than in all other CTFs reported to date. We comprehensively characterize the materials and discuss their sorption capacities and selectivities as a function of their microporous surface area and nitrogen contents, thus revealing a major dependency of the CO₂ uptake on the microporous surface area and only minor relevance of the total nitrogen contents. In contrast, the high CO₂ over N₂ selectivities are largely attributed to the nitrogen content.

4.2.2 EXPERIMENTAL SECTION

Materials and Methods

All reactions were carried out under an argon atmosphere in flame-dried glassware. Anhydrous solvents and liquid reagents were transferred by syringe or cannula. Unless otherwise noted, all materials were obtained from commercial suppliers (see Supporting Information, Table 8.1.3.1) and used without further purification. Column chromatography was performed using an Isolera Four (Biotage AB, Sweden) with Biotage SNAP cartridges (40-65 μm silica). Tri(2-furyl)phosphine (tfp),^[32] 5,5'-dicyano-2,2'-bipyridine^[31] and 5-bromo-2-iodopyrimidine^[33] were synthesized according to published procedures. THF was continuously refluxed and freshly distilled from sodium benzophenoneketyl under argon.

Argon, carbon dioxide and nitrogen adsorption/desorption measurements were performed at 87, 273, 298 and 313 K with an Autosorb-iQ surface analyzer (Quantachrome Instruments, USA). Samples were outgassed in vacuum at 120-300 °C for 6-12 h to remove all guests. Pore-size distributions were

determined using the calculation model for Ar at 87 K on carbon (slit pore, QSDFT equilibrium model) or for CO₂ at 273 K on carbon (NLDFT model) of the ASiQwin software (v2.0) from Quantachrome. For BET calculations pressure ranges of the Ar isotherms were chosen with the help of the BET Assistant in the ASiQwin software. In accordance with the ISO recommendations multipoint BET tags equal or below the maximum in $V \cdot (1 - P/P_0)$ were chosen. The isosteric heats of adsorption were calculated from the CO₂ adsorption isotherms based on the Clausius-Clapeyron equation using the Quantachrome software ASiQwin (v2.0).

High-pressure hydrogen adsorption/desorption measurements were performed on an automated Sievert's type apparatus (PCTPro-2000) with a so-called micro-doser (MD) from HyEnergy. The original setup was upgraded by a heating and cooling device to regulate the sample temperature. The adsorption and desorption isotherms (0-25 bar) were measured at various temperatures (77-298 K) in a sample cell volume of ≈ 1.3 mL using ultra high purity hydrogen gas (99.999%). Samples were outgassed in vacuum ($4.5 \cdot 10^{-6}$ mbar) at 200 °C for 6 h to remove all guests. The isosteric heat of adsorption is calculated from the absolute adsorbed hydrogen according to a variant of the Clausius-Clapeyron equation (see ESI).

Infrared (IR) spectroscopy measurements were carried out on a Perkin Elmer Spektrum BX II (Perkin Elmer, USA) with an attenuated total reflectance unit.

Powder X-ray diffraction (XRD) was measured on a BRUKER D8 Avance (Bruker AXS, USA) in Bragg-Brentano geometry.

Elemental analysis (EA) was carried out with an Elementar vario EL (Elementar Analysensysteme, Germany).

Magic angle spinning (MAS) solid-state nuclear magnetic resonance (ssNMR) spectra were recorded at ambient temperature on a BRUKER DSX500 Avance NMR spectrometer (Bruker Biospin, Germany) with an external magnetic field of 11.75 T. The operating frequencies are 500.1 MHz and 125.7 MHz for ¹H and ¹³C, respectively, and the spectra were referenced relative to TMS. The samples were contained either in 2.4 or 4 mm ZrO₂ rotors.

Solution-state NMR spectroscopy was performed on a JEOL DELTA NMR (JEOL, Japan) by single pulse experiments. The spectra were referenced against CDCl₃ ($\delta(^1\text{H})$ 7.26 ppm, $\delta(^{13}\text{C}\{^1\text{H}\})$ 77.16 ppm).

Microwave reactions were carried out in a Biotage Initiator (Biotage AB, Sweden) in 10-20 mL microwave vials from Biotage.

Pyrimidine-2,5-dicarbonitrile^[34]

A microwave vial was charged with dry DMF (20 mL), 5-bromo-2-iodopyrimidine (1.14 g, 4 mmol), Zn(CN)₂ (517 mg, 4.4 mmol), Pd(PPh₃)₄ (462 mg, 0.4 mmol) and 1,5-bis(diphenylphosphino)pentane (182 mg, 0.4 mmol) and the vial was sealed. The yellow mixture was heated in the microwave for 2 h at 150 °C. The now orange suspension was quenched by the addition of water (150 mL) and a

saturated aqueous solution of NaHCO_3 (150 mL). The water layer was extracted with dichloromethane (3×300 mL), the combined organic layers were dried over Na_2SO_4 and concentrated *in vacuo*. The crude product was purified by two times flash column chromatography (first: $\text{CHCl}_3/\text{Hexane}$ 9:1, second: $\text{EtOAc}/\text{Hexane}$ 1:4) to give pyrimidine-2,5-dicarbonitrile as colorless crystals (372 mg, 2.86 mmol, 72%). ^1H NMR (400 MHz; CDCl_3): δ 9.71 (2 H, s, Ar); $^{13}\text{C}\{^1\text{H}\}$ NMR (68 MHz; CDCl_3): δ 160.6, 146.3, 114.8, 112.7, 111.8.

2,6-Dimethylpyridine-3,5-dicarbonitrile^[35]

2,6-Dimethylpyridine-3,5-dicarbonitrile was synthesized in a modified literature procedure.^[36] 3-Aminocrotonitrile (1.64 g, 20 mmol) and hafnium trifluoromethanesulfonate (775 mg, 1 mmol) were put in a microwave vial and degassed three times. Chloroform (16 mL) and ethyl orthoformate (3.29 mL, 20 mmol) were added and the vial was sealed. The mixture was heated in the microwave for 10 min at 120 °C. The dark orange solution was quenched with a saturated aqueous solution of NaHCO_3 (200 mL) and the water layer was extracted with dichloromethane (3×200 mL). The combined organic phases were dried over K_2CO_3 and the solvent was evaporated *in vacuo*. The crude product was purified by flash column chromatography ($\text{Hexane}/\text{EtOAc}$ 4:1) to give 2,6-dimethylpyridine-3,5-dicarbonitrile as yellow crystals (778 mg, 5.0 mmol, 50%). ^1H NMR (270 MHz; CDCl_3): δ 8.08 (1 H, s, Ar), 2.81 (6 H, s, Me); $^{13}\text{C}\{^1\text{H}\}$ NMR (68 MHz; CDCl_3): δ 165.0, 143.5, 115.2, 107.3, 24.3.

Synthesis of Covalent Triazine Frameworks

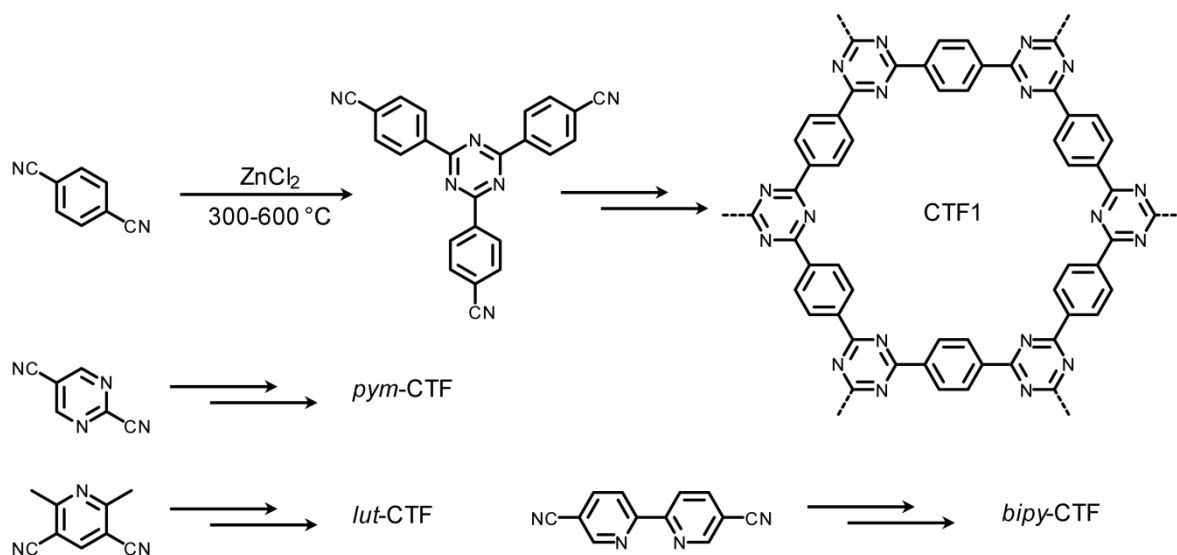
In a typical CTF synthesis a Duran ampoule (1 x 12 cm) was charged with the dinitrile (100 mg) and ZnCl_2 (1-10 equivalents, see Table 8.1.3.2) within a glove box. The ampoule was flame sealed under vacuum and was subjected in a tube oven to temperatures between 300-600 °C (for temperature programs, see Table 8.1.3.3). After cooling to ambient temperature, the ampoule was opened and its content ground thoroughly. The crude product was stirred in H_2O (50 mL) for 1 h, filtered, and washed with 1 M HCl (2×50 mL). The mixture was then stirred at 90 °C in 1 M HCl (50 mL) over night, filtered, and subsequently washed with 1 M HCl (3×30 mL), H_2O (12×30 mL), THF (2×30 mL), and dichloromethane (1×30 mL). Finally, the powder was dried overnight in a desiccator.

4.2.3 RESULTS AND DISCUSSION

Synthesis and Characterization

The synthesis of CTFs is carried out through the Lewis acid catalyzed trimerization of nitriles. The two main procedures generally used include an ionothermal approach using ZnCl_2 at temperatures above 300 °C and the super acid mediated synthesis using trifluoromethanesulphonic acid at 0-

120 °C.^[20,22,29] In both cases the Lewis acid acts as both solvent and catalyst. In this work we followed the ionothermal procedure using pyrimidine-2,5-dicarbonitrile (*pym*-CTF) and 2,6-dimethylpyridine-3,5-dicarbonitrile (*lut*-CTF) as two new precursors, and 5,5'-dicyano-2,2'-bipyridine^[31] (*bipy*-CTF) and 1,4-dicyanobenzene^[20,22] (CTF1) as known precursors to produce a series of CTFs (Scheme 4.2.1). The resulting black powders are not soluble in water, acids, bases and organic solvents indicating that fully condensed networks are formed. Previous works revealed that CTFs synthesized at low temperatures (300-400 °C) have rather well-defined local structures, but at the same time low surface areas (SA). Syntheses at higher temperatures show a dramatic increase in the SAs accompanied by different extents of structural degradation. As increased SAs can lead to higher adsorption capacities for CO₂, a series of temperatures was tested for the syntheses of the new and known CTFs, which are displayed in Table 8.1.3.2.



Scheme 4.2.1. Schematic synthesis of the CTFs discussed in this work: CTF1 (top), *pym*-CTF (middle), *lut*-CTF (bottom left) and *bipy*-CTF (bottom right).

The synthesized materials were tested with respect to their crystallinity by X-ray powder diffraction (Figure 8.1.3.1). As expected, only CTF1-400 showed little degrees of crystallinity, which is comparable to previous results,^[20] whereas the other materials were found to be amorphous. IR spectroscopy was used to survey whether trimerization of the samples was completed and the organic linkers were still intact. In Figure 4.2.1 the IR spectra of the as-synthesized materials are presented. For all CTFs the signal of the nitrile group ($\approx 2200 \text{ cm}^{-1}$) is missing, which suggests that complete conversion of the monomers via trimerization has occurred. The IR spectra of *bipy*-CTF300 and 400 look similar and show the same significant bands compared to our previous work.^[31] As expected, the IR spectra of *bipy*-CTF500 and 600 are rather featureless, indicating carbonization of the systems at higher synthesis temperatures. Comparable results are found for CTF1. CTF1-400 exhibits the same bands as described in the literature,^[20] while CTF1-500 and 600 show no well-

defined bands, again indicating carbonization and the lack of functional groups at higher synthesis temperatures.

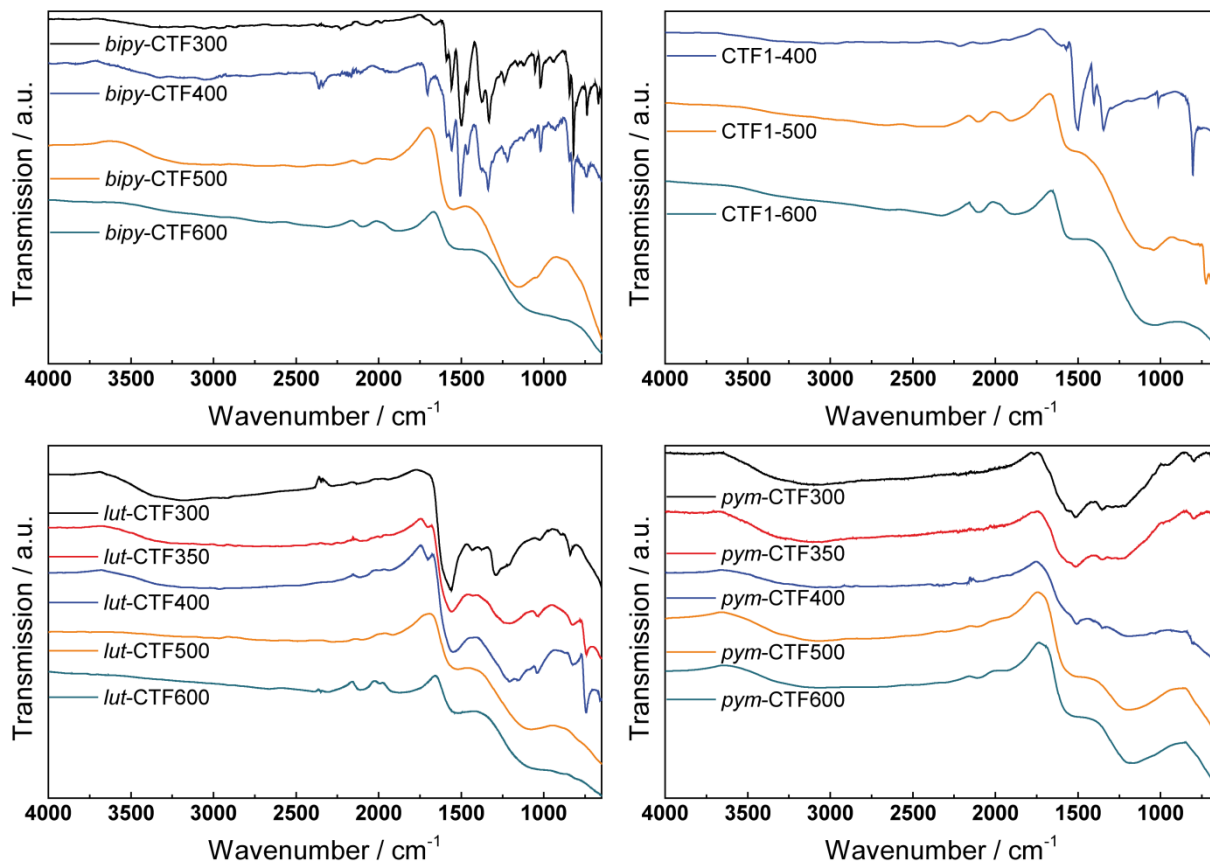


Figure 4.2.1. IR spectra of *bipy*-CTF300-600 (top left), CTF1-400-600 (top right), *lut*-CTF300-600 (bottom left) and *pym*-CTF300-600 (bottom right).

The IR spectra of *lut*-CTF show rather broad and ill-defined bands already at synthesis temperatures below 400 °C. The bands at 1559, 1290 and 842 cm^{-1} in *lut*-CTF300 may indicate the formation of triazine moieties, but can also be assigned to C-C ring vibrations. Again, at higher synthesis temperatures the bands broaden, suggesting a change and heterogenization of the local structure. Similar results are found for *pym*-CTF, with even broader bands. The materials synthesized between 300 and 400 °C show only small signals at 1505, 1351 and 810 cm^{-1} , which are weakly reminiscent of triazine rings. For *pym*-CTF500 and 600 the bands are significantly broadened, thus indicating carbonization of the samples. It is noteworthy that the IR spectra of all CTFs obtained at temperatures of 500 °C or higher look alike with only minor differences in the band positions, irrespective of the building blocks used. Therefore, we assume that the overall compositions and local structures of the different CTFs become gradually similar at higher temperatures, even if their micro- and nanostructures may significantly differ.

We used ssNMR spectroscopy to obtain more detailed information on the local structure of the new *lut*-CTFs and *pym*-CTFs. The spectra of the *lut*-CTFs are shown in Figures 4.2.2 and 8.1.3.2. In contrast to the IR spectra the ssNMR spectra reveal an intact lutidine unit in *lut*-CTF300 and *lut*-CTF350 and

signals in the nitrile region (100-120 ppm). Although the signals in the spectrum of *lut*-CTF300 are more distinct, both spectra feature a signal at 21 ppm corresponding to the methyl groups, and signals between 100-170 ppm, which are attributed to the aromatic carbons. Although no clear triazine peak is visible, which would be expected at 160-170 ppm, a shoulder in the signal at 156 ppm in *lut*-CTF300 is observed, which may relate to the existence of triazine units in the material.

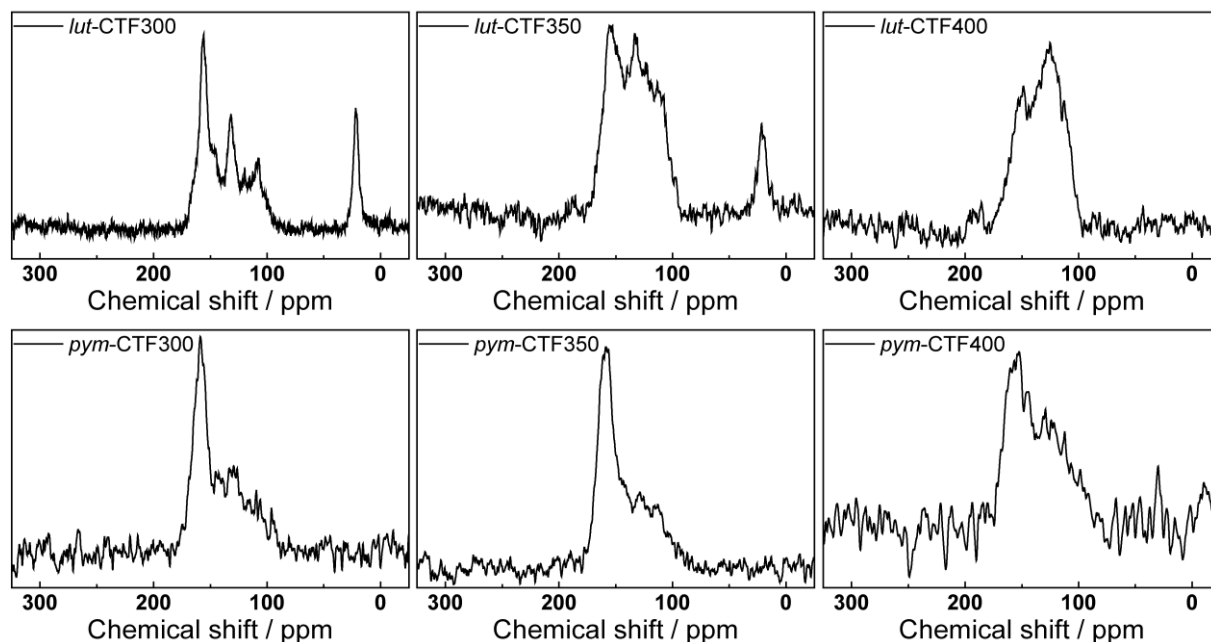


Figure 4.2.2. ^{13}C MAS ssNMR spectra of *lut*-CTF300 (top left), *lut*-CTF350 (top middle), *lut*-CTF400 (top right), *pym*-CTF300 (bottom left), *pym*-CTF350 (bottom middle) and *pym*-CTF400 (bottom right).

The *lut*-CTFs synthesized above 350 °C do not exhibit a methyl peak and aromatic signals weaken with synthesis temperature, indicating ongoing degradation of the systems. Among the *pym*-CTFs only *pym*-CTF300, *pym*-CTF350 and *pym*-CTF400 show signals in the ssNMR measurements (Figure 4.2.2, bottom). In line with the IR measurements, the spectra of *pym*-CTF300 and *pym*-CTF350 look similar, while the spectrum of *pym*-CTF400 exhibits rather weak and broad signals in agreement with the carbonization of the sample. The most prominent signals found for *pym*-CTF300 and *pym*-CTF350 at 159 ppm likely relate to the carbons at position 4 and 6 in the pyrimidine ring, while the signals around 130 ppm can be assigned to the remaining two carbons in the ring. Again, in contrast to the IR spectra, there are indications for residual nitrile groups based on the signals between 100-120 ppm. Taken the IR and ssNMR measurements together, we conclude that the pyrimidine unit withstands the synthesis conditions up to 350 °C, but unequivocal proof for the presence of triazine units is elusive in all *pym*-CTFs as well as *lut*-CTFs.

To obtain a more detailed picture of the extent of degradation in the CTFs as a function of temperature, elemental analysis was used. As can be seen in Table 4.2.1 the C/N ratio of the materials synthesized at low temperatures are close to the theoretical values. With rising synthesis temperature the C/N ratio increases dramatically. Remarkably, the nitrogen content of the samples

never decreases below 10 wt% corresponding to $\approx 40\%$ of the theoretical composition of the intact frameworks, leaving nitrogen functionalities as possible binding sites for CO₂ in the materials. Interestingly, the *pym*-CTFs show very high nitrogen contents at all temperatures, while there is no evidence for intact pyrimidine, triazine or nitrile units at synthesis temperatures above 400 °C.

Table 4.2.1. Elemental analysis of the CTFs obtained at different temperatures.

Sample	N	C	H	C/N
<i>pym</i> theory	43.06	55.39	1.55	1.29
<i>pym</i> -CTF300	33.74	45.31	3.28	1.34
<i>pym</i> -CTF350	34.82	46.19	3.16	1.33
<i>pym</i> -CTF400	34.04	48.26	3.16	1.42
<i>pym</i> -CTF500	33.81	47.54	2.78	1.41
<i>pym</i> -CTF600	27.77	52.03	1.89	1.87
CTF1 theory	21.86	74.99	3.15	3.43
CTF1-400	18.60	70.20	3.30	3.77
CTF1-500	12.39	76.45	2.06	6.17
CTF1-600	10.37	79.16	1.34	7.63
<i>bipy</i> theory	27.17	69.90	2.93	2.57
<i>bipy</i> -CTF300	23.77	64.09	3.19	2.70
<i>bipy</i> -CTF400	20.14	64.28	3.71	3.19
<i>bipy</i> -CTF500	16.42	63.14	2.67	3.85
<i>bipy</i> -CTF600	13.61	67.53	2.01	4.96
<i>lut</i> theory	26.73	68.78	4.49	2.57
<i>lut</i> -CTF300	18.56	56.55	4.70	3.05
<i>lut</i> -CTF350	19.05	63.42	3.62	3.33
<i>lut</i> -CTF400	17.46	66.98	2.83	3.84
<i>lut</i> -CTF500	14.25	70.50	2.52	4.95
<i>lut</i> -CTF600	11.64	74.57	1.39	6.41

It has been shown before that the increase in synthesis temperature yields materials with higher SAs, which however show less local order and lower nitrogen content.^[22,25,31,37] Therefore, argon and carbon dioxide physisorption measurements were performed, which confirm this trend. As can be seen in Table 4.2.2, the BET surfaces of the materials increase dramatically when synthesized at temperatures above 400 °C. The highest SA was found for *lut*-CTF600 (2815 m² g⁻¹), ranging in the upper field of all CTF materials reported to date. It should be mentioned that there were only sorption measurements in the BET range performed for *pym*-CTF300-500 and *bipy*-CTF300 (Figure 8.1.3.3), since *pym*-CTF300, *pym*-CTF350 and *pym*-CTF400 showed a very low SA and *pym*-CTF500 and *bipy*-CTF300 were not measureable because of abnormally high equilibrium times. The sluggish equilibration times suggest the presence of pores with sizes just accessible to Ar atoms. In Figure 4.2.3 (top) and Figure 8.1.3.4 (left) the Ar adsorption and desorption isotherms of the remaining samples are shown. The materials *bipy*-CTF400, CTF1-400, *lut*-CTF300, *lut*-CTF350 and *lut*-CTF400 show typical shapes of a type I isotherm, featuring rapid uptake of argon at low relative pressures ($p/p_0 < 0.05$), which is characteristic for micropores.^[38] The isotherms of *bipy*-CTF500, *bipy*-CTF600, *lut*-CTF500 and *pym*-CTF600 (Figure 8.1.3.4) show similar shapes, but cannot be

described as type I because of continuous adsorption of argon at higher pressures, indicating additional mesoporosity with a broad mesopore size distribution.^[38] Notably, the isotherm of *bipy*-CTF600 shows a hysteresis of type H4 spanning the range $p/p_0 = 0.3-0.9$, which is characteristic of systems with slit-shaped pores.^[38] Finally, the isotherms of CTF1-500, CTF1-600 and *lut*-CTF600 show a combination of type I and IV isotherms, where the micropore filling is followed by mesopore filling. The hysteresis around $p/p_0 = 0.4$ are of type H2, describing systems with rather ill-defined pore sizes and shapes, which is often observed for amorphous materials.

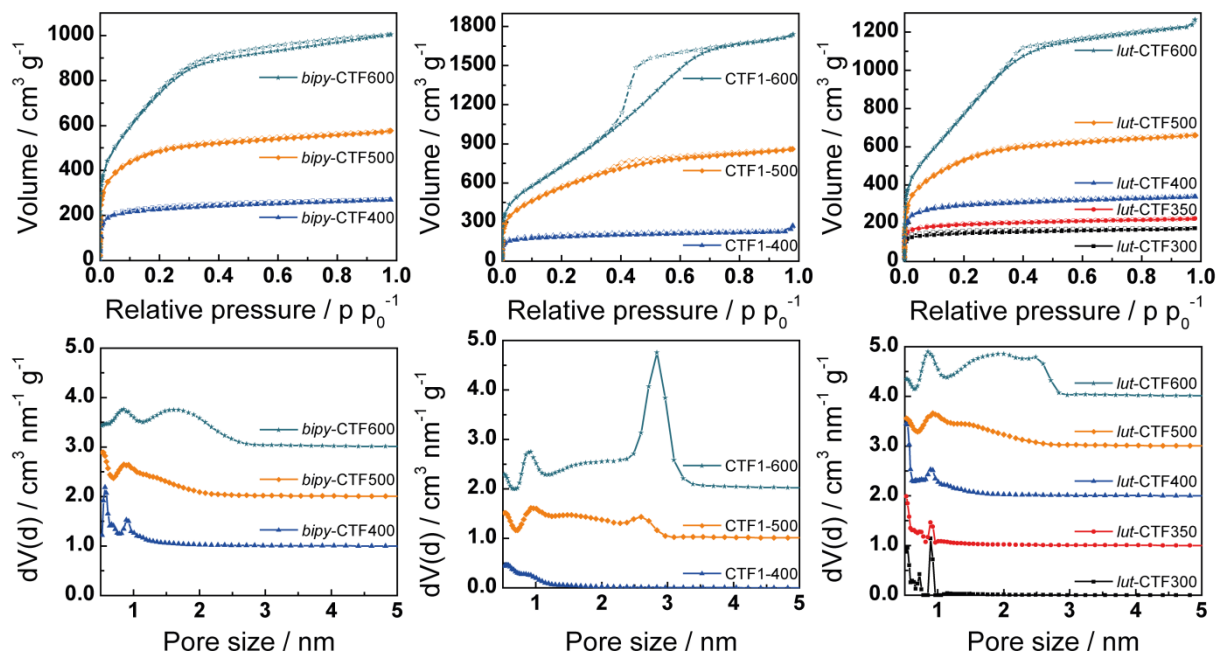


Figure 4.2.3. Argon adsorption (filled symbols) and desorption (open symbols) isotherms (top) and pore size distributions (bottom) of *bipy*-CTF, CTF1 and *lut*-CTF. The curves of the pore size distributions are shifted vertically in steps of $1 \text{ cm}^3 \text{ nm}^{-1} \text{ g}^{-1}$ for clarity.

The pore size distributions (Figure 4.2.3, bottom) from QSDFT calculations clearly depict the pore size evolution as a function of the synthesis temperatures. Almost all samples show distinct pore sizes around 0.5 and 1 nm. With higher synthesis temperature a wider pore size distribution with an increasing amount of supermicropores and small mesopores with diameters between 1 and 3 nanometers emerges, which is best visible for the materials *bipy*-CTF600, CTF1-600 and *lut*-CTF600.

The pore size distributions of the materials suggest the presence of pores that are smaller than 0.5 nm (ultramicropores), the detection limit for Ar physisorption experiments. Therefore, we performed CO_2 physisorption measurements at 273 K, which allow us to analyze pores down to ≈ 0.35 nm. Figure 4.2.4 (left) depicts the CO_2 sorption isotherms of the synthesized CTFs. The isotherms feature a prototypical shape and are fully reversible, except the ones of *pym*-CTF300, *pym*-CTF350 (see Figure 8.1.3.13) and *pym*-CTF400, which exhibit a significant hysteresis over the whole pressure range. Here, the value of adsorbed CO_2 increases with increasing synthesis temperature of the CTFs. Interestingly, the pore size distributions of *lut*-CTF, *pym*-CTF, *bipy*-CTF and

CTF1 are similar with three distinct peaks around 0.35, 0.6 and 0.8 nm, which are indicative of similar pore structures in all investigated CTFs, both at lower and higher synthesis temperatures, respectively (Figure 4.2.4, right).

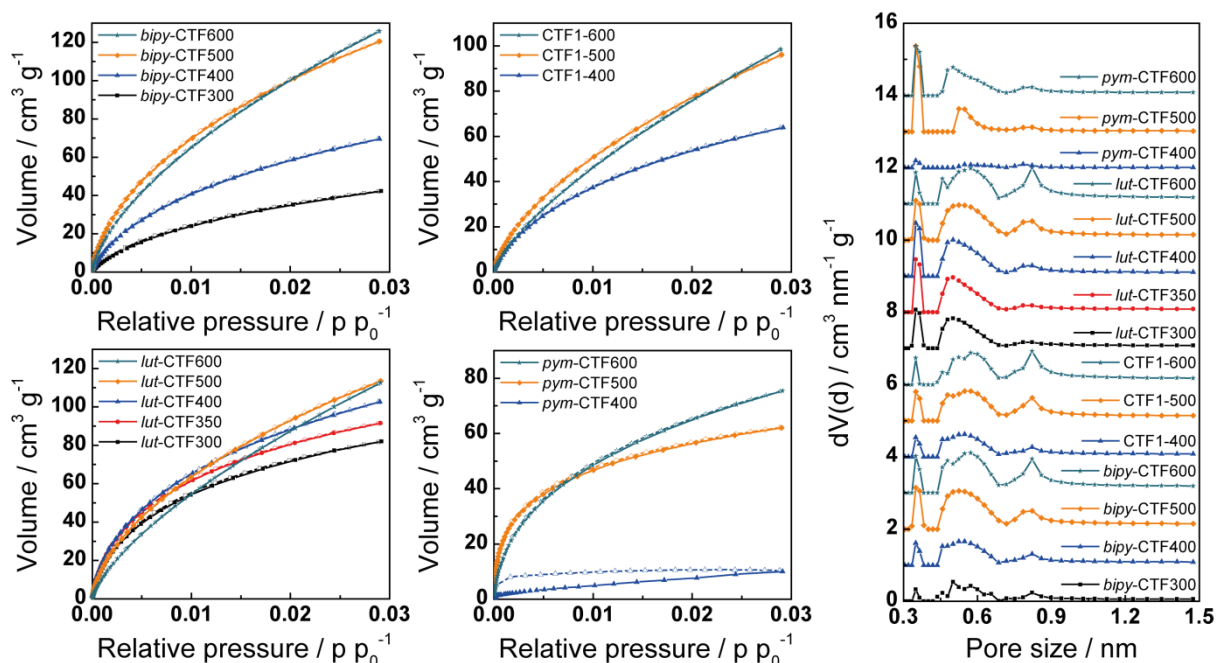


Figure 4.2.4. Carbon dioxide adsorption (filled symbols) and desorption (open symbols) isotherms (left) and pore size distributions (right) of *bipy*-CTFs, CTF1s, *lut*-CTFs and *pym*-CTFs measured at 273 K. The curves of the pore size distributions are shifted vertically in steps of 1 cm³ nm⁻¹ g⁻¹ for clarity.

CO₂ uptake and selectivity

To further investigate the CO₂ physisorption characteristics of the presented CTFs, we additionally performed temperature-dependent uptake measurements at 298 and 313 K (Figures 8.1.3.14-15) and calculated the heats of adsorption (Q_{st}). The adsorbed values of CO₂ at 273 K shown in the previous chapter are remarkably high and are summarized together with the measured values at 298 and 313 K in Table 4.2.2 and 8.1.3.6. At 273 K the highest CO₂ uptake was found for *bipy*-CTF600 (5.58 mmol g⁻¹, 223 mg g⁻¹), followed by *bipy*-CTF500 (5.34 mmol g⁻¹, 214 mg g⁻¹). The *lut*-CTFs and CTF1s show high adsorptions as well, most of them exceeding uptakes of 4 mmol g⁻¹. Only the *pym*-CTFs performed in the lower class of CTFs in terms of CO₂ sorption capacity, most likely due to their low SAs. Compared to the literature, the value measured for *bipy*-CTF600 is even slightly higher than that obtained for the fluorinated CTF FCTF-600 (5.53 mmol g⁻¹)^[39] and therefore represents the highest value reported for all CTFs so far and the second best value among all POPs, where *bipy*-CTF600 is outperformed only by the porous polymer framework PPF-1 (6.12 mmol g⁻¹), an imine-linked polymer.^[40] Notably, other high performance CO₂ sorbents – materials such as benzimidazole-linked polymers (BILPs; 2.91-5.34 mmol g⁻¹),^[14,16,18,41] azo-linked polymers (ALPs; 3.52-

5.37 mmol g⁻¹)^[17] and amination-linked porous organic polymers (APOPs; 2.27-4.45 mmol g⁻¹)^[42] – show lower CO₂ uptakes compared to *bipy*-CTF600.

Table 4.2.2. BET surface areas, CO₂, H₂ and N₂ uptake behavior, heats of CO₂ adsorption and CO₂/N₂ selectivities of the presented CTFs.

Sample	BET SA ^a [m ² g ⁻¹]	CO ₂ uptake ^b [mmol g ⁻¹]			H ₂ uptake ^c [wt%]		N ₂ uptake ^d [mmol g ⁻¹]	Q _{st} [kJ mol ⁻¹]		Selectivity ^f	
		273 K	298 K	313 K	1 bar	25 bar		Max ^e	Min	Henry	IAST ^g
<i>pym</i> -CTF300	1.50	0.28	-	-	-	-	-	-	-	-	-
<i>pym</i> -CTF350	3.51	0.33	-	-	-	-	-	-	-	-	-
<i>pym</i> -CTF400	0.45	0.45	-	-	-	-	-	-	-	-	-
<i>pym</i> -CTF500	208	2.75	1.77	1.26	-	-	0.13	40.5	39.0	189	502
<i>pym</i> -CTF600	689	3.34	2.15	1.44	-	-	0.16	37.4	30.5	126	124
CTF1-400	610	2.83	1.52	0.98	-	-	0.08	33.7	30.2	59	45
CTF1-500	1830	4.26	2.23	1.47	1.70	3.36	0.19	35.3	27.0	36	29
CTF1-600	2557	4.36	2.21	1.39	2.12	4.34	0.23	31.6	24.6	26	17
<i>bipy</i> -CTF300	360	1.87	0.98	0.61	-	-	0.05	33.3	30.7	47	41
<i>bipy</i> -CTF400	753	3.08	1.78	1.18	-	-	0.10	35.2	28.0	50	40
<i>bipy</i> -CTF500	1548	5.34	3.07	1.77	1.63	2.71	0.25	34.2	31.0	61	42
<i>bipy</i> -CTF600	2479	5.58	2.95	1.84	2.10	4.00	0.28	34.4	27.0	37	24
<i>lut</i> -CTF300	486	3.63	2.14	1.51	-	-	0.14	36.6	31.4	69	57
<i>lut</i> -CTF350	635	4.06	2.41	1.59	1.22	1.79	0.16	37.4	33.9	76	66
<i>lut</i> -CTF400	968	4.55	2.72	1.80	1.36	2.09	0.20	37.5	30.8	63	53
<i>lut</i> -CTF500	1680	5.04	2.58	1.71	1.60	2.90	0.23	38.2	30.0	27	27
<i>lut</i> -CTF600	2815	4.99	2.52	1.66	2.00	4.18	0.22	33.3	24.9	26	23

^aFrom Ar sorption measurements. ^bAt 1 bar. ^cAt 77 K. ^dAt 1 bar and 298 K. ^eAt zero coverage. ^fCO₂/N₂ at 298 K. ^gA CO₂:N₂ ratio of 15:85 was used.

As can be seen in Table 4.2.2 and Figure 4.2.5 (middle), the CO₂ uptake does not directly correlate with the BET SAs of the materials. *bipy*-CTF600 has a BET SA just less than CTF1-600, but takes up significantly more CO₂ and additionally outperforms *lut*-CTF600, which has a significantly higher SA. As mentioned above, the incorporation of nitrogen in the materials has been demonstrated to lead to higher CO₂ adsorption in POPs,^[7,12-18] which is in line with our finding that the integration of pyridine units (*bipy*-CTF and *lut*-CTF) lead to higher CO₂ uptakes compared to CTF1 with a purely carbon-based linker. Interactions between CO₂ and basic nitrogen sites would indeed explain the higher amount of CO₂ adsorbed by *bipy*-CTF600 compared to CTF1-600 and *lut*-CTF600 which have lower nitrogen contents, but not compared to all other samples which have higher nitrogen contents and most likely more intact pyridine units (see Figure 8.1.3.42). We therefore assume that the nitrogen content is a secondary effect weakly enhancing the CO₂ uptake in a series of compounds with comparable surface areas. In contrast, the micropore SAs shown in Table 8.1.3.4 reveal a very clear correlation with the amount of adsorbed CO₂ (see Figure 4.2.5, left), indicating that the small micropores accessible to CO₂ contribute most significantly to the observed CO₂ storage capacities. Therefore, we assume that a combination of the micropore SA and nitrogen content governs the CO₂ uptake behavior, with the presence of small micropores being the main contributing factor. The higher accessible micropore SA also contributes to a higher degree of *accessible* nitrogen sites and is therefore a “vehicle” to efficiently utilize the nitrogen sites present in the sample.

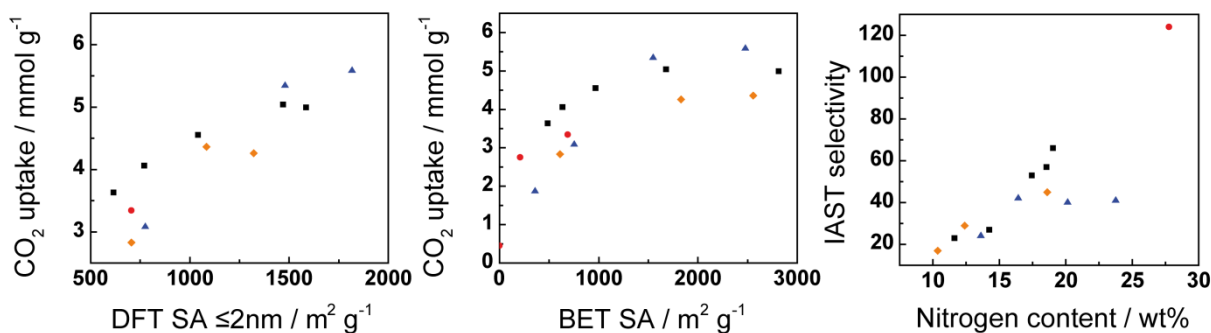


Figure 4.2.5. Dependencies of CO₂ uptake on the micropore SA (≤ 2 nm, left) and BET SA (middle), and of the IAST selectivity on the nitrogen content (right). *lut*-CTFs (black squares), *pym*-CTFs (red circles) *bipy*-CTFs (blue triangles) and CTF1s (orange diamonds).

The nitrogen content and type of nitrogen sites present should influence the interaction energy between the material and CO₂ sorptive as a consequence of Lewis acid - Lewis base interactions. The heats of adsorption (Q_{st}) can be considered as a rough estimate of these interaction energies. The calculated curves are shown in Figure 8.1.3.16 and the maxima and minima are listed in Table 4.2.2. Q_{st} values of 30-50 kJ mol⁻¹ are preferred for CO₂ capture materials since in principle higher values lead to higher adsorption and selectivities, while materials with Q_{st} values exceeding 50 kJ mol⁻¹ need high energies for desorption and, hence, regeneration.^[43] The Q_{st} values at zero coverage of the presented CTFs all exceed 30 kJ mol⁻¹ and even at high loading the values of most of the materials do not drop below that mark. This finding indicates relatively strong interactions of the sorbent and sorbate, thus giving a rationale to the observed overall high CO₂ capacities of the materials.

The flue gas of coal-fired powerplants consists of approximately 15% CO₂, 5% H₂O, 5% O₂ and 75% N₂.^[4,8] Therefore, the sorption selectivity of CO₂ over N₂ is particularly relevant in order to evaluate the CTFs as potential flue gas sorbents. We calculated the selectivities by the ratios of the initial slopes in the Henry region and the ideal adsorbed solution theory (IAST) at 298 K (see Supporting Information). The values listed in Table 4.2.2 show a discrepancy between the two different theories with higher selectivities found by Henry calculations. Since the Henry calculations only take the initial slopes into account, while the IAST calculations consider the whole pressure range, it may be concluded that the materials show high selectivities towards CO₂ in the low pressure range, which decreases with higher working pressures, as shown in Figure 8.1.3.25. The highest selectivities (Henry: 189, IAST: 502) were found for *pym*-CTF500 which to the best of our knowledge outperforms all POPs measured so far, including PPN-6-CH₂DETA (IAST: 442)^[13] and azo-COP-2 (Henry: 142, IAST: 131).^[44] Overall, the selectivities decrease with increasing adsorption capacity (Figure 8.1.3.42), which is a general trend in POP chemistry.^[8] An even better correlation is found between the nitrogen content and the selectivity as can be seen in Figure 4.2.5 (right). The best compromise of high CO₂ uptakes and high selectivities was found for *lut*-CTF350 (Henry: 76, IAST: 66), *lut*-CTF400 (Henry: 63, IAST: 53) and *bipy*-CTF500 (Henry: 61, IAST: 42), which besides good

selectivities show uptakes above 4 mmol g⁻¹. For comparison PPF-1, the best POP for CO₂ uptakes reported to date, shows low IAST selectivities of 15 at 273 K.^[40]

H₂ storage

We further performed hydrogen storage measurements at 77, 87 and 298 K up to 25 bar with the materials that showed the highest CO₂ uptake capacities (Table 4.2.2, Figures 4.2.6 and 8.1.3.22-23). The highest H₂ uptake was found for CTF1-600 (4.34 wt%), which is comparable to that reported for *fl*-CTF400 (4.36 wt%, 20 bar),^[25] but higher than that observed for 2D COFs (1.46-3.88 wt%, sat. pressure)^[45] and polymers of intrinsic microporosity (PIMs, 1.45-2.71 wt%, 10 bar), while a direct comparison is difficult due to the different pressure conditions.^[46-50] The highest values for POPs were found so far for the highly porous 3D COFs (6.98-7.16 wt%, sat. pressure),^[45] PAFs (4.2-7.0 wt%)^[51-52] and PPNs (8.34 wt%, 55 bar),^[13] which however were measured at higher pressures. Other CTFs were only studied with respect to their H₂ capacities up to 1 bar, where CTF-1 adsorbs 1.55 wt%,^[20] PCTF-1 1.86 wt%^[24] and PCTF-2 0.9 wt%.^[24] CTF1-600 (2.12 wt%), *bipy*-CTF600 (2.10 wt%) and *lut*-CTF600 (2.00 wt%) studied here substantially outperform these materials and show even higher adsorptions than *fl*-CTF400 (1.95 wt%) at that pressure. In contrast to the CO₂ uptakes, the H₂ uptakes at 77 K and 25 bar, strictly depend on the BET SAs: The higher the total SA, the higher the observed H₂ adsorption. This observation supports our previous observations, namely that the adsorption of CO₂ is promoted – at least to some extent – by the accessible nitrogen sites due to electrostatic interactions, which seems to be irrelevant for H₂ adsorption.

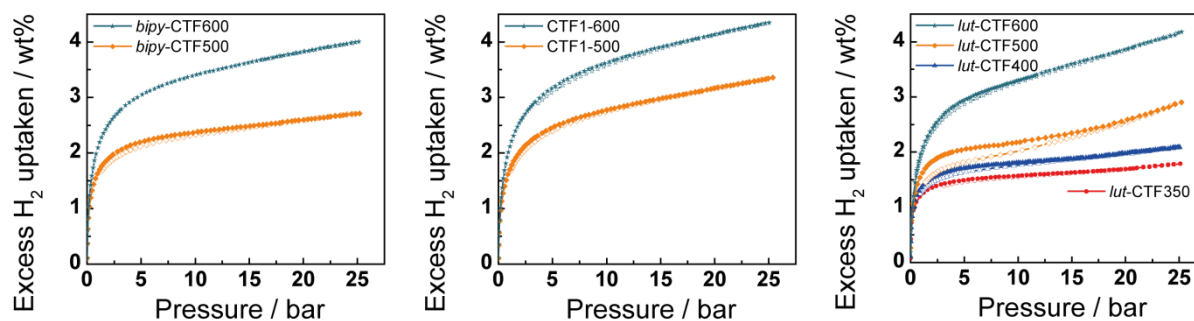


Figure 6. Hydrogen adsorption (filled symbols) and desorption (open symbols) isotherms of *bipy*-CTFs, CTF1s and *lut*-CTFs measured at 77 K.

4.2.4 CONCLUSION

Two new covalent triazine frameworks – *lut*-CTF and *pym*-CTF – were obtained by ionothermal synthesis at different temperatures and their composition, porosity as well as CO₂ and H₂ uptakes were analyzed and compared to those of *bipy*-CTF and CTF1. While the heterocyclic building blocks show varying levels of thermal stability, all materials were found to be microporous with high surface areas up to 2815 m² g⁻¹ and show very high CO₂ uptakes. The best uptakes were found for the pyridine based materials *bipy*-CTF600 (5.58 mmol g⁻¹), *bipy*-CTF500 (5.34 mmol g⁻¹) and *lut*-CTF500

(5.04 mmol g⁻¹), with *bipy*-CTF600 being the second best performing material of all POPs and the best performing CTF reported to date. Our work reveals a common trend according to which the CO₂ uptake capacities predominantly scale with the microporous, rather than the total BET SA, while the nitrogen content has a comparatively weak influence on the uptake behavior. The latter however was found to be the main contributor to the high CO₂/N₂ selectivities found for the CTFs. In fact, the porous material with the highest nitrogen content, *pym*-CTF500, showed the highest selectivity (Henry: 189, IAST: 502) found for all POPs so far. Finally, H₂ sorption measurements reveal high uptake capacities at ambient and high pressures, rendering the presented CTFs interesting candidates as prospective CCS and hydrogen storage materials.

4.2.5 BIBLIOGRAPHY

Acknowledgment

The authors acknowledge financial support by the Max Planck Society, the Deutsche Forschungsgemeinschaft (DFG; SPP-1362, LO 1801/2-1), the Nanosystems Initiative Munich (NIM), the Center for Nanoscience (CeNS) and the Fonds der Chemischen Industrie (FCI). H. Oh was supported for this research through a stipend from the International Max Planck Research School for Advanced Materials (IMPRS-AM). We thank Christian Minke for ssNMR measurements. We acknowledge Prof. Thomas Bein for access to the respective measurement facilities.

References

- [1] *Climate Change 2013: The Physical Science Basis. Contribution of Working Group I to the Fifth Assessment Report of the Intergovernmental Panel on Climate Change* Cambridge University Press, Cambridge, United Kingdom and New York, USA, **2013**.
- [2] *World Energy Outlook 2013*, International Energy Agency, Paris, **2013**.
- [3] M. E. Boot-Handford, J. C. Abanades, E. J. Anthony, M. J. Blunt, S. Brandani, N. Mac Dowell, J. R. Fernandez, M.-C. Ferrari, R. Gross, J. P. Hallett, R. S. Haszeldine, P. Heptonstall, A. Lyngfelt, Z. Makuch, E. Mangano, R. T. J. Porter, M. Pourkashanian, G. T. Rochelle, N. Shah, J. G. Yao, P. S. Fennell, *Energy Environ. Sci.* **2014**, *7*, 130-189.
- [4] D. M. D'Alessandro, B. Smit, J. R. Long, *Angew. Chem. Int. Ed.* **2010**, *49*, 6058-6082.
- [5] R. S. Haszeldine, *Science* **2009**, *325*, 1647-1652.
- [6] G. T. Rochelle, *Science* **2009**, *325*, 1652-1654.
- [7] P.-Z. Li, Y. Zhao, *Chem. Asian J.* **2013**, *8*, 1680-1691.
- [8] R. Dawson, A. I. Cooper, D. J. Adams, *Polym. Int.* **2013**, *62*, 345-352.
- [9] Z. Xiang, D. Cao, *J. Mater. Chem. A* **2013**, *1*, 2691-2718.
- [10] S.-Y. Ding, W. Wang, *Chem. Soc. Rev.* **2013**, *42*, 548-568.

- [11] R. Dawson, A. I. Cooper, D. J. Adams, *Prog. Polym. Sci.* **2012**, *37*, 530-563.
- [12] T. Islamoglu, M. Gulam Rabbani, H. M. El-Kaderi, *J. Mater. Chem. A* **2013**, *1*, 10259-10266.
- [13] W. Lu, J. P. Sculley, D. Yuan, R. Krishna, Z. Wei, H.-C. Zhou, *Angew. Chem. Int. Ed.* **2012**, *51*, 7480-7484.
- [14] M. G. Rabbani, H. M. El-Kaderi, *Chem. Mater.* **2011**, *23*, 1650-1653.
- [15] L.-H. Xie, M. P. Suh, *Chem. Eur. J.* **2013**, *19*, 11590-11597.
- [16] M. G. Rabbani, H. M. El-Kaderi, *Chem. Mater.* **2012**, *24*, 1511-1517.
- [17] P. Arab, M. G. Rabbani, A. K. Sekizkardes, T. İslamoğlu, H. M. El-Kaderi, *Chem. Mater.* **2014**, *26*, 1385-1392.
- [18] S. Altarawneh, S. Behera, P. Jena, H. M. El-Kaderi, *Chem. Commun.* **2014**, *50*, 3571-3574.
- [19] K. D. Vogiatzis, A. Mavrandonakis, W. Klopffer, G. E. Froudakis, *Chem. Phys. Chem.* **2009**, *10*, 374-383.
- [20] P. Kuhn, M. Antonietti, A. Thomas, *Angew. Chem. Int. Ed.* **2008**, *47*, 3450-3453.
- [21] P. Kuhn, A. Forget, J. Hartmann, A. Thomas, M. Antonietti, *Adv. Mater.* **2009**, *21*, 897-901.
- [22] P. Kuhn, A. Thomas, M. Antonietti, *Macromolecules* **2009**, *42*, 319-326.
- [23] A. Bhunia, I. Boldog, A. Moller, C. Janiak, *J. Mater. Chem. A* **2013**, *1*, 14990-14999.
- [24] A. Bhunia, V. Vasylyeva, C. Janiak, *Chem. Commun.* **2013**, *49*, 3961-3963.
- [25] S. Hug, M. B. Mesch, H. Oh, N. Popp, M. Hirscher, J. Senker, B. V. Lotsch, *J. Mater. Chem. A* **2014**, *2*, 5928-5936.
- [26] P. Katekomol, J. Roeser, M. Bojdys, J. Weber, A. Thomas, *Chem. Mater.* **2013**, *25*, 1542-1548.
- [27] J. Liu, H. Chen, S. Zheng, Z. Xu, *J. Chem. Eng. Data* **2013**.
- [28] X. Liu, H. Li, Y. Zhang, B. Xu, S. A, H. Xia, Y. Mu, *Polym. Chem.* **2013**, *4*, 2445-2448.
- [29] S. Ren, M. J. Bojdys, R. Dawson, A. Laybourn, Y. Z. Khimyak, D. J. Adams, A. I. Cooper, *Adv. Mater.* **2012**, *24*, 2357-2361.
- [30] W. Wang, H. Ren, F. Sun, K. Cai, H. Ma, J. Du, H. Zhao, G. Zhu, *Dalton Trans.* **2012**, *41*, 3933-3936.
- [31] S. Hug, M. E. Tauchert, S. Li, U. E. Pachmayr, B. V. Lotsch, *J. Mater. Chem.* **2012**, *22*, 13956-13964.
- [32] D. W. Allen, B. G. Hutley, M. T. J. Mellor, *J. Chem. Soc., Perkin Trans. 2* **1972**, 63-67.
- [33] G. Vlád, I. T. Horváth, *J. Org. Chem.* **2002**, *67*, 6550-6552.
- [34] Z. Buděšínský, J. Vavřina, *Collect. Czech. Chem. Commun.* **1972**, *37*, 1721-1733.
- [35] T. McNally, A. C. Tinker, *J. Chem. Soc., Perkin Trans. 1* **1988**, 1837-1844.
- [36] T. Sasada, F. Kobayashi, M. Moriuchi, N. Sakai, T. Konakahara, *Synlett* **2011**, *22*, 2029-2034.
- [37] P. Kuhn, A. I. Forget, D. Su, A. Thomas, M. Antonietti, *J. Am. Chem. Soc.* **2008**, *130*, 13333-13337.

- [38] K. S. W. Sing, D. H. Everett, R. A. W. Haul, L. Moscou, R. A. Pierotti, J. Rouquérol, T. Siemieniewska, *Pure Appl. Chem.* **1985**, *57*, 603-619.
- [39] Y. Zhao, K. X. Yao, B. Teng, T. Zhang, Y. Han, *Energy Environ. Sci.* **2013**, *6*, 3684-3692.
- [40] Y. Zhu, H. Long, W. Zhang, *Chem. Mater.* **2013**, *25*, 1630-1635.
- [41] M. G. Rabbani, A. K. Sekizkardes, O. M. El-Kadri, B. R. Kaafarani, H. M. El-Kaderi, *J. Mater. Chem.* **2012**, *22*, 25409-25417.
- [42] W.-C. Song, X.-K. Xu, Q. Chen, Z.-Z. Zhuang, X.-H. Bu, *Polym. Chem.* **2013**, *4*, 4690-4696.
- [43] Y.-S. Bae, R. Q. Snurr, *Angew. Chem. Int. Ed.* **2011**, *50*, 11586-11596.
- [44] H. A. Patel, S. Hyun Je, J. Park, D. P. Chen, Y. Jung, C. T. Yavuz, A. Coskun, *Nat. Commun.* **2013**, *4*, 1357.
- [45] H. Furukawa, O. M. Yaghi, *J. Am. Chem. Soc.* **2009**, *131*, 8875-8883.
- [46] N. B. McKeown, P. M. Budd, D. Book, *Macromol. Rapid Commun.* **2007**, *28*, 995-1002.
- [47] N. B. McKeown, B. Ghanem, K. J. Msayib, P. M. Budd, C. E. Tattershall, K. Mahmood, S. Tan, D. Book, H. W. Langmi, A. Walton, *Angew. Chem. Int. Ed.* **2006**, *45*, 1804-1807.
- [48] B. S. Ghanem, K. J. Msayib, N. B. McKeown, K. D. M. Harris, Z. Pan, P. M. Budd, A. Butler, J. Selbie, D. Book, A. Walton, *Chem. Commun.* **2007**, 67-69.
- [49] J.-Y. Lee, C. D. Wood, D. Bradshaw, M. J. Rosseinsky, A. I. Cooper, *Chem. Commun.* **2006**, 2670-2672.
- [50] P. M. Budd, A. Butler, J. Selbie, K. Mahmood, N. B. McKeown, B. Ghanem, K. Msayib, D. Book, A. Walton, *Phys. Chem. Chem. Phys.* **2007**, *9*, 1802-1808.
- [51] T. Ben, C. Pei, D. Zhang, J. Xu, F. Deng, X. Jing, S. Qiu, *Energy Environ. Sci.* **2011**, *4*, 3991-3999.
- [52] T. Ben, H. Ren, S. Ma, D. Cao, J. Lan, X. Jing, W. Wang, J. Xu, F. Deng, J. M. Simmons, S. Qiu, G. Zhu, *Angew. Chem. Int. Ed.* **2009**, *48*, 9457-9460.

5 COVALENT TRIAZINE FRAMEWORKS IN ENERGY CONVERSION AND STORAGE

The storage of energy from renewable energy sources with fluctuating performance such as solar energy and wind energy is a major challenge in research. The most obvious approach is the storage as chemical energy in batteries. Still, such battery systems need improvements in energy density, lifetime and environmental cleanness. Another method in storing energy as chemical energy is by the production of clean fuels such as hydrogen. Especially the hydrogen generation from water by solar energy would enable a green energy cycle without concomitant emissions of greenhouse gases besides water.

In the following chapter recent results are shown from light-driven hydrogen evolution photocatalyzed by CTF1. The synthesis of CTF1 at lower temperatures led to materials capable of photocatalyzing hydrogen generation from water in the visible light region.

The second chapter will focus on recent results concerning the use of CTFs as bipolar materials in lithium ion batteries. The results of the performance of *bipy*-CTF in such systems compared to CTF1 will be discussed.

5.1 COVALENT TRIAZINE FRAMEWORKS FOR PHOTOCATALYTIC HYDROGEN EVOLUTION

Stephan Hug, Katharina Schwinghammer and Bettina V. Lotsch

5.1.1 INTRODUCTION

The conversion of solar energy to chemical energy by producing hydrogen from water enables a green energy cycle.^[1] However, the development of a cost-effective process has yet to be developed.^[1] Since the discovery of water splitting on a *n*-type semiconducting TiO₂ electrode by Fujishima and Honda in 1972,^[2] research largely focused on inorganic semiconductors, mainly based on rare or costly transition metals, entailing disadvantages such as complicated scalability, increasing costs and environmental concerns.^[3] The development of light element semiconductors is therefore a promising research field and has been shown recently in a few examples based on polymers,^[4] graphite oxides,^[5] carbon nitrides^[6-8] and COFs.^[9] Especially the incorporation of triazine units seems to significantly increase the hydrogen evolution.^[6-7,9-10] Therefore, CTFs should be capable of producing hydrogen by water splitting when illuminated with light, indicated by experimental and theoretical results showing strong UV-Vis absorptions.^[11-12] In this chapter the synthesis of CTF1 under ionothermal conditions at low temperatures (300-350 °C) is presented, leading to materials of light yellow to brown color, which exhibit strong absorption in the UV-Vis region and show significant catalytic activity in the photoinduced hydrogen evolution reaction.

Basic principles of photocatalytic water splitting

In the first step of photocatalytic water splitting a photocatalyst (usually a semiconductor) absorbs light greater than its band gap energy, causing excitation of electrons in the valence band to the conduction band, leaving holes in the valence band. The state consisting of these bound electron-hole-pairs – so-called excitons – is the photo-excited state and the energy difference between the conduction and valence band is the band gap of the photocatalyst. In the second step the electron-hole-pairs migrate to the surface where they can react in a third step as reducing and oxidizing agents due to the chemical potentials of the electrons (+0.5 to -1.5 V versus the normal hydrogen electrode, NHE) and holes (+1.0 to +3.5 V).^[13] This third step is the actual water splitting reaction



which needs to overcome the Gibbs free energy change of 237 kJ mol⁻¹ or 1.23 eV associated with the splitting of water into oxygen and hydrogen. Thus, the band gap energy of the photocatalyst has to exceed at least 1.23 eV, which corresponds to a wavelength of smaller than 1000 nm. In order to

utilize visible light for this process, the wavelength range used should however be larger than 400 nm, equivalent to 3.0 eV or less. Notably, additional overvoltage due to kinetic inhibition increases the barrier of the reaction to about 1.6-1.8 eV,^[14] which can be reduced by the use of co-catalysts.^[15] A competitive process in photocatalysis is the recombination of electrons and holes by emitting light or generating phonons. This process is particularly pronounced in organic semiconductors with low dielectric constants, the latter giving rise to strongly bound Frenkel-type excitons. Two strategies are applied to reduce charge recombination to a small extent: The first one is to add electron donors or acceptors which recombine with the holes or electrons, respectively, more easily than water does and hence provide efficient charge separation. The second strategy uses co-catalysts which form hetero-junctions with the semiconductor which enable separation of the electron-hole-pairs and therefore induce faster charge carrier migration.

5.1.2 EXPERIMENTAL

Methods

Argon adsorption/desorption measurements were performed at 87 K with an Autosorb-iQ surface analyzer (Quantachrome Instruments, USA). Samples were outgassed in vacuum at 120 °C for 6-12 h to remove all guests. For BET calculations pressure ranges of the Ar isotherms were chosen with the help of the BET Assistant in the ASiQwin software. In accordance with the ISO recommendations multipoint BET tags equal or below the maximum in $V \cdot (1 - P/P_0)$ were chosen.

Infrared (IR) spectroscopy measurements were carried out on a Perkin Elmer Spektrum BX II (Perkin Elmer, USA) with an attenuated total reflectance unit.

Powder X-ray diffraction (XRD) was measured on a BRUKER D8 Avance (Bruker AXS, USA) in Bragg-Brentano geometry.

Elemental analysis (EA) was carried out with an Elementarvario EL (Elementar Analysensysteme, Germany).

Magic angle spinning (MAS) solid-state nuclear magnetic resonance (ssNMR) spectra were recorded at ambient temperature on a BRUKER DSX500 Avance NMR spectrometer (Bruker Biospin, Germany) with an external magnetic field of 11.75 T. The operating frequencies are 500.1 MHz and 125.7 MHz for ¹H and ¹³C, respectively, and the spectra were referenced relative to TMS. The samples were contained either in 2.4 or 4 mm ZrO₂ rotors.

Optical diffuse reflectance spectra of the solids were collected at room temperature with a UV-Vis-NIR diffuse reflectance spectrometer Cary 5000 (Agilent Technologies, USA) at a photometric range of 250-800 nm. Powders were prepared in a sample carrier with a quartz glass window at the edge of

the integrating sphere with BaSO₄ as the optical standard. Kubelka-Munk spectra were calculated from the reflectance data.

Hydrogen evolution experiments in UV and visible light were carried out in a continuously cooled 230 mL quartz glass reactor with a PTFE septum under argon atmosphere. The catalyst (10 mg) was suspended in a 0.5 M pH7 phosphate buffer solution (9 mL) and triethanolamine (TEoA) as the sacrificial electron donor (1 mL) and H₂PtCl₆ (6 μL of 8 wt% in H₂O, ≈ 2.2 wt% Pt) as the precursor for the *in situ* formation of the Pt co-catalyst was added while stirring. The addition of the basic electron donor led to a pH of 8.9. The flask was evacuated and purged with argon to remove any dissolved gases in the solution. Samples were simultaneously top-illuminated (top surface = 15.5 cm²) at a distance of 22 cm with a 300 W xenon lamp with a water filter and dichroic mirror blocking wavelengths <420 nm for visible light and <250 nm for UV-Vis measurements while stirring, which amounts to a light intensity of about 0.3 W cm⁻² on the surface of the sample. The headspace of the reactor was periodically sampled with an online injection system and the gas components were quantified by gas chromatography (thermal conductivity detector, argon as carrier gas). A high hydrophobicity of the CTF1 samples was noticed at the beginning which was reduced during the photocatalytic experiment.

Materials

All reactions were carried out under an argon atmosphere in flame-dried glassware. 1,4-Dicyanobenzene (98%) was obtained from Acros Organics and anhydrous zinc chloride (99.995%) from Sigma-Aldrich and used without further purifications.

Synthesis of Covalent Triazine Frameworks. In a typical CTF synthesis a Duran ampoule (1.5 x 12 cm) was charged with 1,4-dicyanobenzene (500 mg, 3.90 mmol) and ZnCl₂ (1-15 equivalents, see Table 5.1.1) within a glove box. The ampoule was flame sealed under vacuum and was subjected in a tube oven to temperatures between 300-350 °C for 96-186 h (see Table 5.1.1). After cooling to ambient temperature, the ampoule was opened and its content ground thoroughly. The crude product was stirred in H₂O (75 mL) for 1 h, filtered, and washed with 1 M HCl (2 × 75 mL). The mixture was then stirred at 90 °C in 1 M HCl (75 mL) overnight, filtered, and subsequently washed with 1 M HCl (3 × 75 mL), H₂O (12 × 75 mL), THF (2 × 75 mL), and dichloromethane (1 × 75 mL). Finally, the powder was dried overnight in a desiccator.

5.1.3 RESULTS AND DISCUSSION

Synthesis and characterization

The syntheses of the CTF1s was done in a way analogous to the original synthesis established by the Antonietti group based on an ionothermal approach in zinc chloride melts.^[16] As already stated in

that work, synthesis at temperatures below 350 °C yielded mainly soluble products after two days of reaction time. As a consequence of the temperature dependency of the reaction rate and the accordingly relatively small reaction rates at 350 °C, we prolonged the reaction times, in accordance with van't Hoff's law. Indeed, reaction times of 96 h for synthesis at 350 °C and 168 h for 300 °C led to polymeric products which were not soluble in organic solvents such as THF, acetone, ethanol, chloroform and dichloromethane, as well as water and hot 1 M HCl. The detailed synthesis conditions are shown in Table 5.1.1. The nomenclature is chosen by adding to the prefix CTF1 first the synthesis temperature and then the equivalents of zinc chloride used in the synthesis.

Table 5.1.1. Synthesis conditions of the produced CTF1s and resulting yields.

Sample	Eq. ZnCl ₂	Synthesis Temperature [°C]	Synthesis Time ^a [h]	Yields [%]
CTF1-300-1	1	300	168	35
CTF1-300-2.5	2.5	300	168	39
CTF1-300-5	5	300	168	20
CTF1-300-10	10	300	168	13
CTF1-300-15	15	300	168	6
CTF1-350-1	1	350	96	55
CTF1-350-10	10	350	96	25
CTF1-400 ^b	1	400	48	

^aHeating in 60 °C h⁻¹ steps and cooling in 10 °C h⁻¹ steps. ^bFrom Chapter 4.2.

Interestingly, the materials showed different colors compared to the samples synthesized at 400 °C, as can be seen in Figure 5.1.1, but the colors did not change with other precursor-ZnCl₂ ratios. However, the yields showed a strong dependency on the amount of ZnCl₂ used, yielding less polymeric products at higher equivalents of ZnCl₂. We assume this is due to the lower synthesis temperatures close to the melting point of ZnCl₂ (290 °C) and the accordingly low molecular diffusivity, which makes it less probable for the molecules to get close to each other and react. Thus, most of the reaction products likely yielded oligomers, which were washed out in the work up process. Further experiments will be necessary to isolate these products and analyze their composition to obtain more detailed information about the reaction behavior of the materials at these synthesis conditions.



Figure 5.1.1. Photographs of CTF1-300-1 (left), CTF1-350-1 (middle) and CTF1-400 (right).

The materials were characterized with the help of IR and ssNMR spectroscopy, XRD, EA, physisorption measurements and UV-Vis spectroscopy and the results were compared with the

sample synthesized at 400 °C (CTF1-400) from Chapter 4.2. The spectra from the IR measurements are shown in Figure 5.1.2. The materials synthesized between 300-350 °C show the same bands as CTF1-400 and an additional signal at 2227 cm^{-1} (highlighted in blue) as well as more well-defined bands in the fingerprint region. The band at 2227 cm^{-1} is due to residues of nitrile groups in the samples, indicating incompletely condensed materials. The characteristic bands for the triazine unit (highlighted in pink) are found at 1506 cm^{-1} (C-N stretching mode)^[17-18] and 1355 cm^{-1} (in-plane ring stretching vibrations),^[19-20] confirming the successful formation of triazine rings at these synthesis conditions.

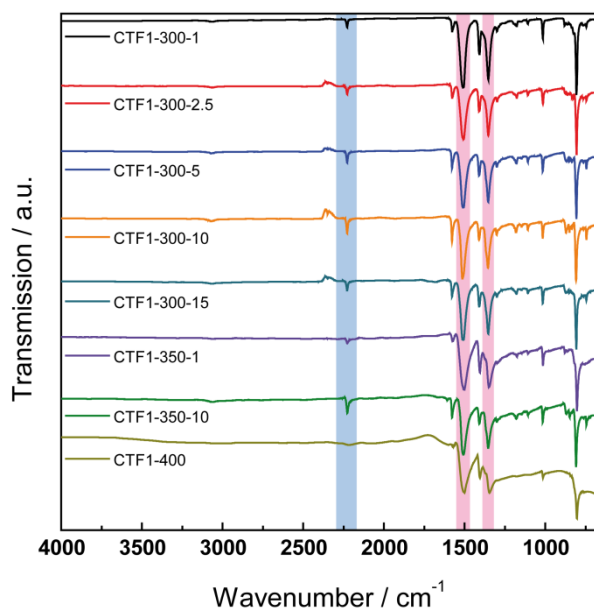


Figure 5.1.2. IR spectra of the CTFs synthesized at 300 °C, 350 °C, and 400 °C (top to bottom). The characteristic bands for nitrile are marked in blue, those for triazine in pink.

The results obtained by IR spectroscopy were further supported by ^{13}C and ^{15}N ssNMR measurements. The ^{13}C MAS ssNMR spectra of CTF1-300-1, CTF1-300-10 and CTF1-400 (Figure 5.1.3) show strong signals at 169, 138, 130 and 115 ppm. The former one can be attributed to the triazine ring carbon atoms,^[21] while the signals at 138 and 130 ppm correspond to the benzyl ring. The signal

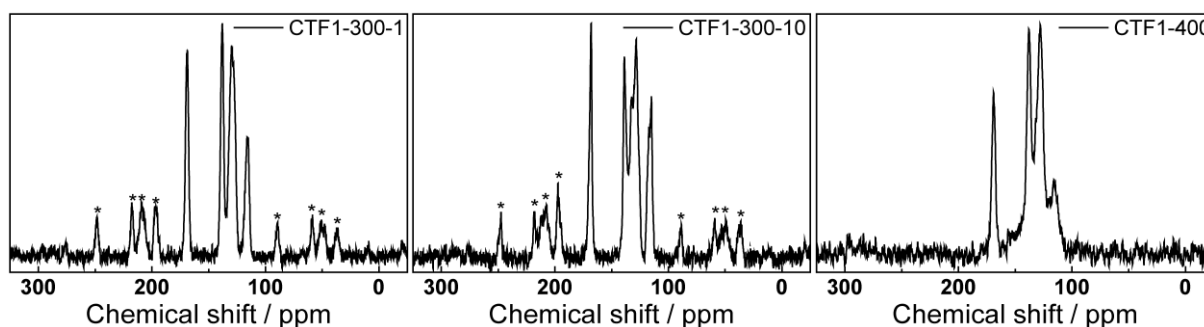


Figure 5.1.3. ^{13}C MAS ssNMR spectra of CTF1-300-1 (left, contact time 5 ms, spinning speed 10 kHz), CTF1-300-10 (middle, contact time 5 ms, spinning speed 10 kHz) and CTF1-400 (right, contact time 5 ms, spinning speed 20 kHz). Asterisks mark rotational side bands.

at 115 ppm, which is significantly weaker in CTF1-400, indicates residual nitrile groups in the materials. Note that the signals at 130 and 115 ppm are split into two signals in CTF1-300-10, indicating small differences in the chemical environment of the assigned carbon atoms.

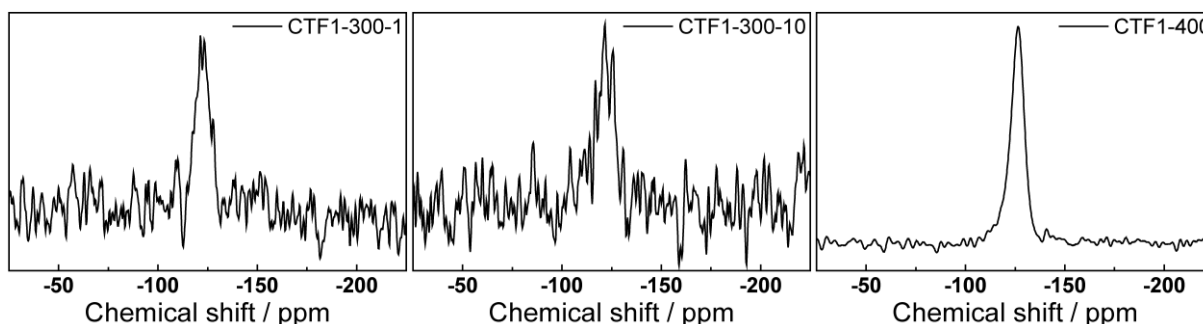


Figure 5.1.4. ^{15}N MAS ssNMR spectra of CTF1-300-1 (left, contact time 5 ms, spinning speed 10 kHz), CTF1-300-10 (middle, contact time 5 ms, spinning speed 10 kHz) and CTF1-400 (right). The CTF1-400 spectrum was provided by the group of Jürgen Senker, University of Bayreuth.

Figure 5.1.4 shows the ^{15}N MAS ssNMR spectra of CTF1-300-1, CTF1-300-10 and CTF1-400, where only one signal is found around -125 ppm, which can be clearly assigned to the triazine unit.^[22] In conclusion, the results from IR and ssNMR spectroscopy strongly indicate the successful formation of triazine rings while the benzyl rings are maintained, although residues of nitrile groups are found in all samples.

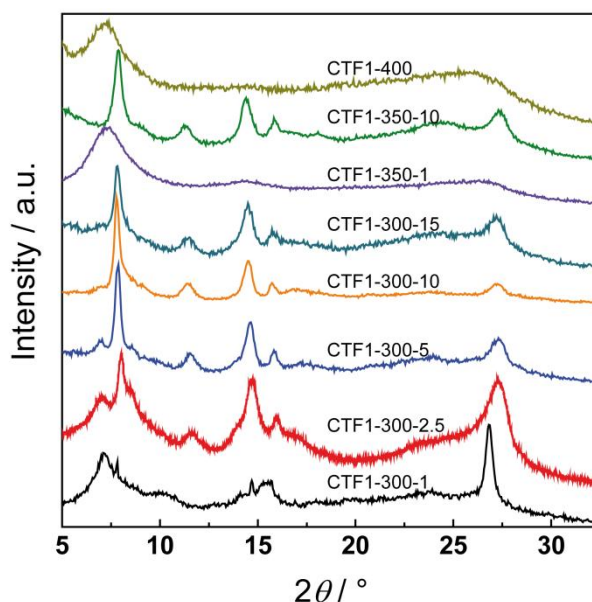


Figure 5.1.5. Powder X-ray diffractograms of the CTFs synthesized at 300 °C, 350 °C, and 400 °C (bottom to top).

We tested the crystallinity of our materials by powder XRD measurements and compared the results with CTF1-400 (Figure 5.1.5). The diffraction patterns of CTF1-300-1, CTF1-350-1 and CTF1-400 are comparable to the one of CTF1 from the original publication^[16] showing reflections around 7, 15.5 and 27° 2θ , although the ones found for our materials are of lower intensities. Interestingly, the

diffraction pattern of CTF1-300-1 shows additional reflections at 7.8 and 14.7° 2 θ , which could not be assigned to the precursor or any known compound. The materials synthesized with zinc chloride ratios above 1:1 showed these two reflections at 7.8 and 14.7° 2 θ , as well as further reflections at 11.5, 15.8 and 27.3° 2 θ . The identity of the additional crystalline phases is not clear at this stage but can likely be related to the occurrence of CTF-oligomers rather than a completely condensed network.

Table 5.1.2. Elemental analysis and BET surface areas of the presented CTFs.

Sample	N [wt%]	C [wt%]	H [wt%]	C/N	BET SA ^a [m ² g ⁻¹]
Theory	21.86	74.99	3.15	3.34	
CTF1-300-1	21.61	74.30	3.29	3.44	66
CTF1-300-2.5	21.38	73.53	3.23	3.44	12
CTF1-300-5	21.57	74.25	3.28	3.44	19
CTF1-300-10	21.69	74.45	3.32	3.43	24
CTF1-300-15	20.99	72.75	3.48	3.47	21
CTF1-350-1	21.13	73.59	3.34	3.48	10
CTF1-350-10	20.39	72.93	3.15	3.58	6
CTF1-400	18.60	70.20	3.30	3.77	610

^aFrom argon physisorption measurements.

Elemental analysis can give detailed information about the composition of the materials. The results are presented in Table 5.1.2 and reveal values very close to the theoretical ones, which is in sharp contrast to the results found by the Antonietti group.^[16] Since the precursor of the synthesis has the same molecular weight as CTF1, no assumption on the extent of trimerization and thus amount of reacted nitrile groups can be made based on elemental analysis alone, but the results nicely demonstrate that no decomposition of the molecules occurred during synthesis.

Argon sorption measurements were done to obtain information on the porosity of the materials. The BET surface areas (SA) are listed in Table 5.1.2 and show significantly lower values in the range 6-66 m² g⁻¹ for the CTFs synthesized below 400 °C. This means that either no distinct and continuous 1D pore system is formed, or pore blocking occurs.

UV-Vis spectra were recorded in order to evaluate the light absorption characteristics of the materials (Figure 5.1.6). When comparing the samples synthesized at different temperatures a strong absorption is observed for CTF1-300-1 in the UV region (340 nm), with a sharp absorption edge around 370 nm, as well as a weak and broad absorption between 380-600 nm. The materials synthesized at 350 and 400 °C show a broad absorption in the whole visible light region, which is not unexpected due to the black colors of these materials. When comparing the UV-Vis spectra of the CTF1-300 samples synthesized with increasing zinc chloride concentrations (Figure 5.1.6, right) a second absorption band around 410 nm becomes prominent with a broad absorption up to 800 nm. We compared the results of the UV-Vis measurements with the calculations done by Butchosa *et al.*, who calculated several molecular clusters based on dendrimers or rings of CTF1 to distinguish the

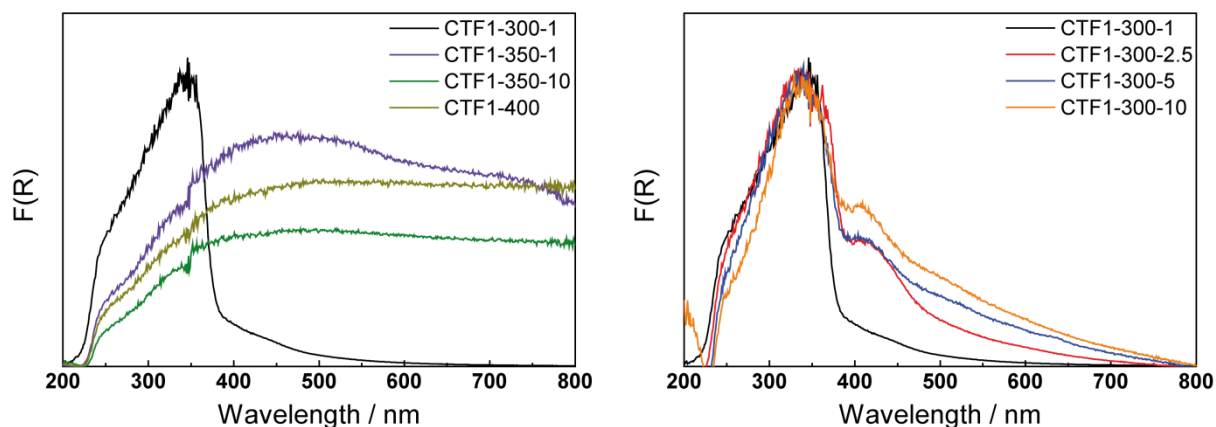


Figure 5.1.6. UV-Vis spectra of CTF1-300-1, CTF1-350-1, CTF1-350-10 and CTF1-400 (left) and of CTF1-300-1, CTF1-300-2.5, CTF1-300-5 and CTF1-300-10 (right).

photoactive parts in the structure.^[12] From their calculations four model clusters are consistent with representative parts of CTF1-300-1 (Figure 5.1.7). The dendrimer clusters shown in Figure 5.1.7 exhibit a strong UV band around 325 nm and a weaker band between 270-290 nm, while the ring cluster shows a strong band around 315 nm and a weaker one around 300 nm. In comparison, for CTF1-300-1 a strong band at 340 nm and a significant shoulder around 260 nm is observed, which fits

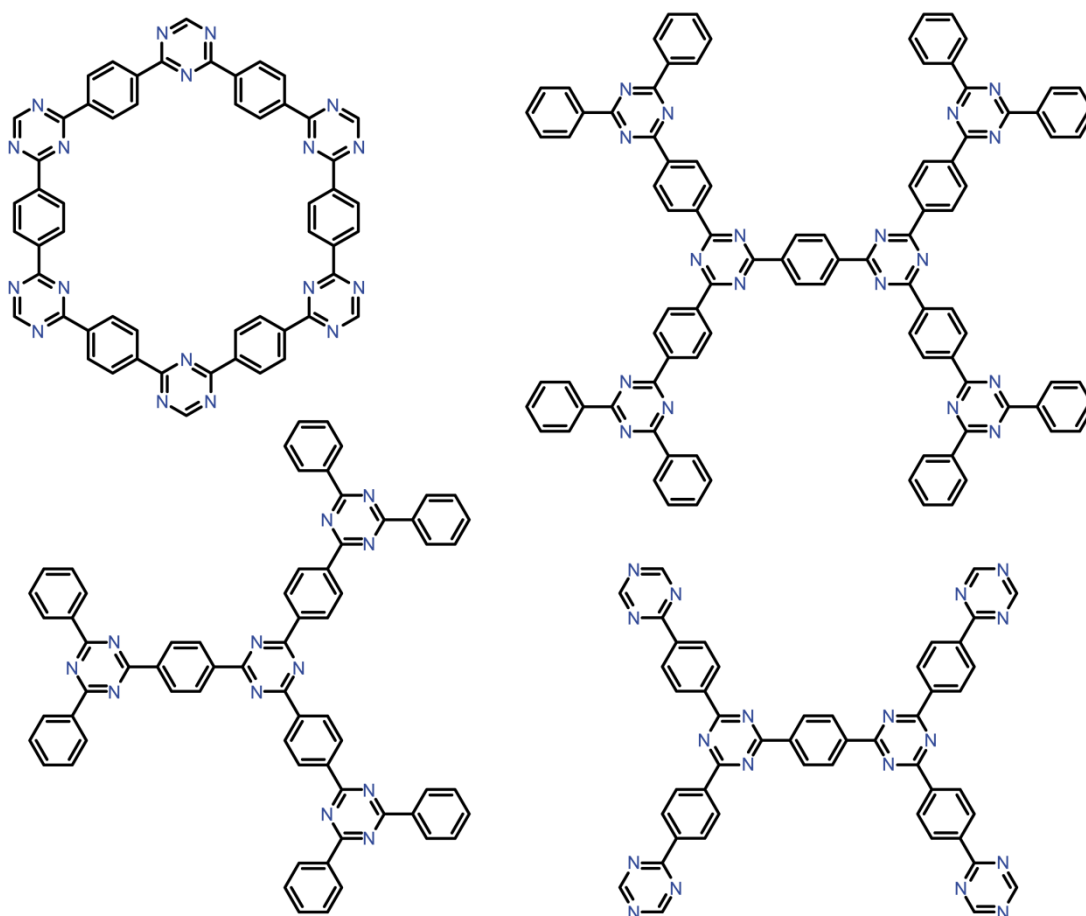


Figure 5.1.7. Ring (left top) and dendrimer clusters for the calculation of UV-Vis spectra for CTF1, according to Ref. [12].

especially well with the dendrimers. Molecular clusters with lower numbers of triazine and benzyl rings did not fit our experimental results, while clusters with higher numbers of rings were not studied. Additionally, no cluster was presented that exhibited absorption in the visible light region. Further, Butchosa *et al.* calculated the influence of stacking of the molecules on the UV-Vis spectra.^[12] They observed a blue shift of the main band and the appearance of new bands in the 320-400 nm spectral range. The positions of the blue- and red-shifted bands were found to shift further with the number of layers stacked, but converged quickly after a few layers. However, the intensity ratio of the red-shifted to the blue-shifted peaks appeared to grow with every layer added. Comparing these results with the UV-Vis spectra in Figure 5.1.6 (right), we may infer that the band above 380 nm results from π -stacking interactions between the 2D CTF layers, where CTFs synthesized with higher zinc chloride concentrations have a larger number of interacting layers in comparison to CTF1-300-1, although in this case no blue-shift of the main peak is observed.

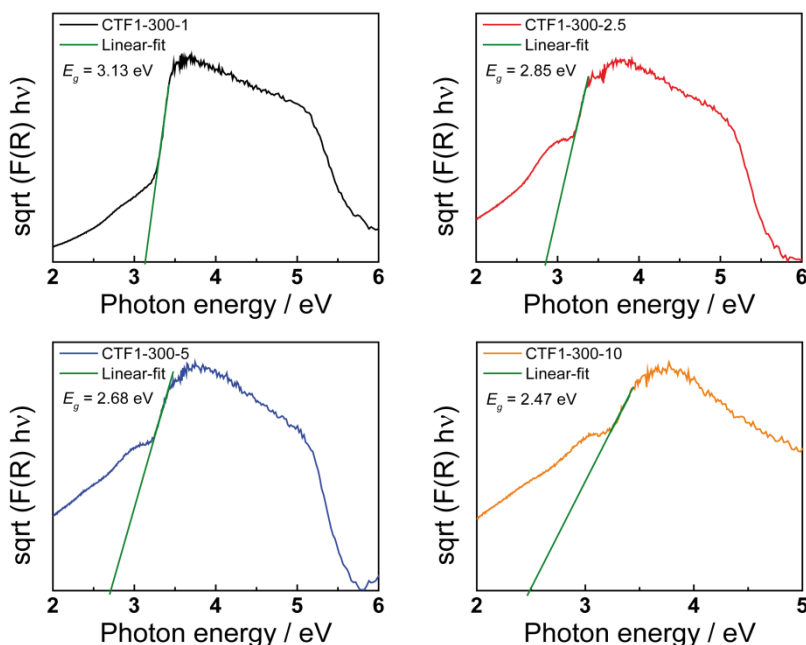


Figure 5.1.8. Linear Tauc-plots and extraction of the optical band gaps of CTF1-300-1, CTF1-300-2.5, CTF1-300-5 and CTF1-300-10.

The UV-Vis spectra from Figure 5.1.6 allow calculating the band gaps (E_g) for the CTF1-300 materials with the help of Tauc-plots (Figure 5.1.8).^[23] To this end, the wavelength values ν were translated to photon energies by the multiplication with the Planck's constant h , and the values of the square root of $F(R) \cdot h \cdot \nu$ where plotted against these photon energies. Applying a linear fit to the absorption edge allows extrapolating E_g by solving the linear equation at $(F(R) \cdot h \cdot \nu)^{1/2} = 0$. Band calculations for CTF1-350-1, CTF1-350-10 and CTF1-400 were not possible, since no absorption edge was observed. The calculated band gaps show decreasing values with increasing zinc chloride concentrations ($E_g(\text{CTF1-300-1}) = 3.13$ eV, $E_g(\text{CTF1-300-2.5}) = 2.85$ eV, $E_g(\text{CTF1-300-5}) = 2.68$ eV, $E_g(\text{CTF1-300-10}) =$

2.47 eV). Note that the linear fitting can lead to different results depending on the chosen range, thus rendering the obtained results only rough estimates.

Light-driven hydrogen generation

As mentioned in the introduction, a significantly increase of hydrogen production in some organic semiconductors is correlated with the incorporation of triazine units.^[6-7,9-10] This, the high chemical and thermal stabilities of CTFs, as well as the calculated band gaps from the previous section should make the presented materials suitable candidates for light-driven photocatalysis in general, and water-splitting in particular. The results of the measurements are shown in Figure 5.1.9 and 5.1.10 and in Table 5.1.3. First investigations were done on CTF1-300-1 by irradiating (at >250 nm) the sample with TEoA as electron donor and H₂PtCl₆ as co-catalyst and with as well as without a pH7 buffer, revealing continuous hydrogen production for tenths of hours (Figure 5.1.9, left). The setup with buffer showed to be significantly more active and did not show decreasing activity in contrast to the setup without buffer. Therefore, in all future measurements the photocatalysis experiments were done in buffered solution. Next, hydrogen production of samples synthesized at different temperatures and zinc chloride concentrations were monitored, where CTF1-300-10 was found to generate almost three times more hydrogen per hour than CTF1-300-1 (Figure 5.1.9, middle). Additionally, the materials synthesized at 350 °C showed almost no hydrogen production, which was expected from the UV-Vis results, since the band gaps in these materials are likely too low or absent due to carbonization of the samples at higher synthesis temperatures.

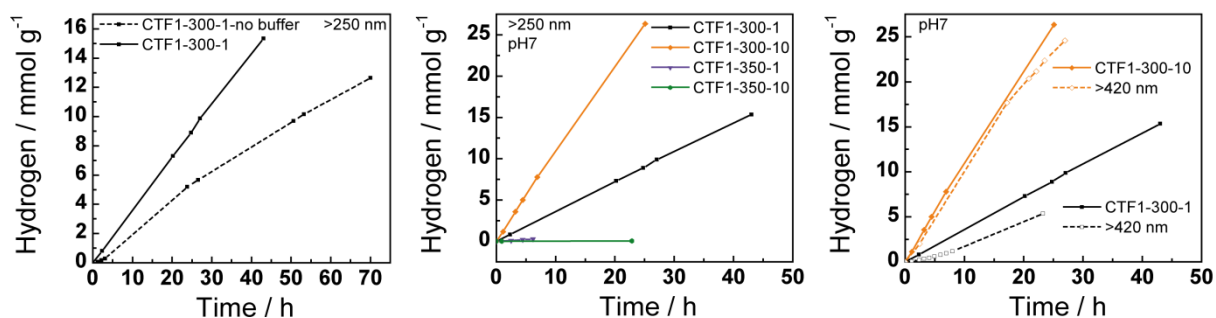


Figure 5.1.9. Hydrogen evolution of CTF1-300-1 with and without pH7 buffer at irradiation >250 nm (left), of CTF1-300-1, CTF1-300-10, CTF1-350-1 and CTF1-350-10 with pH7 buffer at irradiation >250 nm (middle) and of CTF1-300-1 and CTF1-300-10 with pH7 buffer at >250 nm or >420 nm irradiation, respectively (right). All measurements were performed with 10 vol% TEoA and 8 wt% H₂PtCl₆.

Since photocatalytic hydrogen generation is more efficient in the visible light region compared to the UV region due to the shape of the solar intensity spectrum,^[1,3] we tested the promising materials CTF1-300-1 and CTF1-300-10 at an irradiation above 420 nm (Figure 5.1.9, right). As can be seen, CTF1-300-1 irradiated above 420 nm exhibits less than half of the hydrogen production found for irradiation at the full spectrum. More promising results were found for CTF1-300-10, which showed almost the same amount of generated hydrogen in the visible light range compared to the full

spectrum tests. This suggests that the low energy absorption band in the UV-Vis spectra is mainly responsible for the hydrogen production. For more detailed information we will proceed with wavelength specific measurements, which will reveal at what wavelength the highest hydrogen production rates are observed. Note that the small kink in the hydrogen time evolution of CTF1-300-10 (> 420 nm) is probably an artifact, since longer measurements show the same production rates. Additionally, another measurement carried out under the same conditions (see Figure 5.1.10, right) shows even increasing rates of hydrogen generation.

Table 5.1.3. Photocatalytic properties of the presented CTFs with pH7 buffer, 10 vol% TEOA and 8 wt% H₂PtCl₆ unless indicated otherwise.

Sample	Irradiation wavelength [nm]	H ₂ generation [mmol h ⁻¹ g ⁻¹]	Comment
CTF1-300-1	250	0.20	without buffer
CTF1-300-1	250	0.36	
CTF1-300-1	420	0.13	
CTF1-300-1	420	0.03	without Pt
CTF1-300-1	420	0.001	without Pt and TEOA
CTF1-300-2.5	420	0.62	
CTF1-300-5	420	0.31	
CTF1-300-10	250	1.08	
CTF1-300-10	420	0.91	
CTF1-300-10	420	0.002	MeOH instead of TEOA
CTF1-300-15	420	0.92	
CTF1-350-1	250	0.04	
CTF1-350-10	250	0.002	
Pt/TEoA	250	0.005	

In cycling experiments CTF1-300-10 was irradiated at >420 nm for 3 h for each cycle. After each cycle the reactor was evacuated and purged with argon and irradiation was restarted. The results did not reveal a decrease, but even an increase of the photocatalytic activity (Figure 5.1.10, middle). A reason could be the exfoliation of the materials, thus increasing the surface area and therefore the photocatalytic activity, which has been shown before in other systems.^[9-10] To prove that the CTF1 materials are active parts in the observed photocatalytic processes and that the process is indeed photo-induced, we compared the results with four blank tests: 1. CTF in pH7 buffer with TEOA and without H₂PtCl₆, 2. CTF in pH7 buffer without TEOA and H₂PtCl₆, 3. pH7 buffer with TEOA, H₂PtCl₆ and without CTF and 4. CTF in pH7 buffer with TEOA and H₂PtCl₆, but without light irradiation (Figure 5.1.10, left). For the latter one no hydrogen production was observed, proving that light is necessary to account for the observed activity. Further, CTF1-300-1 catalyzes the hydrogen production even without H₂PtCl₆ for several hours with small signs for attenuation (0.03 mmol h⁻¹ g⁻¹), while without TEOA marginal activity was found (0.001 mmol h⁻¹ g⁻¹), which underlines the importance of an electron donor in the system. Photocatalytic experiments on TEOA

with H_2PtCl_6 and no CTF1-300-1 exhibited almost no hydrogen production ($0.005 \text{ mmol h}^{-1} \text{ g}^{-1}$), proving that CTF1 is crucial for the process.

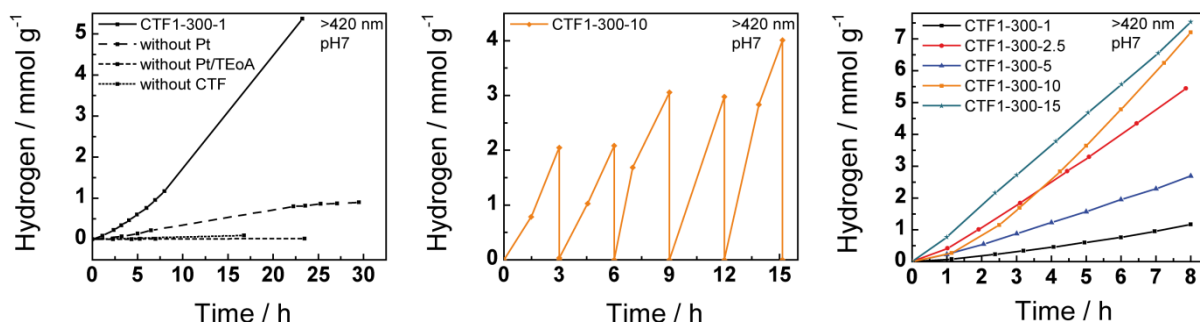


Figure 5.1.10. (Left) Hydrogen evolution of CTF1-300-1 with H_2PtCl_6 and TEOA (straight line), with TEOA and without H_2PtCl_6 (dashes), without H_2PtCl_6 and TEOA (short dashes), and of H_2PtCl_6 with TEOA and without CTF1-300-1 (dots). (Middle) Cycling of CTF1-300-10 in 3 h intervals. After each interval the reactor was evacuated and purged with argon. (Right) Hydrogen evolution of CTF1-300-1, CTF1-300-2.5, CTF1-300-5, CTF1-300-10 and CTF1-300-15. All measurements were performed with pH7 buffer and irradiation at $>420 \text{ nm}$.

Since CTF1-300-10 was found to be more active in catalysis than CTF1-300-1, we tested a series with varying zinc chloride concentrations as can be seen in Figure 5.1.10 (right). These experiments revealed a trend showing increasing hydrogen production with increasing amounts of zinc chloride used in the synthesis, with the exception of CTF1-300-2.5. The higher activities of the materials synthesized with higher amounts of zinc chloride could result from a higher number of oligomers which we expect in these materials. In comparison to the XRD measurements, the materials with the highest activities show only the new crystalline phase and no sign of the CTF1 phase found by the group of Antonietti.

The efficiency of photocatalytic hydrogen production can be evaluated by measuring the amount of hydrogen produced within a certain time. Nevertheless, different set-ups of the measurements, such as the used light sources (xenon or mercury lamp), the irradiation type (inner or top irradiation) and the size of the measurement cell may give different results for the same photocatalyst.^[1] This makes

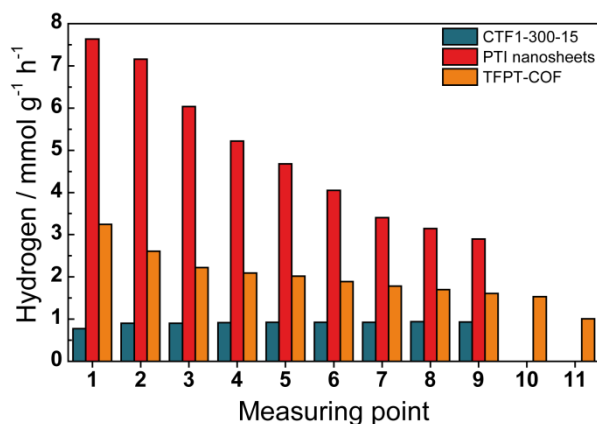


Figure 5.1.11. Hydrogen production rates of CTF1-300-15, PTI nanosheets^[10] and TFPT-COF^[9] at different measurement points within a 22 h measurement.

it difficult to compare results from different groups. Therefore, we here compare CTF1 with two other materials measured with our set-up under the same conditions, namely TFPT-COF and PTI nanosheets.^[9-10] Figure 5.1.11 shows the hydrogen production rates of CTF1-300-15, PTI nanosheets and TFPT-COF at different measurement points within a 22 h measurement. Although CTF1-300-15 was found to have lower hydrogen production rates than TFPT-COF and PTI nanosheets, the latter materials exhibit decreasing rates with increasing measurement time while CTF1 shows stable hydrogen production, indicating a better long-time stability of this material.

5.1.4 CONCLUSION AND OUTLOOK

The foregoing discussion shows the successful synthesis of CTF1 at temperatures below 400 °C, by prolonging the synthesis times up to 168 h. The materials synthesized with different amounts of zinc chloride revealed two different crystalline phases: While the known CTF1 phase was found to be present in CTF1-300-1 and CTF1-350-1, the other materials were mainly composed of the new, as yet unidentified phase. Since elemental analysis, IR and ssNMR measurements of the latter suggest the presence of intact polymeric structures and triazine units along with remaining nitrile units, we suggest the formation of oligomeric species at the rather low reaction temperatures. Further investigations, including mass spectrometry and quantitative ssNMR measurements, as well as structural modelling are expected to give more insights into the structure of these materials.

The photocatalytic activities towards water splitting were investigated and showed significant amounts of hydrogen evolution in the visible light region. The hydrogen production did not decrease even after several hours, thus highlighting the pronounced stability of the materials under the conditions chosen. To demonstrate complete water splitting with this material, including oxygen evolution, further experiments are necessary and currently ongoing.

5.1.5 REFERENCES

- [1] X. Chen, S. Shen, L. Guo, S. S. Mao, *Chem. Rev.* **2010**, *110*, 6503-6570.
- [2] A. Fujishima, K. Honda, *Nature* **1972**, *238*, 37-38.
- [3] H. Tong, S. Ouyang, Y. Bi, N. Umezawa, M. Oshikiri, J. Ye, *Adv. Mater.* **2012**, *24*, 229-251.
- [4] S. Yanagida, A. Kabumoto, K. Mizumoto, C. Pac, K. Yoshino, *J. Chem. Soc., Chem. Commun.* **1985**, 474-475.
- [5] T.-F. Yeh, J.-M. Syu, C. Cheng, T.-H. Chang, H. Teng, *Adv. Funct. Mater.* **2010**, *20*, 2255-2262.
- [6] Y. Ham, K. Maeda, D. Cha, K. Takanabe, K. Domen, *Chem. Asian J.* **2013**, *8*, 218-224.
- [7] K. Schwinghammer, B. Tuffy, M. B. Mesch, E. Wirnhier, C. Martineau, F. Taulelle, W. Schnick, J. Senker, B. V. Lotsch, *Angew. Chem. Int. Ed.* **2013**, *52*, 2435-2439.

- [8] X. Wang, K. Maeda, A. Thomas, K. Takanabe, G. Xin, J. M. Carlsson, K. Domen, M. Antonietti, *Nat. Mater.* **2009**, *8*, 76-80.
- [9] L. Stegbauer, K. Schwinghammer, B. V. Lotsch, *Chem. Sci.* **2014**, DOI: 10.1039/C4SC00016A.
- [10] K. Schwinghammer, M. B. Mesch, V. Duppel, C. Ziegler, J. Senker, B. V. Lotsch, *J. Am. Chem. Soc.* **2014**, *136*, 1730-1733.
- [11] S. Ren, M. J. Bojdys, R. Dawson, A. Laybourn, Y. Z. Khimyak, D. J. Adams, A. I. Cooper, *Adv. Mater.* **2012**, *24*, 2357-2361.
- [12] C. Butchosa, T. O. McDonald, A. I. Cooper, D. J. Adams, M. A. Zwijnenburg, *J. Phys. Chem. C* **2014**, *118*, 4314-4324.
- [13] M. R. Hoffmann, S. T. Martin, W. Choi, D. W. Bahnemann, *Chem. Rev.* **1995**, *95*, 69-96.
- [14] J. A. Turner, *Science* **1999**, *285*, 687-689.
- [15] J. Yang, D. Wang, H. Han, C. Li, *Acc. Chem. Res.* **2013**, *46*, 1900-1909.
- [16] P. Kuhn, M. Antonietti, A. Thomas, *Angew. Chem. Int. Ed.* **2008**, *47*, 3450-3453.
- [17] M. J. Bojdys, J. Jeromenok, A. Thomas, M. Antonietti, *Adv. Mater.* **2010**, *22*, 2202-2205.
- [18] V. G. Manecke, D. Wöhrle, *Makromol. Chem.* **1968**, *120*, 176-191.
- [19] P. Kuhn, A. Thomas, M. Antonietti, *Macromolecules* **2009**, *42*, 319-326.
- [20] M. R. Liebl, J. Senker, *Chem. Mater.* **2013**, *25*, 970-980.
- [21] B. Jürgens, E. Irran, J. Senker, P. Kroll, H. Müller, W. Schnick, *J. Am. Chem. Soc.* **2003**, *125*, 10288-10300.
- [22] S. Hug, M. E. Tauchert, S. Li, U. E. Pachmayr, B. V. Lotsch, *J. Mater. Chem.* **2012**, *22*, 13956-13964.
- [23] J. Tauc, R. Grigorovici, A. Vancu, *Phys. Status Solidi B* **1966**, *15*, 627-637.

5.2 COVALENT TRIAZINE FRAMEWORKS AS BIPOLAR ELECTRODE MATERIALS IN ENERGY STORAGE DEVICES

Kimberly See,^[1] Stephan Hug, Bettina V. Lotsch and Ram Seshadri^[1]

5.2.1 INTRODUCTION

Lithium-ion batteries are found today in almost every new electronic portable device because of its light weight and therefore high energy density. The current technology is dominated by cathode materials based on transition metals, such as LiCoO_2 , LiMn_2O_4 , LiFePO_4 and $\text{LiMn}_{1/3}\text{Li}_{1/3}\text{Co}_{1/3}\text{O}_2$, while the anode is usually composed of graphite and the electrolyte LiPF_6 in a carbonate solvent.^[2] Since the production and recycling of such batteries is accompanied by high carbon dioxide emissions and resources for lithium are running short, making their mining even more energy intensive, the search for alternative cathode materials is crucial.^[3-4] To target this aim, emerging research lines are focusing on redox active polymer materials based on carbonyls, thioethers, disulfides and nitroxides, which are low-cost and abundant.^[4] Recently, Sakaushi *et al.* presented a Li- and Na-ion battery using amorphous CTF1 as bipolar electrode.^[5-7] It was hypothesized that the triazine units act as redox centers, thus advancing the performance of the otherwise carbon-based material. In contrast, the group of Zhi proposed that structural changes of the CTF1 materials synthesized at different temperatures or zinc chloride ratios, especially cross-linking between the sheets and formation of mesopores in the system, is responsible for lower resistance and higher specific capacitance.^[8] Notably, Sakaushi *et al.* proposed a redox-type energy storage principle while Zhi and co-workers suggested capacitive storage to be dominating. Here we present the use of CTF1 and *bipy*-CTF synthesized at 400-600 °C as electrodes in Li-ion batteries and compared the results with the work by Sakaushi *et al.*^[7] and Hao *et al.*^[8] revealing that the structural changes and concomitant high surface areas are responsible for the observed performance of the electrodes, rather than the presence of triazine units.

5.2.2 EXPERIMENTAL

Methods

Argon adsorption/desorption measurements were performed at 87 K with an Autosorb-iQ surface analyzer (Quantachrome Instruments, USA). Samples were outgassed in vacuum at 150 °C for 6-12 h to remove all guests. For BET calculations pressure ranges of the Ar isotherms were chosen with the help of the BET Assistant in the ASiQwin software. In accordance with the ISO recommendations

multipoint BET tags equal or below the maximum in $V \cdot (1 - P/P_0)$ were chosen. The BET fits are shown in Chapter 8.1.3.

Infrared (IR) spectroscopy measurements were carried out on a Perkin Elmer Spektrum BX II (Perkin Elmer, USA) with an attenuated total reflectance unit.

Powder X-ray diffraction (XRD) was measured on a BRUKER D8 Avance diffractometer (Bruker AXS, USA) in Bragg-Brentano geometry.

Elemental analysis (EA) was carried out with an Elementar vario EL (Elementar Analysensysteme, Germany).

Electrochemical experiments were performed in loose powder Swagelok® cells with a Li metal anode, 1 M LiPF₆ in ethylene carbonate/dimethyl carbonate (EC/DMC) electrolyte and a glass filter dryer (GFD) separator. Composite powders were prepared by hand grinding the CTF materials with Super P® carbon additive at a 1:1 ratio. The powders were then dried under vacuum overnight at 70 °C. All cells were prepared in an argon glove box. Galvanostatic cycling experiments were done on a Bio-Logic Variable Multichannel Potentiostat at room temperature. All electrochemical experiments were performed by Kimberly See from the group of Prof. Ram Seshadri (University of California, Santa Barbara, USA).

Materials

The covalent triazine frameworks CTF1-400-1, CTF1-500, CTF1-600 and *bipy*-CTF500 were synthesized as described in Chapter 4.2, and CTF1-400-10 and *bipy*-CTF400 were likewise synthesized in the same fashion.

5.2.3 RESULTS AND DISCUSSION

Synthesis and characterization

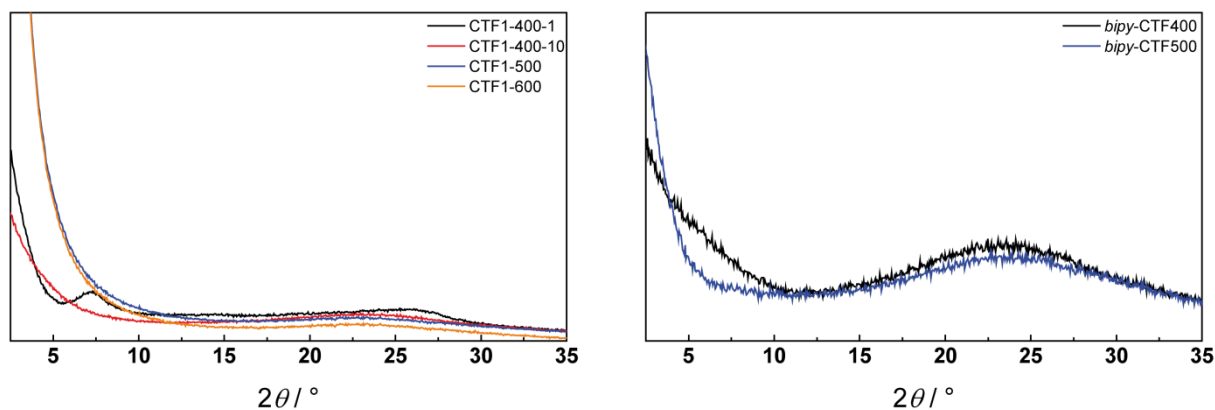
The syntheses of the CTFs were performed according to the original synthesis from Antonietti and co-workers in a zinc chloride melt, which acts as Lewis acidic trimerization catalyst, at 400-600 °C (see Table 5.2.1).^[9] The materials CTF1-400-1 and CTF1-400-10 are analogues of crystalline CTF-1 and amorphous CTF-1 (ACTF-1), respectively, and were synthesized as described by Sakaushi *et al.*^[7] We investigated the crystallinity and local structure of the CTFs by XRD, IR, EA and physisorption measurements.

The XRD patterns are shown in Figure 5.2.1 and reveal that only CTF1-400-1 shows moderate crystallinity, which is in accordance with literature findings.^[7,9] IR spectroscopy gives more insights into the local structure and composition of the materials as can be seen in Figure 5.2.2. CTF1-400-1 and *bipy*-CTF400 show distinct bands corresponding to the triazine units at ≈ 1500 and ≈ 1350 cm⁻¹, while the other CTFs exhibit broad, rather undefined bands. As the broadening of the bands in the

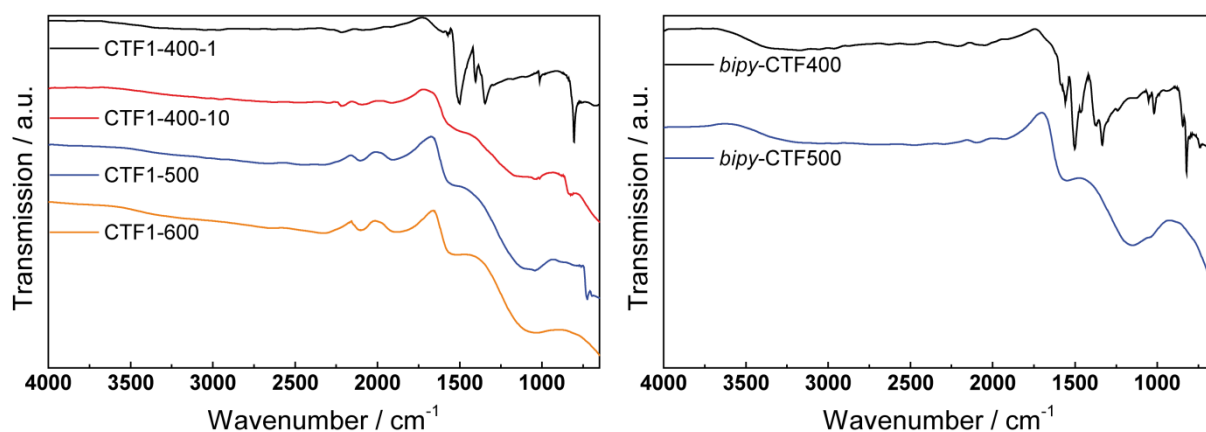
Table 5.2.1. Synthesis conditions used in the synthesis of the different CTF1 and *bipy*-CTF materials.

Sample	Eq. ZnCl ₂	Synthesis Temperature [°C]	Synthesis Time ^a [h]
CTF1-400-1 ^b	1	400	48
CTF1-400-10	10	400	48
CTF1-500 ^b	5	500	48
CTF1-600 ^b	5	600	48
<i>bipy</i> -CTF-400	5	400	48
<i>bipy</i> -CTF-500 ^b	5	500	48

^aHeating in 60 °C h⁻¹ steps and cooling in 10 °C h⁻¹ steps. ^bAdapted from Chapter 4.2.

**Figure 5.2.1.** XRD patterns of the different CTF1 (left) and *bipy*-CTF (right) materials.

materials synthesized at higher temperatures is assigned to the degradation of the materials,^[10-12] the broad bands in CTF1-400-10 probably result from amorphization due to the higher zinc chloride concentrations, which was also found by Kuhn *et al.*^[9] and Sakaushi *et al.*^[7] The observed absence of triazine units in this material, which has been found to be most active in the work by Sakaushi *et al.*, raises doubts as to the theory that triazine units are primarily responsible for the good performances of the batteries.^[5-7]

**Figure 5.2.2.** IR spectra of the different CTF1 (left) and *bipy*-CTF (right) materials.

The elemental composition as measured by elemental analysis can provide important information on the composition and stoichiometry of the materials. The results in Table 5.2.2 reveal a trend of decreasing nitrogen content with increasing synthesis temperature and zinc chloride concentrations.

This supports the findings from the IR measurements, showing degradation of the systems through a loss of nitrogen functionalities at higher temperatures as well as with increasing salt content.

Table 5.2.2. Elemental analysis and BET surface areas of the produced CTF1s and *bipy*-CTFs.

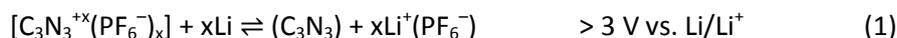
Sample	N [wt%]	C [wt%]	H [wt%]	C/N	BET SA ^a [m ² g ⁻¹]
CTF1 theory	21.86	74.99	3.15	3.43	
CTF1-400-1 ^b	18.60	70.20	3.30	3.77	610
CTF1-400-10	14.63	70.34	3.62	4.81	496
CTF1-500 ^b	12.39	76.45	2.06	6.17	1830
CTF1-600 ^b	10.37	79.16	1.34	7.63	2557
<i>bipy</i> -CTF theory	27.17	69.90	2.93	2.57	
<i>bipy</i> -CTF-400	20.42	58.85	4.08	2.88	590
<i>bipy</i> -CTF-500 ^b	16.42	63.14	2.67	3.85	1680

^aFrom argon physisorption measurements. ^bAdapted from Chapter 4.2.

Further, we investigated the surface areas (SAs) of the CTFs by argon physisorption experiments. The BET SAs shown in Table 5.2.2 reveal increasing SAs with increasing synthesis temperatures. This finding was previously attributed to a “foaming” of the network, which increases the amount of mesopores by leaving the micropore volumes intact.^[10,12]

Electrochemical properties

Sakaushi *et al.* proposed that the triazine units of CTFs are reduced and oxidized in the electrochemical reaction involved in the cyclic voltammetry measurements, which is contradictory to their findings that the material with a higher degree of order and apparently more intact triazine units (crystalline CTF1) is less active than amorphous CTF1.^[7] Depending on the applied potential, it is assumed that the triazine units are either *p*-doped (charge compensated by the PF₆⁻ anion, Equation 1) or *n*-doped (charge compensated by Li⁺ cations, Equation 2), giving rise to a linear bipolar charge storage mechanism which takes advantage of both the reducibility and oxidizability of the triazine ring:



The group of Zhi, on the other hand, compared CTF1 synthesized at temperatures between 400–700 °C and proposed a supercapacitive energy storage of the materials.^[8] The materials described in that work exhibit increasing specific capacitance for the CTFs with increasing synthesis temperatures up to 550 °C, and decreasing storage capacities with further increase in the synthesis temperatures. These findings were attributed to different structural and chemical changes in the materials when synthesized at higher temperatures: Increasing SAs, increasing amount and sizes of mesopores, decreasing nitrogen contents and decreasing resistances. The increasing SAs and decreasing resistances are beneficial in terms of the electrochemical performance, while the decreasing amount

of nitrogen is detrimental. The increasing amount and sizes of mesopores may be beneficial to some extent, but negatively effects the storage capacities when the pore sizes become too large.

Based on these rather controversial interpretations, we reproduced these measurements and compared them to the results obtained for CTF1s synthesized at higher temperatures as well as *bipy*-CTFs. The energy storage characteristics of the materials were measured versus a lithium anode in 1 M LiPF_6 in EC/DMC between 1.5-4.5 V (versus Li/Li^+) at 0.1 A g^{-1} (Figure 5.2.3).

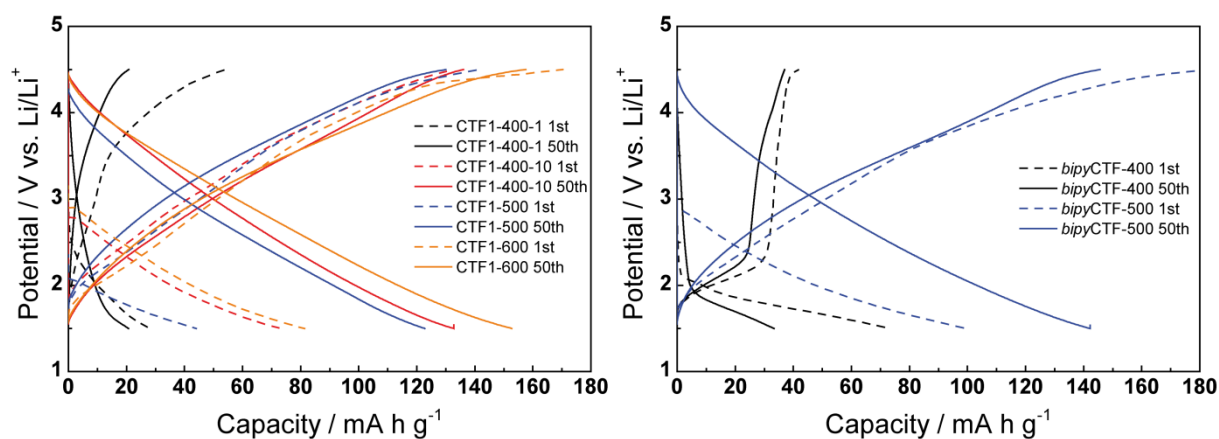


Figure 5.2.3. Charge-discharge profiles of the 1st (dashed line) and 50th (solid line) cycle of CTF1s (left) and *bipy*-CTFs (right) at a current density of 0.1 A g^{-1} .

The CTF1-400-1 electrode shows significantly lower specific capacities already at the first and after 50 cycles ($\approx 20 \text{ mA h g}^{-1}$) than the other CTF1s ($\approx 130\text{-}160 \text{ mA h g}^{-1}$), which is in accordance with previous results.^[7] Interestingly, CTF1-400-10 exhibits higher capacities ($\approx 135 \text{ mA h g}^{-1}$), although having less nitrogen content and lower BET SAs. The lower nitrogen content and the amorphous nature of CTF1-400-10 may suggest more highly condensed networks with more extensively cross-linked (*i.e.* 3D) structures and likely a higher degree of carbonization, giving rise to a lower resistance of the material. Additionally, CTF1-500 and CTF1-600 exhibit the highest capacities in spite of having less order and showing no sign of triazine units. Comparable results are found for the *bipy*-CTFs, where the *bipy*-CTF400 electrode shows low specific capacities of $\approx 40 \text{ mA h g}^{-1}$, while *bipy*-CTF500 exhibits $\approx 150 \text{ mA h g}^{-1}$. Therefore, we assume that the amount of triazine units are of marginal importance and the nitrogen rather generates a doping effect,^[13] while the structural changes such as crosslinking and a higher degree of carbonization give rise to the enhanced electrochemical properties, as postulated by Zhi and co-workers.^[8] The shapes of the charge-discharge profiles suggest capacitive storage for the materials, but further investigations by cyclic voltammetry are planned to exclude Faradaic processes involved in the storage principles.

The cycle performances of the CTFs were studied and revealed high stabilities and high Coulombic efficiencies of close to 100% over at least 100 cycles (Figure 5.2.4). The spikes in CTF1-500 and CTF1-600 are most likely artefacts due to temperature fluctuations in the laboratory, but will be further investigated to exclude other phenomena.

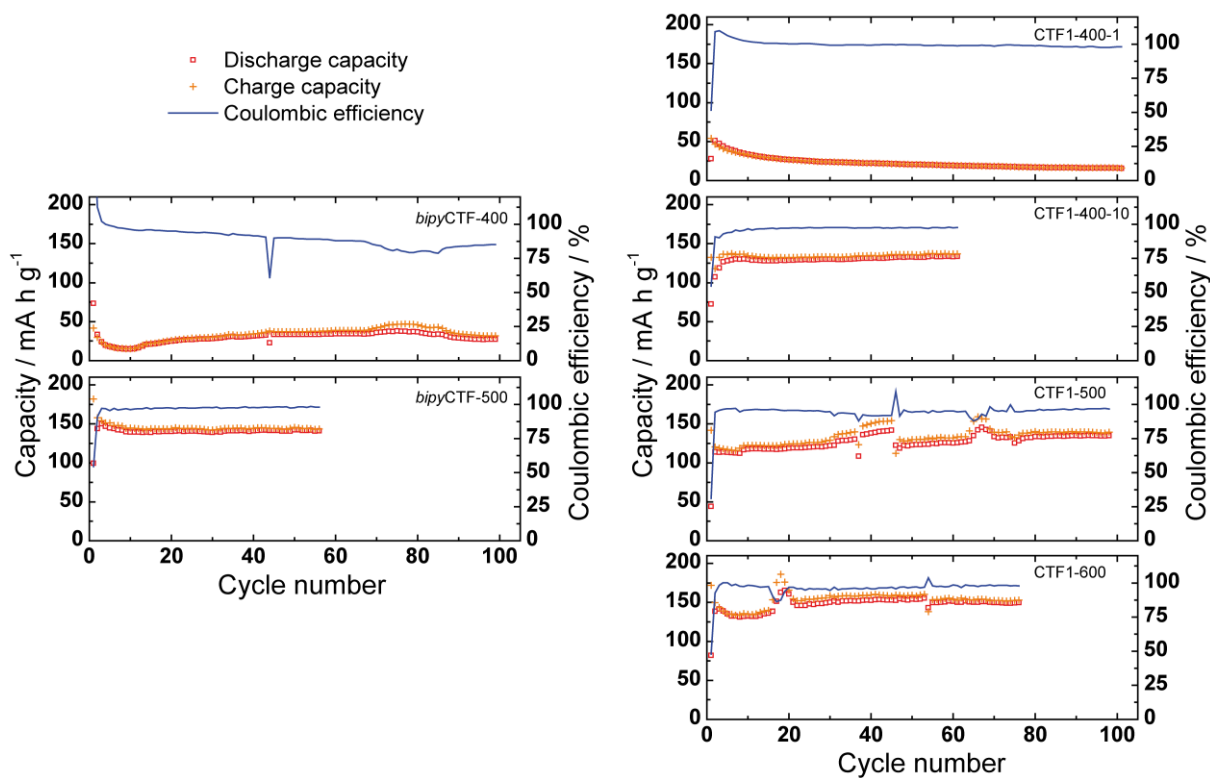


Figure 5.2.4. Cycle performances of CTF1s (right) and *bipy*-CTFs (left) at a current density of 0.1 A g^{-1} .

5.2.4 CONCLUSION AND OUTLOOK

In conclusion, we were able to successfully reproduce the results reported by Sakaushi *et al.* and we extended our studies to *bipy*-CTFs, revealing comparable specific capacities for *bipy*-CTF500. From our observations we conclude that CTFs synthesized at higher temperatures – having less nitrogen contents and higher SAs – exhibit enhanced performances, and we assume that the structural changes, such as higher SAs and transition from a 2D to a 3D structure through cross-linking give rise to the observed high specific capacities. In addition, we find an inverse correlation between the triazine content and the specific capacity, which suggests that the presence of nitrogen results in an *n*-type doping effect and a concomitant increase of the conductivity of the materials. The performance of *bipy*-CTF600 is currently tested in ongoing experiments and further electrochemical measurements are planned with the materials introduced in Chapters 4.1 and 4.2, which likewise show high SAs and/or high nitrogen contents. By creating a larger set of model systems, we aim to carve out clear trends depending on the structural features of the CTFs, such as nitrogen contents, specific SAs and pore size distribution.

5.2.5 REFERENCES

- [1] Department of Chemistry and Biochemistry, University of California, Santa Barbara, CA 93106, USA.

- [2] H. D. Yoo, E. Markevich, G. Salitra, D. Sharon, D. Aurbach, *Mater. Today* **2014**, *17*, 110-121.
- [3] H. Chen, M. Armand, G. Demailly, F. Dolhem, P. Poizot, J.-M. Tarascon, *ChemSusChem* **2008**, *1*, 348-355.
- [4] P. Poizot, F. Dolhem, *Energy Environ. Sci.* **2011**, *4*, 2003-2019.
- [5] K. Sakaushi, E. Hosono, G. Nickerl, T. Gemming, H. Zhou, S. Kaskel, J. Eckert, *Nat. Commun.* **2013**, *4*, 1485.
- [6] K. Sakaushi, E. Hosono, G. Nickerl, H. Zhou, S. Kaskel, J. Eckert, *J. Power Sources* **2014**, *245*, 553-556.
- [7] K. Sakaushi, G. Nickerl, F. M. Wissler, D. Nishio-Hamane, E. Hosono, H. Zhou, S. Kaskel, J. Eckert, *Angew. Chem. Int. Ed.* **2012**, *51*, 7850-7854.
- [8] L. Hao, B. Luo, X. Li, M. Jin, Y. Fang, Z. Tang, Y. Jia, M. Liang, A. Thomas, J. Yang, L. Zhi, *Energy Environ. Sci.* **2012**, *5*, 9747-9751.
- [9] P. Kuhn, M. Antonietti, A. Thomas, *Angew. Chem. Int. Ed.* **2008**, *47*, 3450-3453.
- [10] P. Kuhn, A. Forget, J. Hartmann, A. Thomas, M. Antonietti, *Adv. Mater.* **2009**, *21*, 897-901.
- [11] P. Kuhn, A. Thomas, M. Antonietti, *Macromolecules* **2009**, *42*, 319-326.
- [12] S. Hug, M. E. Tauchert, S. Li, U. E. Pachmayr, B. V. Lotsch, *J. Mater. Chem.* **2012**, *22*, 13956-13964.
- [13] D. Hulicova-Jurcakova, M. Kodama, S. Shiraishi, H. Hatori, Z. H. Zhu, G. Q. Lu, *Adv. Funct. Mater.* **2009**, *19*, 1800-1809.

6 SUMMARY

6.1 SYNTHESIS OF NEW COVALENT TRIAZINE FRAMEWORKS

CTFs feature high chemical and thermal stabilities as well as high surface areas and tunable pore sizes. The integration of functional building blocks in CTFs is yet limited to a pyridine-based CTF (see Chapter 1.1.1), although features such as functionality and tunability of CTFs are advantageous for applications in catalysis and carbon capture and storage. In this thesis the synthesis of CTFs with good local order based on 2,2'-bipyridine and fluorene units was successfully carried out under ionothermal conditions in zinc chloride melts at 400 °C for *bipy*-CTF and 300 °C for *fl*-CTF, respectively. At higher synthesis temperatures (up to 700 °C) the materials exhibit higher surface areas (up to 3219 m² g⁻¹ for *bipy*-CTF and 2862 m² g⁻¹ for *fl*-CTF), but lower local order and nitrogen contents due to partial degradation of the systems. The same synthesis conditions were tested for CTFs based on lutidine and pyrimidine building units. The *lut*-CTFs and *pym*-CTFs showed intact lutidine and pyrimidine structures, respectively, at low synthesis temperatures (300-350 °C), but only weak indications for the presence of triazine moieties. As already observed for *bipy*-CTF and *fl*-CTF, the synthesis at higher temperatures led to materials with higher surface areas (up to 2815 m² g⁻¹ for *lut*-CTF and 689 m² g⁻¹ for *pym*-CTF), but lower nitrogen contents. Further, the *pym*-CTFs were found to exhibit the highest nitrogen contents (up to 35 wt%) of all materials.

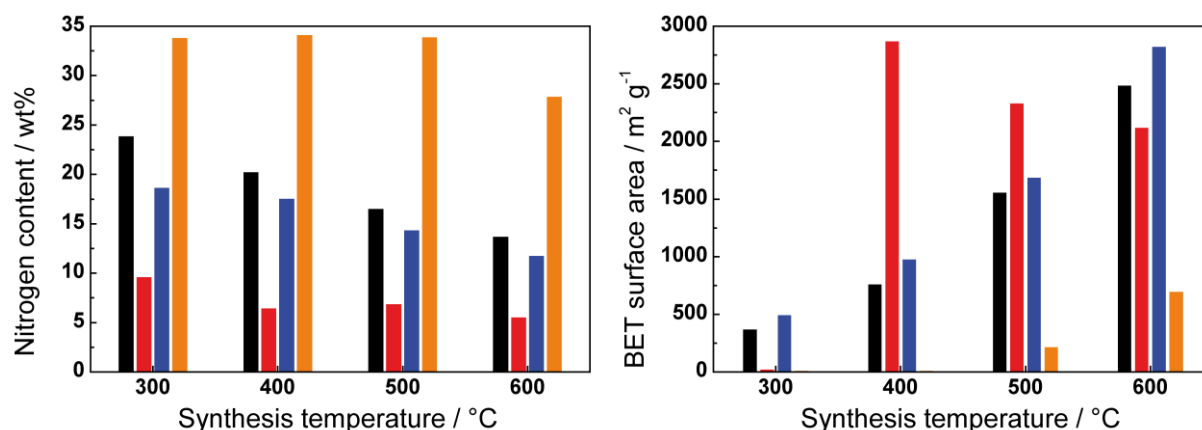


Figure 6.1.1. Nitrogen contents (left) and BET surface areas (right) of *bipy*-CTFs (black), *fl*-CTFs (red), *lut*-CTFs (blue) and *pym*-CTFs (orange) obtained at different synthesis temperatures.

6.2 METAL DOPING OF *bipy*-CTFs

Previous reports on the synthesis of a CTF based on pyridine building units and its application in heterogeneous catalysis bode well for the potential of CTFs as stable metal-coordination scaffolds (see Chapter 1.1.1 and 3.1). The incorporation of 2,2'-bipyridine units in *bipy*-CTF promises even stronger interactions with metal cations due to the chelating effect of the bipyridine units. The bipyridine unit of the *bipy*-CTFs was found to provide specific and strong binding sites for the transition metal ions Co, Ni, Pt and Pd. The highest metal uptakes (up to 38 wt%) were found for the CTF synthesized at 500 °C, which showed a high surface area combined with an intact bipyridine unit according to IR and solid-state NMR spectroscopic investigations. The degree of metal loading was tunable by the metal concentration in solution and was dependent on both the type of transition metal as well as the temperature at which the CTF was synthesized.

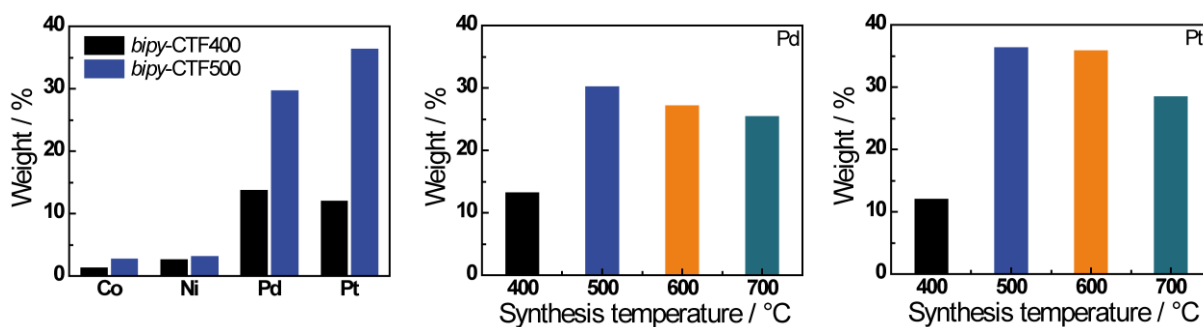


Figure 6.1.2. Metal uptakes by *bipy*-CTF400 (black) and *bipy*-CTF500 (blue) in wt% (left). Palladium (middle) and platinum (right) uptakes by *bipy*-CTFs synthesized at different temperatures.

6.3 CARBON DIOXIDE UPTAKES AND GAS SELECTIVITIES OF COVALENT TRIAZINE FRAMEWORKS

The high porosities and nitrogen contents as well as the chemical and thermal stabilities are promising features of CTFs for applications in CCS. The series of all synthesized CTFs, namely *bipy*-CTFs, *fl*-CTFs, *lut*-CTFs and *pym*-CTFs, was tested towards their carbon dioxide capacities at 273, 298 and 313 K at 1 bar and the results were compared to the previously reported CTF1. The materials showed high carbon dioxide uptakes (up to 5.58 mmol g⁻¹ for *bipy*-CTFs, 4.28 for *fl*-CTFs, 5.04 for *lut*-CTFs, 3.34 for *pym*-CTFs and 4.36 for CTF1s), which are amongst the highest reported for porous polymers to date and were found to be dependent on both the micropore surface area and the nitrogen content, with less impact of the latter one. The selectivities towards carbon dioxide over nitrogen were the highest for the *pym*-CTFs (124-502), followed by *lut*-CTFs (23-66), CTF1s (17-45), *bipy*-CTFs (24-42) and *fl*-CTFs (12-37) and showed to be strongly correlated with the nitrogen contents of the CTFs.

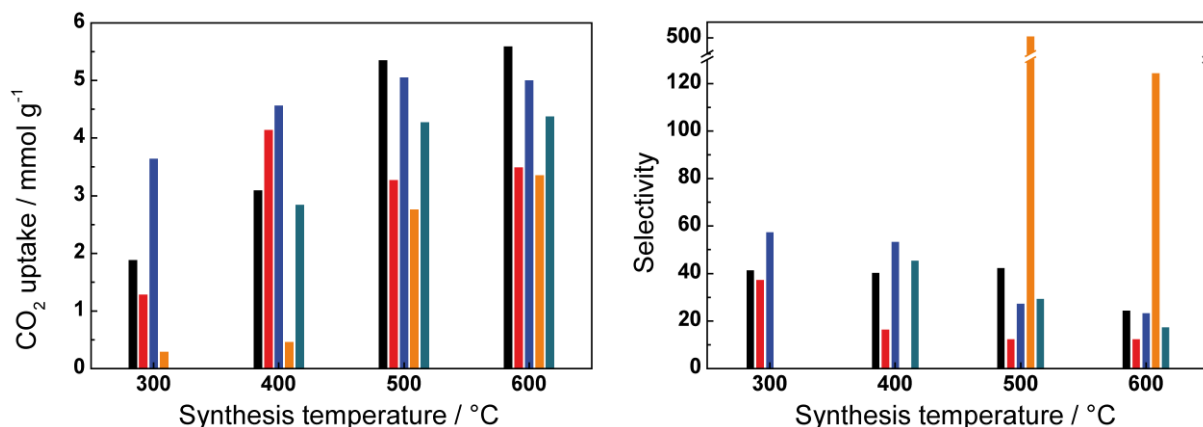


Figure 6.1.3. Carbon dioxide uptakes at 273 K (left) and CO₂/N₂ IAST selectivities at 298 K (right) of *bipy*-CTFs (black), *fl*-CTFs (red), *lut*-CTFs (blue), *pym*-CTFs (orange) and CTF1s (turquoise) obtained at different synthesis temperatures.

6.4 HYDROGEN STORAGE OF COVALENT TRIAZINE FRAMEWORKS

The high carbon dioxide uptakes of the CTFs suggest that also good performances in hydrogen storage applications may be expected. The hydrogen uptakes of the CTFs with the highest BET surface areas were analyzed at pressures up to 25 bar at 77 K (collaboration with the group of Dr. Michael Hirscher, Max Planck Institute for Intelligent Systems, Stuttgart). The hydrogen capacities at high pressures were found to be primarily dependent on the total surface areas of the CTFs, rather than the amount of micropores and the nitrogen contents. The highest uptakes were found for the *fl*-CTFs (4.36 wt%, 20 bar), followed by the CTF1s (4.34 wt%, 25 bar), *lut*-CTFs (4.18 wt%, 25 bar) and *bipy*-CTFs (4.00 wt%, 25 bar).

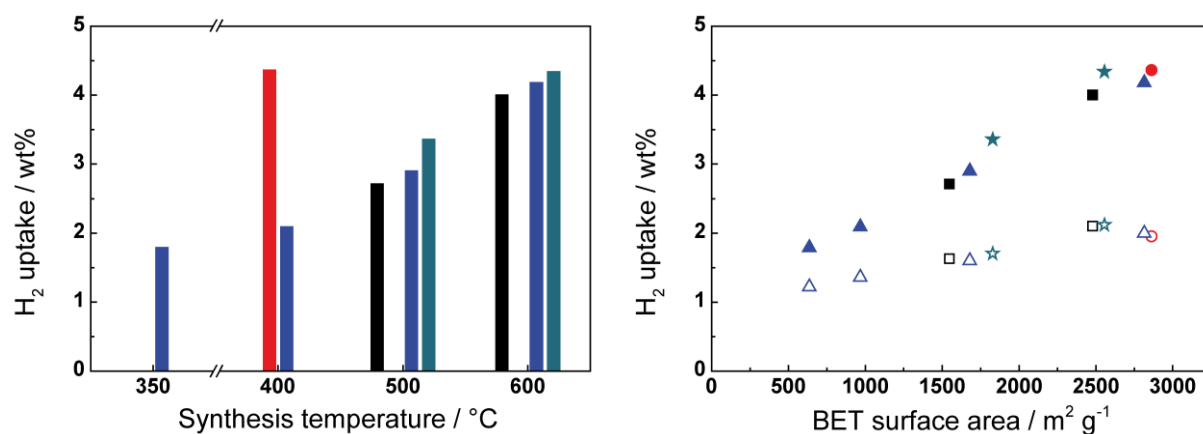


Figure 6.1.4. (Left) Hydrogen uptakes at high pressures (20-25 bar) at 77 K of *bipy*-CTFs (black), *fl*-CTFs (red), *lut*-CTFs (blue) and CTF1s (turquoise) obtained at different synthesis temperatures and (right) correlations of hydrogen uptakes at 1 bar (open symbols) and high pressures (closed symbols) at 77 K of *bipy*-CTFs (black squares), *fl*-CTFs (red circles), *lut*-CTFs (blue triangles) and CTF1s (turquoise stars) to the BET surface areas.

6.5 COVALENT TRIAZINE FRAMEWORKS IN PHOTOCATALYSIS

Organic semiconductors featuring triazine units have been found to be applicable as photocatalysts in light-driven hydrogen evolution (see Chapter 5.1), suggesting that CTFs may also be promising materials for photocatalysis due to their high level of triazine units and high chemical stabilities. Heating of 1,4-dicyanobenzene in zinc chloride melts at temperatures below 400 °C led to materials with two different crystalline phases, depending on the zinc chloride concentration. While one phase was primarily found for precursor/zinc chloride ratios of 1:1 and could be assigned to CTF1, the other phase was found for higher zinc chloride ratios and is unidentified as yet, but the formation of oligomers is very likely. The materials synthesized at 300 °C showed high catalytic activities in the photoinduced hydrogen evolution in the visible light region over many hours (up to 0.92 mmol g⁻¹ h⁻¹), while CTFs synthesized at higher temperatures exhibited almost no hydrogen production. The activities increased with increasing zinc chloride ratios used in the synthesis. The materials were found to be active without platinum as co-catalyst as well, which is a promising finding in the context of metal-free carbon nitride photocatalysis, and exhibited stable hydrogen production over several cycles.

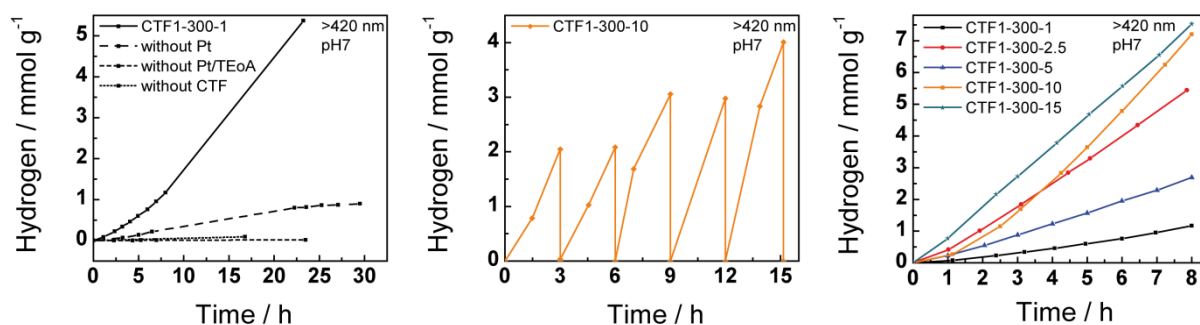


Figure 6.1.5. (Left) Hydrogen evolution of CTF1-300-1 with H₂PtCl₆ and TEoA (straight line), with TEoA and without H₂PtCl₆ (dashes), without H₂PtCl₆ and TEoA (short dashes), and of H₂PtCl₆ with TEoA and without CTF1-300-1 (dots). (Middle) Cycling of CTF1-300-10 in 3 h intervals. After each interval the reactor was evacuated and purged with argon. (Right) Hydrogen evolution of CTF1-300-1, CTF1-300-2.5, CTF1-300-5, CTF1-300-10 and CTF1-300-15. All measurements were performed with pH7 buffer and irradiation at >420 nm.

6.6 COVALENT TRIAZINE FRAMEWORKS IN ENERGY STORAGE DEVICES

CTF1 was recently reported as cathode material in lithium and sodium ion batteries, as well as a promising material for supercapacitors (see Chapter 5.2). In this thesis, the energy storage characteristics of CTF1s and *bipy*-CTFs were measured at working potentials of 1.5-4.5 V versus Li/Li⁺ and at a current density of 0.1 A g⁻¹ and compared to the literature results on CTF1s. The materials were found to cycle very well for at least 60 cycles with high Coulombic efficiencies close to 100%. The CTFs with high local order (CTF1-400-1 and *bipy*-CTF400) showed low specific capacities (≈ 20-40 mA h g⁻¹), while the disordered materials exhibited high values (up to 160 mA h g⁻¹). The high

capacities were primarily attributed the structural changes, such as higher SAs and transition from a 2D to a 3D structure through cross-linking, and only to a minor extent to the nitrogen level in the materials.

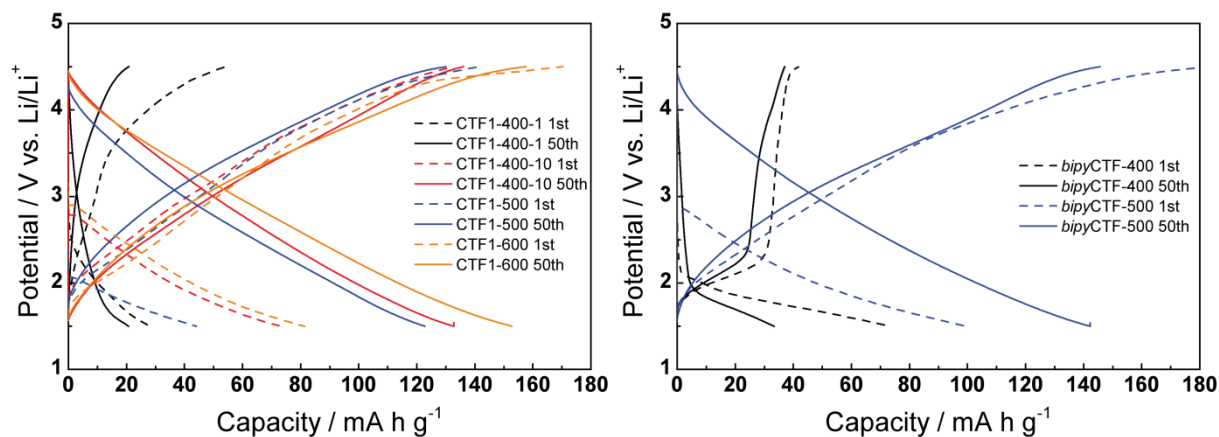


Figure 6.1.6. Charge-discharge profiles of the 1st (dashed line) and 50th (solid line) cycle of CTF1s (left) and *bipy*-CTFs (right) at a current density of 0.1 A g⁻¹.

7 CONCLUSION AND OUTLOOK

Since the first publication on CTFs in 2008 there has been active research on these porous materials targeting their applications in gas capture and storage,^[1-9] catalysis,^[8,10-13] membranes^[14] and electronic devices.^[15-18] The tunability of the porosity and surface area is an important feature of CTFs, which can be controlled by the choice of precursor, the zinc chloride concentration and the synthesis temperature.^[1,19-22] Another key element of the materials is their nitrogen functionalities, both from the triazine rings formed *in situ* and from the *N*-heterocycles used as building units. These are able to bind carbon dioxide molecules through quadrupole-dipole and quadrupole-induced dipole interactions,^[23] which is beneficial for carbon capture and storage, CCS. Additionally, the triazine and other heterocyclic moieties such as bipyridine promote the binding of metals for catalysis,^[10-12] and triazine units are claimed to be responsible for the good performance of CTF-1 in batteries as cathode material.^[15-16,18]

In this thesis, four new CTFs based on 2,2'-bipyridine,^[24] fluorene,^[25] lutidine^[26] and pyrimidine^[26] units were introduced and their tunability as a function of the synthesis conditions was confirmed. The *bipy*-CTF impregnated with various transition metal salts exhibited high metal loadings, making the materials interesting for heterogeneous catalysis, for example for the selective oxidation of methane to methanol^[10,27] or for palladium-catalyzed cross-coupling reactions. In addition, the high nitrogen contents of the materials and the other CTFs as well as their microporosity were found to be beneficial for the selective uptake of carbon dioxide, rendering the materials promising for CCS applications. In the future, further experiments measuring gas mixtures at different humidities should be applied for simulating real-life scenarios, where the hydrophobicity observed for most CTFs is expected to be beneficial for the selective uptake of CO₂ in the presence of water. The storage of captured carbon dioxide is still a challenging process, since storage sites have to keep and store the carbon dioxide for thousands of years without leakages.^[28] Further, the availability of storage sites is limited and they have to be monitored at all times. Therefore, the usage of carbon dioxide and conversion for the production of fuels right upon adsorption would not just decrease the needed storage space, but would also enable a green energy cycle, giving that the energy for the generation of the fuels would come from renewable sources. Along these lines, the photochemical reduction of

carbon dioxide is a promising technique, which could fulfill these requirements, but the high energy and kinetic barriers for this process are still challenging issues.^[29] Examples of photocatalysts known to date are primarily based on metal complexes or extended solids such as TiO₂, and the energy efficiencies are still very low.^[29] One of the most promising molecular systems is based on ruthenium-bipyridine complexes (Ru(bpy)₃²⁺),^[30] which suggests that it may be possible to use *bipy*-CTF as a scaffold for such complexes.

Lutidine is a Lewis base, which can form a so-called frustrated Lewis pair with the Lewis acid B(C₆F₅)₃.^[31] Such stable adducts can serve as metal-free catalysts for the hydrogenation of various hydrocarbons and can even activate carbon dioxide.^[32] The presence of lutidine units in *lut*-CTF300 and *lut*-CTF350 suggests the use of these CTFs as Lewis basic scaffolds, in which the Lewis acid B(C₆F₅)₃ can be stabilized by forming frustrated Lewis pairs. Such a material could be utilized as heterogeneous catalyst, with the advantages of being insoluble and therefore easily recovered by filtration.

Post-functionalization is a powerful tool to tune pore sizes and pore functionalities and has been shown for COFs^[33-35] and other POPs^[36-41] mainly to tune the gas uptake and selectivity properties of the materials. Since CTFs show high thermal and chemical stabilities they offer the possibilities to use post-functionalization reactions requiring harsh conditions, such as nitration with concentrated HNO₃ and H₂SO₄.^[36]

CTF-1 was previously reported as cathode material in lithium and sodium ion batteries.^[15-16,18] We were able to reproduce these results and furthered these studies by additionally investigating the *bipy*-CTFs under similar conditions. First results show comparable capacities compared to CTF-1 and indicate a correlation to the structural changes of the materials, such as more extensively cross-linking to 3D structures and a higher degree of carbonization, rather than on the content of triazine units. In further experiments we will extend our studies to the other CTF materials presented in this work with the goal of carving out trends in the structure-property relationships in these materials.

Photocatalytic activities in water splitting reactions were found for CTF1s synthesized at 300 °C. The materials with higher activities most likely consist of insoluble oligomers, rather than having the idealized, fully extended CTF1 structure. Therefore, optimization of the synthesis conditions towards phase pure materials should be of highest priority, and the identification of the types of oligomers formed. Additionally, the activity of the materials towards oxygen production should be investigated, to target full water splitting, which would enable “green”, light-driven energy production within a carbon free energy cycle. Additionally, the alternative synthesis route for CTFs introduced by Cooper and co-workers using super acids as catalyst for the trimerization of the nitriles led to materials with light yellow color and strong UV-Vis absorptions.^[9] CTFs synthesized by this route should be promising for photocatalytic water splitting reactions. Finally, exfoliation of carbon nitrides^[42-43]

revealed a significant enhancement of the photocatalytic properties of these materials, most likely due to the exposure of active sites and enhanced light harvesting, as well as charge separation.^[43] Since CTF1 is a layered material, it should be prone to exfoliation, giving rise to enhanced photochemical properties.

7.1 REFERENCES

- [1] P. Kuhn, M. Antonietti, A. Thomas, *Angew. Chem. Int. Ed.* **2008**, *47*, 3450-3453.
- [2] A. Bhunia, I. Boldog, A. Moller, C. Janiak, *J. Mater. Chem. A* **2013**, *1*, 14990-14999.
- [3] A. Bhunia, V. Vasylyeva, C. Janiak, *Chem. Commun.* **2013**, *49*, 3961-3963.
- [4] W. Zhang, C. Li, Y.-P. Yuan, L.-G. Qiu, A.-J. Xie, Y.-H. Shen, J.-F. Zhu, *J. Mater. Chem.* **2010**, *20*, 6413-6415.
- [5] W. Wang, H. Ren, F. Sun, K. Cai, H. Ma, J. Du, H. Zhao, G. Zhu, *Dalton Trans.* **2012**, *41*, 3933-3936.
- [6] X. Liu, H. Li, Y. Zhang, B. Xu, S. A, H. Xia, Y. Mu, *Polym. Chem.* **2013**, *4*, 2445-2448.
- [7] Y. Zhao, K. X. Yao, B. Teng, T. Zhang, Y. Han, *Energy Environ. Sci.* **2013**, *6*, 3684-3692.
- [8] P. Katekomol, J. Roeser, M. Bojdys, J. Weber, A. Thomas, *Chem. Mater.* **2013**, *25*, 1542-1548.
- [9] S. Ren, M. J. Bojdys, R. Dawson, A. Laybourn, Y. Z. Khimiyak, D. J. Adams, A. I. Cooper, *Adv. Mater.* **2012**, *24*, 2357-2361.
- [10] R. Palkovits, M. Antonietti, P. Kuhn, A. Thomas, F. Schüth, *Angew. Chem. Int. Ed.* **2009**, *48*, 6909-6912.
- [11] C. E. Chan-Thaw, A. Villa, P. Katekomol, D. Su, A. Thomas, L. Prati, *Nano Lett.* **2010**, *10*, 537-541.
- [12] C. E. Chan-Thaw, A. Villa, L. Prati, A. Thomas, *Chem. Eur. J.* **2011**, *17*, 1052-1057.
- [13] J. Roeser, K. Kailasam, A. Thomas, *ChemSusChem* **2012**, *5*, 1793-1799.
- [14] X. Zhu, C. Tian, S. M. Mahurin, S.-H. Chai, C. Wang, S. Brown, G. M. Veith, H. Luo, H. Liu, S. Dai, *J. Am. Chem. Soc.* **2012**, *134*, 10478-10484.
- [15] K. Sakaushi, G. Nickerl, F. M. Wisser, D. Nishio-Hamane, E. Hosono, H. Zhou, S. Kaskel, J. Eckert, *Angew. Chem. Int. Ed.* **2012**, *51*, 7850-7854.
- [16] K. Sakaushi, E. Hosono, G. Nickerl, T. Gemming, H. Zhou, S. Kaskel, J. Eckert, *Nat. Commun.* **2013**, *4*, 1485.
- [17] L. Hao, B. Luo, X. Li, M. Jin, Y. Fang, Z. Tang, Y. Jia, M. Liang, A. Thomas, J. Yang, L. Zhi, *Energy Environ. Sci.* **2012**, *5*, 9747-9751.
- [18] K. Sakaushi, E. Hosono, G. Nickerl, H. Zhou, S. Kaskel, J. Eckert, *J. Power Sources* **2014**, *245*, 553-556.
- [19] P. Kuhn, A. Forget, J. Hartmann, A. Thomas, M. Antonietti, *Adv. Mater.* **2009**, *21*, 897-901.

- [20] P. Kuhn, A. I. Forget, D. Su, A. Thomas, M. Antonietti, *J. Am. Chem. Soc.* **2008**, *130*, 13333-13337.
- [21] P. Kuhn, K. Kruger, A. Thomas, M. Antonietti, *Chem. Commun.* **2008**, 5815-5817.
- [22] P. Kuhn, A. Thomas, M. Antonietti, *Macromolecules* **2009**, *42*, 319-326.
- [23] K. D. Vogiatzis, A. Mavrandonakis, W. Klopper, G. E. Froudakis, *Chem. Phys. Chem.* **2009**, *10*, 374-383.
- [24] S. Hug, M. E. Tauchert, S. Li, U. E. Pachmayr, B. V. Lotsch, *J. Mater. Chem.* **2012**, *22*, 13956-13964.
- [25] S. Hug, M. B. Mesch, H. Oh, N. Popp, M. Hirscher, J. Senker, B. V. Lotsch, *J. Mater. Chem. A* **2014**, *2*, 5928-5936.
- [26] S. Hug, H. Oh, M. Hirscher, B. V. Lotsch, *Energy Environ. Sci.* **2014**.
- [27] R. A. Periana, D. J. Taube, S. Gamble, H. Taube, T. Satoh, H. Fujii, *Science* **1998**, *280*, 560-564.
- [28] M. E. Boot-Handford, J. C. Abanades, E. J. Anthony, M. J. Blunt, S. Brandani, N. Mac Dowell, J. R. Fernandez, M.-C. Ferrari, R. Gross, J. P. Hallett, R. S. Haszeldine, P. Heptonstall, A. Lyngfelt, Z. Makuch, E. Mangano, R. T. J. Porter, M. Pourkashanian, G. T. Rochelle, N. Shah, J. G. Yao, P. S. Fennell, *Energy Environ. Sci.* **2014**, *7*, 130-189.
- [29] N. MacDowell, N. Florin, A. Buchard, J. Hallett, A. Galindo, G. Jackson, C. S. Adjiman, C. K. Williams, N. Shah, P. Fennell, *Energy Environ. Sci.* **2010**, *3*, 1645-1669.
- [30] E. Fujita, *Coord. Chem. Rev.* **1999**, *185-186*, 373-384.
- [31] S. J. Geier, D. W. Stephan, *J. Am. Chem. Soc.* **2009**, *131*, 3476-3477.
- [32] D. W. Stephan, G. Erker, *Angew. Chem. Int. Ed.* **2010**, *49*, 46-76.
- [33] A. Nagai, Z. Guo, X. Feng, S. Jin, X. Chen, X. Ding, D. Jiang, *Nat. Commun.* **2011**, *2*, 536.
- [34] X. Chen, M. Addicoat, S. Irle, A. Nagai, D. Jiang, *J. Am. Chem. Soc.* **2013**, *135*, 546-549.
- [35] H. Xu, X. Chen, J. Gao, J. Lin, M. Addicoat, S. Irle, D. Jiang, *Chem. Commun.* **2014**, *50*, 1292-1294.
- [36] T. Islamoglu, M. Gulam Rabbani, H. M. El-Kaderi, *J. Mater. Chem. A* **2013**, *1*, 10259-10266.
- [37] W. Lu, J. P. Sculley, D. Yuan, R. Krishna, Z. Wei, H.-C. Zhou, *Angew. Chem. Int. Ed.* **2012**, *51*, 7480-7484.
- [38] H. A. Patel, C. T. Yavuz, *Chem. Commun.* **2012**, *48*, 9989-9991.
- [39] S. J. Garibay, M. H. Weston, J. E. Mondloch, Y. J. Colon, O. K. Farha, J. T. Hupp, S. T. Nguyen, *CrystEngComm* **2013**, *15*, 1515-1519.
- [40] W. Lu, D. Yuan, J. Sculley, D. Zhao, R. Krishna, H.-C. Zhou, *J. Am. Chem. Soc.* **2011**, *133*, 18126-18129.
- [41] H. Ma, H. Ren, X. Zou, F. Sun, Z. Yan, K. Cai, D. Wang, G. Zhu, *J. Mater. Chem. A* **2013**, *1*, 752-758.

- [42] S. Yang, Y. Gong, J. Zhang, L. Zhan, L. Ma, Z. Fang, R. Vajtai, X. Wang, P. M. Ajayan, *Adv. Mater.* **2013**, *25*, 2452-2456.
- [43] K. Schwinghammer, M. B. Mesch, V. Duppel, C. Ziegler, J. Senker, B. V. Lotsch, *J. Am. Chem. Soc.* **2014**, *136*, 1730-1733.

8 APPENDIX

8.1 SUPPORTING INFORMATION	119
8.1.1 SUPPORTING INFORMATION FOR CHAPTER 3.1	119
8.1.2 SUPPORTING INFORMATION FOR CHAPTER 4.1	125
8.1.3 SUPPORTING INFORMATION FOR CHAPTER 4.2	146
8.2 LIST OF PUBLICATIONS	170
8.3 CONFERENCES AND WORKSHOPS.....	171

8.1 SUPPORTING INFORMATION

8.1.1 SUPPORTING INFORMATION FOR CHAPTER 3.1

Materials

Table 8.1.1.1. List of used materials with supplier, purity, and purification information.

Chemical	Molecular Formula	Supplier	Purity	Purification
Bis(dibenzylideneacetone)palladium(0)	C ₃₄ H ₂₈ O ₂ Pd	Sigma-Aldrich	-	-
1,5-Bis(diphenylphosphino)pentane	C ₂₉ H ₃₀ P ₂	Alfa Aesar	97%	-
5-Bromo-2-idopyridine	C ₅ H ₃ BrI	Alfa Aesar	98%	-
Cobalt(II) chloride hexahydrate	Cl ₂ Co · 6H ₂ O	AppliChem	97%	-
1,2-Dibromoethane	C ₂ H ₄ Br ₂	Fluka	98%	-
Dimethylformamide	C ₃ H ₇ NO	Alfa Aesar	99%	-
Lithium chloride	CLi	Grüssing	99%	-
Magnesium	Mg	Grüssing	99%	-
Nickel(II) chloride hexahydrate	Cl ₂ Ni · 6H ₂ O	Grüssing	98%	-
Potassium tetrachloro platinate(II)	Cl ₄ K ₂ Pt	Alfa Aesar	99.9%	-
Sodium tetrachloropalladate(II) trihydrate	Cl ₄ Na ₂ Pd · 3H ₂ O	Strem Chemicals	99%	-
Tetrahydrofuran	C ₄ H ₈ O	BASF	-	Predried over CaH ₂ and refluxed over Na benzophenoneketyl
Trimethylsilyl chloride	C ₃ H ₉ ClSi	Sigma-Aldrich	98%	-
Zinc chloride	Cl ₂ Zn	BDH Prolabo	98%	6h, 140 °C, HV
Zinc cyanide	C ₂ N ₂ Zn	ABCR	98%	-

Temperature programs

Table 8.1.1.2. Temperature programs for the *bipy*-CTF synthesis.

Program	Sample	Heating rate [°C h ⁻¹]	T1 [°C]	Holding time T1 [h]	T2 [°C]	Holding time T2 [h]	Cooling rate ^a [°C h ⁻¹]
1	1,2,3,4	60	375	48	-	-	10
2	5,6,7,8	60	400	48	-	-	10
3	9	60	450	48	-	-	10
4	10	60	500	48	-	-	10
5	11	60	600	48	-	-	10
6	12	60	700	48	-	-	10
7	13	60	400	40	600	0.2	10
8	14	60	400	40	600	20	10
9	15	60	400	40	600	40	10
10	16	60	400	40	600	80	10

^aAt 240 °C the oven was turned off.

Elemental analysis

Table 8.1.1.3. Elemental composition of *bipy*-CTF materials synthesized under different reaction conditions (in wt%).

Sample	N	C	H
calc.	27.17	69.90	2.93
5	23.09	67.06	3.01
9	20.50	65.78	3.11
10	16.95	64.14	1.81
11	13.48	75.24	1.66
12	7.61	82.44	1.44
13	17.75	71.28	1.74
14	15.59	72.57	1.62
15	14.67	74.94	0.74
16	14.33	75.41	1.48

Metal doping

Table 8.1.1.4. Metal uptake by different *bipy*-CTFs in wt% and mol%.

Metal	CTF	Uptake [wt%]	Uptake ^a [mol%]	Metal	CTF	Uptake [wt%]	Uptake ^a [mol%]
Pt	400	10.2	12.5	Pd	400	15.2	39.4
Pt	400	10.1	12.4	Pd	400	11.9	28.8
Pt	400	11.8	14.9	Pd	400	12.1	29.4
Pt	400	15.3	20.4	Pd	500	30.3	118.6
Pt	500	37.8	82.5	Pd	500	28.9	108.0
Pt	500	34.7	69.6	Pd	500	33.2	144.0
Pt	600	35.8	73.9	Pd	600	25.2	84.2
Pt	600	31.4	58.0	Pd	600	29.0	108.7
Pt	700	28.4	49.0	Pd	700	24.9	82.5
				Pd	700	25.9	88.3
Co	400	0.5	1.8	Ni	400	1.8	6.6
Co	400	1.8	6.6	Ni	400	3.1	11.7
Co	500	2.6	9.7	Ni	500	3.0	11.3
Co	400/600	2.5	9.2	Ni	400/600	3.1	11.9

^aMol% calculated by assumption that metal salts are adsorbed as M(II)Cl₂.

Methods

Nitrogen and Argon adsorption/desorption measurements were performed at 77 K (87 K for Ar) with an Autosorb-iQ instrument (Quantachrome Instruments, Boynton Beach, Florida, USA). Samples were outgassed in vacuum at 300 °C for analysis station was equipped with high-precision pressure transducers and a turbo molecular pump. Pore-size distribution was determined using the calculation model N₂ at 77 K on carbon (slit-/cylinder pores, non-local DFT (equilibrium model)) of the ASiQwin software (version 1.11) from Quantachrome. For BET calculations pressure ranges were chosen with the help of the BET Assistant in the ASiQwin software (version 2.0). In accordance with the ISO recommendations multipoint BET tags equal or below the maximum in $V \cdot (1 - P/P_0)$ were chosen.

Infrared (IR) spectroscopy measurements were carried out on a Perkin Elmer Spektrum BX II (Perkin Elmer, Waltham, Massachusetts, USA) with an attenuated total reflectance unit.

Powder X-ray diffraction (XRD) was measured on a BRUKER D8 Avance (Bruker AXS, Madison, Wisconsin, USA) in Bragg-Brentano geometry or on a HUBER G670 (HUBER Diffractionstechnik, Rimsting, Germany) in Guinier geometry equipped with an imaging plate detector.

Elemental analysis (EA) was carried out with an Elementar vario EL (Elementar Analysensysteme, Hanau, Germany).

Inductively coupled plasma atomic emission spectroscopy (ICP-AES) was done on a VARIAN VISTA RL simultaneous spectrometer (Agilent Technologies, Santa Clara, California, USA) with a CCD-detector.

Solution-state NMR spectroscopy was performed on a JEOL DELTA NMR (JEOL, Tokyo, Japan) by single pulse experiments. The spectra were referenced against CDCl_3 ($\delta(^1\text{H})$ 7.26 ppm, $\delta(^{13}\text{C}\{^1\text{H}\})$ 77.16 ppm).

Magic angle spinning (MAS) solid-state nuclear magnetic resonance (ssNMR) spectroscopy measurements were carried out on a BRUKER DSX500 Avance spectrometer (Bruker AXS, Madison, Wisconsin, USA) with a proton resonance frequency of 500 MHz using a 4 mm MAS-rotor (ZrO_2) in an 11.75 T magnet field with a spinning frequency of 10 kHz.

Differential thermal analysis and thermogravimetry (DTA/TG) were measured on a SETARAM TG-DTA92-2400 combined DTA-TG-thermobalance (SETARAM Instrumentation, Caluire, France) in aluminum oxide crucibles. Heating was performed from room temperature to 1000 °C with a heating rate of 5 °C min⁻¹ under helium atmosphere.

Scanning electron microscopy (SEM) and energy dispersive X-ray analysis (EDX) were performed using either a JEOL JSM-6500F electron microscope (JEOL, Tokyo, Japan) with a field emission source equipped with an EDX detector model 7418 (Oxford Instruments, Oxfordshire, UK) or a Tescan Vega TS 5130MM electron microscope equipped with an Si/Li EDX detector (Oxford Instruments).

Transmission electron microscopy (TEM) was operated on a Philips CM30 ST, 300 kV S/TEM (FEI, Hillsboro, Oregon, USA) with a Si/Li EDX-detector from Thermo Fischer, NSS.

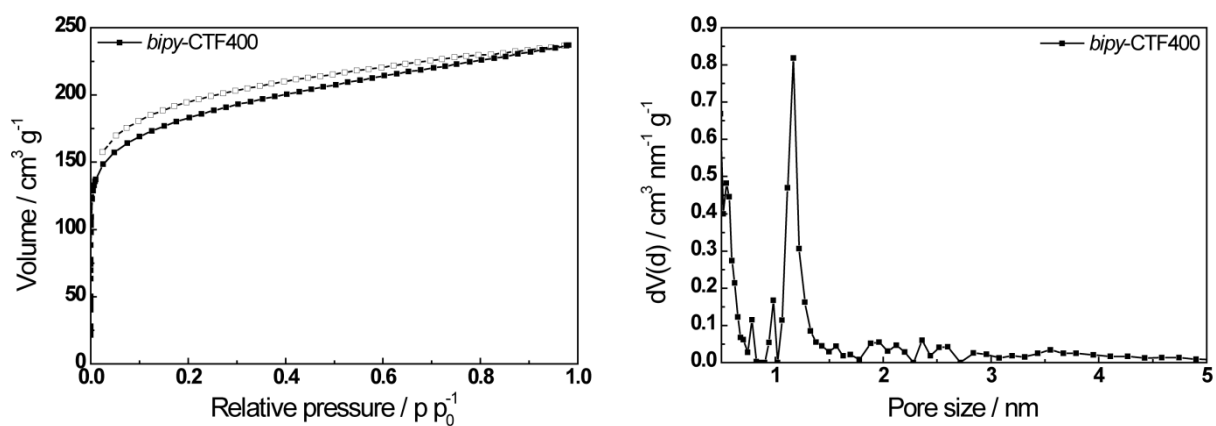
Sorption measurements

Figure 8.1.1.1. N_2 physisorption isotherm (left) and pore size distribution (right) of *bipy*-CTF400 with $671 \text{ m}^2 \text{ g}^{-1}$ surface area.

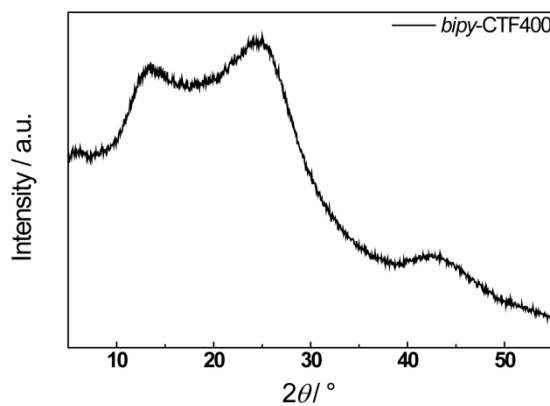
X-ray powder diffraction

Figure 8.1.1.2. X-Ray powder pattern of *bipy*-CTF400 (recorded on BRUKER D8).

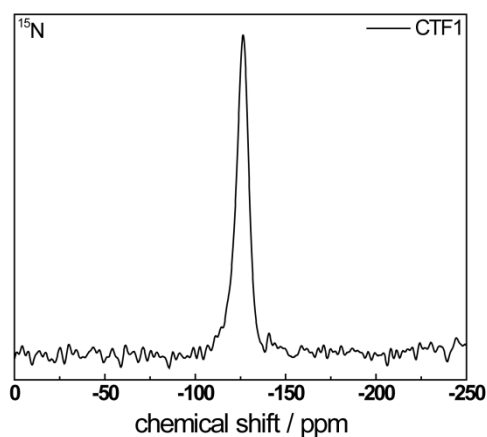
Solid-state MAS NMR spectroscopy

Figure 8.1.1.3. ^{15}N solid-state MAS NMR spectrum of CTF-1.

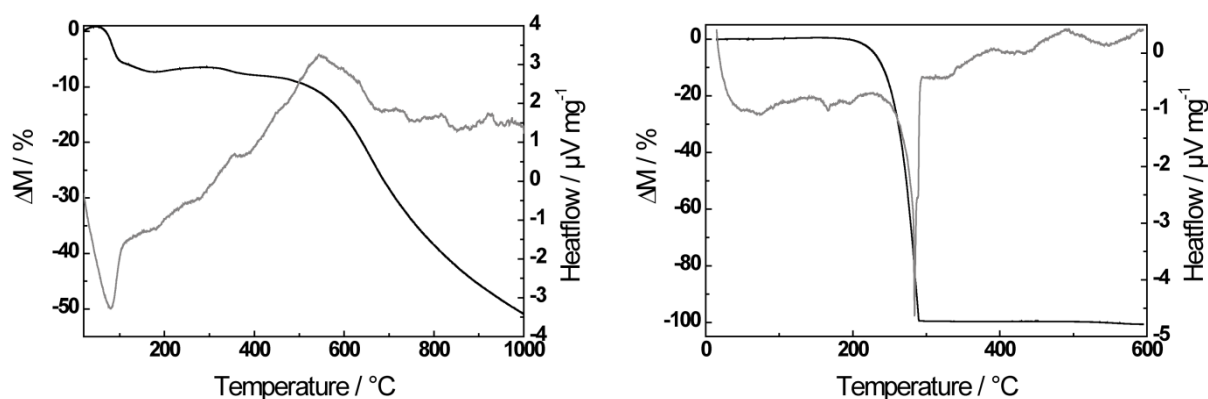
Differential thermal analysis and thermogravimetry

Figure 8.1.1.4. TG (black) and DTA (gray) curves of *bipy*-CTF400 (left) and 5,5'-dicyano-2,2'-bipyridine (right).

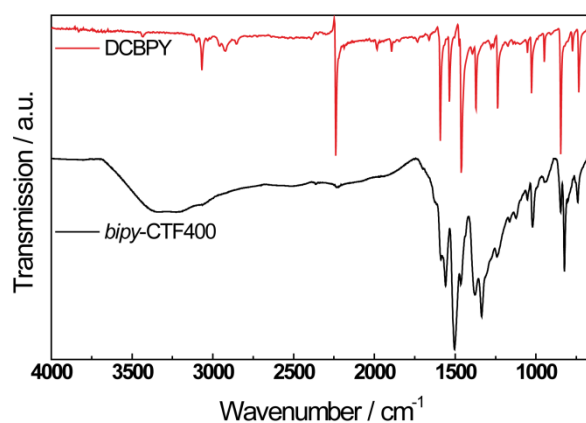
Infrared spectroscopy

Figure 8.1.1.5. IR spectra of *bipy*-CTF400 and DCBPY.

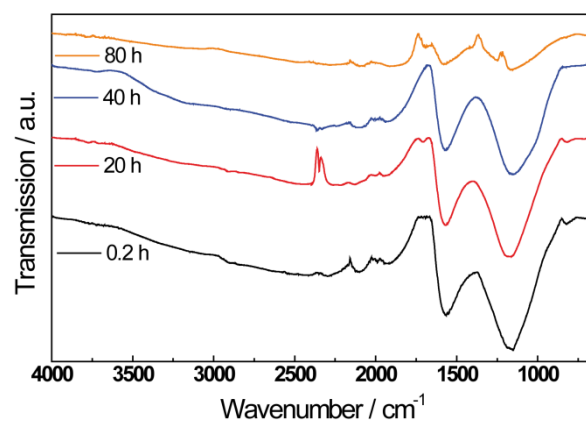


Figure 8.1.1.6. IR spectra of *bipy*-CTFs obtained with different temperature programs (black 0.2 h, dark gray 20 h, gray 40 h and light gray 80 h).

Scanning electron microscopy

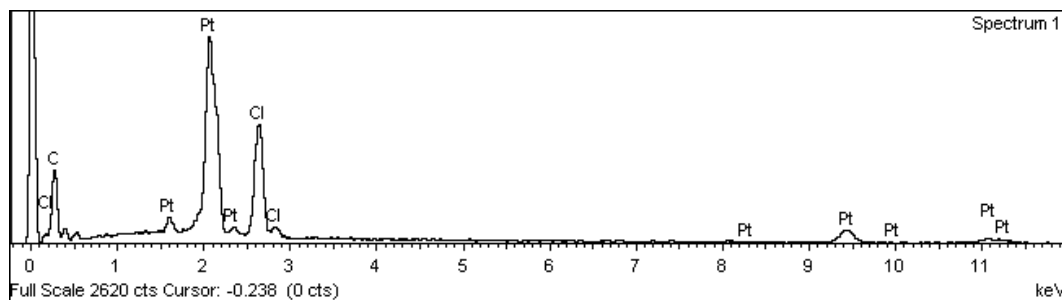
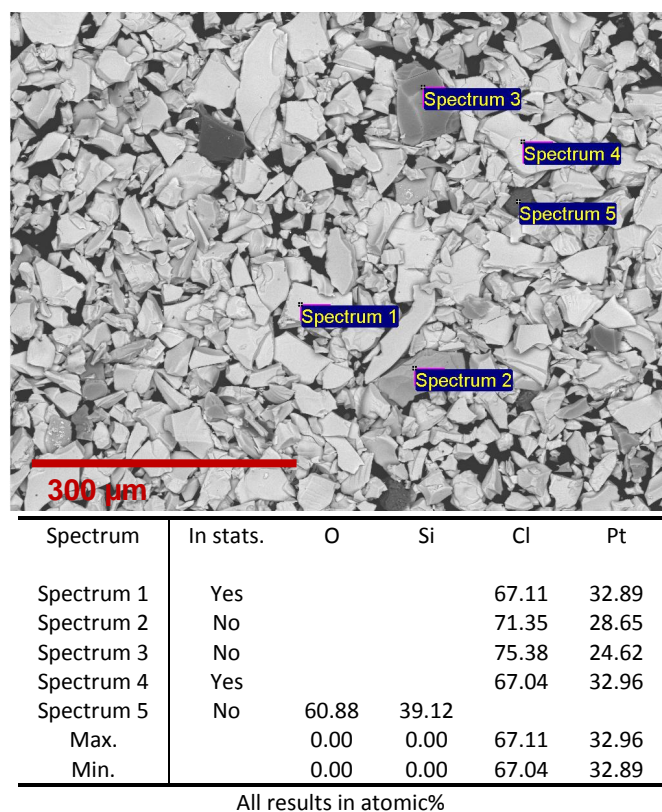


Figure 8.1.1.7. SEM image of a Pt loaded sample with corresponding EDX values and the EDX spectra of the spot Spectrum 1.

Elemental analysis

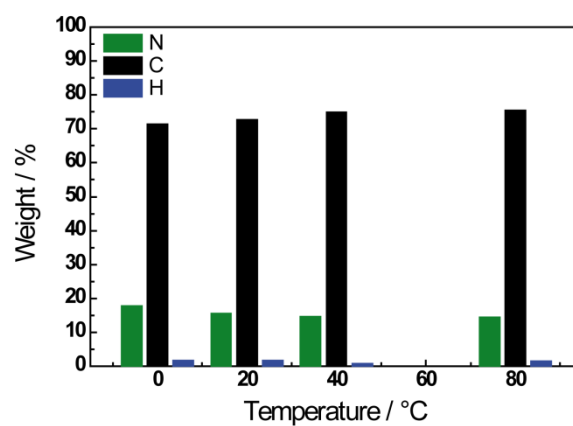


Figure 8.1.1.8. Variation of carbon, hydrogen and nitrogen contents as a function of the synthesis time at 600 °C.

8.1.2 SUPPORTING INFORMATION FOR CHAPTER 4.1

Temperature Programs

Table 8.1.2.1. Temperature programs used for the *fl*-CTF synthesis.

Program	Sample	Heating rate [$^{\circ}\text{C h}^{-1}$]	T [$^{\circ}\text{C}$]	Holding time <i>t</i> [h]	Cooling rate ^a [$^{\circ}\text{C h}^{-1}$]
1	<i>fl</i> -CTF300	60	300	96	10
2	<i>fl</i> -CTF350	60	350	96	10
3	<i>fl</i> -CTF400	60	400	48	10
4	<i>fl</i> -CTF500	60	500	48	10
5	<i>fl</i> -CTF600	60	600	48	10

^aAt 240 $^{\circ}\text{C}$ the oven was turned off.

Elemental Analysis

Table 8.1.2.2. Elemental Analysis of *fl*-CTFs. All values are displayed in wt%.

Sample	N	C	H
calc. <i>fl</i> -CTF	12.95	83.32	3.73
<i>fl</i> -CTF300	9.52	80.69	3.40
<i>fl</i> -CTF350	7.71	81.64	3.11
<i>fl</i> -CTF400	6.33	84.95	2.77
<i>fl</i> -CTF500	6.77	84.36	2.71
<i>fl</i> -CTF600	5.43	82.61	1.43

Powder X-Ray Diffraction

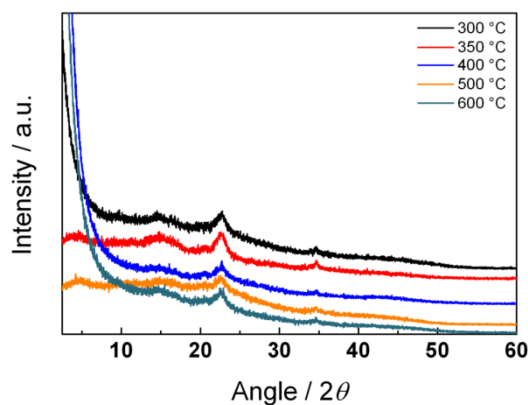


Figure 8.1.2.1. Powder X-Ray diffraction measurements of the samples *fl*-CTF300, *fl*-CTF350, *fl*-CTF400, *fl*-CTF500 and *fl*-CTF600.

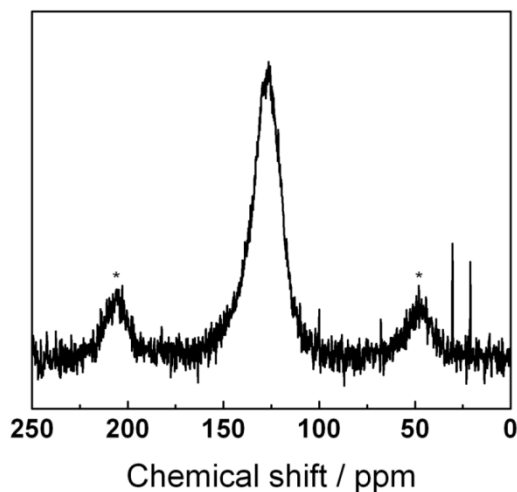
Solid-State NMR Spectra

Figure 8.1.2.2. ^{13}C MAS ssNMR spectrum of *fl*-CTF500.

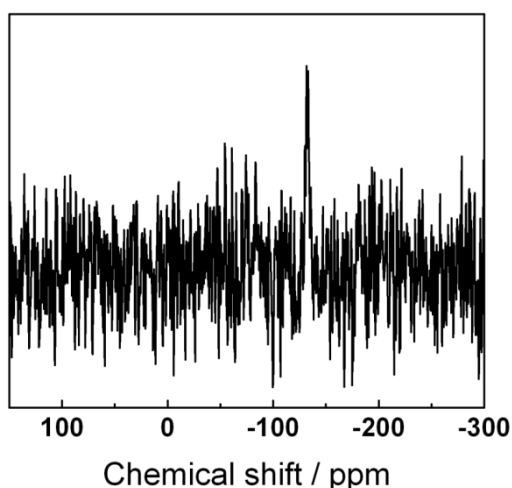


Figure 8.1.2.3. ^{15}N MAS ssNMR spectrum of tris(9*H*-fluoren-2-yl)-1,3,5-triazine.

CPPI Analysis

As the signal at 50 ppm could not be assigned to the reactant nor the product, a cross polarization with polarization inversion (CPPI) measurement^[1-2] was carried out to get information about the number of covalently bonded protons. Starting from maximum magnetization it decays and becomes negative with increasing inversion time. This decay has a characteristic form according to the number of bonded protons and was fitted using the following equation^[3]

$$M(\tau_i) = M^0 \left[\frac{2}{n+1} \exp\left(-\frac{\tau_i}{T_D}\right) + \frac{2n}{n+1} \exp\left(-\frac{3\tau_i}{2T_D}\right) \exp\left(-\frac{\tau_i^2}{T_C^2}\right) - 1 \right] \quad (1)$$

T_C = decay related to dipolar coupling to nearby protons

T_D = decay caused by isotropic spin-diffusion

n = number of directly bonded protons

τ_i = inversion time

The spectra of *fl*-CTF300 with increasing inversion times are displayed in Figure 8.1.2.4.

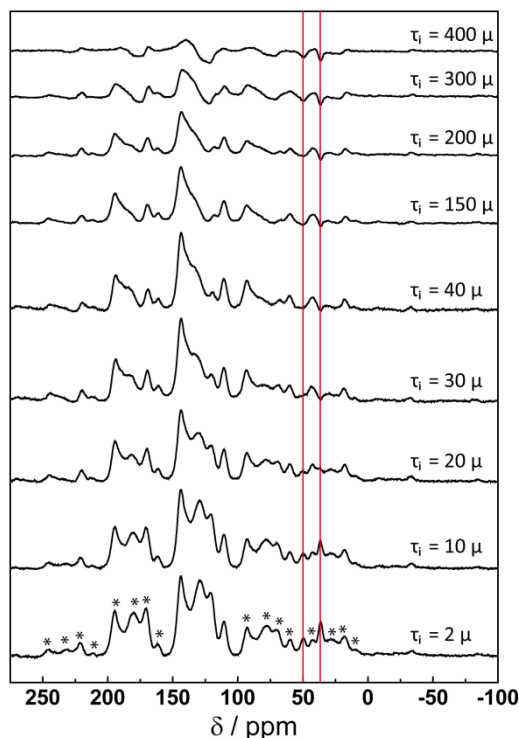


Figure 8.1.2.4. ^{13}C CPPI MAS ssNMR spectra of *fl*-CTF300 for different inversion times. Sidebands are marked with asterisks. Relevant signals for the CPPI experiment are indicated using red lines.

The curves extracted from the CPPI measurements are presented in Figure 8.1.2.5 and the relevant fitting parameters are depicted in Table 8.1.2.3. For the signal at 50 ppm n is very close to 1 and, therefore, the signal can be assigned to a CH group. For the second signal n is 2.45, which strongly supports the assignment to a CH_2 group. The deviation of 0.45 regarding the optimal value results from difficulties in the integration due to overlapping spinning sidebands.

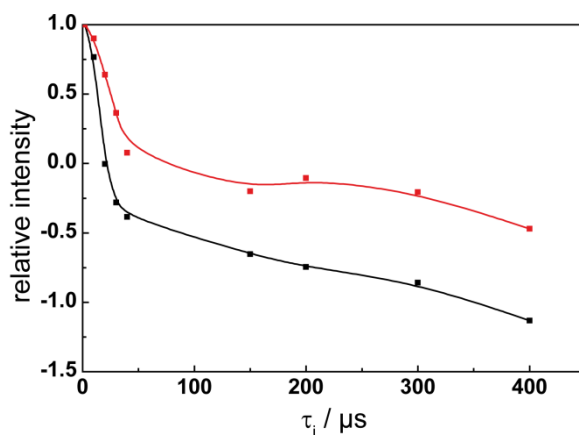


Figure 8.1.2.5. Normalized signal intensities plotted against the inversion time for the signal at 36.9 ppm (blue) and the signal at 50 ppm (red) of the ^{13}C MAS ssNMR CPPI spectra of *fl*-CTF300.

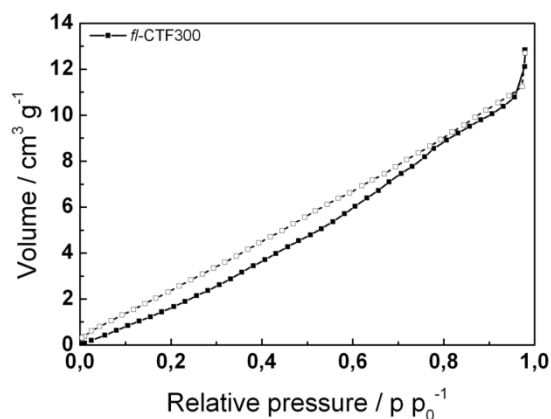
Table 8.1.2.3. Fitting parameters for the CPPI curves.

Shift [ppm]	n	TC	TD
36.9	2.45	250.00	22.13
50	0.95	816.02	30.56

Argon Physisorption Measurements**Table 8.1.2.4.** Specific Surface Areas and Pore Volumes of *fl*-CTFs.

Sample	Surface Area [$\text{m}^2 \text{g}^{-1}$]			Pore Volume [$\text{cm}^3 \text{g}^{-1}$]					
	BET _{Ar}	DFT _{Ar} ^a	DFT _{CO₂} ^b	V _{Ar,mic} ^c	V _{Ar,mic,DFT} ^d	V _{Ar,tot} ^e	V _{Ar,tot,DFT} ^f	V _{CO₂,tot,DFT} ^g	V _{Ar,mic,DFT} /V _{Ar,tot,DFT}
<i>fl</i> -CTF300	15	-	297	-	-	-	-	0.09	-
<i>fl</i> -CTF350	1235	1385	1020	0.48	0.57	0.69	0.67	0.33	0.85
<i>fl</i> -CTF400	2862	2084	1211	1.04	1.13	1.49	1.45	0.49	0.78
<i>fl</i> -CTF500	2322	1643	793	0.76	0.77	1.33	1.29	0.28	0.60
<i>fl</i> -CTF600	2113	1608	844	0.71	0.70	1.19	1.16	0.30	0.60

^aAr QSDFT slit pore model on carbon at 87 K. ^bCO₂ NLDFT model on carbon at 273 K. ^cCalculated pore volume at $p/p_0 = 0.17$. ^dPore volume for pores smaller than 2 nm calculated from the Ar QSDFT model. ^eCalculated total pore volume at $p/p_0 = 0.95$. ^fTotal pore volume from the Ar QSDFT model. ^gTotal pore volume from the CO₂ NLDFT model.

**Figure 8.1.2.6.** Argon adsorption (filled symbols) and desorption (open symbols) isotherm of *fl*-CTF300.

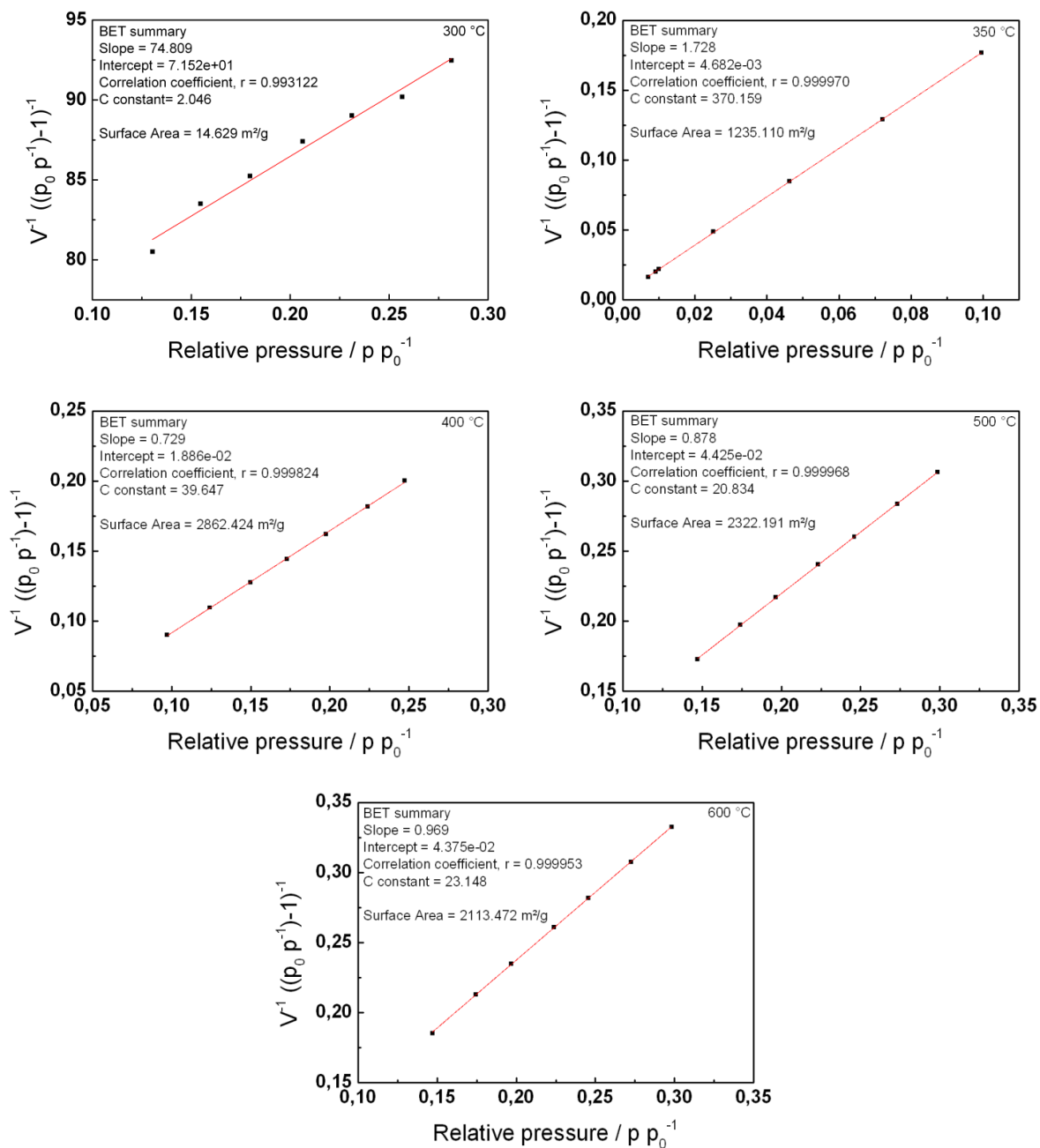


Figure 8.1.2.7. BET plots of the samples *fl*-CTF300, *fl*-CTF350, *fl*-CTF400, *fl*-CTF500 and *fl*-CTF600 from argon isotherms at 87 K.

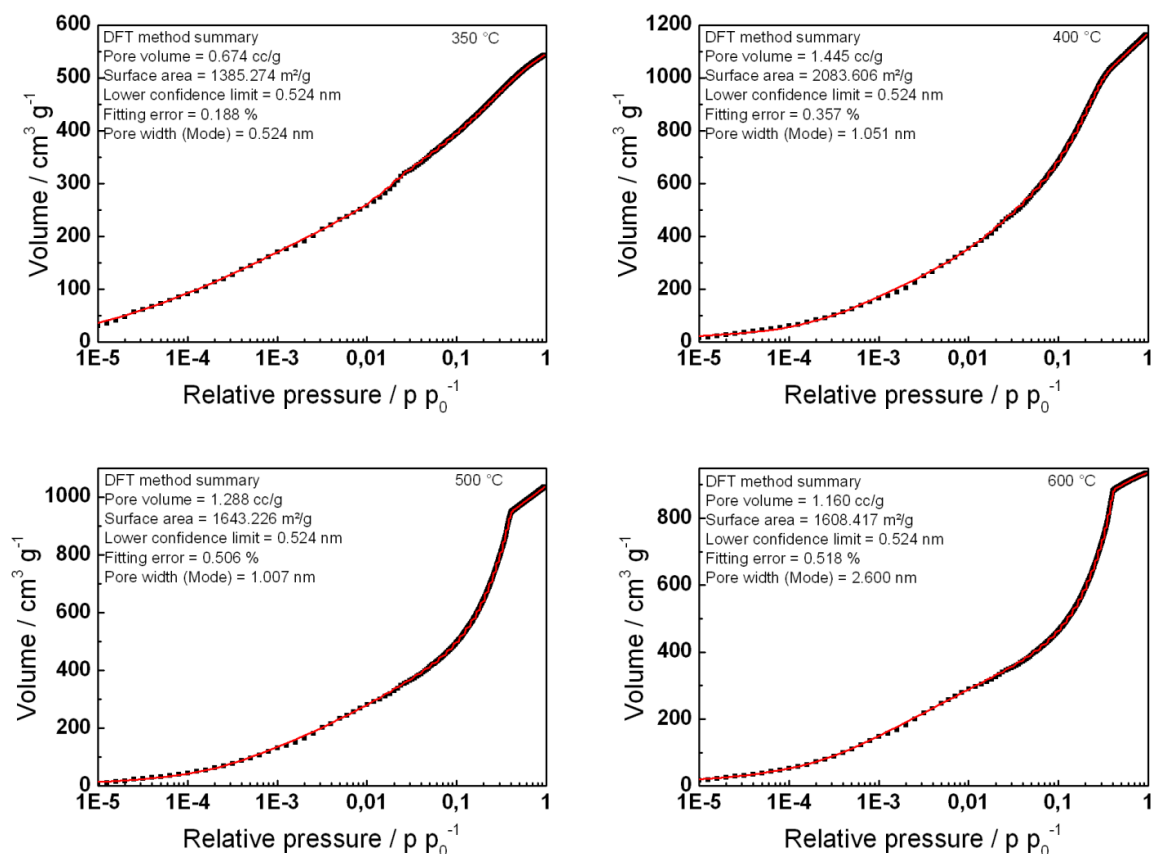


Figure 8.1.2.8. QSDFT fittings for the argon sorption isotherms of the samples *fl*-CTF350, *fl*-CTF400, *fl*-CTF500 and *fl*-CTF600.

H₂ Physisorption Measurements

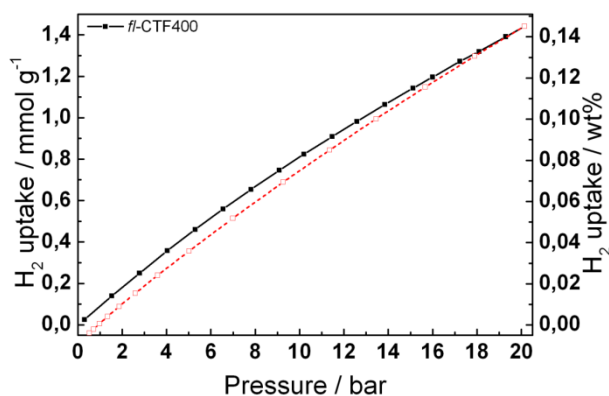


Figure 8.1.2.9. Hydrogen adsorption (filled symbols) and desorption (open symbols) isotherm of *fl*-CTF400 at 298 K.

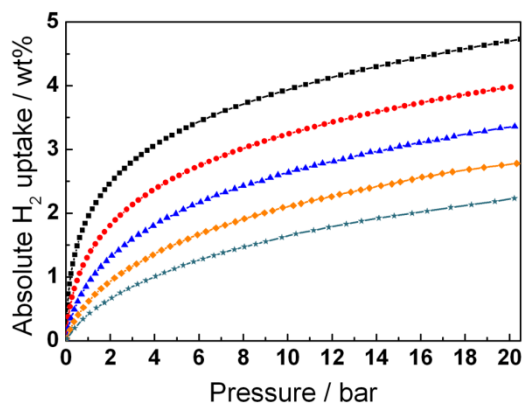


Figure 8.1.2.10. Fully reversible absolute hydrogen uptake in *fl*-CTF400 at 77, 87, 97, 107 and 117 K (from top to bottom).

Evaluation of the isosteric heat of adsorption

The isosteric heat of adsorption is calculated from the measured absolute isotherms according to the Clausius-Clapeyron equation

$$\Delta H = R \cdot \left(\frac{\partial \ln(P)}{\partial \frac{1}{T}} \right)_{\theta} \quad (2)$$

where θ is the surface coverage, R is the gas constant, P the pressure and T the temperature. Therefore $\ln(P)$ is plotted versus the reciprocal temperature $1/T$ for different surface coverages θ . The slope of the linear fit to this data for each surface coverage θ is proportional to the isosteric heat of adsorption.

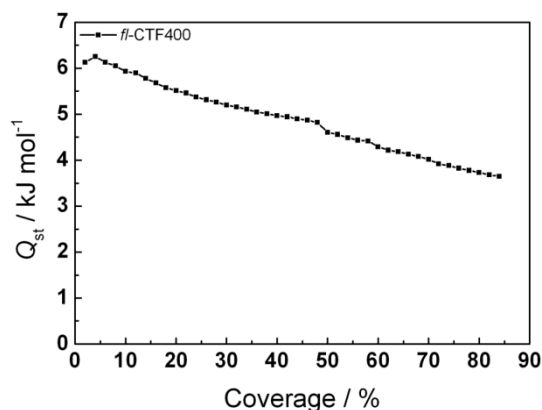


Figure 8.1.2.11. Heat of adsorption (Q_{st}) of *fl*-CTF400 calculated from the absolute hydrogen isotherms (77 K ~ 117 K) as a function of the normalized surface coverage.

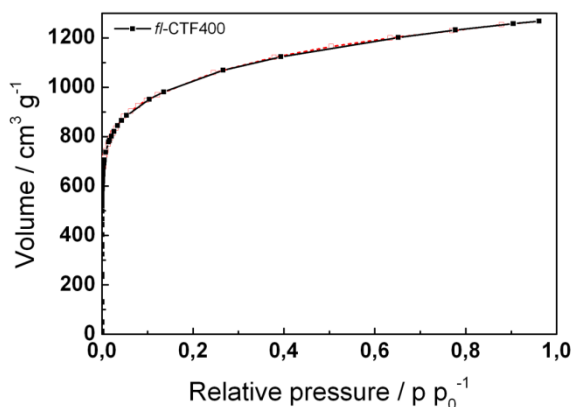


Figure 8.1.2.12. Low pressure hydrogen adsorption (filled symbols) and desorption (open symbols) isotherm of *fl*-CTF400 at 20 K.

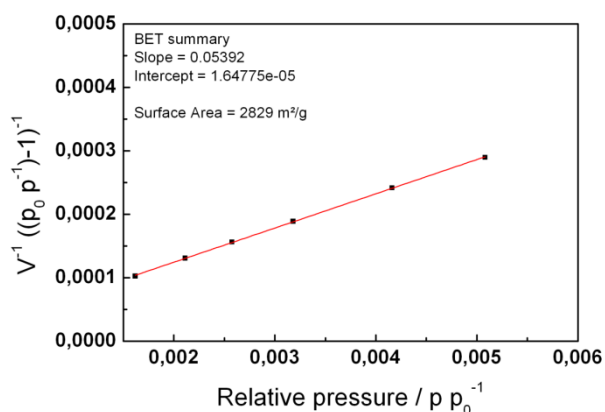


Figure 8.1.2.13. BET plot of *fl*-CTF400 from the hydrogen isotherm at 20 K.

Table 8.1.2.5. Textural characteristics of *fl*-CTF400 determined from hydrogen adsorption/desorption isotherms.

Sample	H ₂ BET [m ² g ⁻¹]	Pore Volume ^a [cm ³ g ⁻¹]	Excess H ₂ uptake [wt%]			Skeletal density [g cm ⁻³]	Q _{st} ^b [kJ mol ⁻¹]
			19.5 K p p ₀ ⁻¹ = 0.9	77 K p = 20 bar	298 K p = 20 bar		
<i>fl</i> -CTF400	2829	1.6	10.2	4.4	0.15	1.6	4.9

^aTotal pore volume at p p₀⁻¹ = 0.9, ^bMean isosteric heat of hydrogen adsorption.

CO₂ Physisorption Measurements

Table 8.1.2.6. CO₂ and N₂ uptakes of *fl*-CTFs.

Sample	CO ₂ uptake [cm ³ g ⁻¹] ^a			N ₂ uptake ^b [cm ³ g ⁻¹]
	273 K	298 K	313 K	
<i>fl</i> -CTF300	28.6	17.6	11.0	1.00
<i>fl</i> -CTF350	96.7	56.5	41.2	4.40
<i>fl</i> -CTF400	93.2	48.5	34.0	4.20
<i>fl</i> -CTF500	73.5	40.6	28.8	5.14
<i>fl</i> -CTF600	78.5	44.5	31.7	5.45

^aAt 1 bar. ^bAt 1 bar and 298 K.

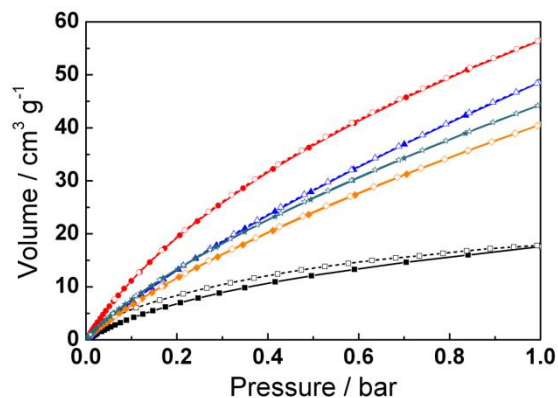


Figure 8.1.2.14. CO₂ adsorption (filled symbols) and desorption (open symbols) isotherms of the samples *fl*-CTF300, *fl*-CTF350, *fl*-CTF400, *fl*-CTF500 and *fl*-CTF600 at 298 K.

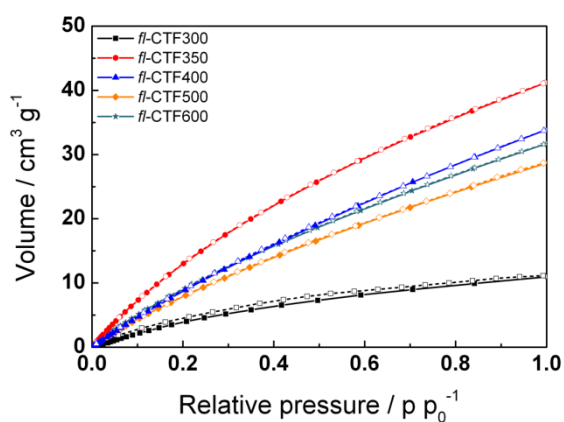


Figure 8.1.2.15. CO₂ adsorption (filled symbols) and desorption (open symbols) isotherms of the samples *fl*-CTF300, *fl*-CTF350, *fl*-CTF400, *fl*-CTF500 and *fl*-CTF600 at 313 K.

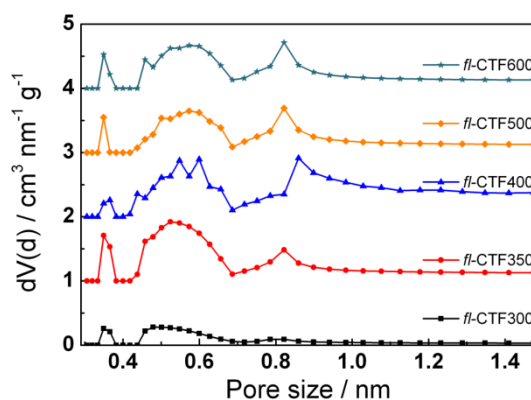


Figure 8.1.2.16. Pore size distributions of *fl*-CTF300, *fl*-CTF350, *fl*-CTF400, *fl*-CTF500 and *fl*-CTF600 from NLDFT calculations. The curves are shifted vertically in steps of 1 cm³ nm⁻¹ g⁻¹.

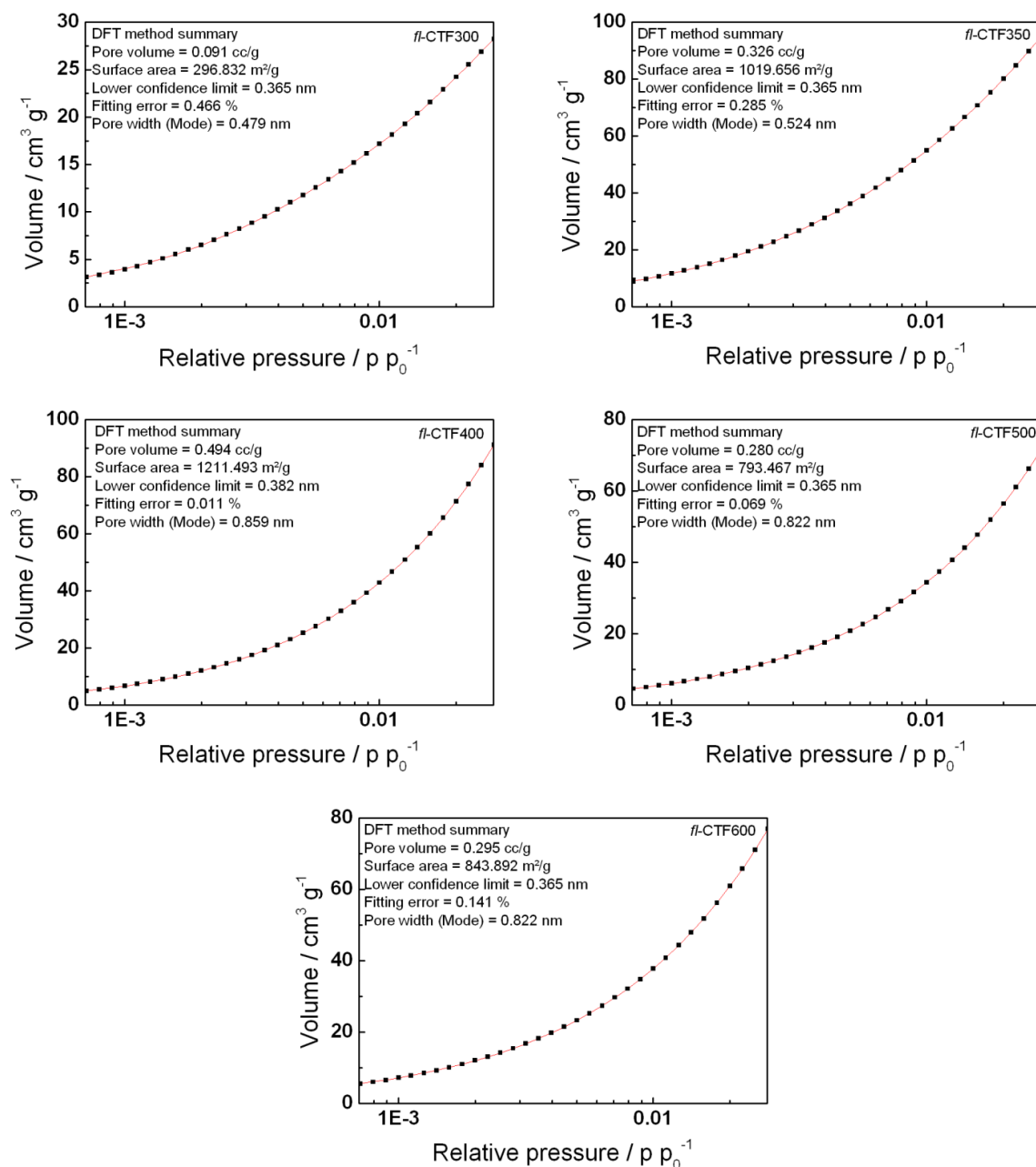


Figure 8.1.2.17. NLDFT-fittings for the argon isotherms of the samples *fl*-CTF300, *fl*-CTF350, *fl*-CTF400, *fl*-CTF500 and *fl*-CTF600.

N₂ Physisorption Measurements

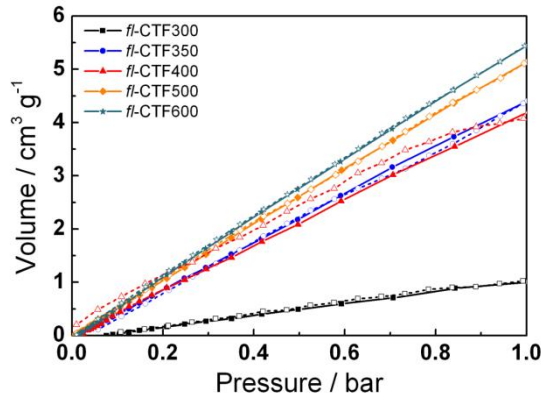


Figure 8.1.2.18. N₂ adsorption (filled symbols) and desorption (open symbols) isotherms of the samples *fl*-CTF300, *fl*-CTF350, *fl*-CTF400, *fl*-CTF500 and *fl*-CTF600 at 298 K.

CO₂/N₂ Selectivity Studies

Henry calculation

For selectivity calculations the ratio of the initial slopes in the Henry region of the adsorption isotherms of two different gases can be used.

The initial slopes are shown in Figure 8.1.2.18.

IAST calculation

Ideal adsorbed solution theory (IAST) calculations can be done by using a single or dual-site *Langmuir* model to fit the adsorption isotherms.^[4]

The single-site Langmuir model is defined as,

$$q = \frac{q_{sat} bp}{1 + bp} \quad (3)$$

q = molar loading of adsorbate

q_{sat} = saturation loading

b = Langmuir constant

The dual-site Langmuir model is defined as

$$q = q_A + q_B = \frac{q_{sat,A} b_A p}{1 + b_A p} + \frac{q_{sat,B} b_B p}{1 + b_B p} \quad (4)$$

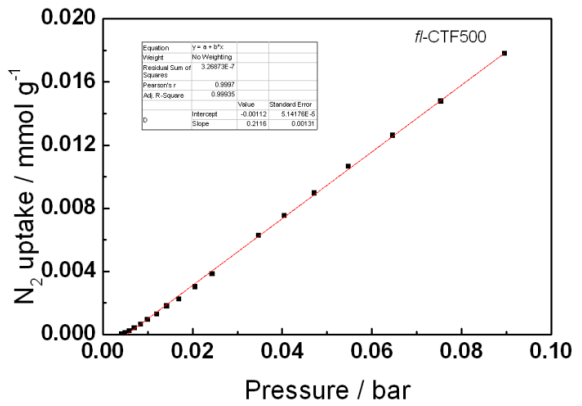
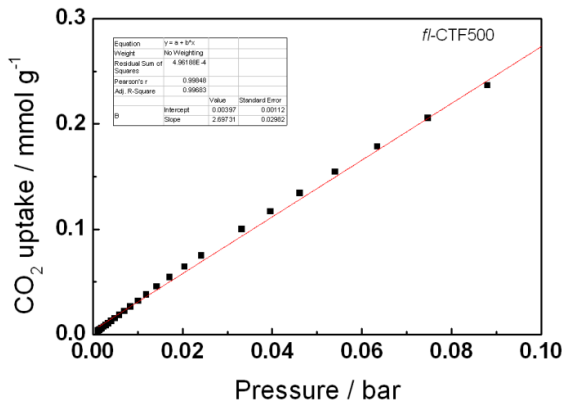
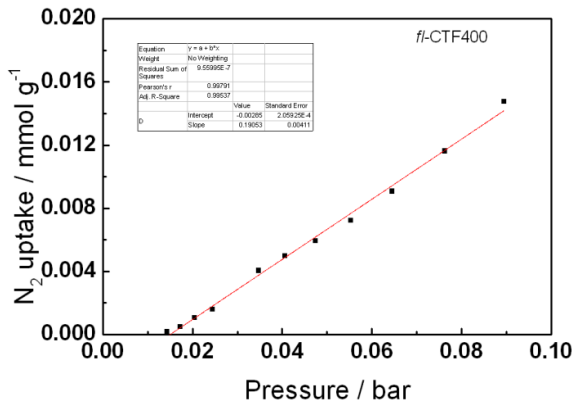
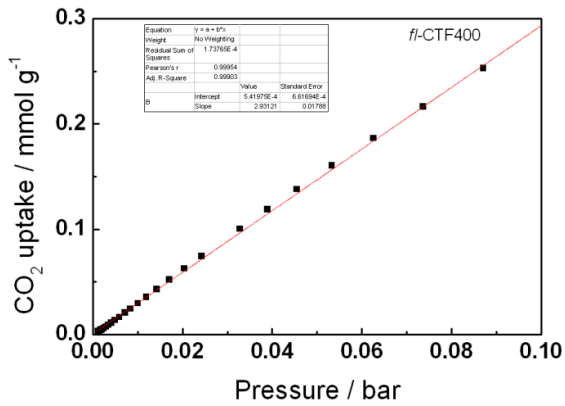
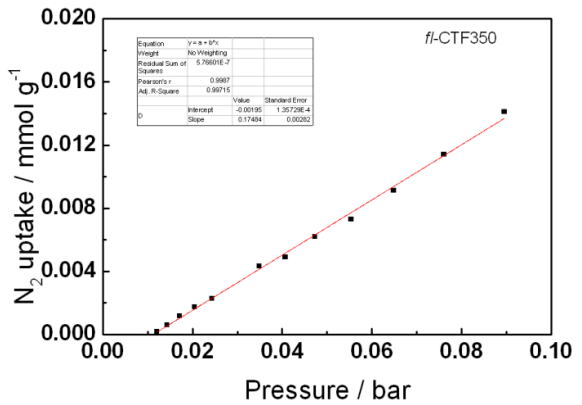
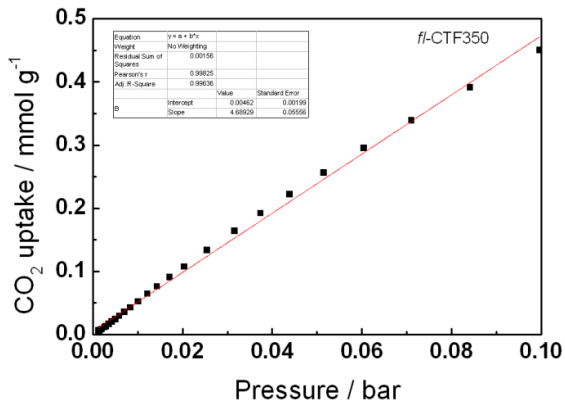
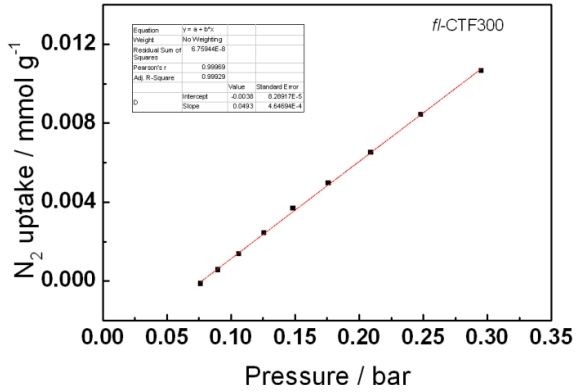
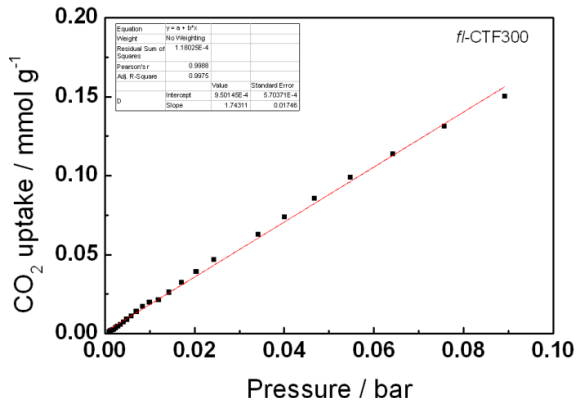
A, B = distinct adsorption sites

For the fitting of the adsorption isotherms the single-site Langmuir model was used. The fitted graphs and the values of the parameters are shown in Figure 8.1.2.19.

The selectivities are calculated using following equation:

$$S = \frac{q_1/q_2}{p_1/p_2} \quad (5)$$

A CO₂:N₂ ratio of 15:85 was used for calculating the gas mixture selectivities.



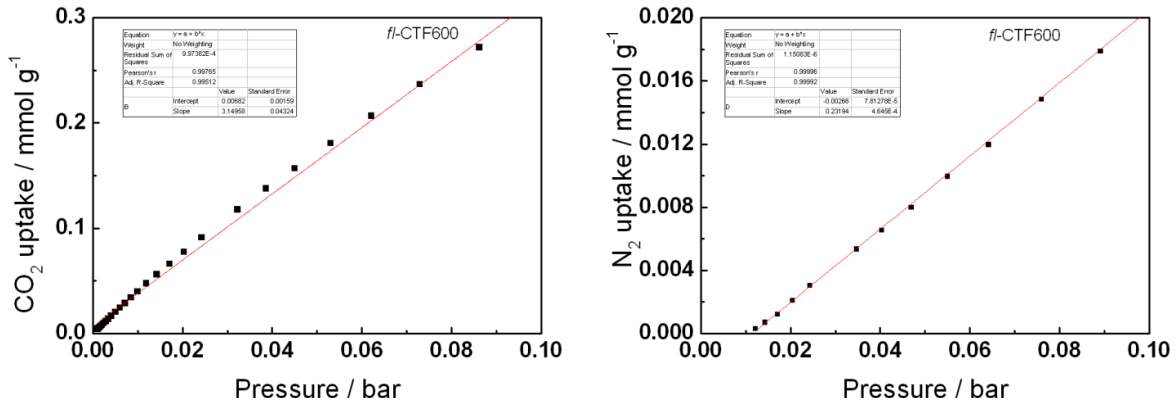
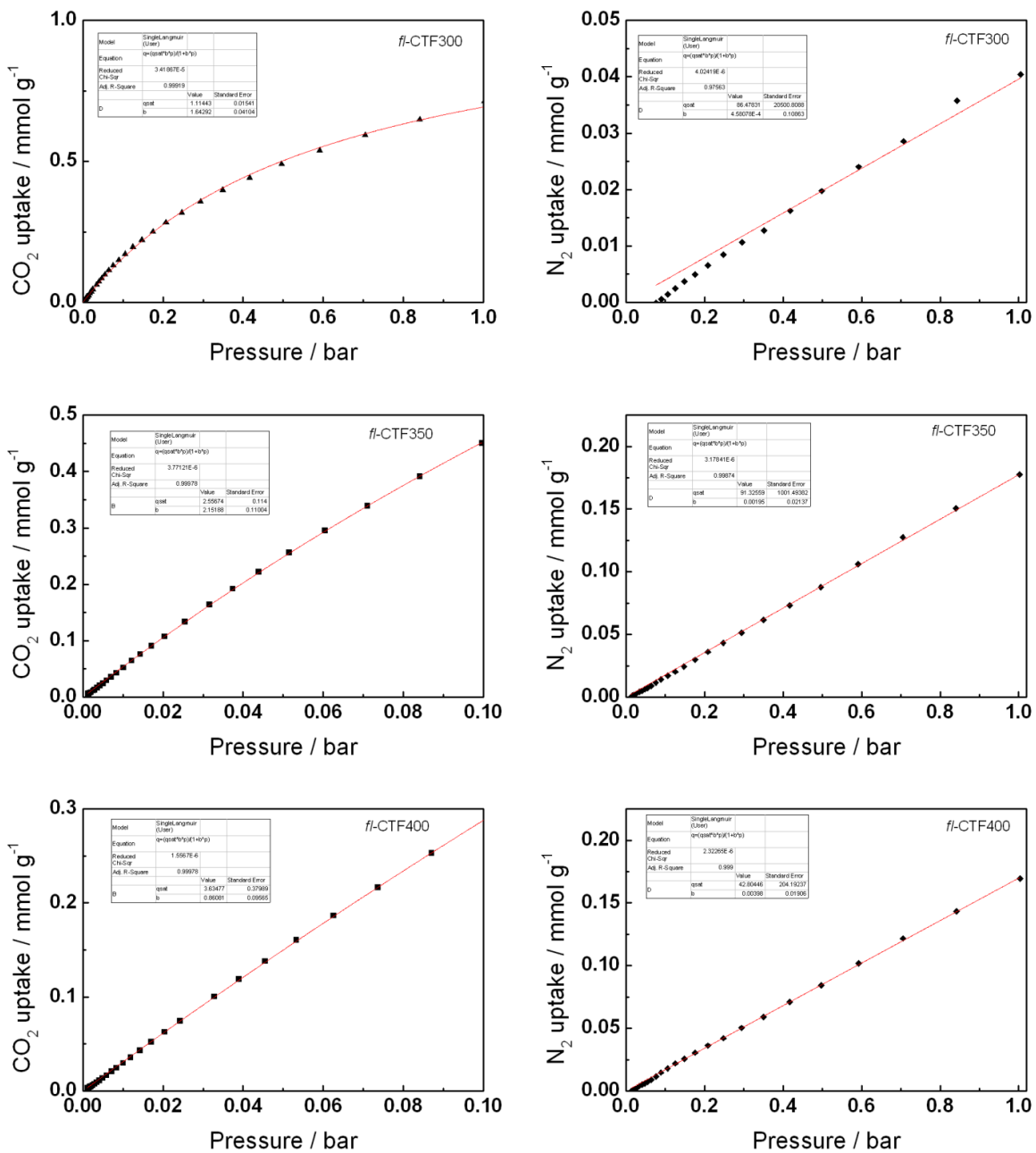


Figure 8.1.2.19. Henry plots of the samples *fl*-CTF300, *fl*-CTF350, *fl*-CTF400, *fl*-CTF500 and *fl*-CTF600 from CO₂ and N₂ isotherms at 298 K.



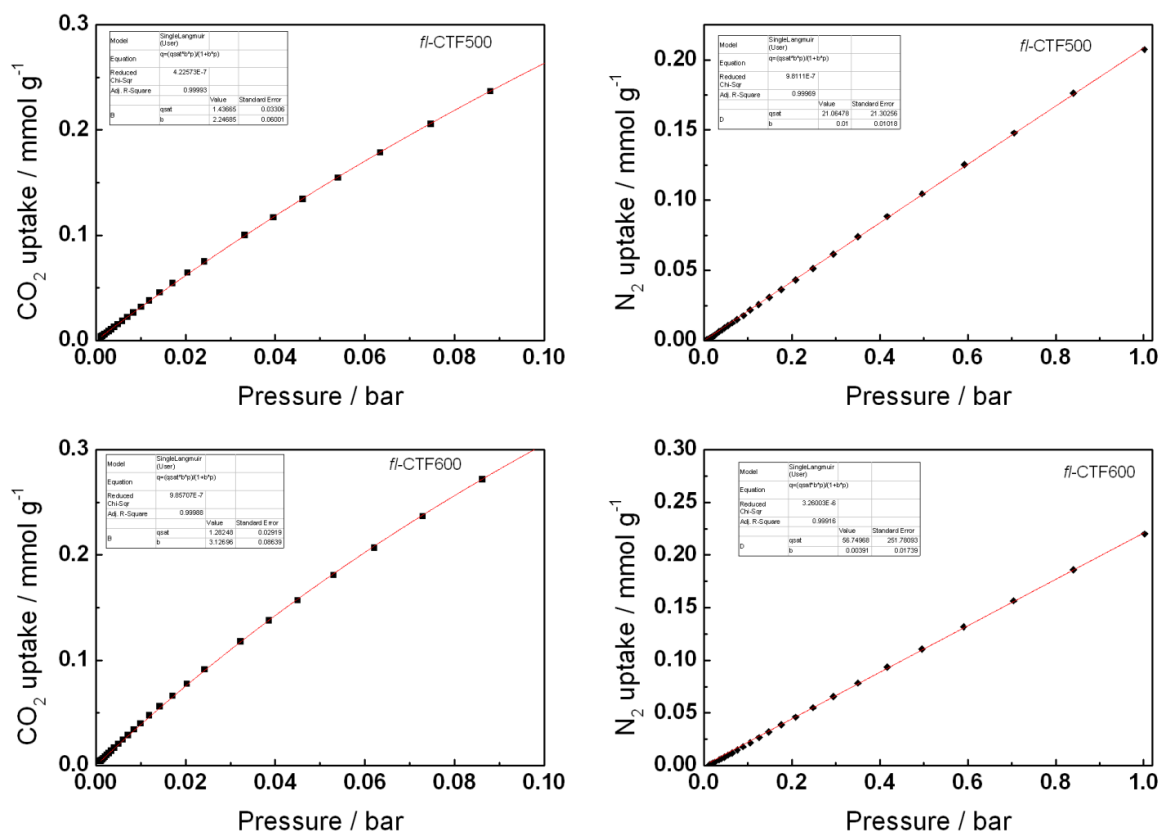


Figure 8.1.2.20. IAST-plots of the samples *fl*-CTF300, *fl*-CTF350, *fl*-CTF400, *fl*-CTF500 and *fl*-CTF600 from CO₂ and N₂ isotherms at 298 K.

Liquid NMR spectra

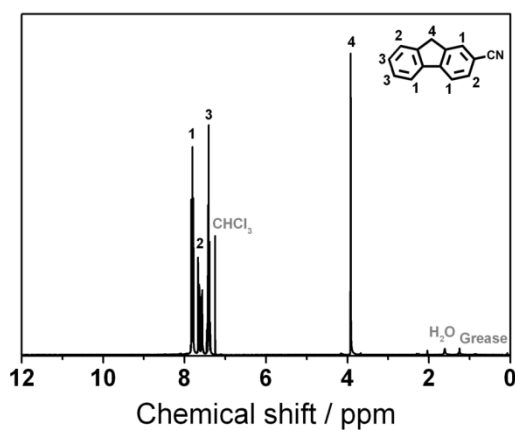


Figure 8.1.2.21. ¹H NMR spectrum of 9H-fluorene-2-carbonitrile.

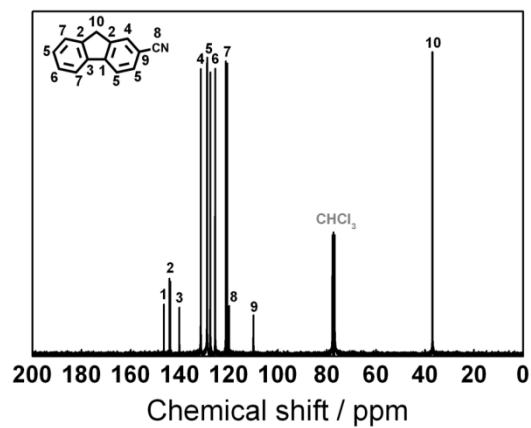


Figure 8.1.2.22. ^{13}C NMR spectrum of 9H-fluorene-2-carbonitrile.

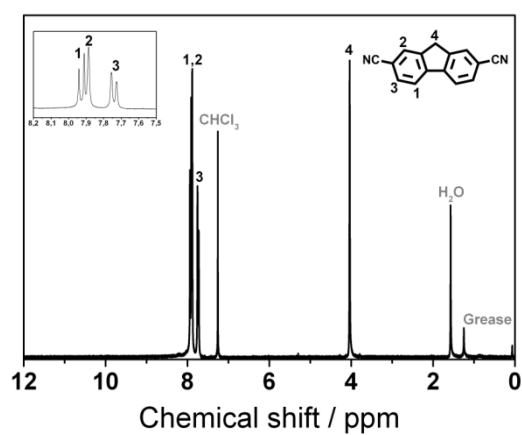


Figure 8.1.2.23. ^1H NMR spectrum of 9H-fluorene-2,7-dicarbonitrile.

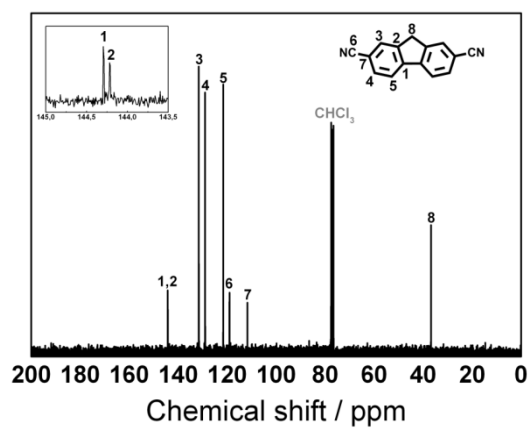
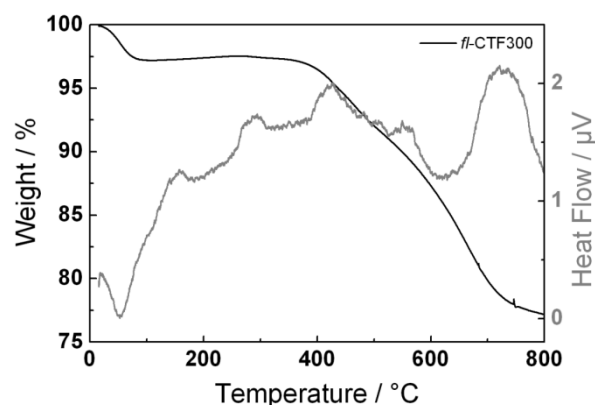
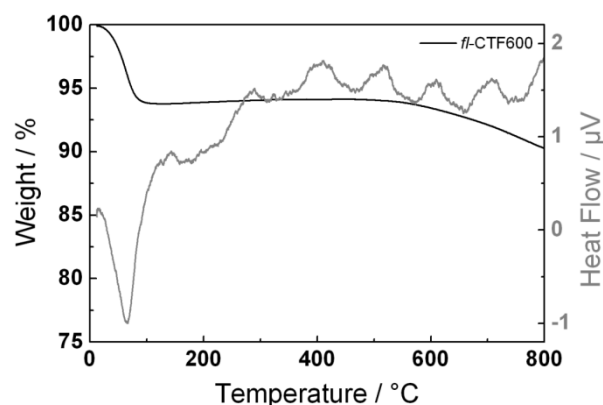


Figure 8.1.2.24. ^{13}C NMR spectrum of 9H-fluorene-2,7-dicarbonitrile.

DTA/TG measurements

Figure 8.1.2.25. DTA/TG measurement of *fl*-CTF300.Figure 8.1.2.26. DTA/TG measurement of *fl*-CTF600.Comparison of the CO₂ adsorption characteristics of POPsTable 8.1.2.7. Comparison of the CO₂ capacities, selectivities and heats of adsorption of some reported POPs.

POP	Porosity [m ² g ⁻¹] BET	CO ₂ capacity [mmol g ⁻¹]		Q _{st} [kJ mol ⁻¹]	Selectivity over N ₂ ^b		References
		273 K	298 K		Henry	IAST	
APOP-1	1298	4.26	2.69	26.6	20.3		
APOP-1-OH	875	2.89	1.86	30.0	26.0		
APOP-1-ONa	760	2.89	1.71	30.6	29.2		
APOP-1-F	724	3.07	2.02	33.3	31.8		[5]
APOP-2	906	2.27	1.30	31.7	20.2		
APOP-3	1402	4.45	2.59	27.5	26.0		
APOP-4	833	2.70	1.64	30.7	23.3		
azo-COP-1	635	2.44	1.48	29.3	113	97	
azo-COP-2	729	2.55	1.53	24.8	142	131	[6]
azo-COP-3	493	1.93	1.22	32.1	122	96	
BILP-1	1172	4.27	2.98	26.5	36		[7]
BILP-2	708	3.89	2.36	28.6	71		
BILP-3	1306	5.11	3.30	28.6	31		
BILP-4	1135	5.34	3.59	28.7	32		[8]
BILP-5	599	2.91	1.98	28.8	36		
BILP-6	1261	4.80	2.75	28.4	39		
BILP-7	1122	4.39	2.77	27.8	34		
BILP-10	787	4.02	~2.5	38.2	59	107	[9]
BLP-1	1360	1.82	0.97	25.3			[10]
BLP-12	2244	3.34	1.82	25.2			

Chapter 8: Appendix

CMP-1	837	2.05	1.18	~27				[11]
COF-1	750	2.32						
COF-5	1670	1.34						
COF-6	750	3.84						
COF-8	1350	1.43						[12-13]
COF-10	1760	1.21						
COF-102	3620	1.56						
COF-103	3530	1.70						
COP-3	413	1.68	1.14	24.5	24	107		[14]
CTF-0	2011	4.22						[15]
CTF-1	746	2.47	1.41	~27.5		20		[16]
CTF-1-600	1553	3.82	2.25	~30.0		13		
CTF-P2	776	1.88				20 ^c		
CTF-P3	571	2.27				23 ^c		
CTF-P4	867	3.12				17 ^c		
CTF-P5	960	3.00				24 ^c		
CTF-P6	1152	3.39				16 ^c		
CTF-P1M	4	0.94				31 ^c		[17]
CTF-P2M	464	1.91				21 ^c		
CTF-P3M	523	2.26				16 ^c		
CTF-P4M	542	1.87				22 ^c		
CTF-P5M	542	2.08				20 ^c		
CTF-P6M	947	4.20				14 ^c		
FCTF-1	662	4.67	3.21	35.0		31		[16]
FCTF-1-600	1535	5.53	3.41	~32		19		
HCP 1	1646	3.01	1.7	23.5				
HCP 2	1684	3.30	1.7	21.2				[18]
HCP 3	1531	3.24	1.6	22.1				
HCP 4	1642	3.92	1.6	21.6				
HCP-BDM	847	2.87	~1.7	33.5	27			
HCP-BA	742	1.92	~1.1	27.4	19			[19]
HCP-BC	746	1.91	~1.1					
HMP Th-1	726	2.88	~1.7	27	39 ^c			
HMP Py-1	437	2.71	~1.7	36	117 ^c			[20]
HMP Fu-1	514	2.21	~1.4	28	50 ^c			
ILCOF-1	2723	1.36	~0.8	18.3				[21]
ILP	744	1.97	1.05					
NC-600	366	2.33	1.65	~49				[22]
NC-700	284	2.13	1.80	~49				
NC-800	263	2.65	1.95	~45				
MCTF300	640	2.25	1.41	24.6				
MCTF400	1060	2.37	1.60	25.4				[23]
MCTF500	1510	3.16	2.26	26.3				
MOP-A (PAF-1)	4077	2.65	1.45	~24	9	8		
MOP-B (COF-300)	1847	3.29	1.63	~22	20	21		
MOP-C (Click network)	1237	3.86	2.20	33	14	20		
MOP-D (Tetrahedral-CMP)	1213	2.42	1.3	~26	12	15		[12]
MOP-E (TPM-HCP)	140	2.95	1.77	~25	9	12		
MOP-F (CMP-NH ₂ CH ₃)	653	1.80	1.08	~27	12	18		
MOP-G (CMP carbazole)	1056	2.15	1.25	~27	15	25		
MOP A-B1	378	2.67	2.01 ^a	30.0		68 ^c		
MOP A-B2	614	2.71	1.90 ^a	33.4		56 ^c		[24]
MOP A-B3	589	2.24	1.71 ^a	28.4		65 ^c		
MPI-1	1454	3.81	~2.2	34.8	102 ^c			
MPI-2	814	3.14	~2.2	30.4	71 ^c			[25]
MPI-3	586	2.25	~1.7	31.4	41 ^c			
NPAF	1790	3.64	2.32	19		88		[26]

Chapter 8: Appendix

NPOF-4	1249	2.50	1.40	23.2	16	12	
NPOF-4-NO ₂	337	2.42	1.56	32.5	66	59	[27]
NPOF-4-NH ₂	554	2.90	1.88	30.1	40	38	
PAF-1	5460	2.07	1.09	15.6	38 ^c		
PAF-3	2932	3.51	1.84	19.2	87 ^c		[28]
PAF-4	2246	2.43	1.16	16.2	44 ^c		
PAF-1-350	4033	3.10		21.2			
PAF-1-380	2881	3.37		23.6			[29]
PAF-1-400	2292	3.71		26.7			
PAF-1-450	1191	4.50		27.8		209 ^c	
PAF-16-2	979	1.90	1.18	30.3			[30]
PBI-1	62	3.00	~1.6	34.2			[31]
PBI-2	85	1.02	~0.2	32.4			
PCTF-1	2235	3.23	1.89 ^a	30	13 ^c	14 ^c	[32-33]
PCTF-2	784	1.84	1.02 ^a	26	9 ^c	14 ^c	
PCTF-3	641	2.16	1.36 ^a	27	16 ^c	25 ^c	
PCTF-4	1090	2.29	1.53 ^a	28	17 ^c	26 ^c	[32]
PCTF-5	1183	2.57	1.52 ^a	27	17 ^c	32 ^c	
PCTF-7	613	2.17	1.35 ^a	25	22 ^c	41 ^c	
PECONF-1	499	1.86	1.34	29	51		
PECONF-2	637	2.85	1.98	31	44		[34]
PECONF-3	851	3.49	2.47	26	41		
PECONF-4	-	2.95	1.96	34	51		
PI-1	506	~2.0	1.41	34	27		[35]
PI-2	568	~1.5	1.00	27	12		
PI1	660	1.66					[36]
PI2	265	0.61					
PI3	366	1.36					
PIF	39		0.31				
PIF-5	121		1.35				
PIF-6	527		3.20	42.7	59		[37]
PIF-7	1038		3.42				
PIF-8	1185		2.75				
POF1B	917	4.23	2.16				[38]
PP-N-100	318	2.54		~40			
PP-N-75	689	3.13		~37			
PP-N-50	1141	3.86		~35			[39]
PP-N-25	1257	4.60		~34			
PP-N-0	1530	3.90		~26			
PPF-1	1740	6.12		25.6		15 ^c	
PPF-2	1470	5.54		29.2		15 ^c	[40]
PPF-3	419	2.09		21.8		20 ^c	
PPF-4	726	2.59		25.1		15 ^c	
PPN-6-CH ₂ DETA	555		4.30	~56		442 ^e	[41]
SMPI-0	574	2.53	1.43	36	30 ^c		
SMPI-10	112	3.15	1.87	33	32 ^c		[42]
SMPI-50	44	2.96	1.61	30	48 ^c		
SMPI-100	23	2.82	1.87	30	58 ^c		
SNU-C1-va	595	3.49	2.31	34.9			[43]
SNU-C1-sca	830	4.38	3.14	31.2			
STP-1	1305	3.67					[44]
STP-2	1990	4.14					
TB-MOP	694	4.05	2.57	29.5	51		[25]
TC-EMC	3840		3.3	30		1.3	
TC-Y1	3519		3.0				
TC-Y2	1815		1.6				[45]
N-TC-EMC	2559		4.0	50		6.1	
N-TC-Y1	1762		3.2				
N-TC-Y2	1361		2.6				
TDCOF-5	2497	2.1	~1.2	21.8			[46]

TPI-1	809	2.45	1.25	34.4	31	
TPI-2	796	2.45	1.23	31.4	34	
TPI-3	40	0.68	0.43	32.3	35	
TPI-4	245	1.85	1.11	33.6	46	[47]
TPI-5	201	1.57	0.96	30.0	46	
TPI-6	510	2.02	1.10	29.2	34	
TPI-7	<10	1.81	1.10	32.4	56	
TpPa-1	535	3.54				
TpPa-NO ₂	129	3.23				
TpPa-2	339	2.79				
TpBD-(NO ₂) ₂	295	2.30				[48]
TpBD	537	1.78				
TpBD-Me ₂	468	1.64				
TpPa-F ₄	438	1.55				
TpBD-(OMe) ₂	330	1.20				
O-TTPP	593	2.26	1.56	28.6	21	[49]
S-TTPP	606	1.81	1.04	28.0	22	

^a at 293K, ^b at 298 K, ^c at 273K, ^d "break through" measurement adjustment, ^e at 295K.

References

- [1] X. L. Wu, K. W. Zilm, *J. Magn. Reson. A* **1993**, *102*, 205-213.
- [2] B. Jürgens, E. Irran, J. Senker, P. Kroll, H. Müller, W. Schnick, *J. Am. Chem. Soc.* **2003**, *125*, 10288-10300.
- [3] C. Gervais, F. Babonneau, J. Maquet, C. Bonhomme, D. Massiot, E. Framery, M. Vaultier, *Magn. Reson. Chem.* **1998**, *36*, 407-414.
- [4] A. L. Myers, J. M. Prausnitz, *AIChE J.* **1965**, *11*, 121-127.
- [5] W.-C. Song, X.-K. Xu, Q. Chen, Z.-Z. Zhuang, X.-H. Bu, *Polym. Chem.* **2013**, *4*, 4690-4696.
- [6] H. A. Patel, S. Hyun Je, J. Park, D. P. Chen, Y. Jung, C. T. Yavuz, A. Coskun, *Nat. Commun.* **2013**, *4*, 1357.
- [7] M. G. Rabbani, H. M. El-Kaderi, *Chem. Mater.* **2011**, *23*, 1650-1653.
- [8] M. G. Rabbani, H. M. El-Kaderi, *Chem. Mater.* **2012**, *24*, 1511-1517.
- [9] M. G. Rabbani, A. K. Sekizkardes, O. M. El-Kadri, B. R. Kaafarani, H. M. El-Kaderi, *J. Mater. Chem.* **2012**, *22*, 25409-25417.
- [10] K. T. Jackson, M. G. Rabbani, T. E. Reich, H. M. El-Kaderi, *Polym. Chem.* **2011**, *2*, 2775-2777.
- [11] R. Dawson, D. J. Adams, A. I. Cooper, *Chem. Sci.* **2011**, *2*, 1173-1177.
- [12] R. Dawson, E. Stockel, J. R. Holst, D. J. Adams, A. I. Cooper, *Energy Environ. Sci.* **2011**, *4*, 4239-4245.
- [13] H. Furukawa, O. M. Yaghi, *J. Am. Chem. Soc.* **2009**, *131*, 8875-8883.
- [14] H. A. Patel, F. Karadas, J. Byun, J. Park, E. Deniz, A. Canlier, Y. Jung, M. Atilhan, C. T. Yavuz, *Adv. Funct. Mater.* **2013**, *23*, 2270-2276.
- [15] P. Katekomol, J. Roeser, M. Bojdys, J. Weber, A. Thomas, *Chem. Mater.* **2013**, *25*, 1542-1548.
- [16] J. Liu, H. Chen, S. Zheng, Z. Xu, *J. Chem. Eng. Data* **2013**.

-
- [17] S. Ren, M. J. Bojdys, R. Dawson, A. Laybourn, Y. Z. Khimyak, D. J. Adams, A. I. Cooper, *Adv. Mater.* **2012**, *24*, 2357-2361.
- [18] C. F. Martin, E. Stockel, R. Clowes, D. J. Adams, A. I. Cooper, J. J. Pis, F. Rubiera, C. Pevida, *J. Mater. Chem.* **2011**, *21*, 5475-5483.
- [19] Y. Luo, S. Zhang, Y. Ma, W. Wang, B. Tan, *Polym. Chem.* **2013**, *4*, 1126-1131.
- [20] Y. Luo, B. Li, W. Wang, K. Wu, B. Tan, *Adv. Mater.* **2012**, *24*, 5703-5707.
- [21] M. G. Rabbani, A. K. Sekizkardes, Z. Kahveci, T. E. Reich, R. Ding, H. M. El-Kaderi, *Chem. Eur. J.* **2013**, *19*, 3324-3328.
- [22] J. Wang, I. Senkovska, M. Oschatz, M. R. Lohe, L. Borchardt, A. Heerwig, Q. Liu, S. Kaskel, *ACS Appl. Mater. Interfaces* **2013**, *5*, 3160-3167.
- [23] X. Liu, H. Li, Y. Zhang, B. Xu, S. A, H. Xia, Y. Mu, *Polym. Chem.* **2013**, *4*, 2445-2448.
- [24] C. Xu, N. Hedin, *J. Mater. Chem. A* **2013**, *1*, 3406-3414.
- [25] X. Zhu, C.-L. Do-Thanh, C. R. Murdock, K. M. Nelson, C. Tian, S. Brown, S. M. Mahurin, D. M. Jenkins, J. Hu, B. Zhao, H. Liu, S. Dai, *ACS Macro Lett.* **2013**, *2*, 660-663.
- [26] D. E. Demirocak, M. K. Ram, S. S. Srinivasan, D. Y. Goswami, E. K. Stefanakos, *J. Mater. Chem. A* **2013**, *1*, 13800-13806.
- [27] T. Islamoglu, M. Gulam Rabbani, H. M. El-Kaderi, *J. Mater. Chem. A* **2013**, *1*, 10259-10266.
- [28] T. Ben, C. Pei, D. Zhang, J. Xu, F. Deng, X. Jing, S. Qiu, *Energy Environ. Sci.* **2011**, *4*, 3991-3999.
- [29] T. Ben, Y. Li, L. Zhu, D. Zhang, D. Cao, Z. Xiang, X. Yao, S. Qiu, *Energy Environ. Sci.* **2012**, *5*, 8370-8376.
- [30] W. Wang, H. Ren, F. Sun, K. Cai, H. Ma, J. Du, H. Zhao, G. Zhu, *Dalton Trans.* **2012**, *41*, 3933-3936.
- [31] H. Yu, M. Tian, C. Shen, Z. Wang, *Polym. Chem.* **2013**, *4*, 961-968.
- [32] A. Bhunia, I. Boldog, A. Moller, C. Janiak, *J. Mater. Chem. A* **2013**, *1*, 14990-14999.
- [33] A. Bhunia, V. Vasyleva, C. Janiak, *Chem. Commun.* **2013**, *49*, 3961-3963.
- [34] P. Mohanty, L. D. Kull, K. Landskron, *Nat. Commun.* **2011**, *2*, 401.
- [35] A. Laybourn, R. Dawson, R. Clowes, J. A. Iggo, A. I. Cooper, Y. Z. Khimyak, D. J. Adams, *Polym. Chem.* **2012**, *3*, 533-537.
- [36] Y. Luo, B. Li, L. Liang, B. Tan, *Chem. Commun.* **2011**, *47*, 7704-7706.
- [37] M. Saleh, J. N. Tiwari, K. C. Kemp, M. Yousuf, K. S. Kim, *Environ. Sci. Technol.* **2013**.
- [38] A. P. Katsoulidis, M. G. Kanatzidis, *Chem. Mater.* **2011**, *23*, 1818-1824.
- [39] Y. Yang, Q. Zhang, S. Zhang, S. Li, *Polymer* **2013**, *54*, 5698-5702.
- [40] Y. Zhu, H. Long, W. Zhang, *Chem. Mater.* **2013**, *25*, 1630-1635.
- [41] W. Lu, J. P. Sculley, D. Yuan, R. Krishna, Z. Wei, H.-C. Zhou, *Angew. Chem. Int. Ed.* **2012**, *51*, 7480-7484.
-

- [42] Y. Yang, Q. Zhang, Z. Zhang, S. Zhang, *J. Mater. Chem. A* **2013**, *1*, 10368-10374.
- [43] L.-H. Xie, M. P. Suh, *Chem. Eur. J.* **2013**, *19*, 11590-11597.
- [44] C. Zhang, Y. Liu, B. Li, B. Tan, C.-F. Chen, H.-B. Xu, X.-L. Yang, *ACS Macro Lett.* **2011**, *1*, 190-193.
- [45] L. Wang, R. T. Yang, *J. Phys. Chem. C* **2011**, *116*, 1099-1106.
- [46] Z. Kahveci, T. Islamoglu, G. A. Shar, R. Ding, H. M. El-Kaderi, *CrystEngComm* **2013**, *15*, 1524-1527.
- [47] M. R. Liebl, J. Senker, *Chem. Mater.* **2013**, *25*, 970-980.
- [48] S. Chandra, S. Kandambeth, B. P. Biswal, B. Lukose, S. M. Kunjir, M. Chaudhary, R. Babarao, T. Heine, R. Banerjee, *J. Am. Chem. Soc.* **2013**, *135*, 17853-17861.
- [49] X. Chen, S. Qiao, Z. Du, Y. Zhou, R. Yang, *Macromol. Rapid Commun.* **2013**, *34*, 1181-1185.

8.1.3 SUPPORTING INFORMATION FOR CHAPTER 4.2

Materials**Used commercially available chemicals****Table 8.1.3.1.** Chemicals used with distributor and purity grade.

Chemical	Formula	Distributor	Purity grade
3-Aminocrotonitrile	C ₄ H ₆ N ₂	Acros Organics	96%
Bis(dibenzylideneacetone)palladium(0)	C ₃₄ H ₂₈ O ₂ Pd	Sigma-Aldrich	-
1,5-Bis(diphenylphosphino)pentane	C ₂₉ H ₃₀ P ₂	Alfa Aesar	97%
Bromine	Br ₂	Merck	99%
5-Bromo-2-iodopyridine	C ₅ H ₃ BrI	Fluorochem	98%
Chlorotrimethylsilane	C ₃ H ₉ ClSi	Sigma-Aldrich	98%
1,2-Dibromoethane	C ₂ H ₄ Br ₂	Fluka	98%
Dichloromethane	CH ₂ Cl ₂	Brenntag	99.9%
1,4-Dicyanobenzene	C ₈ H ₄ N ₂	Acros Organics	98%
<i>N,N</i> -dimethylaniline	C ₈ H ₁₁ N	Sigma-Aldrich	99%
<i>N,N</i> -dimethylformamide	C ₃ H ₇ NO	Acros Organics	99.8%
Ethyl orthoformate	C ₇ H ₁₆ O ₃	Sigma-Aldrich	98%
Hafnium trifluoromethanesulfonate	C ₄ F ₁₂ HfO ₁₂ S ₄	Alfa Aesar	98%
Hydrogen iodide	HI in H ₂ O	Merck	57%
2-Hydroxypyrimidine hydrochloride	C ₄ H ₄ N ₂ O·HCl	Alfa Aesar	98%
Lithium chloride	LiCl	Grüssing	99%
Magnesium	Mg	Grüssing	99%
Phosphorus oxychloride	POCl ₃	Acros Organics	99%
Tetrahydrofuran	C ₄ H ₈ O	AppliChem	99.5%
Tetrakis(triphenylphosphine)palladium(0)	C ₇₂ H ₆₀ P ₄ Pd	Sigma-Aldrich	99%
Zinc chloride	ZnCl ₂	Sigma-Aldrich	99.995%
Zinc cyanide	Zn(CN) ₂	ABCR	98%

Precursor synthesis

(5-Bromopyridin-2-yl)zinc(II) chloride.^[1] In a Schlenk tube dry LiCl (2.24 g, 52.8 mmol) and Mg turnings (1.46 g, 60 mmol) were suspended in dry THF (22 mL). 1,2-Dibromoethane (0.10 mL, 1.2 mmol) and chlorotrimethylsilane (0.15 mL, 1.2 mmol) were added and the suspension heated shortly to reflux. The reaction was cooled to 25 °C and a solution of ZnCl₂ in THF (1 M, 26.4 mL, 26.4 mmol) and, subsequently, 5-bromo-2-iodopyridine (6.95 g, 24 mmol) were added. The mixture was stirred for 6 h at 25 °C and left for three days to precipitate metal residues. The resulting solution was used without any further purification. The concentration of (5-Bromopyridin-2-yl)zinc(II) chloride was determined by iodolysis^[2] (0.48 M, 97 %).

5,5'-Dibromo-2,2'-bipyridine.^[3] (5-bromopyridin-2-yl)zinc(II) chloride (0.48 M in THF, 45.0 mL, 21.6 mmol), Pd(dba)₂ (311 mg, 0.54 mmol), and tri(2-furyl)phosphine (251 mg, 1.08 mmol) were mixed in a Schlenk flask. 5-bromo-2-iodopyridine (5.21 g, 18 mmol) in dry THF (15 mL) was slowly added and the mixture was stirred for 1 h at 50 °C. The reaction was quenched by the addition of a saturated aqueous solution of NH₄Cl (200 mL) and the resulting mixture was extracted with CHCl₃.

(5 × 200 mL). The combined organic layers were dried over Na₂SO₄ and concentrated *in vacuo*. The crude product was purified by flash column chromatography (CH₂Cl₂/n-hexane 2:1, 0.5% NEt₃) yielding 5,5'-dibromo-2,2'-bipyridine as tanned crystals (3.09 g, 9.84 mmol, 55 %). ¹H NMR (270 MHz; CDCl₃): δ 8.70 (2 H, d, ⁴J_{HH} = 2 Hz, C^{5/5'}H), 8.29 (2 H, d, ³J_{HH} = 9 Hz, C^{2/2'}H), 7.93 (2 H, dd, ³J_{HH} = 9 Hz, ⁴J_{HH} = 2 Hz, C^{3/3'}H); ¹³C{¹H} NMR (68 MHz; CDCl₃): δ 153.6 (C^{1/1'}), 150.3 (C^{5/5'}), 139.8 (C^{3/3'}), 122.4 (C^{2/2'}), 121.6 (C^{4/4'}).

5,5'-Dicyano-2,2'-bipyridine.^[4] A microwave vial was charged with degassed DMF (13.0 mL), 5,5'-dibromo-2,2'-bipyridine (801 mg, 2.55 mmol), Zn(CN)₂ (599 mg, 5.10 mmol), Pd(PPh₃)₄ (177 mg, 0.15 mmol), and 1,5-bis(diphenylphosphino)pentane (69.5 mg, 0.15 mmol). A stream of argon was then bubbled through the mixture for 2 min and the vial was sealed. The yellow mixture was heated in the microwave for 5 min at 150 °C. The now turquoise suspension was quenched by the addition of water (75 mL) and a saturated aqueous solution of NaHCO₃ (75 mL). The water layer was extracted with CHCl₃ (4 × 150 mL), the combined organic layers were dried over Na₂SO₄ and concentrated *in vacuo*. The crude product was purified by flash column chromatography (100% CHCl₃) to give 5,5'-dicyano-2,2'-bipyridine as colorless crystals (499 mg, 2.42 mmol, 95 %). ¹H NMR (400 MHz; CDCl₃): δ 8.96 (2 H, d, ⁴J_{HH} = 2 Hz, C^{5/5'}H), 8.63 (2 H, dd, ³J_{HH} = 8 Hz, ⁵J_{HH} = 1 Hz, C^{2/2'}H), 8.13 (2 H, dd, ³J_{HH} = 8 Hz, ⁴J_{HH} = 2 Hz, C^{3/3'}H); ¹³C{¹H} NMR (100 MHz; CDCl₃): δ 157.0 (C^{1/1'}), 152.2 (C^{5/5'}), 140.6 (C^{3/3'}), 121.8 (C^{2/2'}), 116.6 (C^{4/4'}), 110.8 (C^{6/6'}).

5-Bromo-2-hydroxypyrimidine.^[5] 2-Hydroxypyrimidine hydrochloride (19.9 g, 150 mmol) was diluted in water (350 mL) and bromine (8.6 mL, 168 mmol) was added slowly. The dark orange solution was stirred at 25 °C for 30 min and then heated at 85 °C until the solution turned light yellow (1 h). The solvent was removed *in vacuo* and the crude product was recrystallized from aqueous ethanol (90%) to give 5-bromo-2-hydroxypyrimidine as yellow solid (18.3 g, 104 mmol, 70%). ¹H NMR (270 MHz; DMSO-d₆): δ 8.40 (2 H, s, Ar), 5.20 (1 H, br, OH); ¹³C{¹H} NMR (68 MHz; DMSO-d₆): δ 158.2, 157.0, 99.1.

5-Bromo-2-chloropyrimidine.^[5] 5-Bromo-2-hydroxypyrimidine (14.4 g, 82.3 mmol) was suspended in POCl₃ (100 mL) in a dry three neck flask. After the addition of *N,N*-dimethylaniline (10.4 mL, 82.3 mmol) the mixture was heated to reflux for 4 h. The reaction was very slowly quenched with 2 L ice water and the water phase was extracted with diethylether (5 × 400 mL). The combined organic phases were washed with a saturated aqueous solution of NaHCO₃ (200 mL), dried over MgSO₄ and concentrated *in vacuo* to give 5-bromo-2-chloropyrimidine as yellow crystals (11.6 g, 59.9 mmol, 73%). ¹H NMR (270 MHz; CDCl₃): δ 8.60 (2 H, s, Ar); ¹³C{¹H} NMR (68 MHz; CDCl₃): δ 160.2, 159.7, 118.9.

5-Bromo-2-iodopyrimidine.^[5] In a 250 mL Schlenk flask 5-bromo-2-chloropyrimidine (11.6 g, 60 mmol) was suspended in dichloromethane (30 mL) and cooled to 0 °C. Hydrogen iodide (39.6 mL,

300 mmol) was added dropwise and the mixture was stirred at 0 °C for 5 h. After neutralization with solid K₂CO₃ and a saturated aqueous solution of NaHCO₃ the mixture was decolorized by the addition of a saturated aqueous solution of Na₂S₂O₅. The water phase was extracted with dichloromethane (5 × 200 mL) and the combined organic phases were dried over K₂CO₃. The solvent was removed *in vacuo* and the crude product was recrystallized from petroleum ether to give 5-bromo-2-iodopyrimidine as colorless crystals (13.5 g, 47.5 mmol, 79%). ¹H NMR (270 MHz; CDCl₃): δ 8.50 (2 H, s, Ar); ¹³C{¹H} NMR (68 MHz; CDCl₃): δ 159.3, 125.9, 121.1.

Parameters used for the CTF synthesis

Table 8.1.3.2. Synthesis parameters used for the CTFs discussed in this work.

Sample	Eq. ZnCl ₂	Temperature	Time
<i>pym</i> -CTF300	5	300 °C	168 h
<i>pym</i> -CTF350	5	350 °C	96 h
<i>pym</i> -CTF400	5	400 °C	48 h
<i>pym</i> -CTF500	5	500 °C	48 h
<i>pym</i> -CTF600	5	600 °C	48 h
CTF1-400	1 ^a	400 °C	48 h
CTF1-500	5	500 °C	48 h
CTF1-600	5	600 °C	48 h
<i>bipy</i> -CTF300	5	300 °C	168 h
<i>bipy</i> -CTF400	5	400 °C	48 h
<i>bipy</i> -CTF500	5	500 °C	48 h
<i>bipy</i> -CTF600	5	600 °C	48 h
<i>lut</i> -CTF300	5	300 °C	168 h
<i>lut</i> -CTF350	5	350 °C	96 h
<i>lut</i> -CTF400	5	400 °C	48 h
<i>lut</i> -CTF500	5	500 °C	48 h
<i>lut</i> -CTF600	5	600 °C	48 h

^aThe precursor/ZnCl₂ ratio was chosen according to Reference [20] within the article.

Temperature programs of CTF synthesis

Table 8.1.3.3. Temperature programs of the different synthesized CTFs.

Sample	Heating rate [°C h ⁻¹]	Target temperature [°C]	Holding time [h]	Cooling rate [°C h ⁻¹]
<i>pym</i> -CTF300	60	300	168	10 ^a
<i>pym</i> -CTF350	60	350	96	10 ^b
<i>pym</i> -CTF400	60	400	48	10 ^c
<i>pym</i> -CTF500	60	500	48	10 ^c
<i>pym</i> -CTF600	60	600	48	10 ^c
CTF1-400	60	400	48	10 ^c
CTF1-500	60	500	48	10 ^c
CTF1-600	60	600	48	10 ^c
<i>bipy</i> -CTF300	60	300	168	10 ^a
<i>bipy</i> -CTF400	60	400	48	10 ^c
<i>bipy</i> -CTF500	60	500	48	10 ^c
<i>bipy</i> -CTF600	60	600	48	10 ^c
<i>lut</i> -CTF300	60	300	168	10 ^a
<i>lut</i> -CTF350	60	350	96	10 ^b
<i>lut</i> -CTF400	60	400	48	10 ^c
<i>lut</i> -CTF500	60	500	48	10 ^c
<i>lut</i> -CTF600	60	600	48	10 ^c

^aAt 80 °C the oven was turned off. ^bAt 150 °C the oven was turned off. ^cAt 240 °C the oven was turned off.

Powder X-ray diffraction

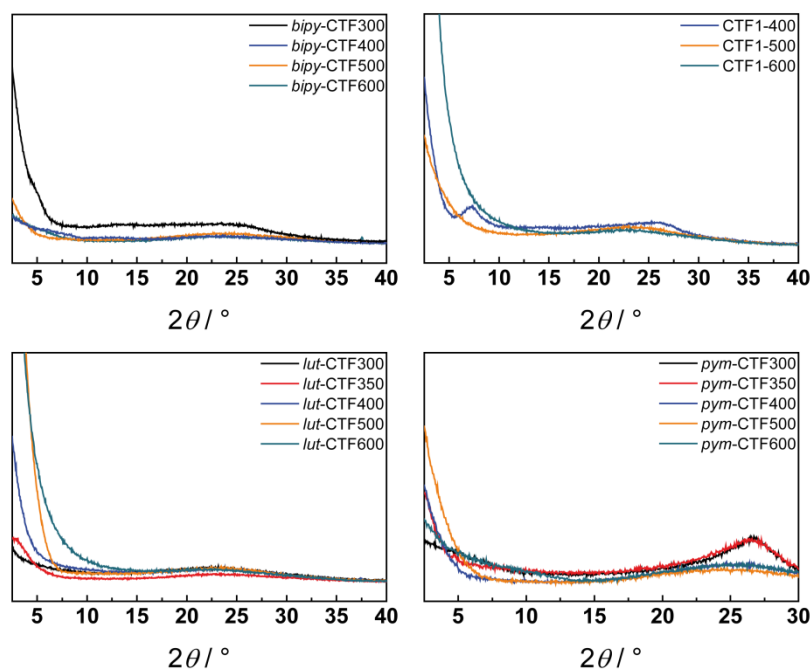


Figure 8.1.3.1. Powder X-ray diffraction measurements of the presented CTFs, indicating that all CTFs are X-ray amorphous.

Solid-state NMR spectra

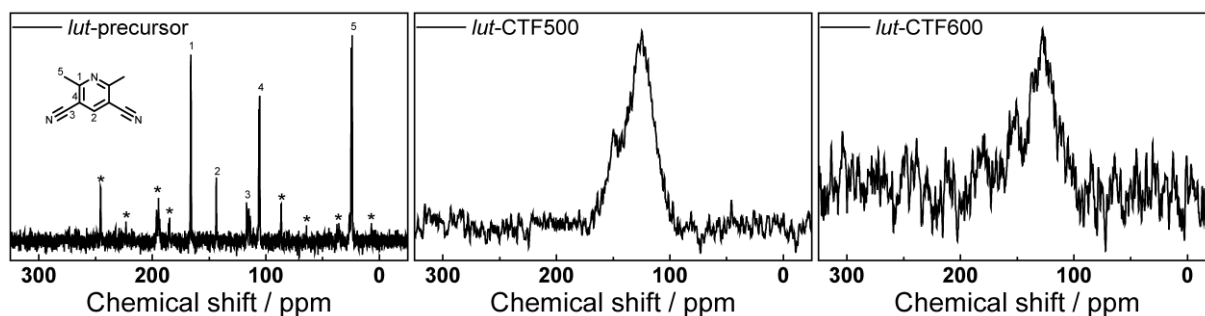


Figure 8.1.3.2. ^{13}C MAS ssNMR spectra of 2,6-dimethylpyridine-3,5-dicarbonitrile (left), *lut*-CTF500 (middle) and *lut*-CTF600 (right). Note that the low signal to noise ratio for the *lut*-CTF600 sample indicates graphitization of the sample.

Argon physisorption measurements

Isotherms and pore size distributions

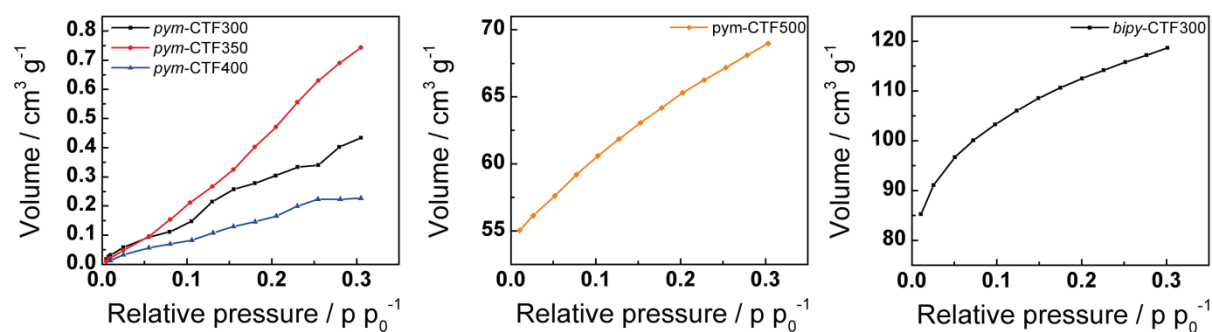


Figure 8.1.3.3. Argon 13-point isotherms of *pym*-CTF300-400 (left), *pym*-CTF500 (middle) and *bipy*-CTF300 (right) for BET calculations.

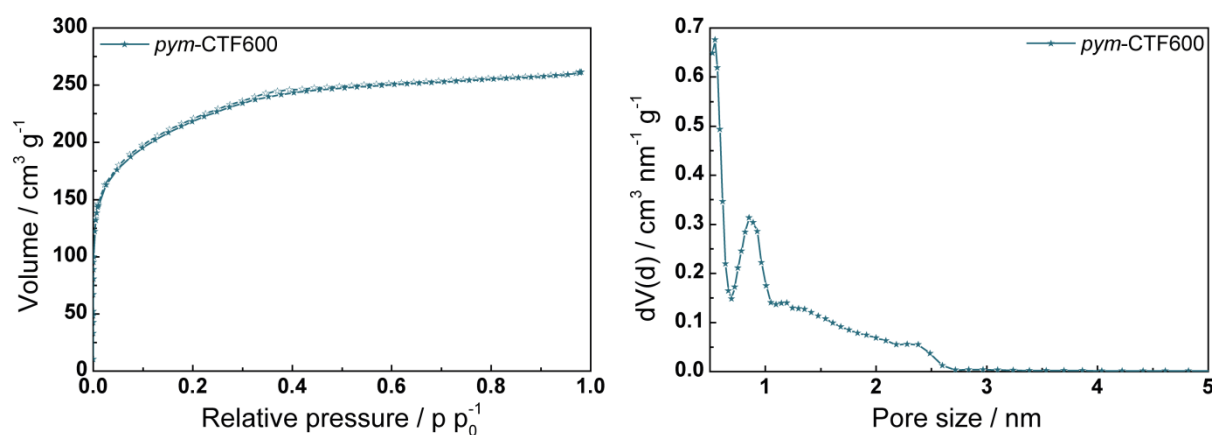
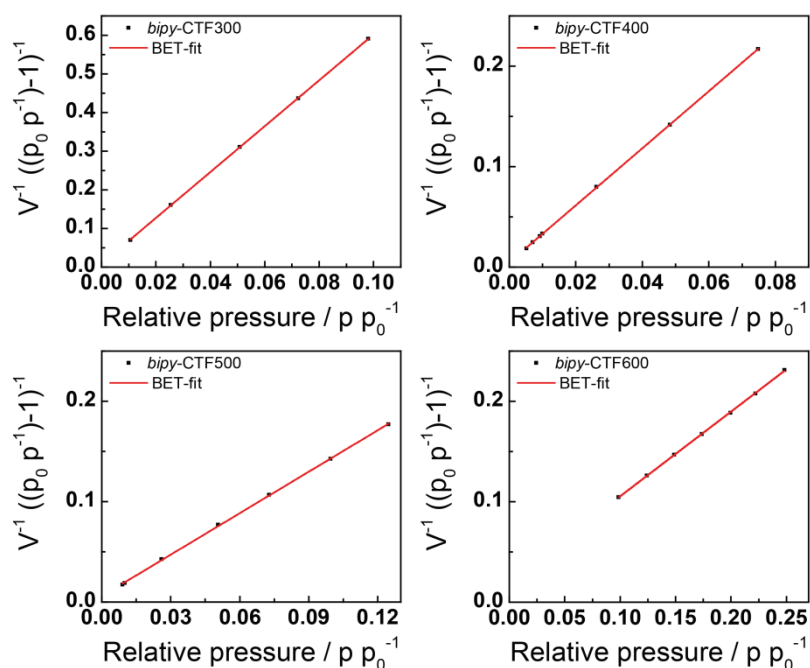


Figure 8.1.3.4. Argon adsorption (filled symbols) and desorption (open symbols) isotherm (left) and pore size distribution (right) of *pym*-CTF600.

Table 8.1.3.4. Ar sorption characteristics of the presented CTFs.

Sample	BET SA ^a	DFT _{Ar} SA ^b	DFT _{Ar,mic} SA ^c	Pore Volume [cm ³ g ⁻¹]		
	[m ² g ⁻¹]	[m ² g ⁻¹]	[m ² g ⁻¹]	V _{Ar,mic,DFT} ^d	V _{Ar,tot,DFT} ^e	V _{Ar,mic,DFT} /V _{Ar,tot,DFT}
<i>pym</i> -CTF300	1.50	-	-	-	-	-
<i>pym</i> -CTF350	3.51	-	-	-	-	-
<i>pym</i> -CTF400	0.45	-	-	-	-	-
<i>pym</i> -CTF500	208	-	-	-	-	-
<i>pym</i> -CTF600	689	729	705	0.28	0.32	0.88
CTF1-400	610	725	705	0.25	0.32	0.78
CTF1-500	1830	1587	1322	0.69	1.07	0.64
CTF1-600	2479	2142	1084	0.63	2.15	0.29
<i>bipy</i> -CTF300	360	-	-	-	-	-
<i>bipy</i> -CTF400	753	794	776	0.31	0.33	0.94
<i>bipy</i> -CTF500	1548	1523	1480	0.64	0.71	0.90
<i>bipy</i> -CTF600	2479	2008	1817	0.98	1.24	0.79
<i>lut</i> -CTF300	486	620	615	0.21	0.21	0.97
<i>lut</i> -CTF350	635	786	771	0.25	0.28	0.89
<i>lut</i> -CTF400	968	1062	1042	0.38	0.42	0.90
<i>lut</i> -CTF500	1680	1556	1470	0.69	0.82	0.84
<i>lut</i> -CTF600	2815	2046	1586	0.93	1.54	0.60

^aFrom Ar sorption measurements. ^bCalculated from the Ar QSDFT model. ^cSurface area of pores smaller than 2 nm calculated from the Ar QSDFT model. ^dPore volume for pores smaller than 2 nm calculated from the Ar QSDFT model. ^eTotal pore volume from the Ar QSDFT model.

BET fitting**Figure 8.1.3.5.** BET plots of *bipy*-CTFs.

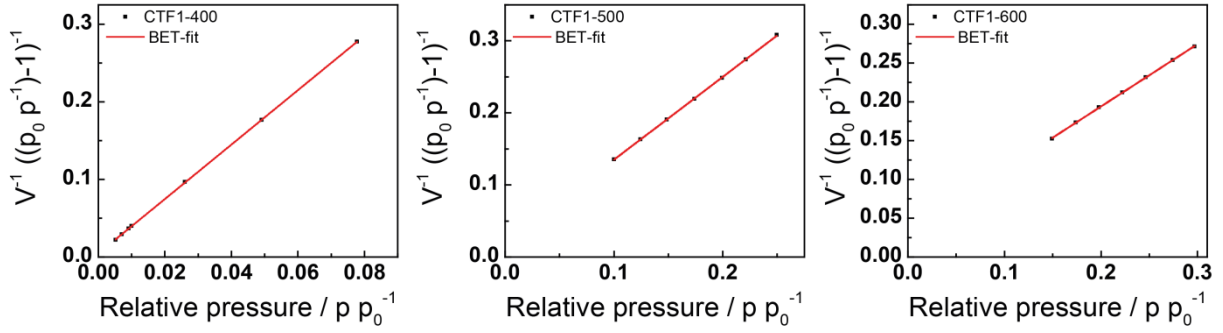


Figure 8.1.3.6. BET plots of CTF1s.

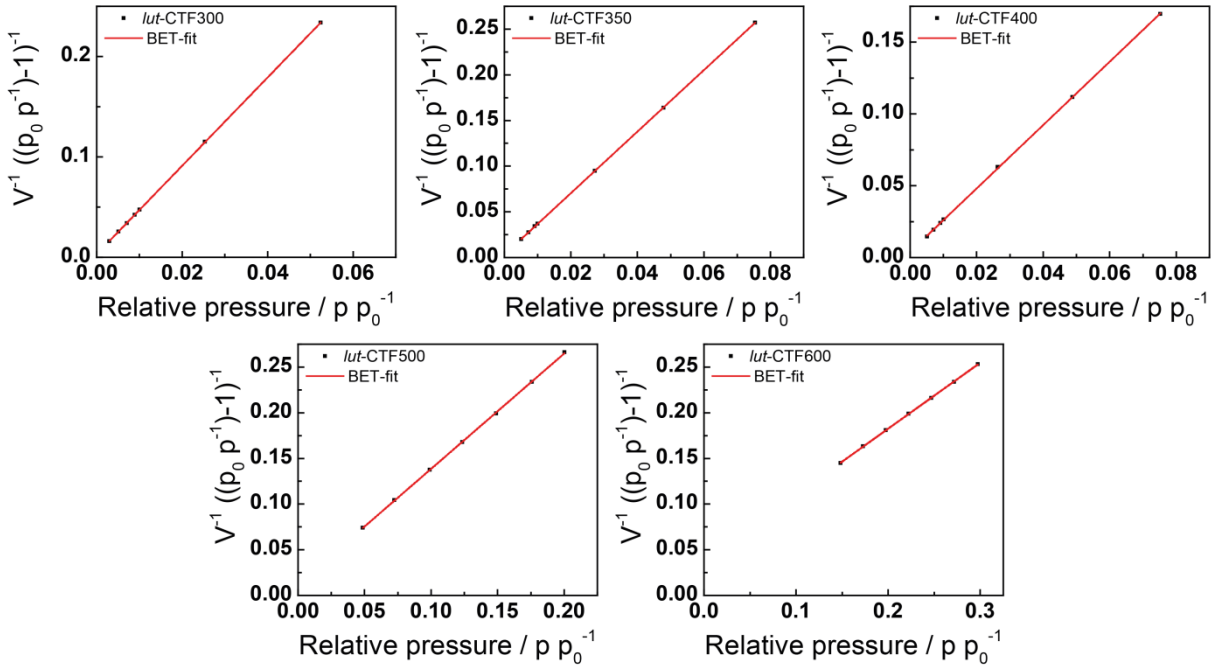


Figure 8.1.3.7. BET plots of lut-CTFs.

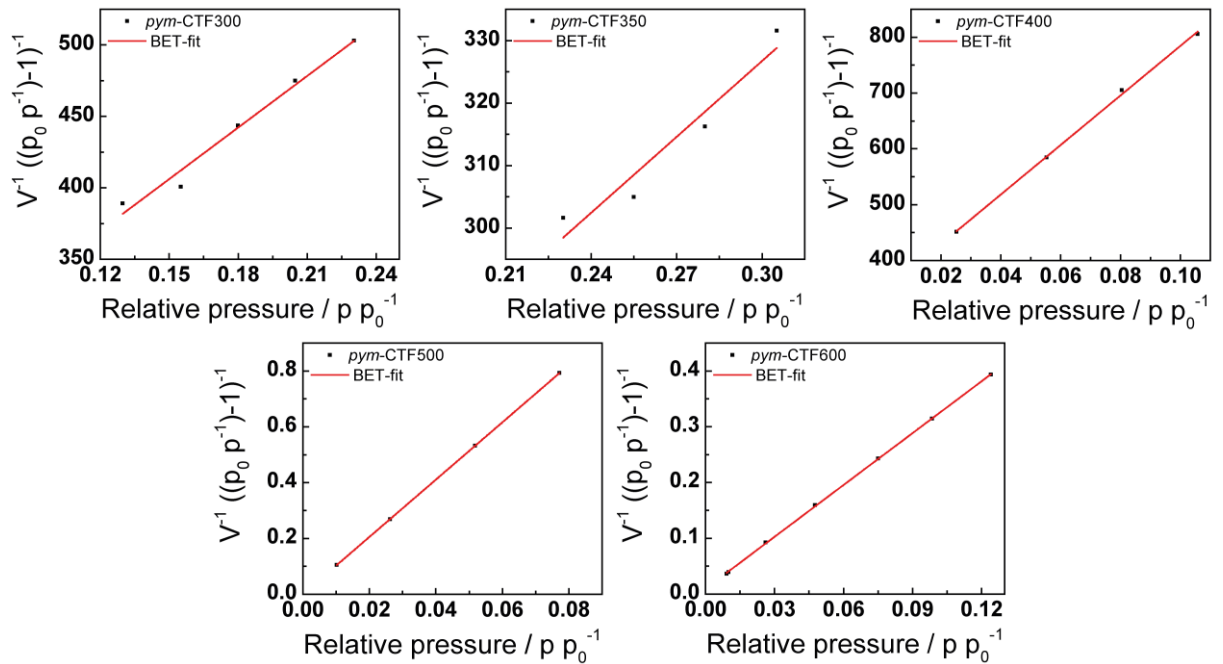


Figure 8.1.3.8. BET plots of pym-CTFs.

Table 8.1.3.5. Fitting parameters of the BET plots.

Sample	BET SA [$\text{m}^2 \text{g}^{-1}$]	Slope	Intercept	C constant
<i>pym</i> -CTF300	1.497	1203.895	2.256E+02	6.337
<i>pym</i> -CTF350	3.508	404.879	2.053E+02	2.972
<i>pym</i> -CTF400	0.448	4438.993	3.406E+02	14.032
<i>pym</i> -CTF500	208.469	10.268	1.261E-04	81422
<i>pym</i> -CTF600	688.573	3.099	9.651E-03	322.132
CTF1-400	609.611	3.507	4.610E-03	761.619
CTF1-500	1829.633	1.150	2.000E-02	58.506
CTF1-600	2557.060	0.804	3.327E-02	25.162
<i>bipy</i> -CTF300	360.197	5.934	8.672E-03	685.304
<i>bipy</i> -CTF400	752.799	2.839	4.730E-03	601.178
<i>bipy</i> -CTF500	1547.863	1.377	5.863E-03	235.887
<i>bipy</i> -CTF600	2479.034	0.842	2.122E-02	40.691
<i>lut</i> -CTF300	486	4.398	3.183E-03	1382.902
<i>lut</i> -CTF350	635	3.367	3.165E-03	1064.887
<i>lut</i> -CTF400	968	2.207	3.995E-03	553.489
<i>lut</i> -CTF500	1680	1.262	1.236E-02	103.084
<i>lut</i> -CTF600	2815	0.722	3.805E-02	19.985

Pore size distribution fittings

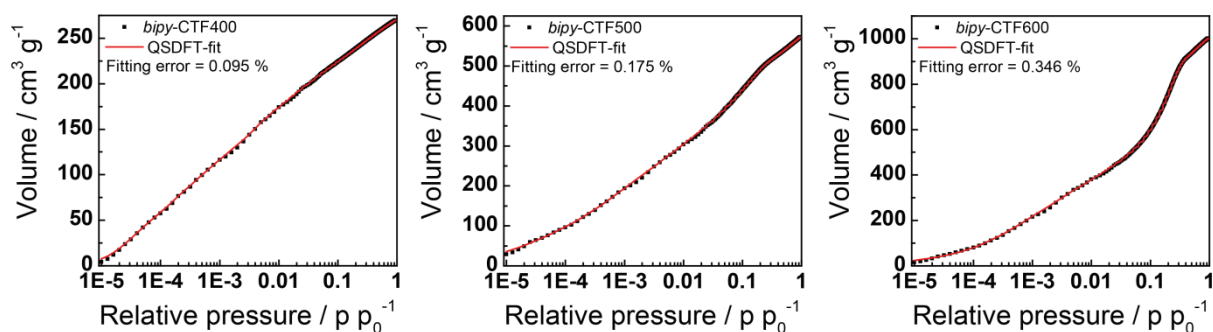
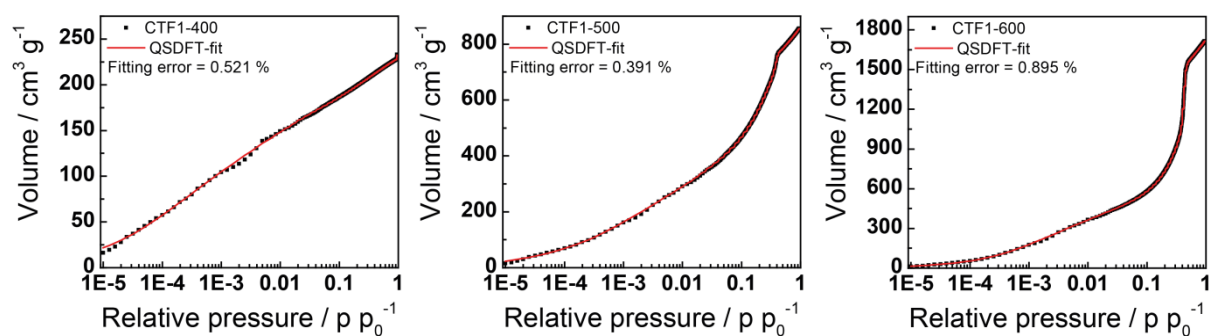
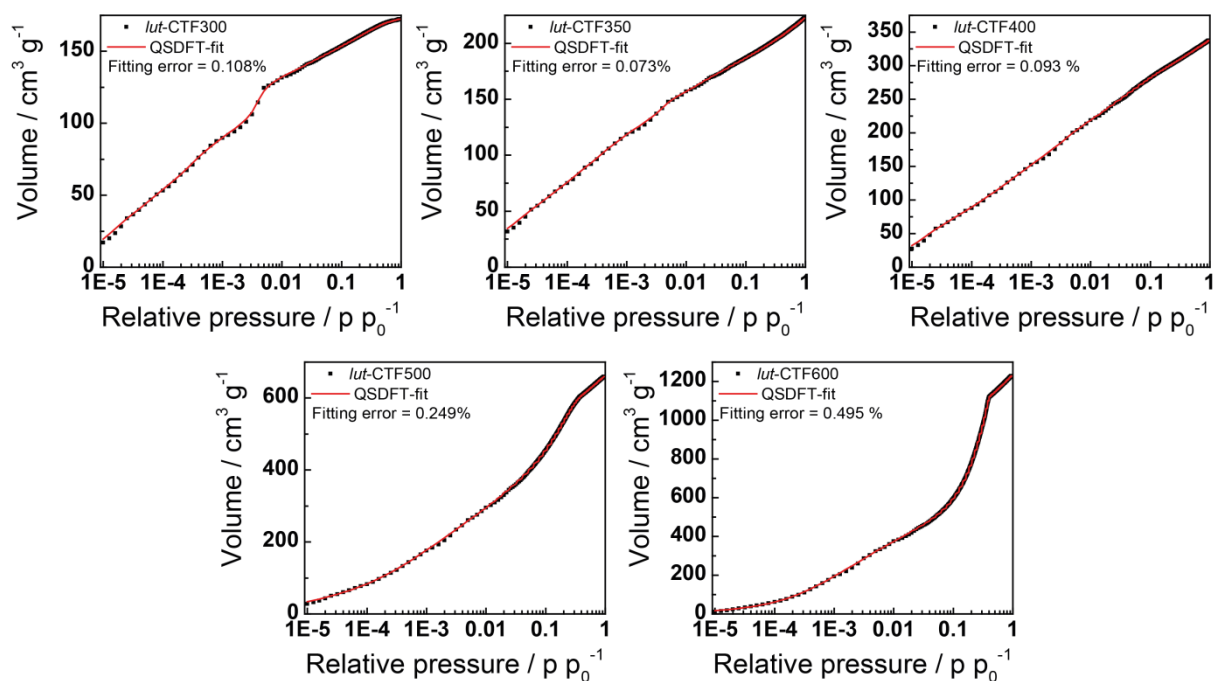
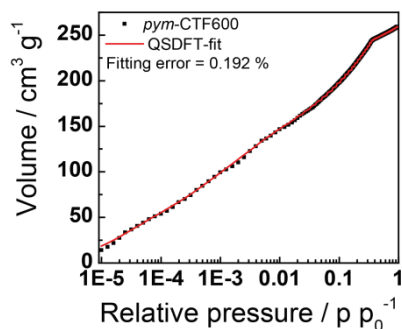
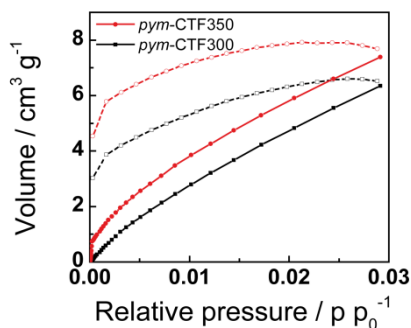
Figure 8.1.3.9. QSDFT fittings of *bipy*-CTFs.

Figure 8.1.3.10. QSDFT fittings of CTF1s.

Figure 8.1.3.11. QSDFT fittings of *lut*-CTFs.Figure 8.1.3.12. QSDFT fitting of *pym*-CTF600.

Carbon dioxide physisorption measurements

Carbon dioxide isotherms

Figure 8.1.3.13. Carbon dioxide adsorption (filled symbols) and desorption (open symbols) isotherms of *pym*-CTF300 and *pym*-CTF350 measured at 273 K.

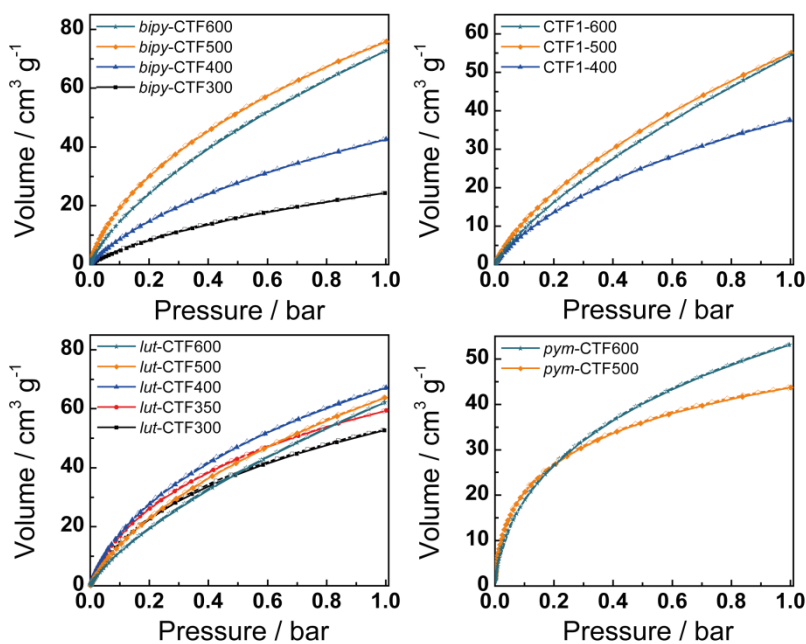


Figure 8.1.3.14. Carbon dioxide adsorption (filled symbols) and desorption (open symbols) isotherms of *bipy*-CTFs, CTF1s, *lut*-CTFs and *pym*-CTFs measured at 298 K.

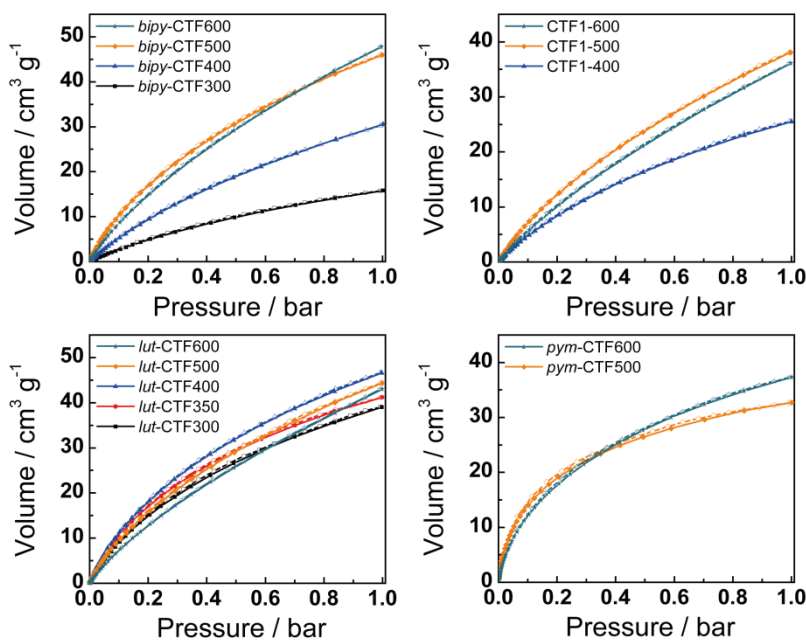


Figure 8.1.3.15. Carbon dioxide adsorption (filled symbols) and desorption (open symbols) isotherms of *bipy*-CTFs, CTF1s, *lut*-CTFs and *pym*-CTFs measured at 313 K.

Table 8.1.3.6. CO₂ sorption characteristics of the presented CTFs.

Sample	DFT _{CO₂} SA ^d [m ² g ⁻¹]	CO ₂ uptake [mg g ⁻¹]		
		273 K	298 K	313 K
<i>pym</i> -CTF300	69	11	-	-
<i>pym</i> -CTF350	76	13	-	-
<i>pym</i> -CTF400	97	18	-	-
<i>pym</i> -CTF500	618	110	71	51
<i>pym</i> -CTF600	783	133	86	58
CTF1-400	672	113	61	39
CTF1-500	1014	170	89	59
CTF1-600	1072	175	89	56
<i>bipy</i> -CTF300	449	75	39	24
<i>bipy</i> -CTF400	734	123	69	47
<i>bipy</i> -CTF500	1253	214	123	71
<i>bipy</i> -CTF600	1339	223	118	74
<i>lut</i> -CTF300	850	145	86	60
<i>lut</i> -CTF350	950	162	96	64
<i>lut</i> -CTF400	1066	182	109	72
<i>lut</i> -CTF500	1178	202	103	69
<i>lut</i> -CTF600	1206	200	101	66

^aFrom Ar sorption measurements. ^bCalculated from the Ar QSDFT model. ^cSurface area of pores smaller than 1.5 nm calculated from the Ar QSDFT model. ^dCalculated from the CO₂ NLDFT model. ^ePore volume for pores smaller than 2 nm calculated from the Ar QSDFT model. ^fTotal pore volume from the Ar QSDFT model.

Heats of adsorption

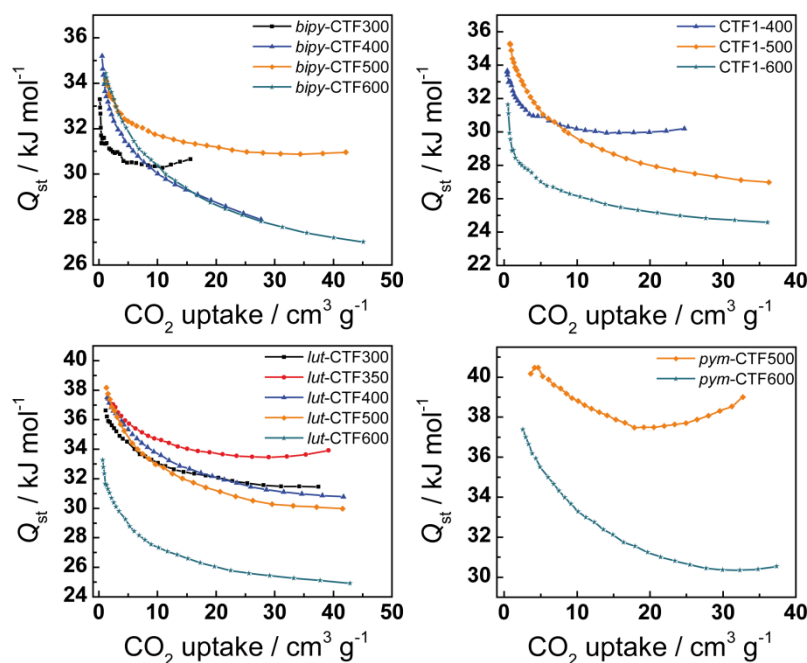


Figure 8.1.3.16. Heats of adsorption of *bipy*-CTFs, CTF1s, *lut*-CTFs and *pym*-CTFs calculated from the carbon dioxide isotherms measured at 273 K, 298 K and 313 K.

Pore size distribution fittings

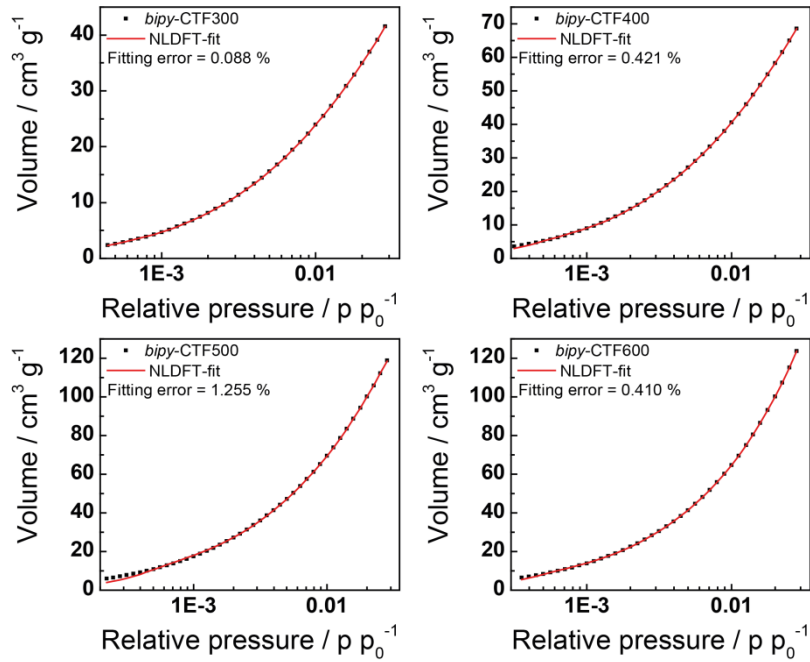
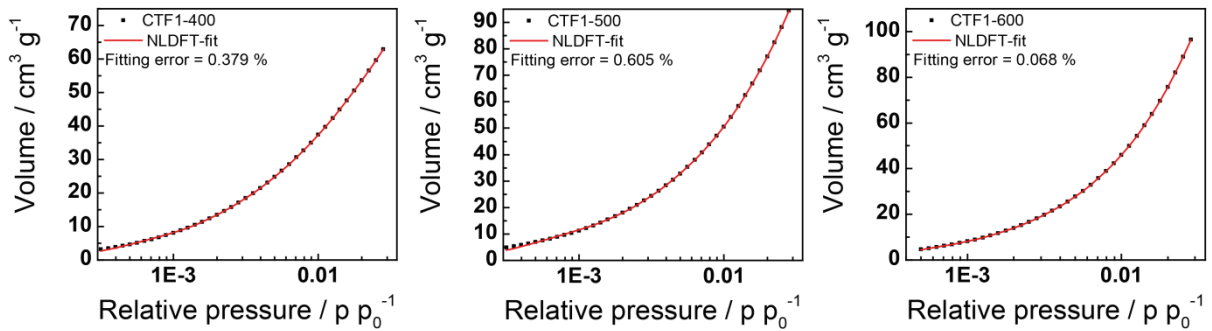
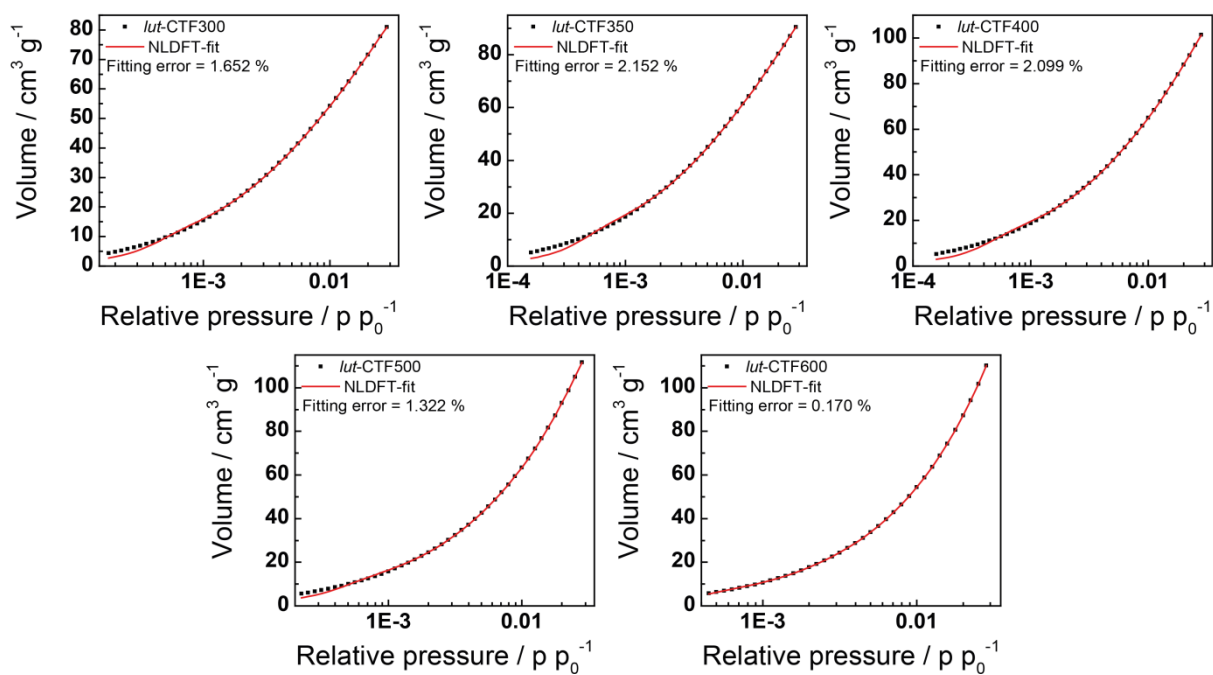
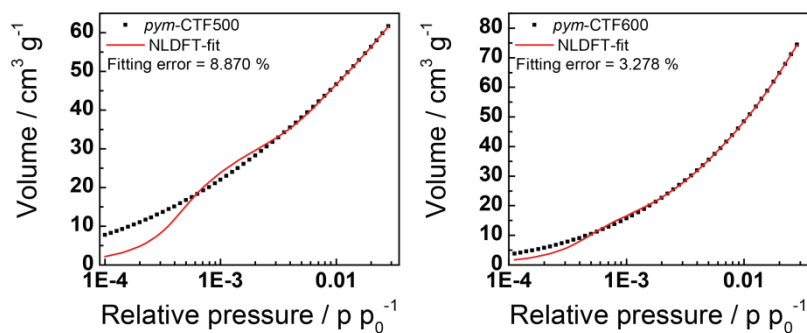
Figure 8.1.3.17. NLDFT fittings of *bipy*-CTFs.

Figure 8.1.3.18. NLDFT fittings of CTF1s.

Figure 8.1.3.19. NLDFT fittings of *lut*-CTFs.Figure 8.1.3.20. NLDFT fittings of *pym*-CTFs.

Nitrogen physisorption measurements

Nitrogen isotherms

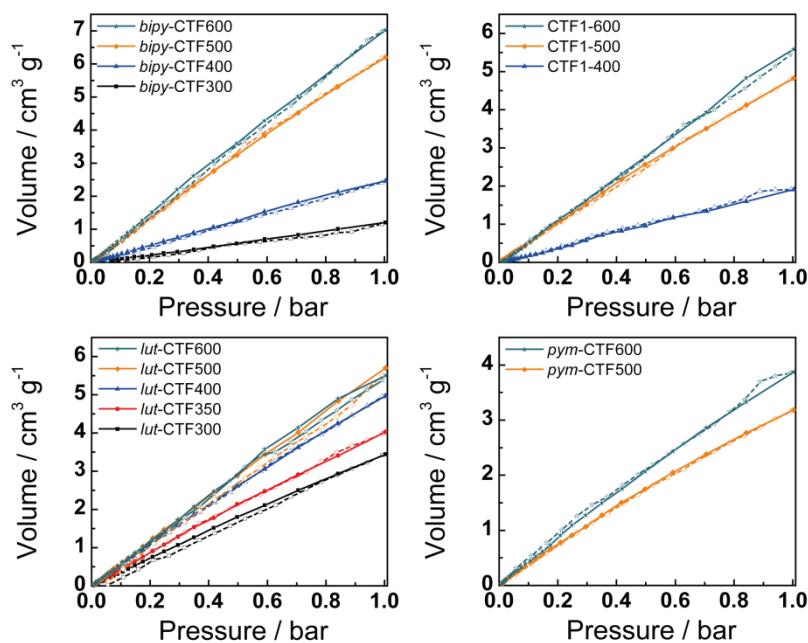


Figure 8.1.3.21. Nitrogen adsorption (filled symbols) and desorption (open symbols) isotherms of *bipy*-CTFs, CTF1s, *lut*-CTFs and *pym*-CTFs measured at 298 K.

Hydrogen physisorption measurements

Hydrogen isotherms

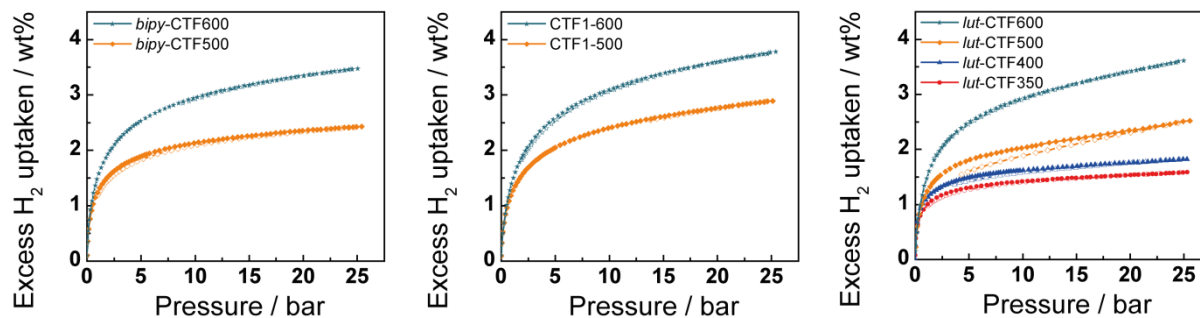


Figure 8.1.3.22. Hydrogen adsorption (filled symbols) and desorption (open symbols) isotherms of *bipy*-CTF500 and 600, CTF1-500 and 600 and *lut*-CTF350-600 measured at 87 K.

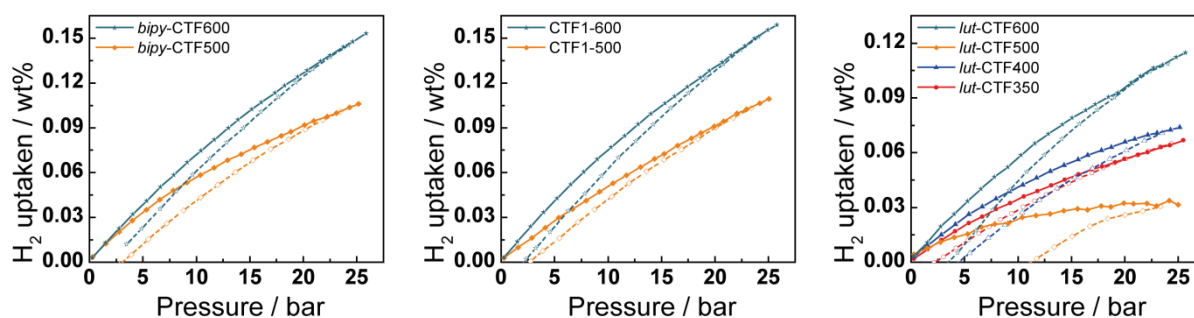


Figure 8.1.3.23. Hydrogen adsorption (filled symbols) and desorption (open symbols) isotherms of *bipy*-CTF500 and 600, CTF1-500 and 600 and *lut*-CTF350-600 measured at 298 K.

Heats of adsorption

The isosteric heat of adsorption is calculated from the measured absolute isotherms according to the Clausius-Clapeyron equation

$$\Delta H = R \cdot \left(\frac{\partial \ln(P)}{\partial \frac{1}{T}} \right)_{\theta} \quad (1)$$

where θ is the surface coverage, R is the gas constant, P the pressure and T the temperature. Therefore, $\ln(P)$ is plotted versus the reciprocal temperature $1/T$ for different surface coverages θ . The slope of the linear fit to these data for each surface coverage θ is proportional to the isosteric heat of adsorption.

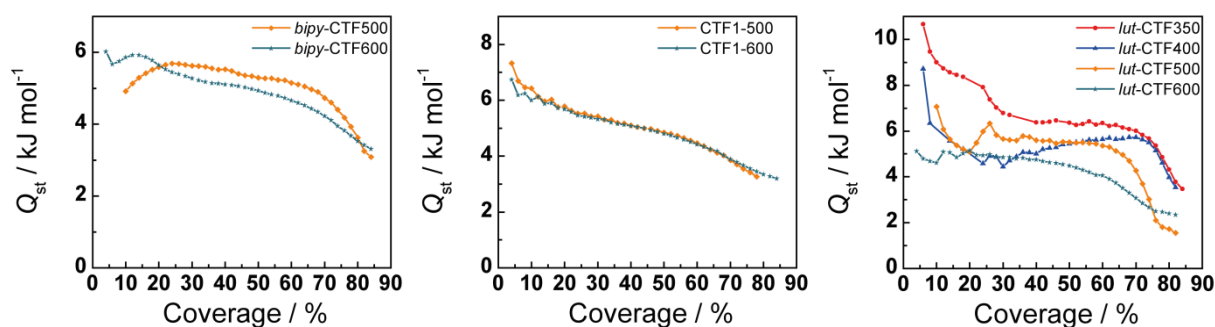


Figure 8.1.3.24. Heats of adsorption (Q_{st}) of *bipy*-CTF500 and 600, CTF1-500 and 600 and *lut*-CTF350-600 calculated from the absolute hydrogen isotherms (77-87 K) as a function of the normalized surface coverage.

CO₂/N₂ selectivity studies

Henry calculation

For selectivity calculations the ratio of the initial slopes in the Henry region of the adsorption isotherms of two different gases can be used. The calculated values of the initial slopes are shown in Figures 8.1.3.26-33.

IAST calculation

Ideal adsorbed solution theory (IAST) calculations can be done by using a single or dual-site Langmuir model to fit the adsorption isotherms.^[6]

The single-site Langmuir model is defined as,

$$q = \frac{q_{sat} bp}{1+bp} \quad (2)$$

q = molar loading of adsorbate

q_{sat} = saturation loading

b = Langmuir constant

The dual-site Langmuir model is defined as

$$q = q_A + q_B = \frac{q_{sat,A} b_A p}{1+b_A p} + \frac{q_{sat,B} b_B p}{1+b_B p} \quad (3)$$

A, B = distinct adsorption sites

For the fitting of the carbon dioxide adsorption isotherms the dual-site Langmuir model was used and for the fitting of the nitrogen adsorption isotherms the single-site Langmuir model. The values of the parameters are shown in Table 8.1.3.7 and the fitted graphs in Figures 8.1.3.34-41.

The IAST gives the analytic relationship of two functions $q_1(p)$ and $q_2(p)$ for two different gases by

$$\int_0^{x_1} \frac{P_t y_1}{x_1} q_1(p) d \ln p = \int_0^{x_2} \frac{P_t y_2}{x_2} q_2(p) d \ln p \quad (4)$$

where P_t is the total pressure of the gas mixture, y_i the mole fraction of component i in the gas phase and x_i the mole fraction of component i in the adsorbed phase. Integration of (4) with two single-site Langmuir functions leads to

$$q_{sat1} \ln \left(1 + b_1 \frac{P_t y_1}{x_1} \right) = q_{sat2} \ln \left(1 + b_2 \frac{P_t y_2}{x_2} \right) \quad (5)$$

The values of y_1 and y_2 are known and the ones of q_{sat1} , q_{sat2} , b_1 and b_2 are obtained from the Langmuir fits. Additionally, it holds that

$$x_1 + x_2 = 1 \quad (6)$$

Therefore x_1 and x_2 can be calculated for specified quantities of P_t . The calculations were done with the software Mathematica 9 (Wolfram, UK).

Finally, the selectivities are calculated using the following equation

$$S = \frac{x_1/y_1}{x_2/y_2} \quad (7)$$

A CO₂:N₂ ratio of 15:85 was used for calculating the gas mixture selectivities.

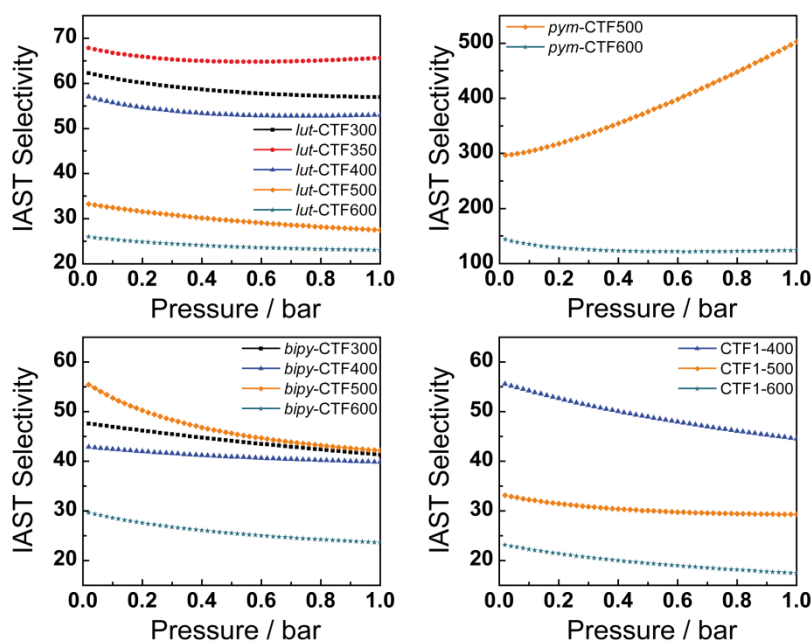


Figure 8.1.3.25. IAST selectivities of *bipy*-CTFs, CTF1s, *lut*-CTFs and *pym*-CTFs at 298 K with a 15:85 CO₂:N₂ ratio.

Table 8.1.3.7. Fitting parameters of the IAST plots.

Sample	Gas	$q_{sat,A}$	b_A	$q_{sat,B}$	b_B
<i>pym</i> -CTF500	CO ₂	0.5404	79.73967	1.70387	2.49376
	N ₂	0.6491	0.24615	-	-
<i>pym</i> -CTF600	CO ₂	0.51794	43.82065	2.86011	1.32712
	N ₂	1.14969	0.15706	-	-
CTF1-400	CO ₂	3.2527	0.61394	0.32763	7.07509
	N ₂	80.58168	9.57E-04	-	-
CTF1-500	CO ₂	0.3398	13.2154	6.20119	0.44547
	N ₂	1.85383	0.11722	-	-
CTF1-600	CO ₂	0.27196	10.23881	9.32725	0.26527
	N ₂	948.30839	2.37E-04	-	-
<i>bipy</i> -CTF300	CO ₂	0.37993	3.4166	2.50461	0.38096
	N ₂	449.91807	1.05E-04	-	-
<i>bipy</i> -CTF400	CO ₂	4.31678	0.44452	0.45274	5.72496
	N ₂	2.41643	0.04332	-	-
<i>bipy</i> -CTF500	CO ₂	0.59365	18.78141	6.20205	0.67451
	N ₂	3.19547	8.53E-02	-	-
<i>bipy</i> -CTF600	CO ₂	0.4686	11.73146	8.94896	0.38902
	N ₂	4.84223	6.21E-02	-	-
<i>lut</i> -CTF300	CO ₂	3.38869	0.92137	0.55163	11.2968
	N ₂	1.96728	0.07603	-	-
<i>lut</i> -CTF350	CO ₂	3.72295	0.99063	0.58336	14.65592
	N ₂	1.6304	0.11014	-	-
<i>lut</i> -CTF400	CO ₂	4.82889	0.82036	0.57315	15.5234
	N ₂	1.86941	0.11991	-	-
<i>lut</i> -CTF500	CO ₂	6.71451	0.42763	0.6478	7.93072
	N ₂	5.5295	0.04325	-	-
<i>lut</i> -CTF600	CO ₂	0.35015	10.1128	9.02817	0.32263
	N ₂	2.76153	0.08948	-	-

Henry plots

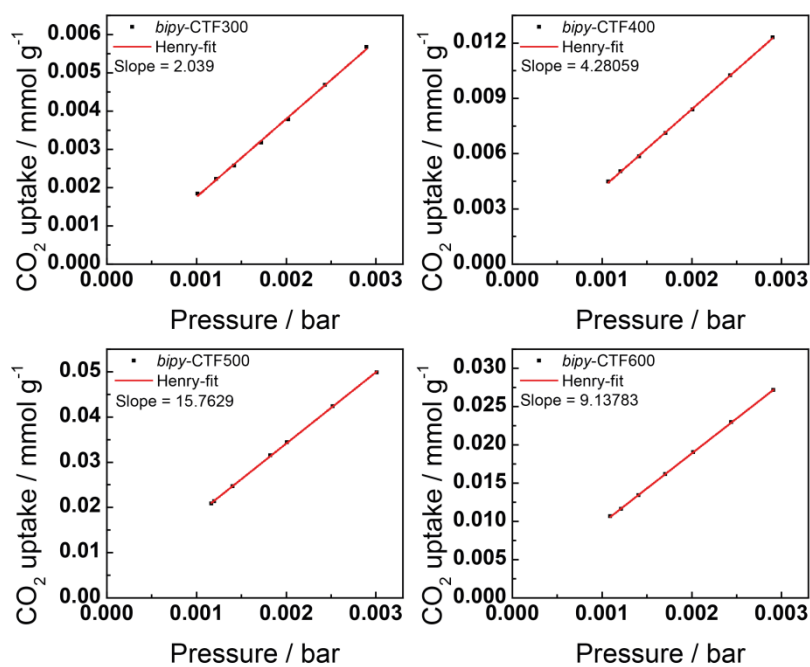


Figure 8.1.3.26. Henry plots of *bipy*-CTFs calculated from the carbon dioxide isotherms measured at 298 K.

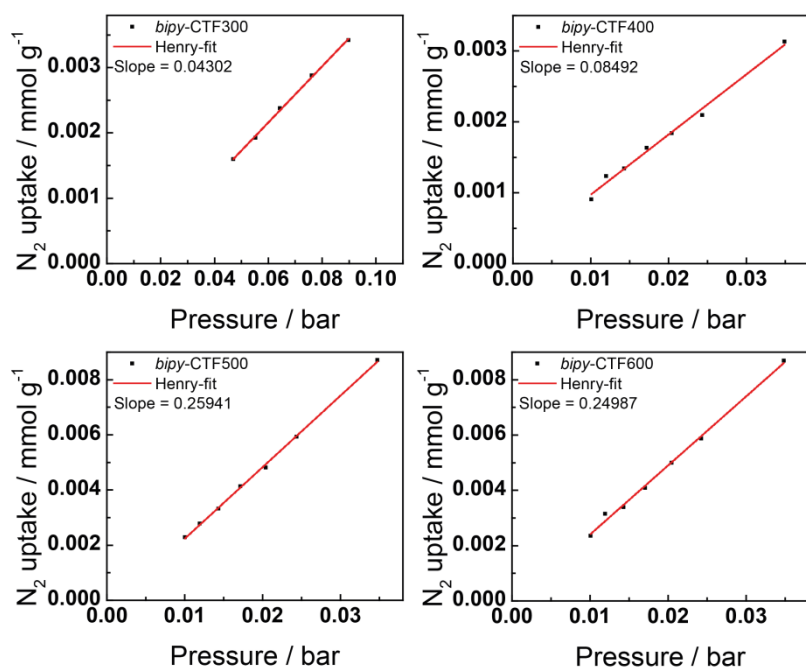


Figure 8.1.3.27. Henry plots of *bipy*-CTFs calculated from the nitrogen isotherms measured at 298 K.

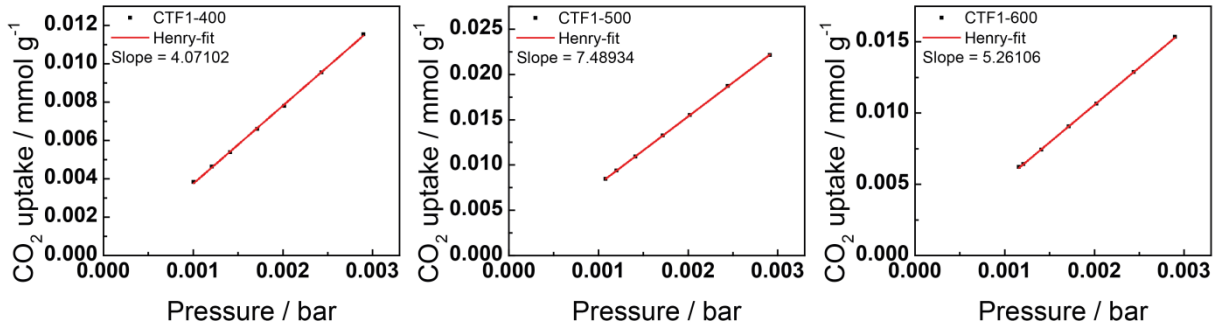


Figure 8.1.3.28. Henry plots of CTF1s calculated from the carbon dioxide isotherms measured at 298 K.

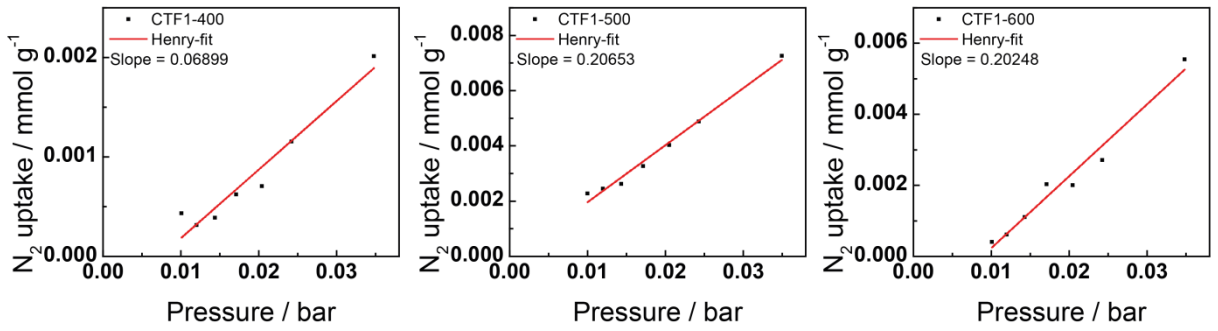


Figure 8.1.3.29. Henry plots of CTF1s calculated from the nitrogen isotherms measured at 298 K.

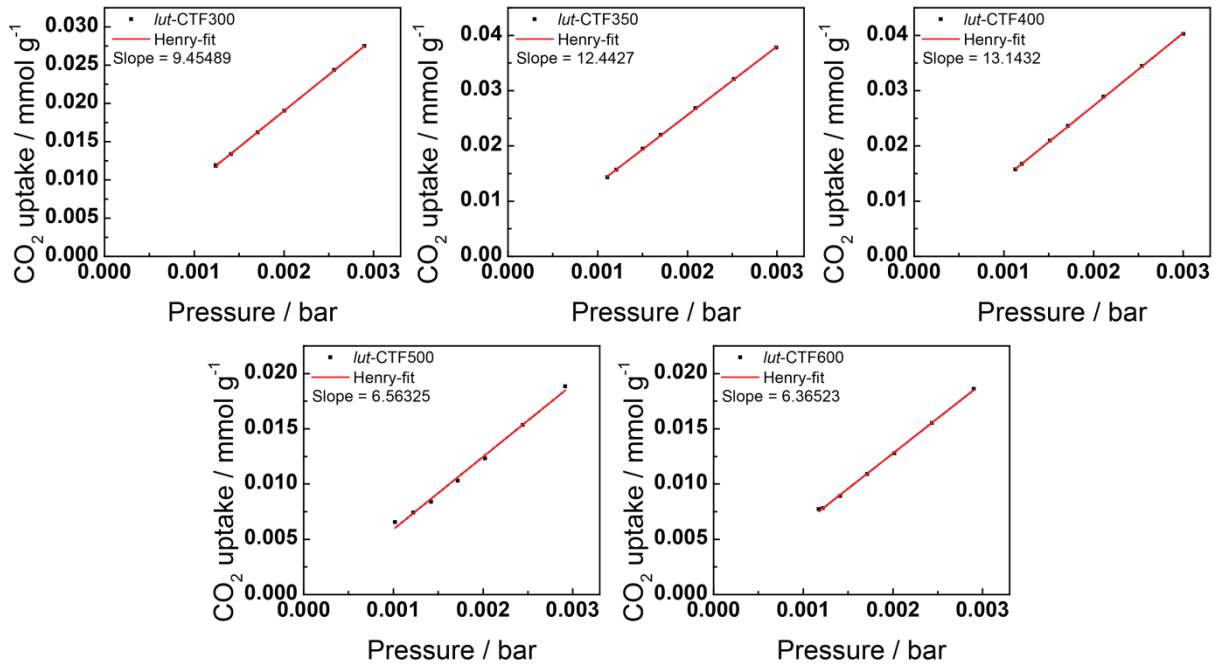


Figure 8.1.3.30. Henry plots of *lut*-CTFs calculated from the carbon dioxide isotherms measured at 298 K.

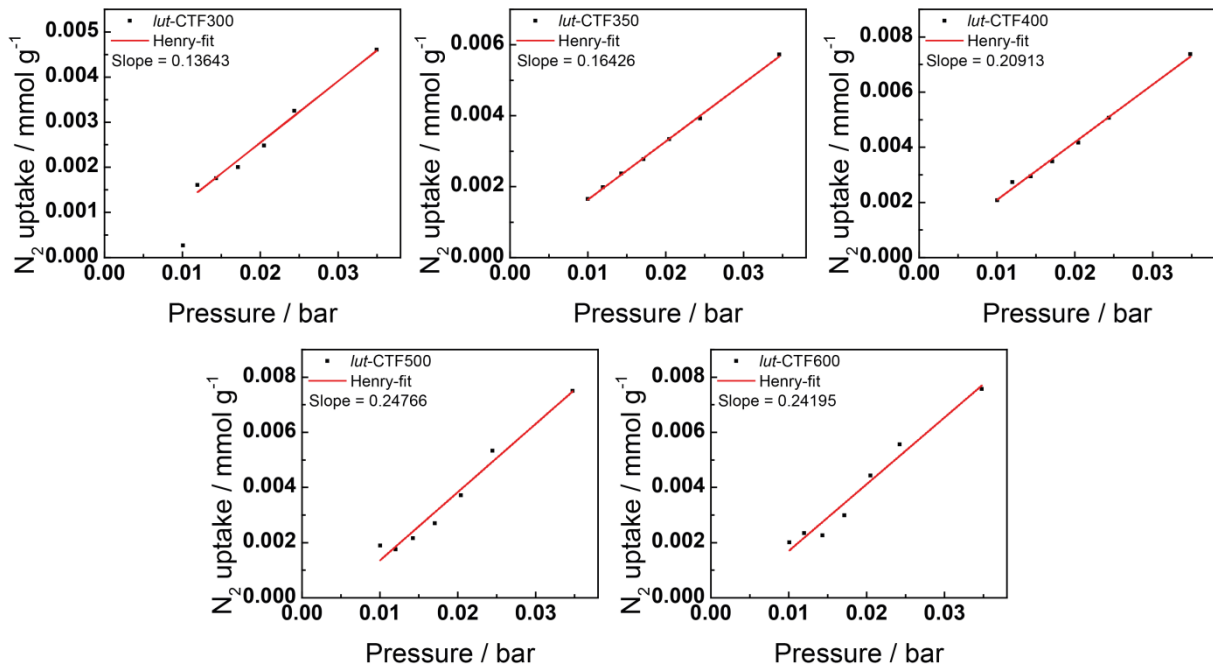


Figure 8.1.3.31. Henry plots of *lut*-CTFs calculated from the nitrogen isotherms measured at 298 K.

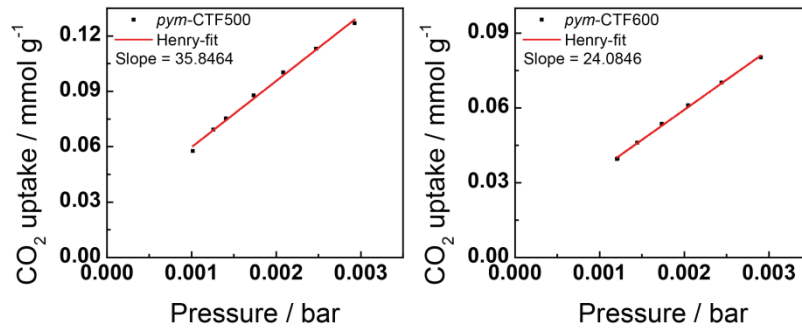


Figure 8.1.3.32. Henry plots of *pym*-CTFs calculated from the carbon dioxide isotherms measured at 298 K.

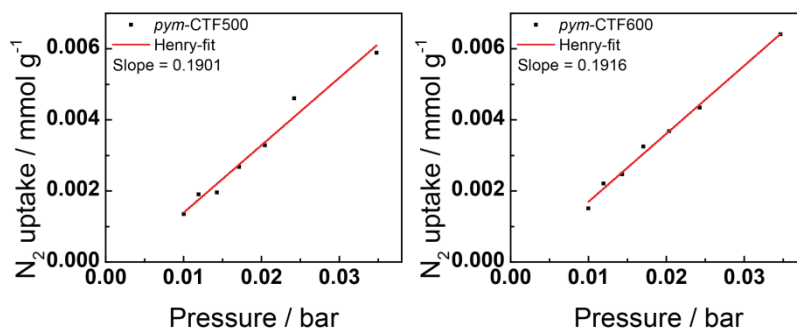
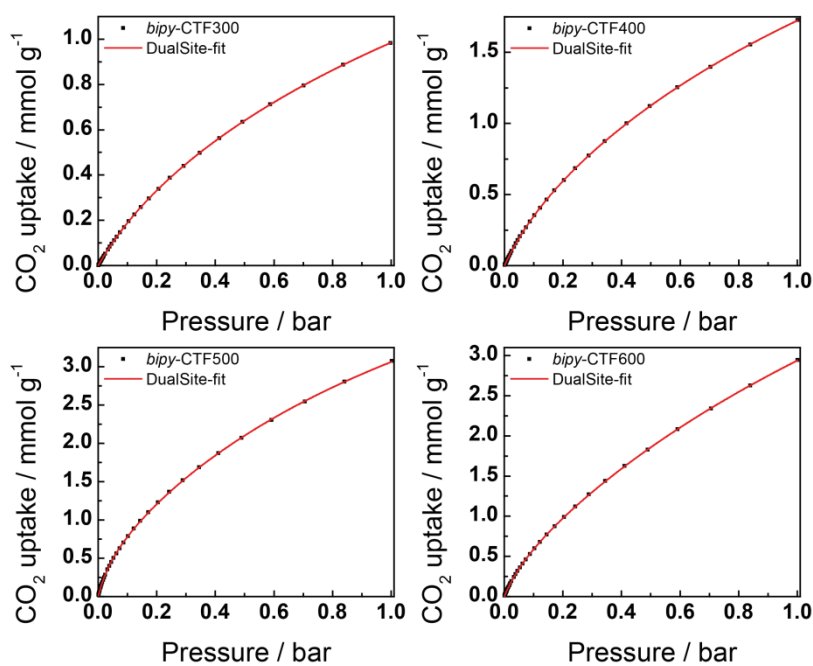
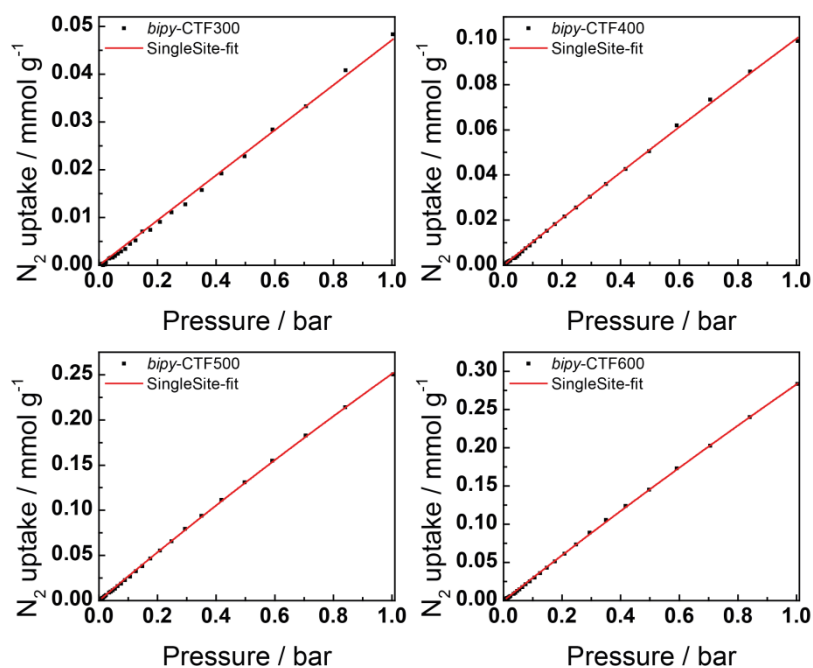


Figure 8.1.3.33. Henry plots of *pym*-CTFs calculated from the nitrogen isotherms measured at 298 K.

IAST plots

Figure 8.1.3.34. IAST plots of *bipy*-CTFs calculated from the carbon dioxide isotherms measured at 298 K.Figure 8.1.3.35. IAST plots of *bipy*-CTFs calculated from the nitrogen isotherms measured at 298 K.

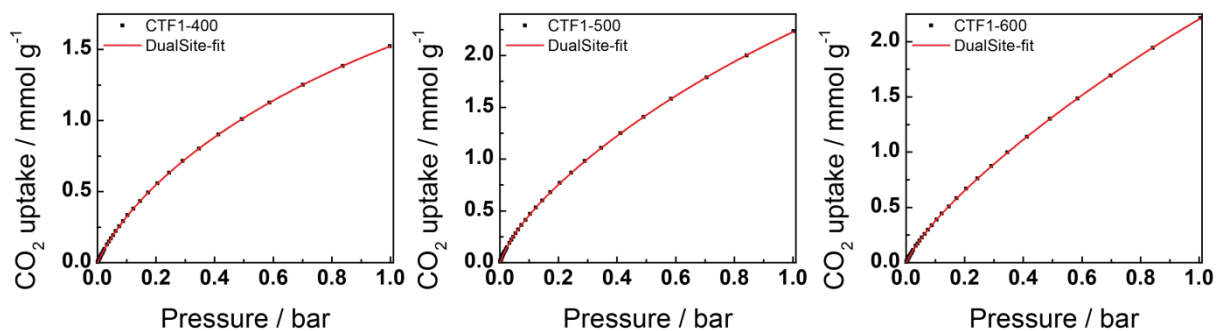


Figure 8.1.3.36. IAST plots of CTF1s calculated from the carbon dioxide isotherms measured at 298 K.

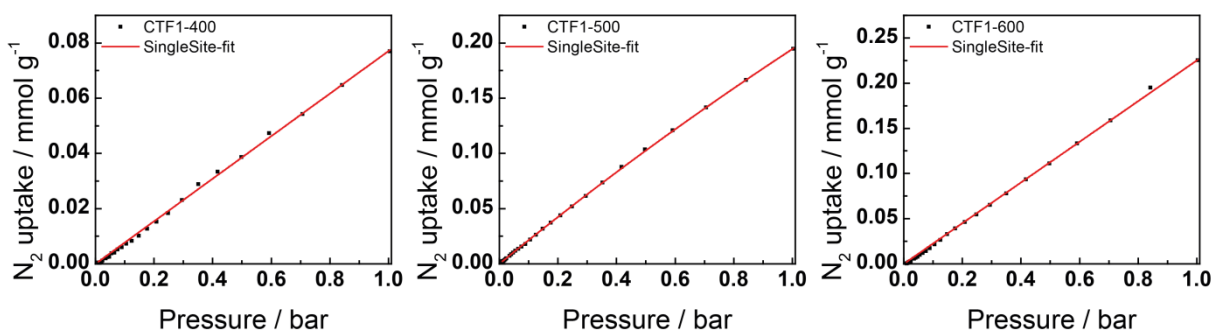


Figure 8.1.3.37. IAST plots of CTF1s calculated from the nitrogen isotherms measured at 298 K.

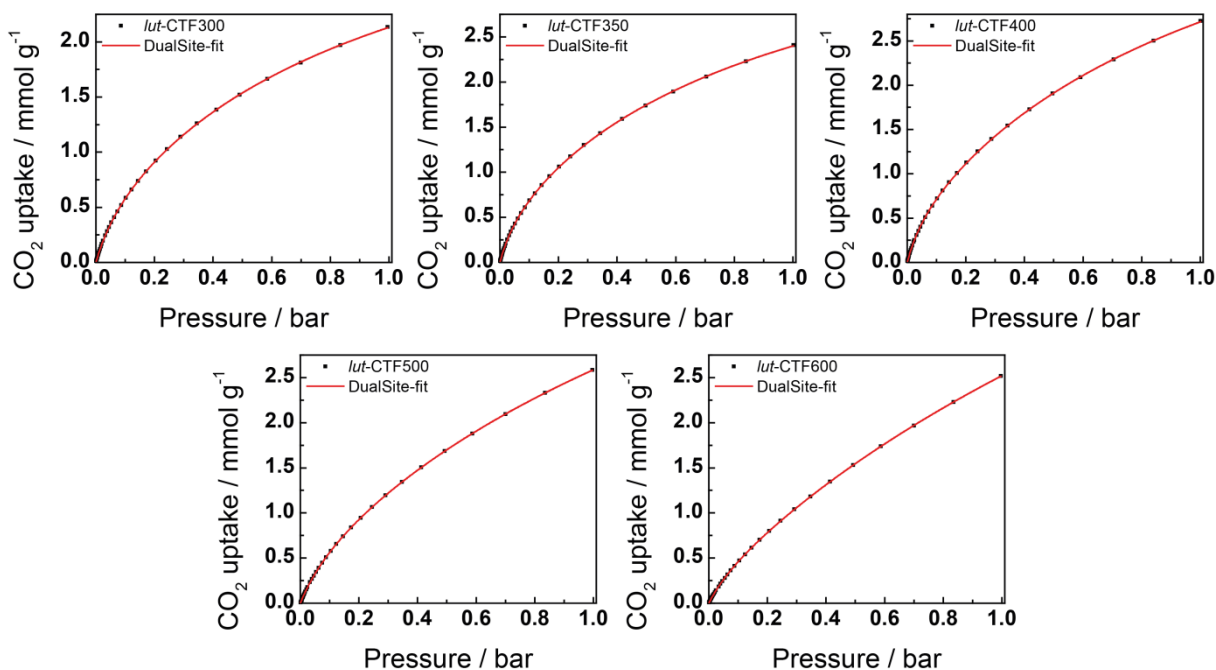


Figure 8.1.3.38. IAST plots of *lut*-CTFs calculated from the carbon dioxide isotherms measured at 298 K.

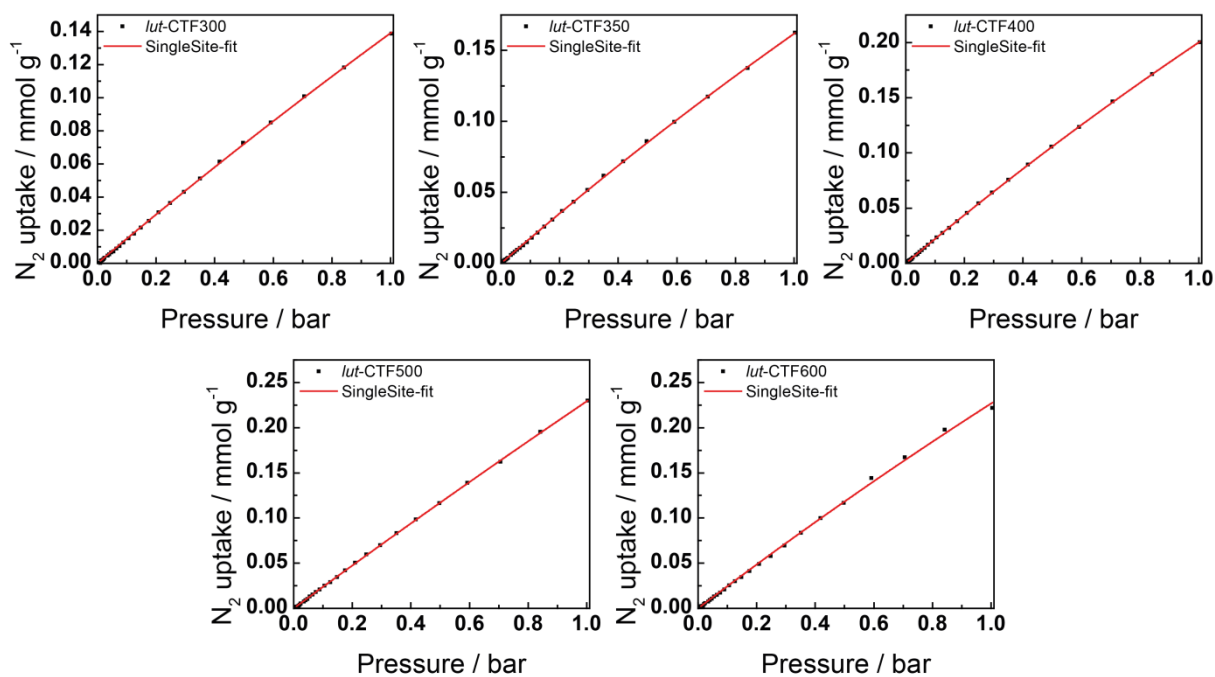


Figure 8.1.3.39. IAST plots of *lut*-CTFs calculated from the nitrogen isotherms measured at 298 K.

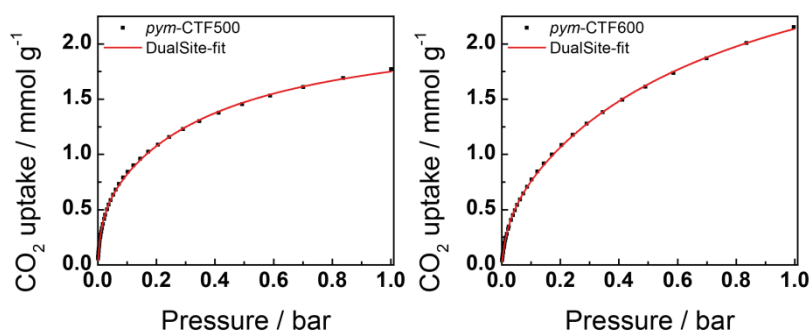


Figure 8.1.3.40. IAST plots of *pym*-CTFs calculated from the carbon dioxide isotherms measured at 298 K.

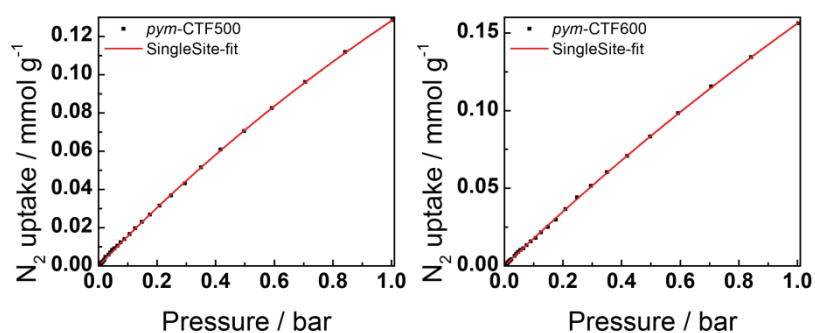


Figure 8.1.3.41. IAST plots of *pym*-CTFs calculated from the nitrogen isotherms measured at 298 K.

Correlation plots

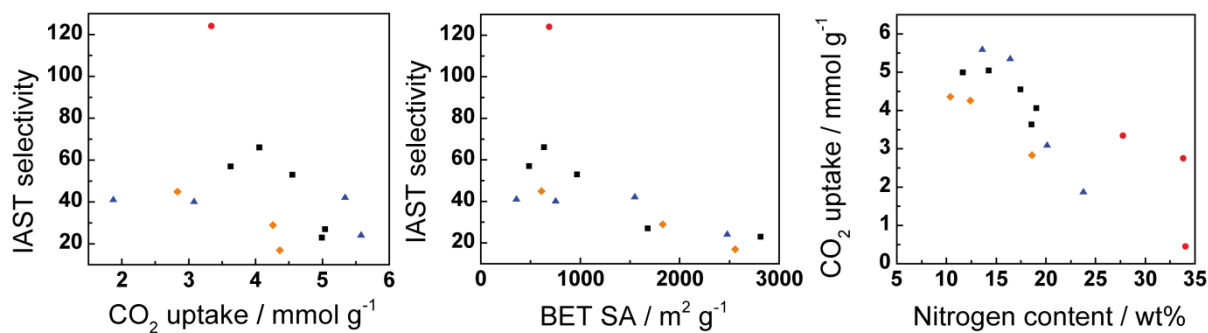


Figure 8.1.3.42. Correlations between IAST selectivity and CO₂ uptake (left) and between IAST selectivity and BET SA (middle), and correlations between the CO₂ uptake and the nitrogen content (right): *lut*-CTFs (black squares), *pym*-CTFs (red circles) *bipy*-CTFs (blue triangles) and CTF1s (orange diamonds).

References

- [1] S. Hug, M. E. Tauchert, S. Li, U. E. Pachmayr, B. V. Lotsch, *J. Mater. Chem.* **2012**, *22*, 13956-13964.
- [2] A. Krasovskiy, P. Knochel, *Synthesis* **2006**, *2006*, 0890-0891.
- [3] F. M. Romero, R. Ziesel, *Tetrahedron Lett.* **1995**, *36*, 6471-6474.
- [4] P. N. W. Baxter, J. A. Connor, *J. Organomet. Chem.* **1988**, *355*, 193-196.
- [5] G. Vlád, I. T. Horváth, *J. Org. Chem.* **2002**, *67*, 6550-6552.
- [6] A. L. Myers, J. M. Prausnitz, *AIChE J.* **1965**, *11*, 121-127.

8.2 LIST OF PUBLICATIONS

Published as part of this thesis

6. **A Fluorene based Covalent Triazine Framework with high CO₂ and H₂ Capture and Storage Capacities,**
Stephan Hug, Maria B. Mesch, Hyunchul Oh, Nadine Popp, Michael Hirscher, Jürgen Senker, Bettina V. Lotsch, *J. Mater. Chem. A* **2014**, 2, 5928-5936.
5. **A functional triazine framework based on N-heterocyclic building blocks,**
Stephan Hug, Michael E. Tauchert, Shen Li, Ursula E. Pachmayr, Bettina V. Lotsch, *J. Mater. Chem.* **2012**, 22, 13956-13964.

Not part of this thesis

4. **Cationically Charged Mn^{II}Al^{III} LDH Nanosheets by Chemical Exfoliation and Their Use As Building Blocks in Graphene Oxide-Based Materials**
Stephan Werner, Vincent Wing-hei Lau, Stephan Hug, Viola Duppel, Hauke Clausen-Schaumann, Bettina V. Lotsch, *Langmuir* **2013**, 29, 9199–9207.
3. **Li₂CaSi₂N₄ and Li₂SrSi₂N₄ – a Synthetic Approach to Three-Dimensional Lithium Nitridosilicates,**
Martin Zeuner, Sandro Pagano, Stephan Hug, Philipp Pust, Sebastian Schmiechen, Christina Scheu, Wolfgang Schnick, *Eur. J. Inorg. Chem.* **2010**, 4945-4951.
2. **Single-Crystal Structure Determination and Solid-State NMR Investigations of Lithium Nitridosilicate Li₂SiN₂ Synthesized by a Precursor Approach Employing Amorphous “Si(CN₂)₂”**
Sandro Pagano, Martin Zeuner, Stephan Hug, Wolfgang Schnick, *Eur. J. Inorg. Chem.* **2009**, 1579-1584.
1. **Nickel-catalyzed cross-coupling reactions of benzylic zinc reagents with aromatic bromides, chlorides and tosylates,**
Matthias A. Schade, Albrecht Metzger, Stephan Hug, Paul Knochel, *Chem. Commun.* **2008**, 3046-3048.

8.3 CONTRIBUTIONS TO CONFERENCES

Oral presentations

1. A Fluorene-Based Covalent Triazine Framework for CO₂ Capture

Stephan Hug, Nadine Popp, Jürgen Senker, Bettina V. Lotsch

NIM Summer Retreat 2013, Jäger von Fall, Germany

Poster presentations

7. A Fluorene-based Covalent Triazine Framework

Stephan Hug, Bettina V. Lotsch

25. Deutsche Zeolith-Tagung 2013, Hamburg, Germany

6. Principles of Covalent Organic Framework Design

Stephan Hug, Bettina V. Lotsch

NIM Summer Retreat 2012, Garmisch-Partenkirchen, Germany

5. A new functional triazine framework based on N-heterocyclic building blocks

Stephan Hug, Michael E. Tauchert, Shen Li, Bettina V. Lotsch

NIM Summer Retreat 2011, Kampenwand, Germany

4. A new functional triazine framework based on N-heterocyclic building blocks

Stephan Hug, Michael E. Tauchert, Shen Li, Bettina V. Lotsch

NIM / CeNS Winterschool 2011, St. Christoph, Austria

3. A new functional triazine framework based on N-heterocyclic building blocks

Stephan Hug, Michael E. Tauchert, Shen Li, Bettina V. Lotsch

School Adsorption on Porous Materials 2011, Prague, Czech Republic

2. A new functional triazine framework based on N-heterocyclic building blocks

Stephan Hug, Michael E. Tauchert, Shen Li, Bettina V. Lotsch

23. Deutsche Zeolith-Tagung 2011, Erlangen, Germany

1. A new functional triazine framework based on N-heterocyclic building blocks

Stephan Hug, Michael E. Tauchert, Shen Li, Bettina V. Lotsch

CeNS Workshop 2010, Venice, Italy